A highly power efficient and miniaturised momentum bias wheel for pico-satellites.

PocketQube momentum bias wheel design and testing.

Master Graduation Thesis

Jari Pols

TU Delft

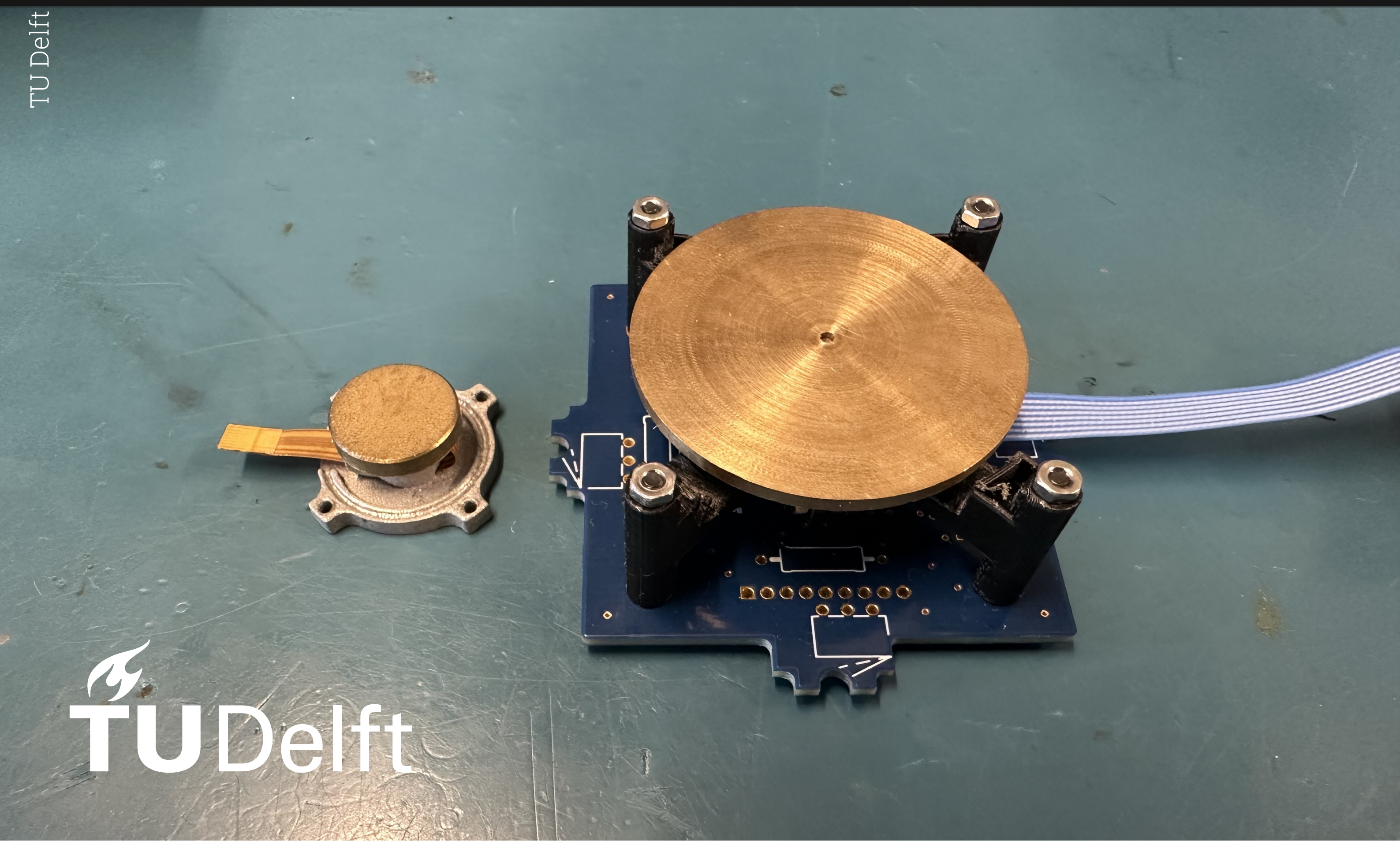

TU Delft

A highly power efficient and miniaturised momentum bias wheel for pico-satellites.

PocketQube momentum bias wheel design and testing.

by

Jari Pols

Supervisor:	Dr. Ir. J. Bouwmeester
Discipline:	Space Engineering
Thesis Duration:	February 12th, 2024 - December 19th, 2024
Faculty:	Faculty of Aerospace Engineering, Delft

Preface

The void of space is the new frontier of exploration. Unfortunately, nowadays it is impossible to board a big pirate ship and explore it all. To get from where we are today as a civilisation in terms of space exploration to the point where we can freely roam the galaxy, harvest the powers of the universe and go beyond borders our forefathers have set, we must continue to become more invested in people interested in space. Whether that would be engineering smaller and smaller satellites, finding the answer to life in the universe using the Fermi paradox, or modelling ultra-relativistic quantum molecular dynamics of the strange matter production in neutron stars.

For myself, ambition was adamant from a young age, leading to a fascination for physics and mechanics. This manifested into passion during my bachelor Mechanical Engineering and master track Space Engineering at the Delft University of Technology. With this thesis, I end the begin of my journey in the wonderful world of space engineering.

This thesis would not have been possible by the excellent and superior expertise of my supervisor Dr. Ir. Japser Bouwmeester. His guidance during the thesis have been adamant to a fulfilling research and design.

The testing phase has been aided by the motor expertise from Faulhaber through Wilbert van der Paal, ensuring the motor could run as efficiently as possible. The vibration testing went smoothly due to the clear instruction and guidance of PhD candidate Burhan Saify.

Last but certainly not least, I would like to thank my parents, without whom I would have never taken on this master as they have always encouraged me to reach for the highest possible level. I would like to thank my fiancée Joyce for always believing in me and supporting me mentally, and Vincent Hoogeboom for being my motivator as nearest competition and for keeping me in check.

Jari Pols
December 19th, 2024

Abstract

Since having set a new standard for small, low cost, technology demonstrating satellites, the Delft University of Technology continues development on its PocketQube satellite class to make sure everyone can access space through miniaturised technology. Through its students, the design, testing and integration of various satellite subsystems can be achieved, such as the reaction wheel or magnetorquer. A design of a momentum bias wheel fit for a PocketQube pico-satellite has not yet been achieved, for which this thesis is dedicated. Finding out whether designing and testing a momentum bias wheel using commercial off the shelf or self-manufactured parts is feasible and whether this concept at PocketQube scale is competitive with other attitude actuators. By realising that a reaction wheel delivers a pointing accuracy below 1 degrees and a magnetorquer delivers one above 5 degrees, a perfect range appears in which the momentum bias wheel can operate to fill this pointing accuracy gap. The momentum bias wheel is thus designed to be able to limit the effect of disturbances; internal and external; to a pointing accuracy of 1 to 5 degrees in a nadir-pointing attitude scheme.

By setting design requirements based on a statistically determined maximum aerodynamic disturbance torque over one orbit endured during the mission, deriving requirements from the PocketQube standard, and using the other attitude actuators to derive competitive requirements, a momentum bias wheel design can be created that can be competitive to the other actuators, perform under required environments and achieve the set out pointing accuracy. The momentum bias wheel must be able to attain and maintain an angular momentum of 6.05 $mNms$ due to the aerodynamics disturbance torque estimated at 83.3 μNm and must maintain a stability throughout its life of 0.180% as to stay within the desired pointing accuracy, while maximising itself to a power draw of 180 mW and weighing no more than 41.4 grams. The design is ultimately derived through three trade-off scenarios; for the motor, the flywheel and mounting of the components to each other. As power usage, size and mass are preliminary set requirement due to the fact of the undone system engineering for the next PocketQube mission, these criteria will be approached and are treated as loose requirements.

Having settled on a design utilising a Faulhaber vacuum proof 1509B motor and SC1801P speed controller, together with a bronze C67500 alloy lathed flywheel, mounted together utilising two PQ9 PCB's and an additively manufactured motor mount and flywheel reinforcement, which unfortunately did not meet the size and mass requirement through prototyping, testing the built prototype through operational, micro-vibration, shaker and vacuum tests were the final steps. The operational modes and analysis thereof for only the motor and the complete momentum bias wheel system confirmed that the momentum bias wheel was able to achieve the angular momentum, stability, the pointing accuracy and nadir-pointing requirement, but for more power than maximally allowed. The motor alone was able to perform the required angular velocity at 256 mW but the complete system was able to perform it at 534 mW. The imbalanced flywheel causes extra torque to be spun at high speeds, which is why the current draw is much high than with only the motor. Through micro-vibration and shaker testing was revealed that the designed mount, although made of plastic for the prototyping phase, was able to survive all its own induced vibrational forces and the launch induces stresses. A small amount of damage to the motor was detected through the decrease in performance post shaker test, meaning the flywheel reinforcement has to be revised. The vacuum test revealed that the steep power increase found during operational testing was due to the increased friction caused by the utilisation of a vacuum lubricant in atmospheric conditions.

Conclusively, a COTS momentum bias wheel for a PocketQube is not feasible, as meeting the technical budget requirements of a PocketQube mission is not feasible given the currently available COTS motors. Furthermore, the availability of high velocity miniaturised vacuum rated electric motors is central in the feasibility and competitiveness of wheeled attitude actuators. The competitiveness of this prototype to the proposed PocketQube reaction wheel systems comes down to the motor utilised. Designing and creating a wheeled attitude actuators borders on what is feasibly possible with commercially available parts.

Contents

List of Figures

List of Tables

Nomenclature

Abbreviation	Meaning
ABS	Acrylonitrile Butadiene Styrene
AC	Alternating Current
ACS	Attitude Control System
ADCS	Attitude Determination and Control System
BEMF	Back Electromotive Force
BLDC	Brushless Direct Current
CAD	Computer Aided Design
CNC	Computer Numerical Control
COM	Centre Of Mass
COTS	Commercial Of The Shelf
CMG	Control Moment Gyro
DC	Direct Current
DGCMG	Dual Gimbal Control Moment Gyro
DMM	Digital Multi-Meter
EDM	Electrical Discharge Machining
EO	Earth Observation
EOL	End Of Life
EoM	Equation(s) of Motion
EPS	Electrical Power System
FDM	Fused Deposition Modelling
LEO	Low Earth Orbit
MBW	Momentum Bias Wheel
MTQ	Magnetorquer
PLA	Polylactic Acid
PCB	Printed Circuit Board
PQ	PocketQube
PSU	Power Supply Unit
RWS	Reaction Wheel System
SLA	Stereolithography
SMAD	Space Mission and Design
SGCMG	Single Gimbal Control Moment Gyro
SRP	Solar Radiation Pressure
VSCMG	Variable Speed Control Moment Gyro
WMM	World Magnetic Model

Symbol	Description	Unit
A_r	Ram area	m^2
$B_\oplus$	Magnetic field magnitude of Earth	T
c_m	Centre of mass	m
c_p	Centre of pressure	m
C_0	Static friction torque	Nm
C_v	Dynamic friction torque	Nm/rpm
D_b	Diameter of the motor body	m
D_{PQ}	Residual dipole of the PocketQube bus	Am^2
h_{orbit}	Satellite orbit altitude	m
h_{MBW}	Angular momentum of momentum bias wheel	Nms
I	Current	A
I_{PQ}	PocetkQube Mass moment of Inertia	kgm^2
k_T	Motor torque constant	Nm/A
k_ω	Motor speed constant	rpm/V
L_b	Length of motor body	m
m_f	Flywheel mass	kg
m_m	Motor mass	kg
m_{PQ}	Mass of the PocketQube bus	kg
$R_\oplus$	Radius of Earth	m
P	Period	s
P	Power	W
T_a	Aerodynamic disturbance torque	Nm
T_g	Gravity gradient disturbance torque	Nm
T_m	Geomagnetic disturbance torque	Nm
T_s	Solar radiation pressure disturbance torque	Nm
U	Voltage	V
V	Velocity	m/s^2
α	Angular acceleration	rad/s^2
θ_a	Pointing accuracy	deg
μ	Average	$-$
$\mu_\oplus$	Gravitational Parameter of Earth	km^3/s^2
ρ_{atm}	Atmospheric air density	kg/m^3
ρ_f	Flywheel material density	kg/m^3
σ	Standard Deviation	$-$
ϕ_I	Z-axis alignment difference	deg
ω_{MBW}	Rotational velocity of the MBW	rad/s

1. Introduction

This chapter is dedicated to introducing the subject in the form of background theory and information, the problem definition in the form of research questions and finally specifying the design and testing process, with specific reasoning.

1.1. Research Background

In the forever development of miniaturising technology, space engineering is at the forefront. Miniaturised technology is required to drive down the cost of new missions, as bringing a single extra gram to low Earth orbit (LEO) could cost up to 23 US dollars [37]. Having set the standard for a new class of spacecraft; the PocketQube or PQ, together with Alba Orbital and Gauss [40], the Delft University of Technology is continuing the search for new technologies applicable to this size of satellite with its platform Delfi-PQ [41]. The PocketQube and the Delfi-PQ belong to the satellite 'pico' class; with a weight limit of 250 gr and size of 50 mm in length, width and height per unit. One unit of a PQ is denoted as 1p, in comparison to the 1U characterisation a CubeSat unit receives, which has a volume eight times bigger than a PQ unit. The pico-satellite class is meant to enable a larger number of players to enter the space industry, due to their low development and production cost. As of now, novel PocketQube missions utilise minimal attitude control, due to the required attitude schemes and their volume and power restrictions. PocketQubes are considered feasible for educational missions, low-cost technology demonstrators, space weather observation missions, communication satellites and space exploration swarm devices, with only Earth observation regarded as infeasible for the PocketQube platform [10]. Earth observation is regarded as infeasible as it is not currently competitive to its CubeSat counterpart, due to the lack of quality attitude control and propulsion for constellation control within PocketQubes. When looking to create attitude actuators for satellites, the accumulative disturbances, external and internal must be limited to a certain pointing accuracy. The inertia of a PocketQube in comparison to a CubeSat decreases tenfold, which would mean that the effect of the dominant disturbance torques for smaller satellites in low Earth orbit become even greater as the satellite size decreases [50]. This would mean that a PocketQube mission would have to devote a larger part of its mass to attitude control to attain the same level of precision [17]. Therefore, research is required into new solutions and feasibility of rotor based momentum exchangers in pico-satellites.

The lack of attitude control in PQ's goes back to the requirement for miniaturised technology, as conventional attitude control actuators such as magnetorquers, reaction wheels, momentum bias wheels or control moment gyros have been widely implemented and are commercially available for CubeSats or larger missions, but are still only in their infancy for pico-satellites. The PQ satellite operates on the limit of volume, mass, power and financial budgeting limits, often requiring a feasibility study per subsystem to envision the applicability of each subsystem. Out of all attitude actuators, the most prominently used option is magnetic control in the form of magnetorquers [9], with reaction wheels as runner up. Reaction wheels have already been designed, tested and integrated for PQ missions, but have never operated during flight [54]. The challenges arising from the small form factor are; a power challenge directly derived from the small surface area of the outer shell of the PQ - four times smaller per unit in comparison to CubeSats [47] - and a mass and volume challenge due to the prescribed required size of the PQ[40], 8 times smaller per unit in comparison to CubeSats. With the increased effect of disturbance torques and decreased mass, volume, power and financial budgets the PQ attitude actuators have to be designed for in mind; a deep dive can be done into the different solutions created for each type of PQ attitude actuator, to find out whether a momentum bias wheel solution is feasible and whether it could become competitive.

1.1.1. Magnetorquers

A magnetorquer or MTQ utilises the magnetic field of the Earth to create magnetic torque through an induced magnetic field over a certain axis to rotate the spacecraft. A magnetorquer attitude control system design is lightweight, relatively inexpensive, robust due to the absence of moving parts and the most magnetically clean when not operated, as the induced magnetic field would only be activated during manoeuvres and not during scientific observation periods, which can be attractive for scientific payloads sensitive to magnetic fields [12]. Even though such scientific instrument are not yet applicable to the pico-satellite scale, it is something that can be taken into account for future development [10]. Additionally, the scalability of the magnetorquer technology makes it a perfect candidate as an auxiliary or complementary attitude actuator, as will be discussed when discussing momentum dumping for reaction wheels or momentum wheels. Furthermore, a magnetorquer is an ideal attitude actuator for a mission where volume is scarce and the attitude control is minimal, as a magnetorquer could be a simple coil on the walls of the PocketQube bus.

However, magnetorquers do not excel in high acceleration rotations, require a high amount of current for its induced magnetic field and are dependent on the magnetic field of Earth. The high amount of current is a limiting factor for attitude control in PocketQubes, as only a small amount of power is available for the entire spacecraft. Additionally, when a high torque movement is required, the power usage of the magnetorquer rises to an extreme level. The coil parallel to the Earth's magnetic field can not create a magnetic torque, and a coil nearly parallel to the Earth's magnetic field would have to create a much larger magnetic field in comparison to when it is perpendicular to the Earth's magnetic field. Furthermore, the Earth's magnetic field is not constant and therefore, the magnetorquers must be designed to be able to deliver multiple times the disturbance torques. The magnetorquers can be used more efficiently, as research is being done to increase the efficiency of magnetorquers in all operation modes, such as a detumbling algorithm utilising a weighted B-dot controller [22], to detumble from a maximum velocity of 180 deg/s and eventually save around 5% of power while sacrificing 0.5% detumbling performance and 3.2 extra orbits to detumble. This shows the possibility of a smart usage of magnetorquers, to assure the power efficient usage of this technology while minimising the extra time required. Another optimisation is to incorporate all magnetorquers into a printed circuit board (PCB), using PCB-embedded coils [24], restricting the size of the attitude control system to a single PCB, within 1p of a PocketQube satellite. These solutions could increase the effectiveness and efficiency of an attitude control system solely based on magnetorquers.

Several PocketQube missions have utilised magnetorquers, such as the Delfi-PQ. Designed by the Delft University of Technology [41], the Delfi-PQ featured three magnetorquers enabling the satellite to detumble from 180 deg/s to 5 deg/s, experienced through deployment of satellite from the launcher. This mission shows that the attitude control system consisting of magnetorquers created with commercial of the shelf (COTS) components is feasible. The design and construction of the magnetorquer system with COTS components was part of a masters thesis, in which van den Bos [6] states in order to improve the design, one can go one of two ways: a more powerful torquer with ferromagnetic cores, or a more volume efficient system with integrated coils in the PCB backplate of the PocketQube. The more powerful magnetorquer system would sacrifice its energy efficiency for a higher torque of 0.25 Am^2 or 12.3 μNm, with the PCB integrated coils generating a maximum torque of only 0.06 Am^2 or 3 μNm, but taking up no volume in the PocketQube bus, only on the PCB. An existing design for a PCB integrated magnetorqeur coil [24], designed for power efficiency, generated a maximum torque of 0.0171 Am^2 with a power efficiency of 2.75 $\cdot 10^{-5}$ Am^2/mW. Both of these designs suffice in missions where the attitude control in minimal and only detumbling has to be countered, but for mission with more precise pointing schemes, an attitude control system based solely on magnetorquers lacks high actuation.

1.1.2. Reaction Wheels

For higher actuation rates in attitude control schemes, a reaction wheel can be introduced. A reaction wheel is purely a momentum-exchange device utilising torque induced upon an integrated flywheel and is not dependent on outside phenomena to operate, which makes it superior to magnetorquers in magnitude and availability of control. Reaction wheels can supply the satellite with a maximum torque one magnitude larger than magnetorquers, which can eliminate the under-actuation of a purely magnetic attitude control system. Reaction wheels are also capable of finer control in comparison to magnetorquers. Reaction wheels can be used solely for one axis or three axis control, as the one reaction wheel would be backed up by a set of magnetorquers, as was implemented for the UWE-3

CubeSat satellite[42], which had the reaction wheel aligned along the Earth's magnetic field vector during operation, to assure three-axis attitude control. Reaction wheels are currently often used in conjunction with magnetorquers to join the advantages of both types of attitude control, and eliminate the disadvantages of both. By combining the two actuators in one attitude control system, a high actuation rate of the reaction wheels and the cheap and lightweight design of magnetorquers are combined, while the momentum saturation of the reaction wheels is contingent on the magnetorquers to be periodically eliminated.

Problems that arise when using reaction wheels are the slightly higher weight of the wheel system compared to magnetorquers, the induced vibrations from impurities in the flywheel, the magnetic disturbance from the permanent magnets used in the motors and the momentum saturation one gets in the case of non-periodic disturbance torques. The higher weight is integral to the reaction wheel design, as it utilises a heavy flywheel and motor to create an angular momentum to counteract disturbance torque or actuate the spacecraft to the desired orientation. In the case of a PocketQube, where the total allotted mass and volume for every subsystem has to be minimised, to ensure higher feasibility for different scientific payloads. Vibrations are due to the fact that moving parts are introduced into the attitude control system by reaction wheels. The moving parts could have inherited impurities from the manufacturing process of the flywheel or axle. The bearing could also have had impurities when installed into the attitude control system, which could lead to rocking. The magnetic disturbance of a reaction wheel or any motor stems from the usage of passive magnets. If the satellite is carrying a scientific payload sensitive to magnetic fields, volume and mass must be dedicated to magnetic insulation [12]. Momentum saturation is a phenomenon that occurs when the reaction wheel has reached its highest angular velocity while controlling the attitude of the spacecraft [38]. This is due to non-periodic disturbance torques that accumulate over time, increasing the speed of the reaction wheel with every orbit. When the wheel is saturated, it can not slow down, as it would transfer its built up momentum back onto the spacecraft, which would render the control of the spacecraft lost. This can solved by introducing a complementary system or including a disturbance dampening device. The complementary system introduced in most missions is an extra set of magnetorquers, to periodically desaturate the wheel.

Reaction wheels specifically designed for PocketQube missions are still in early development, with only a few designs within the limited power and weight budget of a PocketQube. One design is the reaction wheel for the UoMBSat-1 PocketQube mission [4], a singular unit PocketQube satellite developed at the University of Malta. This spacecraft uses three 37 mm diameter reaction wheels and six integrated planar magnetorquer coils on each wall for the desaturation of the reaction wheels. The design of this satellite bus does differ from the Delfi-PQ, as the UoMBSat-1 is not a stacked satellite, but a fully integrated 1p PocketQube, which allows for more complex motor configurations, and does not restrict the placement and orientation of subsystems. This does increase the complexity of the satellite, and is most certainly more expensive, as the design and production of the interconnected parts and structure would take up more time and therefore design budget.

The implementation and testing of the reaction wheels provided challenges, in terms of the volumetric limitations of the PocketQube constricting the sensing of the acceleration of the reaction wheels' motors [5]. This is solved by adding a specifically designed compact optical sensor, which creates feedback of the angular velocity of the reaction wheel. This means that the extra control for the reaction wheels requires an extra set of sensors, increasing complexity, cost, total mass and volume and power usage.

Another reaction wheel design is the miniature reaction wheel designed by Tom Vergoossen as part of his master thesis at the Delft University of Technology [54]. The reaction wheel is specifically designed for the Delfi-PQ and was made with COTS components as a feasibility study of the technology at pico-satellite scale. This reaction wheel is sized to be 20 by 20 by 12 mm and weighing 14.73 g, supplying the spacecraft with a torque of at approximately 0.16 mNm, proving that the reaction wheel, even when produced with COTS components and designed by a student outperforms a commercially available magnetorquer actuator by a magnitude of ten. Vergoossen goes on to design a preliminary three-wheel assembly for possible three axis control via reaction wheels, coming to a size of 31 by 31 by 22 mm. The single reaction wheel or the three wheel design together with the PCB integrated magnetorquer design could prove to be the best three axis control in terms of torque, but would require a steep amount of power. This combination is relatively small, so it could be used within a Delfi-PQ type spacecraft.

An honourable mention is the master thesis by Atzori [3], who studied the miniaturisation limit of attitude actuators in a PocketQube satellite, designing an attitude control system for a 1p PocketQube consisting of three reaction wheels. These three reaction wheels take up the upper half of the satellite, but would eventually fail, resulting in no test data, only simulations.

Commercially available reaction wheels, such as those from CubeSpace [15] are designed for CubeSats but can be adapted volume-wise to PocketQube, but the listed prices for these wheels are a very convincing point to go for a reaction wheel produced with COTS components, rather than a COTS reaction wheel. Not only is the financial cost breaching budget, the volume and power budget are also being challenged, as the specified power levels are tenfold higher than the university produced reaction wheels.

Below, table 1.1 is provided with all specifications of the two university made reaction wheels compared to the COTS reaction wheels, with all the sources gathered. From this table, it is easily visible that a wheeled momentum exchange device using half of the volume of a PocketQube unit is feasible, and does not require exorbitant amounts of power for such values of torque like a magnetorquer.

Table 1.1: Reference specification for miniature reaction wheel systems.

Source	Size (mm)	Torque (μNm)	Momentum ($mNms$)	Power (mW)
UoMBSat-1 [4]	Ø37 x 3 + Ø6 x 9	3	2.36	43
Vergoossen [54]	20 x 20 x 12	0.293	0.11	25
CubeSpace CW0017 [15]	28 x 28 x 26	5	1.77	300

1.1.3. Momentum Bias Wheels

An alternate wheeled attitude actuator for three axis control to a reaction wheel system (RWS) is a momentum bias wheel or MBW, an often heavier flywheel spinning at a constant high angular velocity, creating a high angular momentum bias. A MBW allows satellites to have a high stability against environmental disturbance torques through gyroscopic stiffness, as the high constant angular momentum bias present limits the effect of the torque exerted on the spacecraft. Also, just like a RWS, a MBW can be used to create torque around its rotational axis, as it houses the same type of parts. The gyroscopic stiffness becomes more effective when the spacecraft bus is much smaller as seen with PQ's, as the bus would have a much lower inertia to initially resist these torques. In comparison to a magnetorquer or RWS, the MBW could ensure more consistent control, as the type of attitude control is fundamentally different from the other attitude controllers, as a MBW maintains the attitude within a certain sway angle instead of rectifying the disturbance. In a situation with an abnormally high disturbance torque, a spacecraft could lose a degree of control between the event of that abnormally high torque and the response of the RWS or magnetorquers. Certainly for magnetorquers, the degree of control lost would be much greater, as the supplied torque is very limited. A MBW also does not need to dump its momentum as it maintains it, but does need to correction of the sway angle obtained. The sway angle obtained comes in the form of precession and nutation.

The prominent problem that are inherent to a MBW design is precession and nutation. Precession is the phenomenon where the angular momentum vector of a body rotates around another axis, like a spinning top just before it falls over. Nutation occurs when the direction of the angular momentum is not perfectly aligned with the principle axis of inertia of the MBW [48]. Nutation thus depicts the change in angle between the angular momentum vector of the body and the rotational axis of the angular momentum vector. To mitigate precession and nutation, a set of magnetorquers can be added to periodically eliminate the precession by supplying the spacecraft with countering torques. An honourable mention is introducing a viscous damper in the system to account for the extra torques. The viscous damper would not use any extra power as the unwanted motion and extra torques would dissipate into heat. This would not completely eliminate precession and nutation, but damp it. A

MBW have not yet been implemented into PocketQube missions, due to the infancy of the PocketQube mission design. MBW's do have a heritage in micro- and nano-satellites, specifically due to the low mass moment of inertia these small satellites have. The momentum wheel would be supplying a surplus stiffness against disturbance torques. Inspiration can be drawn from multiple CubeSat or micro-satellite missions to relate and interpolate the required angular momentum of the MBW in PocketQube missions. Missions in similar orbit environments are selected and discussed.

Starting with one of the smallest known satellites to have flown successfully with a MBW on board, would be the ZDPS-1A nano-satellite [56], developed by the Zhejiang University. This satellite, at a size of 15 by 15 by 15 cm, would house a MBW for damping the disturbance torques and providing gyroscopic stiffness and three complementary magnetorquers, made with COTS components. In this mission and all other missions regarding MBW usage discussed, utilised a secondary set of attitude actuators; a set of magnetorquers. The choice to use COTS components to produce the system instead of using COTS systems, has the benefit of being low in mass, power and cost. The momentum wheel would deliver 2 $mNms$ of angular momentum at approximately 7800 rpm for a pointing accuracy of 5 deg in three-axis control, pointing towards the Earth (nadir). The satellite is even able to keep the pointing accuracy within 2 deg, but the on-board data analysis suggested stability within 5 deg of pointing accuracy. The size of this MBW system is estimated through its motor size and pictures provided in the article. The motor utilised was a Faulhaber 2224U 003SR, which sports a size of ∅ 22 by 24 mm, mounted to a thick flywheel, result in a volume assumption of 30 by 30 by 40 mm. Even though this satellite is 27 times bigger than a PocketQube unit, or 9 times bigger than a 3p PocketQube satellite, this is the closest relevant system in size. The other missions specified after this one will be larger still.

Many satellites utilise a commercially acquired reaction wheel as a MBW, mostly whenever the financial budget and bus volume is quite a bit larger than with a PocketQube mission. The fact that the MBW used in mission was a reaction wheel, shows the interchangeability between rotor based attitude control technologies. The ZA-AeroSAT [49], a 2U CubeSat, used a MBW together with three magnetorquer coils and rods are used to minimise deflection due to external disturbances and mitigate those minimal deflections. The MBW used was the CubeWheel Gen 1 manufactured by CubeSpace. This reaction wheel could deliver approximately 1 $mNms$ and had a size of 28 by 28 by 26 mm. This reaction wheel could physically fit into a PocketQube unit, but is quite high in power usage and price, as earlier discussed. The power draw of the CubeWheel Gen 1 at 2000 rpm is stated to be 0.3 W, while the 1 $mNms$ for the ZA-AeroSAT mission was achieved at 4000 rpm, which can lead to the assumption of a doubling of the power draw, to 0.6 W.

The ExoCube [45] was 3U CubeSat mission using three magnetorquers for precise control and a MBW for disturbance torque damping. The larger issue was the spin up of the momentum wheel, which was solved by altering the attitude controller, making sure the torque levels of the momentum wheel were sufficiently low such that the magnetorquers were able to counter those torques. The MBW was a COTS reaction wheel, the Sinclair Interplanetary RW-0.01-4, featuring a 10 $mNms$ angular momentum and sporting a size of 50 by 50 by 40 mm, to create a pointing accuracy of 10 deg. Sinclair Interplanetary has been acquired by Rocket Lab, so the Sinclair Interplanetary RW-0.01-4 is now the Rocket Lab 10 $mNms$ RW as stated in their product catalogue.

Using the data from the missions described and discussed above and summarised in table 1.2 below, a relation between required angular momentum (h_{MBW}), pointing accuracy (θ_a), sizes and power usage can be drawn. Firstly, it can be seen that each MBW system allows the spacecraft to operate with a required pointing accuracy between 2 and 10 deg. This would mean, that for this mission, a similar pointing accuracy must be achieved to ensure similarity to MBW systems at other scales.

Furthermore, the power usage of these wheeled actuators concern only one motor, similar to the power values presented in table 1.1. Whereas only motor is required for a MBW system and three are required for three axis control when using reaction wheels, the power draw can triple when all wheels are saturated. Therefore, the 90 mW of power drawn for the ZDPS-1A satellites MBW shows that for smaller MBW, a power efficient solution is capable of providing a pointing accuracy of 5 deg.

Table 1.2: Reference specification for miniature momentum bias wheel systems.

Source	S/C Mass (kg)	S/C Size (cm^3)	MBW Size (mm^3)	$\mathbf{h_{MBW}}$ ($mNms$)	$\theta_\mathbf{a}$ (deg)	Power (mW)
ZA-AeroSat [49]	2.66	20 x 10 x 10	28 x 28 x 26	1	10	600
ZDPS-1A [56]	3.5	15 x 15 x 15	30 x 30 x 40	2	5	90
ExoCube [45]	3.99	30 x 10 x 10	50 x 50 x 40	10	2	100

1.1.4. Control Moment Gyros

The usage of a pivoted momentum bias wheel or control moment gyro (CMG) within a very small spacecraft is an option worth exploring, for their unique capabilities due to their high torque and angular momentum capabilities [38]. A pivoted wheel or control moment gyro is more used as a reaction wheel, as torque is generated by pivoting the spinning wheel. Control moment gyros can feature one or two gimbals, with the two gimbals offering two-axis control. To achieve three axis control, at least two control moment gyros are used, with four single gimballed control moment gyros in a pyramid positioning to be the most popular. The control moment gyro could also have a variable speed controller, varying the angular velocity to create a torque in the direction of the angular velocity vector, resulting in three axis control. Research is also being done for alternative control methodologies for a singular double gimballed control moment gyro to achieve three axis control [52]. This is achieved through the nutational motion generated by the double gimballed control moment gyro. In comparison to the variable speed control moment gyro, this control method would not create a singularity in the control in the form of momentum saturation. The momentum saturation would occur in the same manner as with regular reaction wheels, where the speed of the wheel is at its maximum, rendering the control of one axis lost.

Control moment gyros have heritage in very large missions and such as the International Space Station (ISS); utilising four dual gimballed control moment gyros with unlimited gimbal freedom about each axis [25]. At such a large scale, when in comparison to PocketQubes, the lifetime of the control moment gyros is years beyond the scope of a PocketQube mission. However, the control moment gyros 1 and 3 on board the ISS did fail, with both control moment gyros experiencing an exceedingly high level of torque, above the healthy limit set for the control moment gyros. This led to a temperature where welding ball bearings was possible, thus the control moment gyro would fail. At a PocketQube scale, where everything is packed together, thermal failure would ensure failure of the entire spacecraft.

Just like momentum bias wheels, control moment gyros have no heritage in PocketQubes, for the same reasons as their non-pivoting brethren. Since control moment gyros are more complex, expensive and larger than conventional momentum bias wheels, a system with unlimited gimbal freedom like the four present on the ISS will not be development for PocketQubes in the near future. However, control moment gyro usage within CubeSats is becoming more and more popular. Gaude and Lappas [23] have developed a miniature, low cost/mass single gimballed control moment gyro actuator, which would fit in a four CMG pyramid cluster within 1U, delivering three-axis control. These actuators were created using COTS components, weighing only 35 g per CMG, 140 g per cluster, but delivering enough torque to rotate a 12U CubeSat 90 ° in 90 seconds. This is more than a reaction wheel with a mass of 140 g can deliver.

A mission that uses COTS produced control moment gyro systems is BILSAT-1 [29], a Turkish micro-satellite using two single gimballed control moment gyros. The twin control moment gyro payload could also be operated as momentum wheel or reaction wheel, as well as variable speed control moment gyro mode. This shows the far superior versatility of a control moment gyro based attitude control system, with torque levels of 55.9 mNm at for only 12 W of power. This is comparable to the performance of a reaction wheel at the same power level. But for a small increase in mass and complexity, an extra gimbal can be added to assure two axis control.

From the missions specified, it can be concluded that the usage of control moment gyros, if possible, would be an excellent solution for the excessive power usage of reaction wheels, while maintaining the advantage of gyroscopic stiffness of momentum bias wheels. Especially gimballed control moment gyros are a significant improvement in comparison to the single axis attitude actuator. However, for the PocketQube scale, the mass, size and control complexity fall beyond its scope. For this thesis, the possibility of CMG usage in PQ satellites will not be investigated.

1.2. Research Question

From the literature presented it is clear that the PocketQube attitude control system is fairly restricted or restrictive. Current reaction wheel technologies are most certainly only in the early stages of development, and require a large chunk of the power, size, financial and mass budget. Since PocketQube missions often do not require such fine pointing as a reaction wheel delivers, a momentum bias wheel might be the perfect candidate for a small scale satellite, performing better in terms of power, volume and mass. Since an upgrade from sole magnetorquer control, shown to be able to control the satellite to an accuracy of 5 deg, is favourable, the momentum bias wheel could be the candidate to fit in this attitude control gap. Together with the fact that the pointing scheme for a PQ is not as precise as a CubeSats pointing scheme, as no Earth observation is regarded as infeasible at pico-satellites scale, the MBW can be used to perfectly fit a more precise pointing scheme than only magnetorquers can provide and fit the volume and power budget of a PQ mission. To find out whether the proposed MBW attitude actuator can fit tick these boxes, a feasibility study has to be done.

The scope of this thesis is thus to introduce a the momentum bias wheel at PocketQube scale through a feasibility study. This thesis will dive into whether the momentum bias wheel is feasible at the PocketQube scale and whether it can perform competitively in terms of power, size, mass and financial cost. Boiling down the thesis purpose into two research questions would results in:

"Is a momentum bias wheel design feasible using self-manufactured and COTS components for a PocketQube satellite?"

and

"How does the momentum bias wheel design compare to a reaction wheel design in pointing accuracy, size, mass and power?"

These questions can be answered through a number of steps, which are formulated into research objectives:

1. To model the theoretical environment and required performance of the new attitude control system;
2. To design a momentum bias wheel actuator using the required performance parameters modelled in the theoretical environment;
3. To create a working prototype of the momentum bias wheel;
4. To test the working prototype in all its encountered environments.

The research objectives can be achieved through following steps. Requirements have to be set to specify the attitude actuator. Top level, stakeholder and system requirements are set in order to specify each level of design of the momentum bias wheel. Requirements are quantified by the disturbance torque calculation, environment model, stakeholders such as the PocketQube team of the Delft University of Technology and literature.

The theoretical environment in which the satellite will be situated has to be modelled to calculate and envision disturbance torques which will angularly deviate the satellite. The disturbance torques will be analysed for the entire lifetime of the spacecraft, ranging from its insertion orbit to the final decayed orbit at which end-of-life (EOL) is declared, of which a worst case scenario will be found. The maximum accumulated torques over one orbit will be used to calculate the required angular momentum of the momentum bias wheel. This can be done through basic formulae and a scenario simulation which will confirm this value through simulating the maximum nutation the spacecraft undergoes with a certain angular momentum in a nadir pointing scheme.

This angular momentum value is then used to find parameter combinations consisting of flywheel mass and size and motor speed and power draw. Preliminary boundaries for flywheel sizes can be set in place, to ensure the correct sizing of the flywheel. The varying parameter combinations would all satisfy the angular momentum requirement, but would range from a solution in which the flywheel is at its lightest to a solution where the angular momentum the flywheel provides is at its maximum due to the preliminary boundaries. These combination will be eventually used in the design trade-off and will be compared to various reaction wheel based attitude control systems named in the literature study.

Analysing the mission, environment and competitors the MBW will operate in and against will be utilised to set up a comprehensive set of requirements, in which the angular momentum requirement will be included. These requirements set up boundaries such that gathering all options regarding materials, orientations, components (electrical and mechanical) and manufacturing methods is finite. The options gathered will be within feasibility as set for a PocketQube mission, excluding over-expensive components for selection in the trade-off or design orientations so complex that the design time or cost would balloon way beyond the scope of a PocketQube mission and a master thesis. Additionally, the options are checked interdisciplinary, to envision and possible prevent any design incompatibilities between any chosen options. Having eliminated any unfavourable combinations, multiple preliminary designs can be made from combining options from each discipline. Using the requirements and favoured characteristics of a momentum bias wheel attitude actuator, weights will be given to certain design aspects, such as complexity, cost, mass or volume; to eventually trade-off the different designs, consisting of combination of materials, orientations, components and manufacturing methods. This would result in one remaining combination of options, which enables the completion of the design.

The completed design requires proven performance, which can be done through a working prototype in multiple tests. The manufacturing of a prototype is meant as a proof of concept rather than the complete development of a flight representative model and a test and validation of several critical or uncertain design aspects. The prototype will thus made within the limitations and accessibility of the production facilities of the Delft University of Technology, and not be outsourced to professionals to be able to close the financial budget. To ensure availability of the manufacturing facilities, the manufacturing sessions will be planned in advance, with back up sessions in case of delay in any part of the preceding design process. Finalising the prototype with the manufactured and COTS components will be followed with operational testing, consisting of testing the functionality of the components selected and a coarse system performance testing. This initial operational testing will reveal shortcomings in the prototype and can possible pave way to a small and sectioned design or component iteration. Having possible iterated the design, it must be tested again to ensure operability.

Finally, the attitude actuator must be tested against the environment it will endure during launch and its lifetime. The scope of these thesis allows for a certain number of tests to be done, with operational and vibration testing to be the most significant. Dependent on parts or methods utilised throughout the design and prototyping phase, vacuum or thermal vacuum tests may be required.

In table 1.3, the above explained research plan is summarised into research objectives and supplementary sub-objectives. Each sub-objective has been given an ID, to ensure traceability when setting requirements for the momentum bias wheel design. Do keep in mind that these are not achieved in this order.

Table 1.3: Sub-objectives per research objective.

Research Objective	ID	Sub-objective
Model the theoretical environment and required performance.	RO01	Model the environmental disturbance torques.
	RO02	Derive the performance requirements from the disturbance torques.
	RO03	Derive required model parameters from performance requirements.
Design a momentum bias wheel using modelled performance.	RO11	Set up requirements regarding the design of the momentum bias wheel.
	RO12	Explore all concurrent options regarding materials, orientations, components and manufacturing methods.
	RO13	Do a complete design trade-off regarding designs from combinations made from materials, orientations, components and manufacturing methods.
	RO14	Synthesise the design from the chosen combination.
Create a working prototype.	RO21	Manufacture the momentum bias wheel prototype based on the previously selected design.
	RO22	Perform a nominal running mode test, displaying performance in all operating modes.
Test the prototype in all environments.	RO31	Perform a vibration test, displaying resilience against launch and operation induced vibration forces.
	RO32	Perform a vacuum test, displaying the performance and resilience in vacuum conditions.
	RO33	Perform a thermal-vacuum test, displaying the performance and resilience in a simulated orbit environment.

The sub-objectives are selected in a manner to create a feasible design process fit for a thesis project. Within the environmental disturbance torque lie the aerodynamic, geomagnetic, solar radiation and gravity gradient disturbance torque that act on the PocketQube, which will be required to be modelled as the required performance will be based on a nadir-pointing PocketQube spacecraft orbiting in a very low Earth orbit.

1.3. Research Structure

This thesis is dedicated to designing and testing a momentum bias wheel fit for a 3p PocketQube. Having set up the research question through a literature study in the past two sections, the requirements of the new subsystem can be quantified, in the next chapter. Chapter 2 will fully encapsulate all set requirements for the project and design. The theoretical model to confirm the angular momentum requirement will be stated in chapter 3, which simulates the complete environment in the form of disturbance torques. In chapter 4, the set of requirements will be used to collect design options for materials, orientations, components and manufacturing methods and trade these off to eventually synthesise a design from the selected options, of which the prototyping will be discussed in chapter 5. The built prototype will be tested in all its nominal operational modes and environments, which will be reported in chapter 6. The test and research results will be stated and analysed in chapter 7, such that they can be concluded upon in chapter 8. Finally, a reflection on the design research will done, including recommendations and future work, in chapter 9.

2. Requirements

This chapter entails the selection of requirements and motivation for this selection. These requirements will be quantified, identified and traced to research objectives or other requirements, to make sure the reasoning behind each requirements is clear. The first step to creating a successful design, top level requirements must be made, through analysing the spacecraft and the mission the momentum bias wheel will operate in. Through these top level requirements, a set of system requirements can be derived from the mission environment, in which the satellite endures disturbances through the launch vehicle and the harsh space environment, and the spacecraft specifications, which dictates the volume, mass and power budgets, correctly constraining the design process.

2.1. PocketQube

The PQ bus, following the restrictions and requirements set in the PocketQube Standard [40], has to adhere to the dimensions and mass for the number of PQ units it consists of, listed in table 2.1. The designed MBW in this thesis will be designed for a PQ bus, whether that would be a 1, 2 or 3p PQ. As an initial design, the MBW will proposed for a 3p PQ, as this would ease the mass, volume and power restrictions on the MBW. Additionally, the past Delfi-PQ mission was also a 3p spacecraft bus, which is why it will be assumed that the next mission will also be 3p.

Table 2.1: Dimensions and mass of a PocketQube bus per unit.

Number of Units (p)	External dimensions without backplate (mm)	Sliding backplate dimension (mm)	Mass (kg)
1	50.0 x 50.0 x 50.0	58.0 x 64.0 x 1.60	0.250
2	50.0 x 50.0 x 114	58.0 x 128 x 1.60	0.500
3	50.0 x 50.0 x 178	58.0 x 192 x 1.60	0.750

The inner housing for the bus is dependent on the maximum outer dimensions and the wall thickness as stated in table 2.1. The maximum width and depth for the new subsystem thus become 46.8 by 46.8 mm.

A second size constraint comes from the requirement of mounting the MBW system on the PQ9 PCB's utilised for the subsystem stacking central in a PQ design[7][8], as illustrated in figure 2.1. The drawing for the PQ9 PCB, as shown in figure 2.2, shows the stand-offs utilised to stack these PCB's onto each other. Fortunately, there are multiple options for stacking height. The four options are displayed in appendix A, ranging from a component height of the above mentioned 4.00 mm to 12.0 mm. The maximum height of the MBW system will thus be 12.0 mm. This results in a volume of 26.3 cm^3, when using the 46.8 mm width and depth.

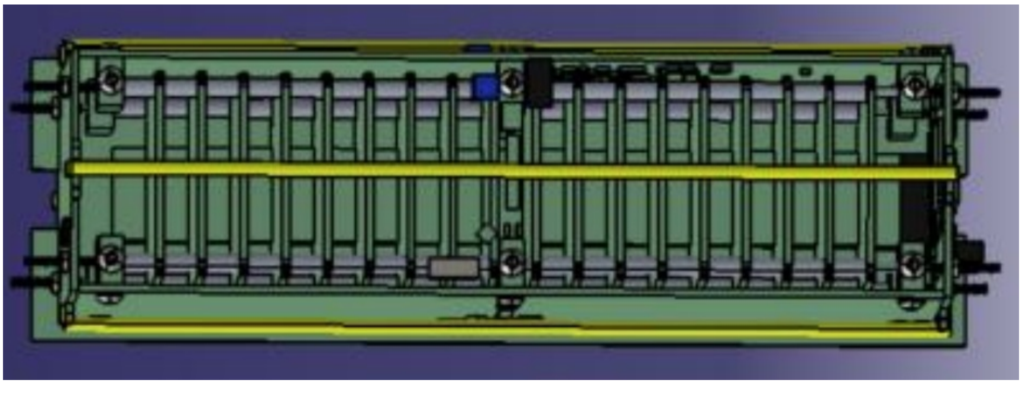

Figure 2.1: The Delfi-PQ cross sectional view, showing the subsystem stack [41].

Additionally, the connector pins shown at the top of the board must be kept clear from, as the boards are interconnected. There is some room for an external protrusion from the board on the sides, but this has to be limited, due to cables from other subsystems that also utilise this external envelope between the boards and the outer PCB walls of the PQ.

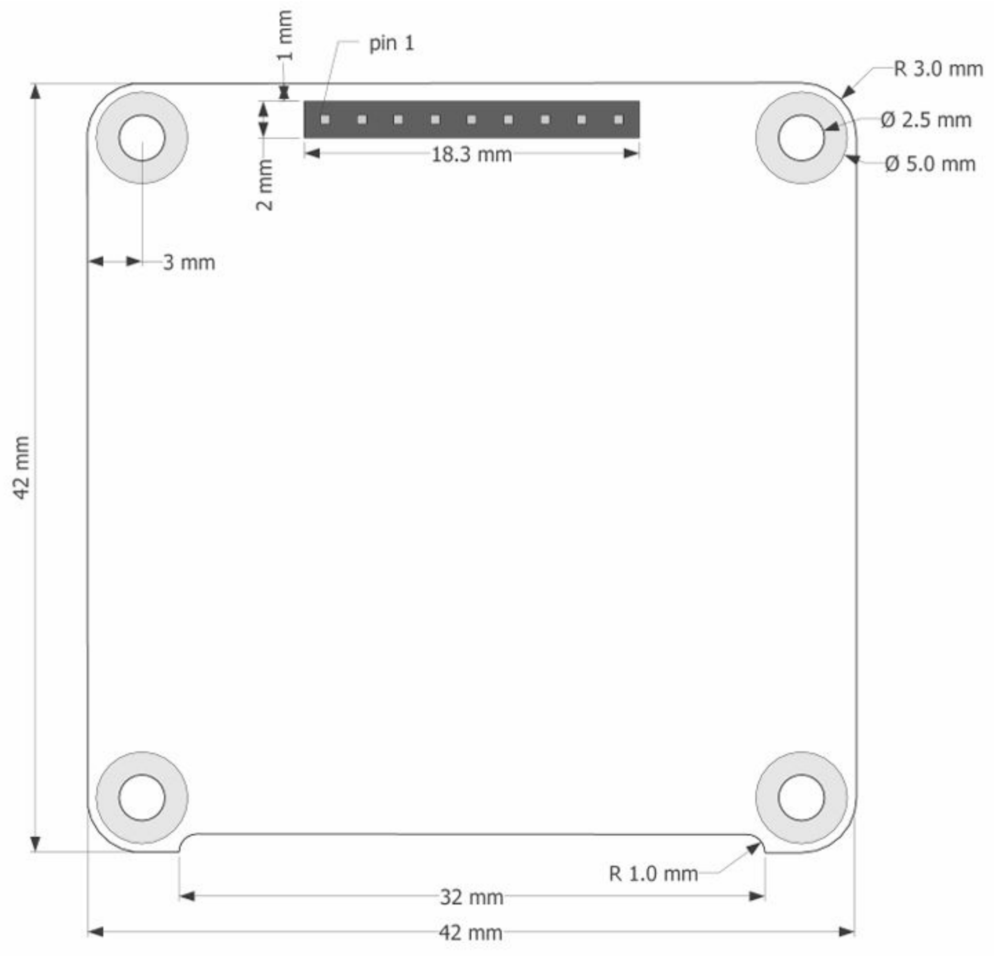

Figure 2.2: The technical drawing for the PQ9 PCB board, complete with dimensions [7][8].

The final size constraint will be retrieved through reference. The three reaction wheel system by Vergoossen [54] has a preliminary volume of 31.0 by 31.0 by 22.0 mm or 21.1 cm^3, which would fit perfectly on the PQ9 board with a height of 12.0 mm. Therefore, the maximum height and maximum volume will be 12.0 mm and 21.1 cm^3.

Using the 750 g maximum mass of the bus and dividing the preliminary volume requirement by the total inner volume of the 3p PQ bus will result in a preliminary mass constraint of 41.4 g.

The power for the new PQ mission will be approximately equal to Delfi-PQ, which has an electrical power system (EPS) distributing an average power of 1.00 W per orbit to all subsystems, with a standard direct current (DC) voltage of 3.30 V. The voltage provided to the motor can be altered utilising a DC-DC voltage converter. Using the average power budget presented in SMAD [55], the ADCS would receive 18.0 % of the total generated power, resulting in 180 mW to the ADCS. This value shall be incorporated as a constraint for the new MBW design.

Finally, PQ's are meant to be low cost satellite systems, the MBW must be low in cost as well. For this thesis, a budget of 500 Euros has been made available for the manufacturing and testing of the prototype.

2.2. Mission

Low Earth orbit (LEO) is the preferred orbit environment for the PocketQube. The new zero debris ruling by ESA [20] states that the LEO protected region is a spherical shell extending 2000 km from the surface of Earth, in which all previous PQ missions have operated. Within the LEO protected region, the orbit lifetime must be less than 5 years and immediate Earth atmospheric re-entry after end of mission is preferred, which dictates the end of life to be at a certain orbit height at which the orbit decay rate is sufficiently high, as the orbit would decay to a re-entry at orbit altitudes close to or below 200 km, as stated in SMAD [55]. Even though the satellite population in the lower part of LEO (< 600 km) has increased over the past decade and will increase over the coming decades, the wise decision is still to aim for an orbit in the lower part of LEO [33], as the higher part of LEO nearly tenfold more crowded. With the increased presence of larger satellite constellations like Starlink, the upper region of LEO already contains more than 11000 small parts (<100 kg), and more than 2000 larger objects.

As mentioned in section 1.1, PQ's are net yet feasible for Earth observation (EO), due to the lack of active attitude control and propulsion for constellation control. However, this thesis would like to break away this assumption by adding upon the array of attitude control system available for PQ's. EO PQ's require nadir pointing, a requirement derived from the scientific payload, which results in one side of the spacecraft always pointing towards Earth. The payload will be assumed to be small enough to point in any direction of the spacecraft. The size limitations intrinsic to the PQ bus probably limits the payload to 1p, which thus allows the payload to be pointing out of each side of the spacecraft. In terms of aerodynamic drag surface, three scenario's can be envisioned in which the payload can point towards Earth. The aerodynamic drag surface is the frontal area of the spacecraft, pointing towards the travel direction of the spacecraft. Using the set dimensions for a 3p PQ (stated in appendix A), the following scenarios are analysed.

- Best case: smallest side towards front, with longest side towards Earth;
- Mid case: 'sideways', with short side towards Earth;
- Worst case: backplate towards travel direction, with short side towards Earth.

The pointing accuracy of the mission can be derived from the gap this new attitude actuator is filling. The pointing accuracy will be in between that of reaction wheels and magnetorquers, resulting in a range of 1 to 5 deg, as stated in section 1.2. Reaction wheels deliver a higher pointing accuracy than momentum bias wheels, which in turn perform better than magnetorquers in terms of pointing accuracy, delivering a maximum of 5 deg. The pointing accuracy by MBW is depicted as the maximum sway caused by nutation from the desired orientation of the spacecraft.

The environment the PQ will endure during its lifetime brings disturbances. The major disturbance torques for small satellites are the aerodynamic, geomagnetic, solar radiation pressure and gravity gradient torque. These will be calculated in section 2.3. During launch, the MBW will endure major acceleration and vibrational forces and are dependent on the launch vehicle selected. The assumption can be made for a launch vehicle to be similar to the one used for the Delfi-PQ, the Falcon 9 by SpaceX [46]. Two comparable small payload launchers to the Falcon 9 are the Rocket Lab Electron and Ariane Space Vega. From these three, a maximum accelerations of the Falcon 9 are shown to be the highest and will therefore be used as design requirements. After orbit insertion, the environment changes from heavy acceleration and vibration loads to temperature fluctuation and a very low air density, very close to vacuum. The direct requirement resulting from this environment is the ability to operate in vacuum and the temperature range experienced in orbit. An assumption can be made for the temperature range to be equal to the one assumed and tested for the Delfi-PQ, from -20 to +50 $°C$ [41].

2.3. Environment

In order to quantify the specifications for the momentum bias wheel design, the environment must be simulated. The worst case aerodynamic, solar radiation pressure, geomagnetic and gravity gradient disturbance torque are calculated below, to investigate which disturbance torques would be used as design torques.

2.3.1. Aerodynamic Disturbance Torque

Starting off with the assumed dominant disturbance, the aerodynamic disturbance involves particles interacting with the spacecraft, resulting in a certain pressure altering the spacecraft's momentum. The atmosphere creates a centre of pressure, resulting in a torque related on the difference between the difference between the centre of pressure and centre of mass of the spacecraft.

$$T_a = \frac{1}{2}\rho_{atm} C_d A_r V^2 (c_{p_a} - c_m) \tag{2.1}$$

With C_d as the drag coefficient of the PQ, A_r is the ram area of the PocketQube, V its velocity, and c_{p_a} and c_m as the vector centre of pressure due to the atmosphere and mass respectively. Calculating an estimate of the aerodynamic disturbance torque can be done to confirm it to be the singular dominant torque.

The drag coefficient can be assumed to be 2.1, due to the rectangular shape of the PQ. Assuming the worst case scenario with the nadir pointing scheme, the ram area will be equal to the backplate area of 5.8 by 19.2 cm. The relation of the centre of mass and pressure will be assumed to be fully dependent on the requirement PQ-Mass-04 of the PocketQube Standard [40], stating a 1 cm maximum offset of the centre of mass from its geometrical centre, in stowed condition. The orbital velocity will be greatest at the lowest operational orbit altitude, due to fundamental astrodynamics, as stated in equation 2.2.

$$V^2 = \frac{\mu_\oplus}{R_\oplus + h_i} \tag{2.2}$$

The air density is a dynamic value, for which the worst case scenario must be used. Three trusted sources will used and compared to find the worst case scenario. The NASA atmosphere model [26], the JB2008 atmosphere model [19] and the SMAD atmosphere data [55] can be used. As solar activity is heavily impacting the atmosphere characteristics, it must be taken into account. Since only the JB2008 model and SMAD data utilise the solar activity, and the SMAD data is a magnitude larger than the JB2008 data, the SMAD data will be utilised. The SMAD data as presented in table 2.2 makes clear that the density decreases with increasing orbit altitude, with the following density data used for the calculation. Utilising all assumed values in equation 2.1 results in a worst case scenario aerodynamic disturbance torque of 18.3 Nm.

$$T_a = \frac{1}{2} \cdot 4.39 \cdot 10^{-11} \cdot 2.1 \cdot (0.192 \cdot 0.0580) \cdot \frac{\mu_\oplus}{R_\oplus + h_i} \cdot 0.01 \tag{2.3}$$

$$T_a = 18.3\ \mu Nm \tag{2.4}$$

Table 2.2: Atmospheric density as retrieved from SMAD table I-1 [55].

Orbit altitude (km)	**Minimum** (kg/m^3)	**Mean** (kg/m^3)	**Maximum** (kg/m^3)
300	$1.07 \cdot 10^{-11}$	$2.30 \cdot 10^{-11}$	$4.39 \cdot 10^{-11}$
325	$5.83 \cdot 10^{-12}$	$1.38 \cdot 10^{-11}$	$2.85 \cdot 10^{-11}$
350	$3.17 \cdot 10^{-12}$	$8.33 \cdot 10^{-12}$	$1.82 \cdot 10^{-11}$
375	$1.81 \cdot 10^{-12}$	$5.24 \cdot 10^{-12}$	$1.25 \cdot 10^{-11}$
400	$1.04 \cdot 10^{-12}$	$3.29 \cdot 10^{-12}$	$8.43 \cdot 10^{-12}$
450	$3.68 \cdot 10^{-13}$	$1.39 \cdot 10^{-12}$	$4.05 \cdot 10^{-12}$
500	$1.40 \cdot 10^{-13}$	$6.15 \cdot 10^{-13}$	$2.03 \cdot 10^{-12}$

2.3.2. Solar Radiation Pressure Disturbance Torque

The solar pressure is present whenever the sunlight reaches the spacecraft. The solar pressure is calculated using the magnitude and direction of the area facing the Sun. In the case of an asymmetrically weight distributed spacecraft, the solar radiation pressure (SRP) disturbance torque can be modelled as a function of the difference between the centre of mass and pressure. The solar panels and antennas can be taken into account, to make sure that the maximum disturbance torque over an orbit can be found.

$$T_s = \frac{F_\oplus \cdot d_\oplus^2}{c \cdot d_s^2} \cdot A_s \cdot cos(\alpha_s) \cdot (1+q)(c_{p_s} - c_m) \tag{2.5}$$

$$\frac{d_s}{d_\oplus} = \frac{d_\oplus - (R_\oplus + h_{orbit})}{d_\oplus} = \frac{149597870 - (6371 + 400)}{149597870} = 0.999954 \approx 1 \tag{2.6}$$

$$T_s = \frac{F_\oplus}{c} \cdot A_s \cdot cos(\alpha_s) \cdot (1+q)(c_{p_s} - c_m) \tag{2.7}$$

With $F_\oplus$ as the solar flux at Earth, $d_\oplus$ as the distance between the Earth and the Sun, d_s as the distance between the PocketQube and the Sun and c as the speed of light, A_s as the Sun-facing surface area, α_s as the angle of incidence of the Sun, c_{p_a} as the vector for the centre of pressure due to the Sun and c_m as the vector for the centre mass of the PocketQube. Since the orbit of the PocketQube is in low Earth orbit, the distances d_s and $d_\oplus$ can be assumed to be equal. Furthermore, due to the Sun's increased activity, the set value of 1368 W/m^2 for solar flux at Earth, is uncertain as it is. To accommodate for this level of uncertainty is beyond the scope of this thesis.

The relation of the centre of mass and pressure will be assumed to be fully dependent on the requirement PQ-Mass-04 of the PocketQube Standard [40], stating a 1 cm maximum offset of the centre of mass from its geometrical centre, in stowed condition. In the worst case scenario, it is assumed that the panel of the Sun facing side is the largest, perfectly reflective and perpendicular to the Sun. With the maximum Sun facing area to be equal to the backplate area of 5.8 by 19.2 cm, the solar radiation pressure torque would be several magnitude smaller than the maximum aerodynamic disturbance torque and will therefore be neglected.

$$T_s = \frac{1368}{2.99 \cdot 10^8} \cdot (0.192 \cdot 0.0580) \cdot 1 \cdot (1+1) \cdot (0.01) = 1.02\ nNm \tag{2.8}$$

2.3.3. Geomagnetic Disturbance Torque

The magnetic field of Earth induces a torque on the residual magnetic moment of spacecraft, whenever these fields are not aligned. The maximum value for the magnetic disturbance torque can be preliminary calculated using equation 2.9.

$$T_m = D_{PQ} \cdot B_\oplus = D_{PQ} \cdot \left(\frac{M \cdot \lambda}{(R_\oplus + h_{orbit})^3} \right) = D_{PQ} \cdot \left(\frac{7.8 \cdot 10^{15} \cdot 2}{((6371 + h_{orbit}) \cdot 10^3)^3} \right) \tag{2.9}$$

With D_{PQ} as the residual magnetic moment of the spacecraft and B as the magnetic field strength of the Earth at a certain location of Earth. The magnetic field can be interpreted as M, the magnetic moment of Earth multiplied by the magnetic constant. Finally, λ is a function of magnetic latitude ranging from 1 at the magnetic equator to 2 at the magnetic poles. To calculate the maximum torque, the magnetic latitude constant is assumed to be 2, as the orbit of the PQ is assumed to be near polar. The residual dipole of the PQ bus has to be assumed, as the current design and orientation of the subsystems, which cause the residual dipole due to electrical interfaces, is incomplete. The Delfi-PQ does not yet have an estimate of a residual, but its forefather, the Delfi-n3xt does. This 3U CubeSat is assumed to have a magnetic residual dipole of approximately 0.001 Am^2.

The World Magnetic Model (WMM) [14], which provides magnetic field parameters based on longitude, latitude, latitude and date, will be incorporated to find the highest magnetic torque. This predictive model is updated every five years and the current model ranges from 2020 to 2025. As the WMM is a prediction, it could deviate from actual values. The deviation increases per year and is stated by the official documentation of the WMM. This deviation, together with a comparison to the values obtained for the magnetic field in equation 2.9 should be taken into account, in the form of safety factors. Analysing this difference by extracting values from the WMM for latitude and longitude per orbit shows an average 10 % increase in comparison the value calculated in equation 2.9. This safety factor will be included in the rewritten equation for the geomagnetic disturbance torque in equation 2.10.

$$T_m = 1.1 \cdot 10^{-3} \cdot \left(\frac{7.8 \cdot 10^{15} \cdot 2}{((6371 + h_{orbit}) \cdot 10^3)^3} \right) \tag{2.10}$$

Equation 2.10 shows the inverse correlation between the orbit altitude and the magnitude of the geomagnetic disturbance torque. The maximum value for the disturbance torque is found at the lowest possible orbit altitude of 300 km and shall thus be used in the calculation, due to the requirement of operation until 300 km. This results in a maximum geomagnetic disturbance torque of 58 nNm. The result is quite low and the uncertainty of the magnetic residual dipole is quite high, therefore the magnetic disturbance torque will be neglected, as it is multiple magnitudes smaller than the assumed maximum aerodynamic disturbance torque.

$$T_m = 58 \ nNm \tag{2.11}$$

2.3.4. Gravity Gradient Disturbance Torque

The gravity gradient disturbance torque is dependent on the difference between the centre of mass and centre of gravity of the spacecraft. The centre of gravity is dependent on the orientation of the PocketQube with respect to Earth and the centre of mass is fixed within the PocketQube. The gravity gradient torque increases when the angle between the axis of the smallest moment of inertia and the axis from Earth's centre to the spacecraft increases. The following formula calculates the torque:

$$T_g = \frac{3\mu_\oplus}{2(R_\oplus + h_{orbit})^3} \cdot \left| I_{yy} - I_{zz} \right| \cdot cos(2\phi_I) \tag{2.12}$$

With I as the moment of inertia of the major and minor axis and ϕ_I represents the angle between the Z-axis of the spacecraft and the line from the centre of the Earth to the centre of the spacecraft. Once again, the maximum disturbance torque is found closest to the orbiting planet. Additionally, the torque is maximum when the angle ϕ_I is 45 deg and when the difference between the major and minor mass moment of inertia is the largest. As mentioned in section 2.1, the final structural design of the new PQ mission is not final, so a uniform density over the spacecraft bus is used. The sliding backplate and any possible imbalances of the spacecraft is neglected for this calculation, as equation 2.16 shows that the value of the gravity gradient torque, equalling 3.7 nNm is several magnitude smaller than the dominant torque created by the aerodynamic disturbance. Therefore, the gravity gradient disturbance torque will be neglected.

$$I_{yy} = \frac{1}{12} \cdot m_{PQ} \cdot (0.0500^2 + 0.178^2) \tag{2.13}$$

$$I_{zz} = \frac{1}{6} \cdot m_{PQ} \cdot 0.0500^2 \tag{2.14}$$

$$T_g = \frac{3 \cdot 3.986 \cdot 10^{14}}{2((6371 + 300) \cdot 10^3)^3} \cdot \left| \frac{1}{12} \cdot m_{PQ} \cdot (0.178^2 - 0.0500^2) \right| \tag{2.15}$$

$$T_g = 3.79 \ nNm \tag{2.16}$$

2.4. Angular Momentum

The aerodynamic disturbance torque is a several magnitudes greater than the three other disturbance torques, showing clear dominance in disturbance. Therefore, the sole disturbance torque taken into account for the design of the new MBW will be the aerodynamic disturbance torque. However, the uncertainty in certain values still remains. As stated before, the density is a very dynamic characteristic of the atmosphere, as is depends on the activity of the Sun. Additionally, the mission and satellite characteristics are uncertain, as the nadir pointing scheme is a requirement, but not specifically requires an exact side to face the Earth, as the payload of a PQ can be small enough to be pointed out of most of the PQ sides. This impacts the certainty of the ram area and drag coefficient while the uncertain satellite characteristics impact the offset between the centres of mass and pressure. The singular certain value within the aerodynamic disturbance torque calculation is assumed to be the orbital velocity, for which equation 2.2 is used.

To then calculate the maximum aerodynamic disturbance torque for which the momentum bias wheel will be designed, normal distributions can be utilised to model the uncertainty of the stated variables. To do this, the standard deviation per variable must be determined, through the assumption that 99.7 % of all data will be between three times negative and positive standard deviation. If thus a maximum is known, this will be equal to the average plus three times the standard deviation. This can be done for the air density values presented in table 2.2, setting the mean of the air density to $2.30 \cdot 10^{-11}$ and its standard deviation to:

$$\sigma_{\rho_{atm}} = \frac{4.39 \cdot 10^{-11} - 2.30 \cdot 10^{-11}}{3} = 0.696 \cdot 10^{-11}\ kg/m^3 \tag{2.17}$$

This can be done for the three other variables dictating the aerodynamic disturbance torque. The offset between the centres of mass and pressure is assumed to have a mean of 0.5 cm and standard deviation of 0.16 cm, as it would thus range between 0 and 1 cm. The ram area would range between the largest and smallest possible area, with the assumption that the frontal area is kept constant and perpendicular to the travel direction due to its required nadir pointing scheme. This would result in a minimum and maximum of 25 and 111.36 cm^2, leading to a mean of 0.00682 m^2 and a standard deviation of 0.00144 m^2. Finally, the drag coefficient is also dependent on the orientation of the spacecraft in orbit. The maximum and minimum would range from an orientation where the largest area is pointing towards the travel direction to where the smallest area is pointing towards the travel direction. Fluid dynamics [13] dictates the rectangular rod drag coefficient to be dependent on the ratio between its length in travel direction and height perpendicular to the travel direction. Utilising the minimum and maximum of the ratio leads to a minimum and maximum drag coefficient of 1.3 and 2.2 respectively. This would result in a mean of 1.75 and a standard deviation of 0.15.

Having set up the normal distribution for the uncertain variables, the aerodynamic disturbance torque distribution can be calculated, resulting in the following normal distribution data. The maximum aerodynamic disturbance torque can be done by extracting and using the mean and standard deviation as stated in equation 2.18.

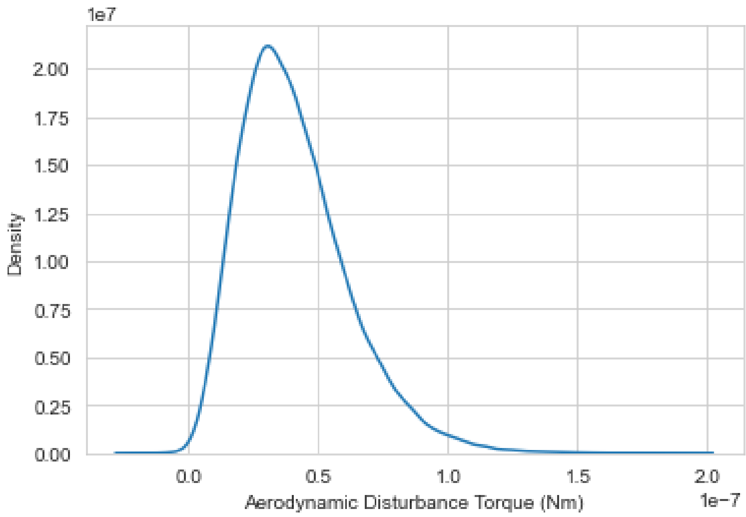

Figure 2.3: The resulting skewed normal distribution of the aerodynamic disturbance torque.

$$T_{a,max} = \mu_{T_a} + 3\sigma_{T_a} = 83.3\ nNm \tag{2.18}$$

The required angular momentum can be preliminary calculated by setting the maximum allowable motion, as presented in equation 2.19, retrieved from SMAD [55]. Luckily, the accuracy requirement mentioned earlier of 1 to 5 degrees allows for a range of maximum allowable motion. To ensure the maximum effectiveness of the MBW system in all configuration of the PQ bus, the maximum allowable motion (θ_a) shall thus be 1 degree. Together with the maximum disturbance torque $T_{a,max}$ from earlier and the orbit the spacecraft will have at the point of the maximum torque, the required momentum of the MBW can be calculated.

$$h_{MBW} = \frac{T_{a,max} \cdot P}{4 \cdot \theta_a} = \frac{T_{a,max} \cdot 2\pi\sqrt{\frac{(R_\oplus + h_i)^3}{\mu_\oplus}}}{4 \cdot 1 \cdot \left(\frac{2\pi}{180}\right)} = 6.05\ mNms \tag{2.19}$$

2.5. Operation

This angular momentum has to be reached through a flywheel spun up to a nominal angular velocity, which both will be designed according the requirements set regarding power, volume and mass budgets. However, spinning up to this nominal operating velocity requires (possibly high) torques that possibly can make the spacecraft lose control required during its lifetime. To prevent this, an additional requirement regarding the maximum torque during spin up phase and stability during operation must be calculated.

The spin up phase is rather simple to calculate for. The maximum torque the motor can exert is dependent on the counter torque the other attitude controllers on board can supply. In this case, it will be assumed that the Delfi-PQ specified magnetorquers designed by van den Bos [6] supply that torque. Using equation 2.20 and the required torque value of the magnetorquers by van den Bos' design of 0.004 Am^2, the maximum torque the motor can deliver is equal to 0.0962 μNm. This value will be translated into a maximum acceleration once the flywheel is designed.

$$T_m = D_{PQ} \cdot B_\oplus = D_{MTQ} \cdot \left(\frac{M \cdot \lambda}{(R_\oplus + h_{orbit})^3}\right) = 4.00 \cdot 10^{-3} \cdot \left(\frac{7.80 \cdot 10^{15} \cdot 1}{((6371 + 500) \cdot 10^3)^3}\right) = 9.62 \cdot 10^{-8}\,Nm \tag{2.20}$$

Another important matter when discussing the pointing accuracy is the desired stability of the new MBW. Through possible imperfections or external disturbances over the axis of rotation can the angular velocity of the MBW differ, and this must be corrected. To ensure the possibility of correction, a motor requirement is to incorporate velocity sensors into the system. The effect of this changing velocity will turn the spacecraft, which has to stay within the pointing accuracy of 1 and 5 deg as set in requirement SYS04. This requirement can be used to calculate a maximum change in the angular momentum over a certain amount of time. A requirement regarding the stability can thus be calculated, through the conservation of momentum and torque calculations in equations 2.21 through 2.26. All time domains will be set to 1 second, for simplicity, and the assumption that the motor is able to correct itself after a period of 1 second due to the velocity sensors feedback.

$$\mathbf{h} = h_{MBW} + h_{PQ} = I_{MBW} \cdot \omega_{MBW} + I_{PQ} \cdot \omega_{PQ} = h_{req} \tag{2.21}$$

$$\frac{\Delta \mathbf{h}}{\Delta t} = \mathbf{T} = T_{MBQ} + T_{PQ} = 0 \tag{2.22}$$

$$\Delta h_{MBW} = T_{MBW} \cdot \Delta t \tag{2.23}$$

$$\theta_a = \frac{1}{2} \alpha \cdot (\Delta t)^2 \tag{2.24}$$

$$\frac{\Delta h_{MBW}}{\Delta t} = T_{MBW} = T_{PQ} = I_{PQ} \cdot \alpha = \frac{1}{12} m_{PQ} \cdot \left(x^2 + y^2\right) \cdot \frac{2 \cdot \theta_a}{(\Delta t)^2} \tag{2.25}$$

$$\Delta h_{MBW} = \frac{1}{12} m_{PQ} \cdot \left(x^2 + y^2\right) \cdot \frac{2 \cdot \theta_a}{\Delta t} \tag{2.26}$$

The change in momentum of the MBW (Δh_{MBW}) is dependent on the torque supplied by the MBW (T_{MBW}) and the time difference (Δt) over which the torque is supplied. As the MBW torque applies and is equal to the torque acted on the spacecraft (T_{PQ}), the acceleration of the spacecraft (α) can be calculated through the smallest moment of inertia of the PQ (I_{PQ_z}), over the length of the spacecraft. The angle the spacecraft would make under that set time through an assumed constant acceleration would have to be equal or lower than the allowed range of motion as specified in requirement SYS04. Filling all this in, through values supplied in table 2.1, the maximum allowed change in momentum would be between 10.9 and 54.5 μNms or between 0.180 and 0.901% of the required angular momentum or required operational velocity, in correspondence to the required pointing accuracy range.

2.6. Requirements Outcome

The outcomes from the previous section has been set up in clear tables to be able to summarise and trace the requirements.

Table 2.3: Top level requirements summarised.

ID	Requirement Description
SYS01	The MBW will be able to store angular momentum around its rotational axis.
SYS02	The MBW will survive the mission environments between its insertion orbit and decay orbit.
SYS03	The MBW will be able to maintain its operational angular momentum over its mission lifetime.
SYS04	The MBW will be able to limit the effect of the disturbance torques over one orbit to be within the pointing accuracy of 1-5 deg.
SYS05	The MBW will enable nadir-pointing for the PQ.
SYS06	The MBW will adhere to the standards and requirements set in the PocketQube Standard 1.0.
SYS07	The MBW will be mounted on the PQ9 PCB backboard.
SYS08	The MBW will not obstruct the connector pins of the PQ9 PCB backboard.

Table 2.4: Momentum bias wheel requirements summarised and traced.

ID	Requirement Description	Trace
MBW01	The maximum volume of the MBW within the PQ bus is 21.1 cm^3.	-
MBW02	The maximum mass of the MBW will be 41.4 g.	-
MBW03	The maximum height of the MBW will be 12.0 mm.	SYS07
MBW04	The maximum power of the MBW is no more than 180 mW average per orbit.	-
MBW05	The maximum cost of the MBW is no more than 500 Euros.	-
MBW06	The MBW motor shall have sensors to be able to correct angular velocity errors.	SYS03
MBW07	The MBW shall have an eigenfrequency high enough to resist the vibration loads during launch.	SYS02
MBW08	The MBW will be able to withstand 8.5 g of acceleration loads.	SYS02
MBW09	The MBW will not yield the PQ9 PCB backboard due to the 8.5 g of acceleration loads.	SYS02, SYS07
MBW10	The MBW will be able to operate in vacuum.	SYS02
MBW11	The MBW will be able to operate in temperatures between -20 and +50 $°C$	SYS02
MBW12	The minimum amount of angular momentum created by the MBW will be 6.05 $mNms$.	SYS01, SYS04
MBW13	The maximum torque the MBW will exert will be 0.0962 μNm.	SYS01
MBW14	The maximum deviation from the required angular momentum of the MBW will be 0.180%.	SYS04

3. Theoretical Model

This chapter will confirm the angular momentum requirement set in the previous chapter. A theoretical model will be made to replicate an orbit scenario of the spacecraft utilising a momentum bias wheel. This will be done through a simulation utilising simplified equations of motions (EoM), for every configuration possible, to ensure the operability of the MBW in any configuration possible within the PQ bus. Furthermore, as explained in subsection 2.3.1, the aerodynamic disturbance torque is dependent on the offset between the centre of mass and pressure. When the spacecraft orientation would change, the centre of pressure would change as well due to the changing ram area and geometry. For the sake of simplicity and time, the changing of the centre of pressure will be neglected in this simulation, due to the small angles this simulation will handle in.

This chapter will handle in two coordinate systems, the fixed Earth reference system and the body reference system. To ensure clarity across this chapter, the same systems are maintained between sections. The orbital situation of the mission will be assumed as constant, with the satellite orbiting the Earth on the Y axis. The Earth fixed frame and body frame are visualised in figures 3.1, 3.2 and 3.3.

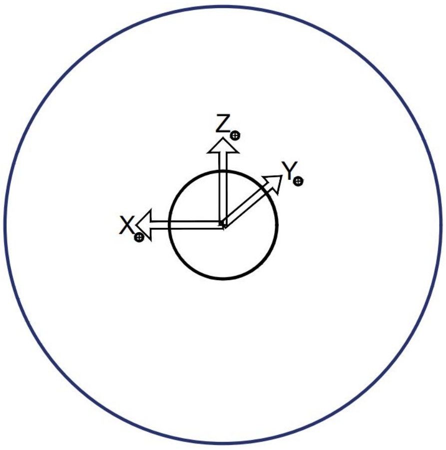

Figure 3.1: The coordinate system used for the fixed Earth reference system.

The three nadir pointing scenarios the bus shall have in these simulations are:

- The length of the body perpendicular to the flight path, with the smallest side towards Earth;
- The length of the body perpendicular to the flight path, with the largest side towards Earth;
- The length of the body along the flight path.

For both scenarios, all positioning options for the MBW and all directions of the disturbance torque will be analysed.

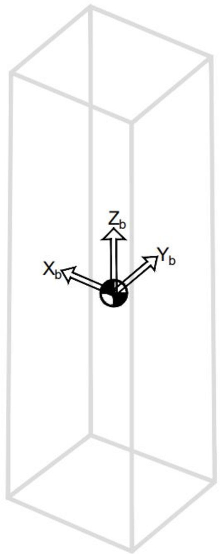

Figure 3.2: The coordinate system used for the body fixed reference system, for the first scenario.

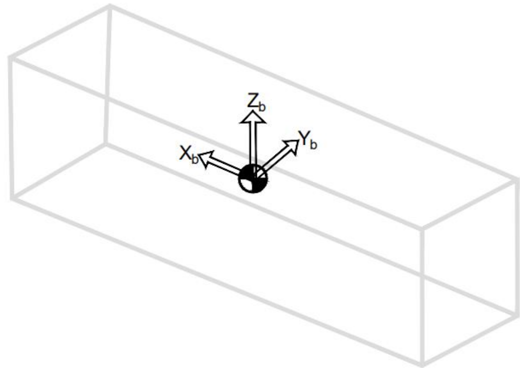

Figure 3.3: The coordinate system used for the body fixed reference system, for the second scenario.

In total, this would add up to 27 scenarios required to be analysed. Only the summary of these results will be presented here, the code utilised will be available in appendix B. Two types of code files will be given. The first has a selector built in, and the second type consisting of three programs, one for each axis, analyses, plots and saves all data concerning the orientation of the PQ over one orbit.

The EoM can be derived through equation 3.1, from which both actuators' EoM will be derived.

$$\vec{T} = \left.\frac{d\vec{H}}{dt}\right|_B + \vec{\omega} \times \vec{H} \tag{3.1}$$

The torques on the spacecraft under vector $\vec{M}$ include the total disturbance torques over all axes and all control torques, which would be the extra attitude control actuators to eliminate the accumulated torques over an orbit. These extra control torques will for now be excluded from the set up of the equations of motion, for the sake of simplicity. Since it is unknown what orientation the spacecraft will face, all directions must be set up. The disturbance torque is set at the found value from the previous chapter, regardless of direction of the spacecraft, but is also tested on all three axis, to ensure the resilience of the momentum bias wheel against disturbance torques over all axes. Writing this out becomes:

$$\vec{T}_d + \vec{T}_c = \frac{d(\vec{H}_B + \vec{H}_w)}{dt} + \vec{\omega} \times (\vec{H}_B + \vec{H}_w) \tag{3.2}$$

$$\vec{T}_d + \vec{T}_c = \vec{I}_B \left.\frac{d\vec{\omega}}{dt}\right|_B + \vec{\omega} \times \vec{I}_B\vec{\omega} + \left.\frac{d\vec{H}_w}{dt}\right|_B + \vec{\omega} \times \vec{H}_w \tag{3.3}$$

The third and fourth term in equation 3.3 are dictated by the behaviour and location of the MBW. The third is only non zero when the MBW is allowed to change its angular velocity in stead of maintaining a nominal velocity to ensure a nominal angular momentum during operation. Requirement SYS03 dictates that the MBW will maintain its velocity over its operational period, thus setting the third term to zero, and setting up an axis system results in equation 3.8. The x direction is along the orbit path, y direction is to the side of the orbit path and the z direction is towards the Earth. The ω terms are the angular velocities within the body fixed reference frame and to convert these to the Earth fixed reference frame, the following relations can be utilised, with n as the mean motion of the spacecraft, dependent on the orbit altitude and θ as the angle of the spacecraft over a respective axis.

$$\omega_x = \dot{\theta}_x - n \cdot \theta_z \tag{3.4}$$

$$\omega_y = \dot{\theta}_y - n \tag{3.5}$$

$$\omega_z = \dot{\theta}_z + n \cdot \theta_x \tag{3.6}$$

$$n = \sqrt{\frac{(R_\oplus + h_{orbit})^3}{\mu_\oplus}} \tag{3.7}$$

Then finally, the following EoM for the MBW can be set up.

$$\begin{bmatrix} T_{d,x} \\ T_{d,y} \\ T_{d,z} \end{bmatrix} = \begin{bmatrix} I_{b,x} \\ I_{b,y} \\ I_{b,z} \end{bmatrix} \begin{bmatrix} \ddot{\theta}_x - n \cdot \dot{\theta}_z \\ \ddot{\theta}_y \\ \ddot{\theta}_z + n \cdot \dot{\theta}_x \end{bmatrix} + \begin{bmatrix} \dot{\theta}_x - n \cdot \theta_z \\ \dot{\theta}_y - n \\ \dot{\theta}_z + n \cdot \theta_x \end{bmatrix} \times \begin{bmatrix} I_{b,x} \cdot (\dot{\theta}_x - n \cdot \theta_z) \\ I_{b,y} \cdot (\dot{\theta}_y - n) \\ I_{b,z} \cdot (\dot{\theta}_z + n \cdot \theta_x) \end{bmatrix} + \begin{bmatrix} \dot{\theta}_x - n \cdot \theta_z \\ \dot{\theta}_y - n \\ \dot{\theta}_z + n \cdot \theta_x \end{bmatrix} \times \begin{bmatrix} H_{w,x} \\ H_{w,y} \\ H_{w,z} \end{bmatrix} \tag{3.8}$$

All scenarios where simulated over one orbit, with all simulations maintaining the spacecraft orientation within the maximum allowable motion. All scenarios were similar and did not change in magnitude considerably due to the changing geometry of the PQ between each scenario. Only the axis of precession changed according to the axis along which the MBW operated.

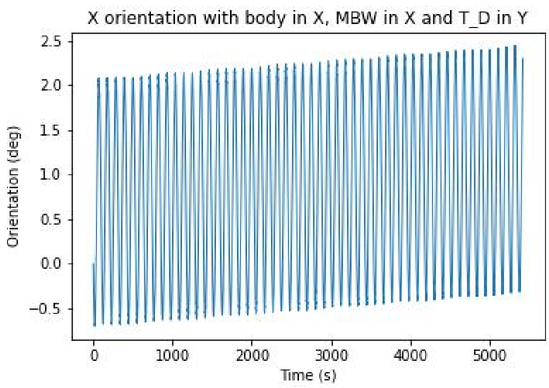

Figure 3.4: Simulated X orientation of a PQ using a MBW.

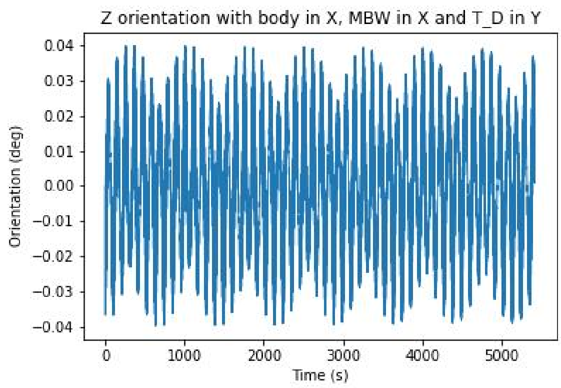

Figure 3.5: Simulated Z orientation of a PQ using a MBW.

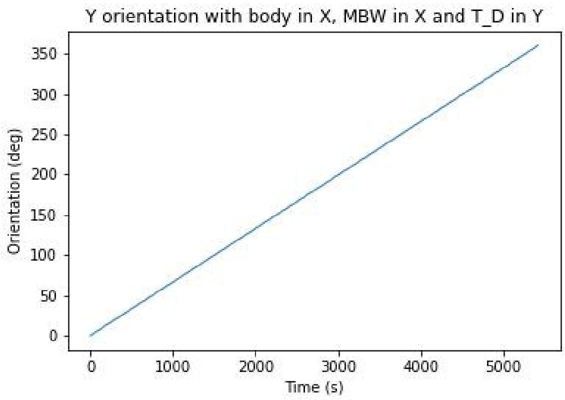

Figure 3.6: Simulated Y orientation of a PQ using a MBW.

In the three figures above, a scenario with the body length orientated along the X-axis (along track), the MBW operating on the X-axis and the torque applied to the Y-axis. Due to the fact that the spacecraft has to rotate to achieve nadir pointing, the Y orientation of the spacecraft rises from 0 to 360 linearly. The X- and Z-axis graphs display the precession and nutation, as the graph oscillates but also changes it centre or amplitude.

4. Design

The design of the momentum bias wheel requires several steps to be able to come to the best design possible within the scope of this thesis. Firstly, design options regarding the materials, orientations, components and manufacturing methods used for the design. These options must then be traded off against weighed criteria to ensure the options in line with the required and best performing are selected. Finally, the design can be finalised, synthesised from the selected options.

The motor and its characteristics, sensors and driver, the flywheel material and shape, flywheel and motor housing as reinforcements against launch forces and possible manufacturing processes are discussed in this chapter.

4.1. Motor Selection

The selected motor is central in the momentum bias wheel design in delivering torque to create an angular momentum sufficient for the maximum allowable motion of the PQ. The type of motor, its characteristics in size, power and speed and the options regarding drive, sensing and lubrication must be taken into account to ensure an optimal operable motor for a vacuum environment within the set financial budget.

4.1.1. Motor Manufacturer

Before selecting the best options for the motor and motivating these choices, manufacturers must be selected to ensure that all the choices made are realistic. Multiple projects [27] [54] involving the design and prototyping of other ACS for PQ missions have utilised motors from Maxon Motors, Faulhaber, Portescap and Orbray in their trade-off, from which motors will be selected according to the requirements set in this thesis. Additionally, manufacturers that excel in creating miniature motors will also be included, such as Precision Microdrives, Ineed Electronics and Vybronics. These seven manufacturers together pool a large amount of miniature high speed motors, for which selections will be made through all its respective important properties. The initial collection of these manufacturers is a wide range of motors, all selected motors are selected on the assumption that the motor would fit the application and adhere to the requirements as set in chapter 2. All selected motors for this selection process are stated in appendix C.

4.1.2. Motor Type

The motor types available at the selected manufacturers are plentiful and must be boiled down to a selection that can be utilised in the MBW design. Since the previous Delfi-PQ EPS delivered DC power to the subsystems, the motor selected will be a DC motor, not an AC motor. The two common options supplied by most manufacturers are brushed and brushless DC (BLDC) motors, both having its advantages and disadvantages [31] [32] [34]. Both motors utilise electromagnetism through windings to induce attractive and repulsive forces to spin the rotor, but brushed DC motors have brushes which are utilised in conjunction with these windings to control which and how the windings are activated. Since the brushes and rotor have to be in contact to transfer electrical power, friction will occur and induce mechanical wear, reducing the lifetime of the motor drastically when driven at high speeds. However, no additional electronics are required to drive the brushed motor.

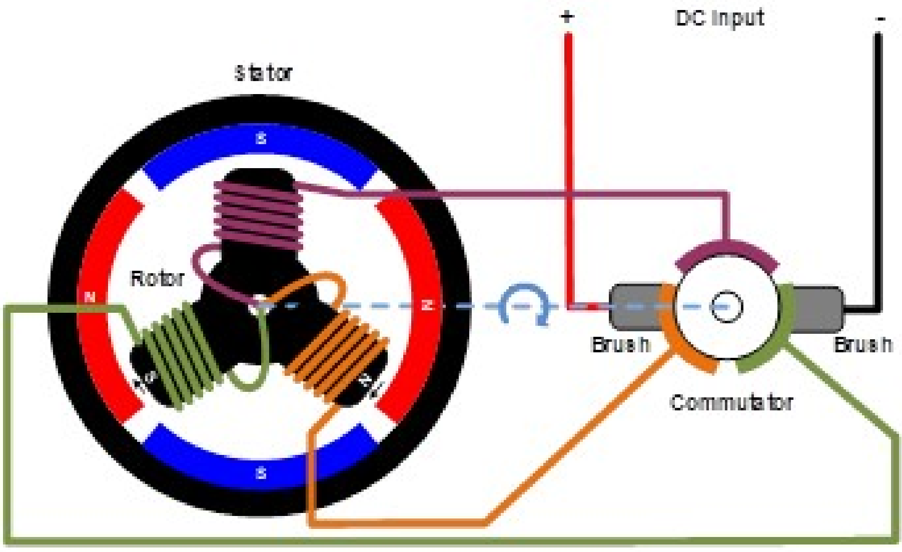

Figure 4.1: Schematic for a four pole brushed DC motor. [34]

In contrast to the brushed motor, the BLDC motor does not contain brushes, has lower mechanical wear but does require additional drive electronics to operate the motor. Within these drive electronics, velocity sensors such as Hall effect sensors or Hall sensors can be implemented to create a feedback loop and add stability and accuracy for the attained operational velocity.

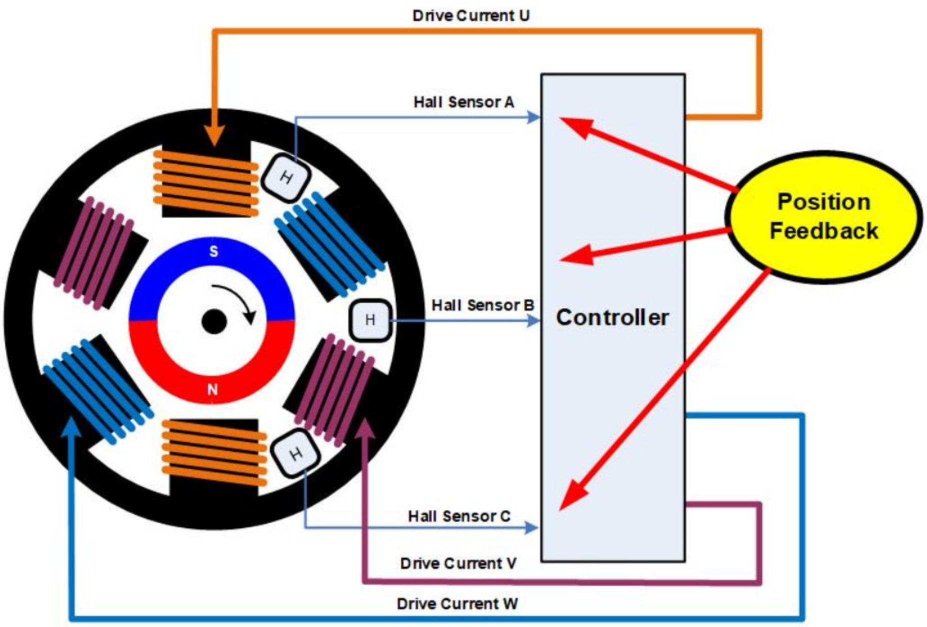

Figure 4.2: Schematic for a two pole BLDC motor. [34]

The superior speed, minimal wear and velocity sensor incorporation makes the BLDC motor the superior option for PQ MBW, as the lifetime, velocity and velocity stability requirements are critical for the success of the ACS. Furthermore, the decision to utilise BLDC type motors eliminates the motor options from Precision Microdrives and Ineed Electronics.

4.1.3. Motor Bearings

One of the critical design aspects of the motor is the bearing and its lubrication technique, as it dictates the power usage during nominal operation and the operability within vacuum. Bearing options commonly used in DC motors are ball or sleeve bearings and use different lubricants. Sleeve bearings mostly use self lubricating materials or oil impregnated materials. This causes issues within a vacuum environment as this type of lubrication would evaporate at the minimal pressure values, due to the vapour pressure of these oils. Ball bearings can utilise vacuum rated lubricants, such as vacuum grease. This would circumvent the issue of the high vapour pressure at high vacuum. So for the MBW motor, ball bearings must be utilised, together with a vacuum lubricant. This does however impact the power usage of the motor during nominal operation [11]. Varying between manufacturers, a different vacuum rated lubricant will be selected the motor.

The decision to utilise ball bearings with a vacuum lubricant eliminates the motor options from Orbray and Vybronics, as these two manufacturers only provide motors with sleeve bearings or provide no information at all about the bearing usage within their motor designs.

An inquiry on the decrease of speed at max power due to the utilisation of vacuum grease has been made to the remaining manufacturers, but none have tested the vacuum thoroughly to have consistent data to offer insight to how much the speed decreases due to this vacuum grease. However, Faulhaber and Maxon Motors engineers agree that the vacuum grease has an impact on the speed through the increased torque required to move the rotor. The exact vacuum rated lubricant friction characteristics are not known, as they only have stated that the current will increase slightly, due to the increased torque required to turn the motor due to the increased friction. They do not disclose how much it increases, so other sources must be used. A research done by NASA in the field of tribology between multiple kinds of vacuum rated lubricants [11], liquid, grease and solid, has yielded that the friction values differ significantly between different lubricant types; with liquid lubrication having a lower friction coefficient, around 20 % lower. NSK has also delved into the difference between oil and grease lubrication [35] and states that grease lubricated bearings are only capable of 80 % of the speed an oil lubricated bearing could achieve. However, the technical documents regarding the difference between a Faulhaber non-vacuum and vacuum rated motor attached to Hoevenaars' work [27] states the dissimilarity of friction coefficient to be non-existent. Due to this inconsistency in data, the best course of action would be to build the prototype with a vacuum rated motor. As for now, the calculations done for this design will be utilising the 20 % decrease in speed. Finally, the presence of atmospheric pressure does affect the performance of a vacuum grease [36], as it can have higher friction coefficients at atmospheric pressure than at vacuum conditions. This is something to keep an eye on during prototyping and testing.

4.1.4. Motor Size, Speed and Power

The size of the motor is to be limited by requirement MBW01 and MBW03, stating the entire system having a maximum volume 21.1 cm^3 and a maximum height of 12.0 mm. In order to make a design fitting of the volume requirement, the shape of the motor would be similar to the flywheel. The limiting factor in motor selection would thus become height. From the few manufacturers left, only Faulhaber [21] and Maxon Motors [30] provide motors with adequate volume to speed and power ratios, thus only these two shall be utilised for the final trade off, as Portescap [39] offers motors a magnitude larger than those of its competitors.

The speed of the motor has to be high enough to deliver the required angular momentum at the maximum power. As the flywheel design is not yet final and thus does not give insight to the required angular velocity, a higher speed is simply more favoured than a lower speed, which is thus used as a trade-off characteristic. The speed at the maximum power of 180 mW has to be calculated using the motor characteristics given via the motor catalogues of the manufacturers. Different manufacturers give various levels of motor characteristics, as Faulhaber gives information on the static and dynamic friction coefficient of their standard lubrication within the motor bearing, whereas Maxon Motors does not. Both do give a speed and torque constants, from which the speed at maximum power can be calculated.

During operation of the MBW, it is assumed that the only torque the motor has to deliver is to counteract its own friction torques. It is assumed that the friction torque of the motor is dependent on two constants, C_0 (mNm) and C_v (mNm/rpm); the static friction torque and dynamic friction coefficient respectively. The static friction torque is the minimum torque the motor has to deliver to turn the axle and is not dependent on the velocity. The dynamic friction coefficient is dependent on and increases linearly with the velocity. Luckily, Faulhaber provides these values for their motors. For other manufacturers, these have to be assumed as no values are given. Below, a calculation for the power usage of the motor is shown.

The power, voltage and current of the motor are indicated as P, U and I. The motor constant k is a motor specific property, specifying the power usage for any speed and torque level, which can be calculated from the speed and torque constant of a motor; k_ω (rpm/V) and k_T (mNm/A). The torque can be rewritten utilising the aforementioned friction constants.

$$P = U \cdot I = k \cdot \omega T \tag{4.1}$$

$$P = U \cdot I = \left(\frac{1}{k_\omega} \cdot \frac{1}{k_T} \right) \cdot \omega (C_0 + C_v \cdot \omega) \tag{4.2}$$

$$P = U \cdot I = \frac{\omega}{k_\omega} \cdot \frac{C_0 + C_v \cdot \omega}{k_T} \tag{4.3}$$

In equation 4.3, it is assumed that the motor delivers no torque, only uses it to overcome the friction. This equation can thus be utilised to calculate the velocity at maximum power. The power requirement MBW04 only depicts the maximum power usage of 180 mW, but does not specify the exact voltage or current utilised. This means that the motor can achieve the highest possible speed within this power budget by utilising a high voltage and lower current in comparison to the supply voltage and current from the PQ EPS. The voltage and current can be calculated with the aforementioned motor constants.

$$U = \frac{\omega}{k_\omega} \quad ; \quad I = \frac{C_0 + C_v \cdot \omega}{k_T} \tag{4.4}$$

Since both the voltage and current are dependent on the delivered velocity, an upper limit to the velocity can be found. First the calculation in equation 4.3 must be rearranged to find a relation between C_0 and C_v by using the no-load speed and corresponding power characteristics.

$$P_0 = U_0 \cdot I_0 = \frac{\omega_0}{k_\omega} \cdot \frac{C_0 + C_v \cdot \omega_0}{k_T} \tag{4.5}$$

$$U_0 \cdot I_0 \cdot k_\omega \cdot k_T = \omega_0 \cdot (C_0 + C_v \cdot \omega_0) \tag{4.6}$$

$$\frac{U_0 \cdot I_0 \cdot k_\omega \cdot k_T}{\omega_0} = C_0 + C_v \cdot \omega_0 \tag{4.7}$$

$$C_v = \frac{U_0 \cdot I_0 \cdot k_\omega \cdot k_T - C_0 \cdot \omega_0}{\omega_0^2} \tag{4.8}$$

Since only one no-load scenario is given of each motor, the static friction torque C_0 of each motor has to be retrieved through the assumption that the shape of the motor impacts this constant. For example, the Faulhaber 1509B and Maxon Motor EC 9.2 Flat are similar body and thus shall share similar values in terms of friction. The calculated speeds at max power per motor are stated in table 4.1, and will be calculated at max power, as stated in equation 4.12. The maximum power is derived from the driver electrical efficiency, which will be discussed in the next section.

$$P_{max} = \frac{\omega_{max}}{k_\omega} \cdot \frac{C_0 + C_v \cdot \omega_{max}}{k_T} \tag{4.9}$$

$$k_T \cdot k_\omega \cdot P_{max} = C_0 \cdot \omega_{max} + C_v \cdot \omega_{max}^2 \tag{4.10}$$

$$\frac{k_T \cdot k_\omega \cdot P_{max}}{C_v} = \frac{C_0}{C_v} \cdot \omega_{max} + \omega_{max}^2 \tag{4.11}$$

$$\omega_{max} = \frac{-\frac{C_0}{C_v} + \sqrt{\left(\frac{C_0}{C_v}\right)^2 + 4 \cdot \frac{k_T \cdot k_\omega \cdot P_{max}}{C_v}}}{2} \tag{4.12}$$

4.1.5. Motor Drive and Sensors

BLDC motors are the superior type of motor for this design but thus require a motor drive board, capable of accurately control the speed of the motor and utilise internal sensors to ensure stability in the angular velocity of the motor. As previously stated, a BLDC can be fitted with Hall sensors to ensure a feedback loop to create stability in its velocity. Faulhaber and Maxon Motors offer multiple motors including internal Hall sensors, and offer driver solutions for these motors. The amount of Hall sensors and the type of driver board does not differ between the motor options with Hall sensors integrated, manufactured by Faulhaber or Maxon Motors, as all utilise three Hall sensors, but do not disclose characteristics for the Hall sensors themselves. It is therefore assumed the feedback these sensors give to be perfectly similar in accuracy between all motors with Hall sensors integrated.

Another possibility is to design a custom feedback loop utilising external velocity sensors such as external optical or external Hall sensors. This is however discarded, as that would be beyond the scope of this thesis, due to the increased difficulty and extra time required of tuning these sensors. Therefore, only motors with internal Hall sensors will only be considered for the final motor trade-off.

To ensure that the motor drive stays within the financial budget and the volume budget, as the motors are already quite expensive and the offered drivers are quite large, it is favourable to be developed in house, to make sure it fits on the PQ9 board. The controller segment in figure 4.2 shall thus be explored here, as the implementation of Hall sensors is a selection criteria, so the driver is required to be designed for handling the feedback from these sensors. BLDC motors can have two configurations for the rotor magnets; sinusoidal and trapezoidal motors, as seen in figure 4.3. The placement and shape of the magnets dictate the waveform the motor produces when turned, but do not dictate which should be used as the waveform of the power width modulation (PWM) signal. It is however the most efficient to match the waveforms. Upon the selection of a motor, the characteristics of the drive electronics shall be decided.

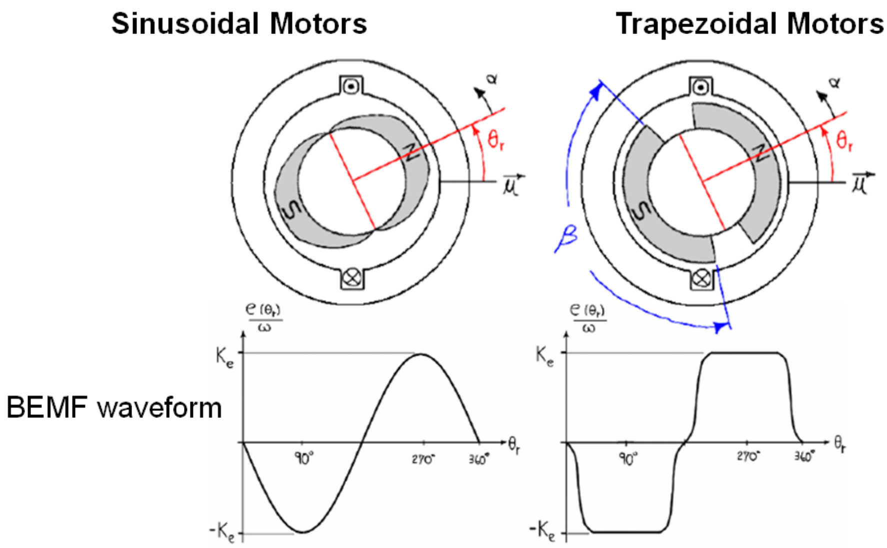

Figure 4.3: The two BLDC motor types with respective back EMF (BEMF) waveforms [1].

The drive electronics will be integrated within the PQ9 board, which allows for a preliminary mass estimation of drive electronics. Just like the power estimate for the drive electronics, both can be made through reference values of motor drives given by manufacturer product catalogues. The miniature motor drivers Faulhaber offers range in mass from 4 to 14 g and all have an electrical efficiency of 95% restricting the motor to only 95% of the maximum power allotted to the motor; 171 mW. With the assumption that the mass of the driver electronics will thus weight 4 g, the total mass allotted to the flywheel can be calculated, once the motor mount is properly proportioned.

4.1.6. Motor Trade-Off

The requirements from chapter 2 have been used in the previous sections to boil down the many motor options. Two honourable mentions must be made, as previous Delfi ACS projects [27] [54] have utilised the Maxon Motors EC 10 Flat and the Faulhaber 1202H004BH. These two motors would have fit perfectly within the power and size budget and all other selection criteria as stated before, sporting ludicrous speeds up to 50000 rpm. These are however discontinued for production by both manufacturers.

Table 4.1: Final selection of motors for the trade-off.

Manufacturer	Model	ω (rpm)	$\mathbf{D_b}$ (mm)	$\mathbf{L_b}$ (mm)	$\mathbf{m_m}$ (g)	$\mathbf{F_a}$ (N)	$\mathbf{F_r}$ (N)
Faulhaber	0620K006B-K179	35000	6	21.9	2.5	10	2
Faulhaber	0824K006B-K179	24350	8	26	5.2	10	2
Faulhaber	1028S006B-K179	13400	10	30	9.4	11	2
Faulhaber	1509T006B-X4192	19250	15	8.8	6.9	15	2
Maxon Motors	EC 9.2 Flat	13900	10	14.8	3.0	15	0.4
Maxon Motors	ECX Speed 4M	50000	4	18.5	1.2	5	0.2
Maxon Motors	ECX Speed 4L	41300	4	26.6	1.8	5	0.2
Maxon Motors	ECX Speed 6M	33660	6	22.8	3.0	5	0.2

Nonetheless, the few options that remain to adhere to the selection criteria are displayed in table 4.1. In which; ω is the speed at the maximum set power (171 mW), D_b is the diameter of the motor body, L_b is the length of the motor body, m_m is the mass of the motor, F_a is the maximum allowed axial force on the motor axle and F_r is the maximum allowed radial force on the motor axle.

Due to the extensive utilisation of selection criteria as described and reasoned within the last few subsections, only these final six characteristics can be utilised as trade-off criteria. To ensure a cohesive manner of scoring, a standardisation and weighing of the trade-off characteristics must be done. The standardisation will create a score (X) for each characteristic between -100 and 100, which will be multiplied by its weight (w). Once each weight has been multiplied with the corresponding score, these can be added up per motor, to be divided by the sum of the weights. This results in the final score per motor between -100 and 100, as displayed in equation 4.13. The final score represents how favourable the motor is in the design, with -100 as completely unfavourable and 100 as most favourable.

$$X_{motor} = \frac{X_\omega \cdot w_\omega + X_{D_b} \cdot w_{D_b} + X_{L_b} \cdot w_{L_b} + X_{m_m} \cdot w_{m_m} + X_{F_a} \cdot w_{F_a} + X_{F_r} \cdot w_{F_r}}{w_\omega + w_{D_b} + w_{L_b} + w_{m_b} + w_{F_a} + w_{F_r}} \tag{4.13}$$

The weights and scoring of the motor attributes are dependant on the importance of the characteristic and the ranking of the characteristic respectively. The importance of the characteristic is subjective to every project. This project favours a high speed motor with small volume and mass. To have sufficient maximally allowed loads are crucial for survival, but not as important as a sufficient speed for a certain volume and mass. The total sum of the weights is not of importance, rather that the ratios between the individual weights are clear and well reasoned. The weights will be given in whole numbers between 1 and 10, to ensure enough but finite weighing differences between the property scores.

- $w_\omega = 10$;
  The weight given to the speed of the motor is the highest, as the speed of the motor at the maximum power is crucial for creating a high enough angular momentum for the given mass budget;

- $w_{D_b} = 1$;
  The weight given to the diameter of the motor is the lowest, as the motors selected all do not posses a large enough diameter to interfere with the system requirement SYS07 or SYS08;
- $w_{L_b} = 9$;
  The weight given to the length of the diameter is quite high, as the length of the motor dictates the height of the complete MBW system, which has to be minimised to 12 mm or below;
- $w_{m_m} = 5$;
  The weight given to the motor mass is reasonably in the middle, to ensure the bulk of the MBW mass budget is utilised for the flywheel, which can be efficiently used;
- $w_{F_a} = w_{F_r} = 3$;
  The weights given to the maximum allowed forces (axial and radial) of the motor are quite low, given that simple countermeasures such as an end cap or mechanical stop can easily ensure survivability of the MBW system.

These weights pave the way to a final selected motor. Calculating the scores is the final step to complete the motor trade-off. The scores per motor are a standardisation between two set values known to be maxima and minima for each property. Below, each score is stated, formulated and reasoned. All properties can not score higher than 100 or lower than -100.

- $X_\omega = 100 \cdot \frac{\omega}{50000}$;
  The scoring of the motor speed is done between 0 and 50000 rpm, speeds micro motors are capable of obtaining. With this ranking, there is no 'bad' speed, there are only better speeds;
- $X_{D_b} = 100 \cdot \frac{40-D_b}{40-4}$;
  The scoring of the diameter of the motor is done between 4 and 40 mm, as the minimum is a diameter known to be feasible from the initial collection of motors, and the maximum is the diameter able to fit on the PQ9 board, between the pins and stacking studs;
- $X_{L_b} = 100 \cdot \frac{12-L_b}{12-2}$;
  The scoring of the motor length is done between 2 and 12 mm, as earlier stated in chapter 2, the maximum height of the MBW system will be 12 mm. This can be utilised as a maximum of the motor height, with a minimum of 2 mm, a minimal height found for the Faulhaber 1202 pancake motor;
- $X_{m_m} = 100 \cdot \frac{10-m_m}{10-1}$;
  The scoring of the motor mass is done between 1 and 10 g, as 1 g is found to be a feasible mass and 10 g is a first maximum mass estimation for the mass;
- $X_{F_a} = 100 \cdot \frac{F_a-2}{2}$;
  The scoring of the maximum allowed axial force of the motor is done with a preliminary calculated force value of 2 N induced by the acceleration forces on the flywheel, assumed to weight 25 g. This scoring is identical to the the radial force scoring, as the direction of the MBW within the PQ is unknown;
- $X_{F_r} = 100 \cdot \frac{F_r-2}{2}$;
  The scoring of the maximum allowed radial force of the motor is done with a preliminary calculated force value of 2 N induced by the acceleration forces on the flywheel, assumed to weight 25 g. This scoring is identical to the the axial force scoring, as the direction of the MBW within the PQ is unknown.

The final scoring is stated in table 4.2, with the **Faulhaber 1509T006B-X4192** as the clear winner. Due to the inconsistent data regarding increase in friction by using a vacuum rated lubricant, a safe estimate of a 20% decrease in speed will be used in further calculations. For the Faulhaber 1509T006B-X4192 means that this speed becomes 15400 rpm. A final assumption is made for the friction characteristics of the motor, C_0 and C_v. For this 20% decrease of the nominal velocity, the friction characteristics must increase by 55.6% if all other motor characteristics are unchanged, as calculated in equation 4.17. These values will be tested against through the theoretical test calculations in chapter 6.

Table 4.2: Final selection of motors for the trade-off.

	Weights	10	1	8	6	3	3	
Manufacturer	**Model**	$\mathbf{X}_{\omega}$	$\mathbf{X}_{\mathbf{D_b}}$	$\mathbf{X}_{\mathbf{L_b}}$	$\mathbf{X}_{\mathbf{m_m}}$	$\mathbf{X}_{\mathbf{F_a}}$	$\mathbf{X}_{\mathbf{F_r}}$	$\mathbf{X}_{\mathbf{motor}}$
Faulhaber	0620K006B-K179	70	94	-99	83	100	0	39.5
Faulhaber	0824K006B-K179	49	89	-100	53	100	-25	8.00
Faulhaber	1028S006B-K179	27	83	-100	7	100	25	-6.70
Faulhaber	1509T006B-X4192	38	69	32	34	100	0	**57.8**
Maxon Motors	EC 9.2 Flat	28	83	-28	78	100	-80	26.6
Maxon Motors	ECX Speed 4M	100	100	-65	98	100	-90	49.2
Maxon Motors	ECX Speed 4L	83	100	-100	91	100	-90	24.3
Maxon Motors	ECX Speed 6M	67	94	-100	78	100	0	26.5

$$P_{max} = U \cdot I \tag{4.14}$$

$$P_{max} = (k_\omega \cdot \omega_{max}) \cdot (k_T \cdot \delta_v \, (C_0 + C_v \cdot \omega_{max})) \tag{4.15}$$

$$\delta_v = \frac{P_{max}}{k_\omega \cdot \omega_{max} \cdot k_T \, (C_0 + C_v \cdot \omega_{max})} \tag{4.16}$$

$$\delta_v = \frac{0.180}{3.73 \cdot 10^{-7} \cdot 15400 \cdot 0.281 \, (0.019 + 3.42 \cdot 10^{-6} \cdot 15400)} = 1.556 \tag{4.17}$$

$$C_{0_v} = 1.556 \cdot 0.019 = 0.030 \tag{4.18}$$

$$C_{v_v} = 1.556 \cdot 3.42 \cdot 10^{-6} = 5.32 \cdot 10^{-6} \tag{4.19}$$

4.2. Flywheel Design

The flywheel is central in the momentum bias wheel design in delivering an angular momentum sufficient for the maximum allowable motion of the PQ. As the required angular momentum has been set, a design collection and trade off follows in order to find the best design possible within the scope of this thesis, in terms of the specific mass moment of inertia, expected strength and complexity. Below, the three aspects of the flywheel will be discussed; the shape and its optimisation, the material selection and the stress analysis. These three must be done in parallel, due to the interconnected aspects of the flywheel design. The shape of the flywheel is critical in determining where the major stress concentrations shall be in the flywheel, as the material density will depict how much stress the flywheel will endure overall. The yield stress of the material then dictates whether the applied stress is too high by the chosen flywheel shape, which could lead to a design iteration.

To start this off, a material collection can be done utilising favoured material properties as selection criteria, resulting in a range of material properties which can be traded off through a shape optimisation and stress analysis of the optimal shape.

4.2.1. Flywheel Material Selection

The material of the flywheel can be selected through the application of specific criteria on material properties onto a material database. The reasoning behind each criterion is stated and grounded.

Table 4.3: Material selection filters with description and reasoning.

Criterion	Description	Reasoning
Density	The material density is larger than 8800 kg/m^3.	This filter is chosen so that the largest density metals remain.
Temperature	The material will be able to operate in temperature between -20 and +50 $°C$.	This criteria is a direct translation of requirement MBW09 from table 2.4.
Magnetic Type	The material will not be magnetic.	The prevention of magnetic interference dictates the material to be non-magnetic.
Critical Element	The material will not consist $> 5wt\%$ critical elements.	Critical elements are assessed to have a supply risk in the future and will thus be prevented of use.
UV Durability	The material will have an excellent UV radiation resistance.	The material will insignificantly degrade due to UV over the mission lifetime.
Adhesive wear	The material will have an excellent galling resistance.	Galling could deform the flywheel, which could induce vibrations, thus this filter is critical.

The ratings for the UV and galling resistance are represented by their respective terms as explained in tables 4.4 and 4.5. The critical element criterion stems forth from the assessed national reserves of certain elements, such as chromium, indium, iridium, osmium, platinum, tin, tungsten and many more. The galling resistance requirement stems from the possibility that the flywheel is attached using glue. This glue can be corrosive to the wrong material, therefore it is used as a filter, to select a material resistant to this corrosion.

Table 4.4: Ratings of the UV resistance of a material as depicted by the Granta database.

Criterion	Reasoning
Excellent	UV radiation has little effect on the material and the UV weathering will take tens of years, as is the case with most metals and ceramics.
Good	UV radiation has some effect on the material and the UV weathering will take years, as is the case with UV-resistant polymers.
Fair	The material requires protection, as the UV weathering will take only months to years, as is the case for majority of polymers and organics.
Poor	The material is very sensitive to UV, as the weathering will take only days to weeks, such as rubber or ABS.

Table 4.5: Ratings of the galling resistance of a material as depicted by the Granta database.

Criterion	Reasoning
Excellent	The material is suitable for applications or mating with materials in which galling is a major issue and will only gall in exceptional circumstances.
Acceptable	The material is suitable for applications which require galling resistance without additional treatments, but have a tendency to gall in some circumstances.
Limited use	The material is suitable for applications which require galling resistance subject to careful lubrication, additional treatments or in specific circumstances.
Unacceptable	The material is not used for any applications which require galling resistance and difficult to process due to this type of wear.

The precise criterion is to have a weight of less than 5 % of all critical elements within the alloy. Many of the selected materials in table 4.6 consist mostly of copper, but some have a small concentration of tin, which is within the allowed limit. Many also consist of lead or zinc, but these are not critical elements. Lastly, the machining speed V_m expressed in meter per minute (mpm) and the specific price (€/kg) are included to ensure a more comprehensive and complete trade-off.

Table 4.6: Selected materials for the flywheel design.

Material	**Alloy**	**Composition**	ρ (kg/m^3)	$\sigma_\mathbf{y}$ (MPa)	$\mathbf{V_m}$ (mpm)	**Price €/kg**
Bronze	C50900	CuSn4	8830 - 8850	390 - 400	33.5	5.75 - 6.21
Bronze	C67500	CuZn19Al6	8800 - 8940	310 - 386	73.2	4.22 - 4.61
Copper	C64700	CuNi2Si	8800 - 8900	450 - 540	24.4	5.55 - 5.82
Copper	C83810	CuSn3Zn8Pb5	8750 - 8850	80 - 130	122	5.27 - 5.70

The selected materials are very similar in density and even overlap in their density ranges. The common density range these materials share is 8830 to 8850 kg/m^3, which is the density range that will preliminary used to calculate the specific mass moments of inertia and stresses. The yield stresses do not overlap and is thus where the distinction between these materials must be made, as will be discussed in subsection 4.2.3. The alloy composition is crucial, as with prototyping, obtaining the material might not fit within the financial budget or will simply not be available for single unit purchase. The material must therefore be approached with similar alloys that share traits with the chosen alloy. This uncertainty undermines the stated machining speed per alloy, as the implemented counterpart may not resemble that machining speed, so the stated machining speed will be neglected. Finally, due to the uncertainty of the prototype material, the small size and mass of the flywheel, and the material market volatility [43], the price differences between the alloys are also neglected.

4.2.2. Flywheel Shape Optimisation

The specific mass moment of inertia per design can be calculated to find the most mass efficient solution, in which the required angular momentum can be integrated to ensure the goal is met. Any derivations for lengthy specific mass moment of inertia calculations are stated in appendix D. Naturally, the specific mass moment of inertia and specific angular momentum are related through the angular velocity.

$$\frac{h}{m} = \dot{h} = \dot{I} \cdot \omega = \frac{I}{m} \cdot \omega \tag{4.20}$$

Multiple designs are considered for the flywheel design, with the eye on the most mass efficient design with increasing manufacturing difficulty. The four principle designs explored are a flywheel with a:

1. **Uniform Thickness**;
   A disc with a uniform thickness across its radius. This design would be the simplest to implement as the least amount of steps to manufacture;
2. **Stepped Thickness**;
   A disc with two uniform thicknesses across its radius. This design can utilise the increased mass moment of inertia of the outer ring to ensure a more mass efficient design, sacrificing only a small amount of simplicity;
3. **Linear Increasing Thickness**;
   A disc with a linearly increasing thickness from a certain radius to the end of the disc. This design, as well as the parabolic design are included to investigate whether these are more mass-efficient than the linear design;
4. **Parabolic Increasing Thickness**;
   A disc with an exponentially increasing thickness from a certain radius to the end of the disc. This design, as well as the linear design are included to investigate whether these are more mass-efficient than the linear design.

These design principles can be combined into so called hybrid designs. These designs are included to investigate ways to negate certain stress concentrations due to high thickness ratios between the inner and outer part of the disc, as will be investigated in section 4.2.3. These three designs are more complex than the previous four, as an extra manufacturing step must be taken to obtain the design.

1. **Hybrid Stepped Thickness**;
   A disc with three uniform thicknesses across its radius;
2. **Hybrid Linear Increasing Thickness**;
   A disc with a linearly increasing thickness between two certain radii, to eventually continue with a uniform thickness to the end of the radius;
3. **Hybrid Parabolic Increasing Thickness**;
   A disc with an exponentially increasing thickness between two certain radii, to eventually continue with a uniform thickness to the end of the radius.

From these seven considered designs, for only one can the most efficient solution be found analytically, which is the simplest design; the uniform thickness disc. The specific mass moment of inertia for a disc of uniform thickness can be calculated using equations 4.21 or D.1. These equations utilise multiple radii and thicknesses to indicate certain design aspects.

$$sI_{MBW} = \frac{I_{MBW}}{m_{MBW}} = \frac{\rho \cdot \pi \cdot \frac{1}{2} \cdot r_1^4 \cdot t_1}{\rho \cdot \pi \cdot r_1^2 \cdot t_1} = \frac{1}{2} r_1^2 \tag{4.21}$$

As an example, a stepped design with two steps in illustrated below, to illustrate the number of these radii and thicknesses, so that the rest of this section is clear.

Figure 4.4: ISO view of a flywheel with a hybrid stepped design.

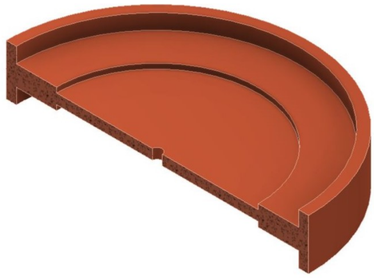

Figure 4.5: Cross section ISO view of a flywheel with a hybrid stepped design.

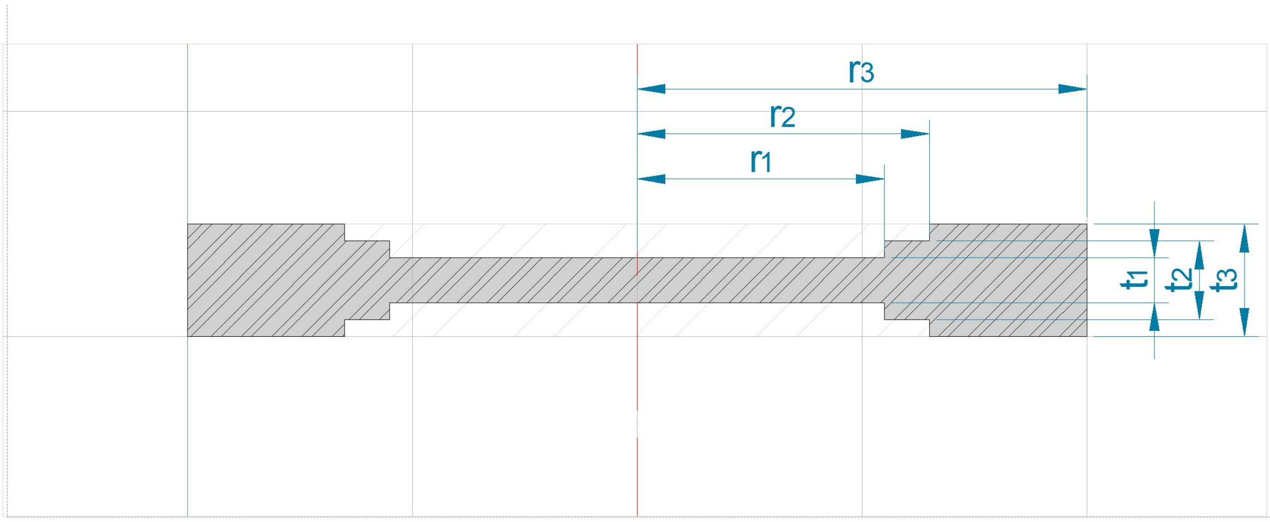

Figure 4.6: Cross sectional drawing of the triple thickness design with all variables noted.

As has become apparent in the calculations for the other specific mass moments of inertia as stated in appendix D, these are not simply analytically solvable and require computerised aid. The Fmincon optimisation function within Matlab can be utilised to find an optimum solution between all offered design options, with set constraints in line with the requirements from chapter 2. The constraints include the maximum mass and maximum dimensions the flywheel is allowed to have, in line with the annotations within figure 4.6. The maximum mass is set to 20 g, as the disc with uniform thickness can supply the required angular momentum for that mass.

$$\begin{cases} h_{MBW} \geq h_{req} \\ m_{MBW} \leq m_{max} \\ r_2 \leq r_1 \\ r_3 \leq r_2 \\ t_2 \leq t_1 \\ t_3 \leq t_2 \end{cases}$$

Below are the ranges within which the optimal specific mass moment of inertia of each design will be calculated. The initial maximum radius and thickness are set at 20 and 5 mm respectively, with the initial density and speed assumption to be 8830 kg/m^3 and 15400 rpm respectively, as stated in section 4.2.1 and 4.1.6 respectively.

$$\begin{cases} r_1 = [0.001, 0.020]\ m \\ r_2 = [0.001, 0.020]\ m \\ r_3 = [0.001, 0.020]\ m \\ t_1 = [0.001, 0.005]\ m \\ t_2 = [0.001, 0.005]\ m \\ t_3 = [0.001, 0.005]\ m \end{cases}$$

Through the Fmincon optimisation, optimal solutions for all seven designs were computed, with the stepped design as the best design in terms of specific mass moment of inertia. The results in table 4.7 make it clear that all hybrid designs have converged to a stepped design, sharing the same dimensions of the stepped optimum design.

Table 4.7: Specifications of optimised designs in terms of specific mass moment of inertia.

Design	$\mathbf{sI_{MBW}}$ (mm^2)	$\mathbf{h_{MBW}}$ $(mNms)$	$\mathbf{m_{MBW}}$ (g)	$\mathbf{r_1}$ (mm)	$\mathbf{r_2}$ (mm)	$\mathbf{r_3}$ (mm)	$\mathbf{t_1}$ (mm)	$\mathbf{t_2}$ (mm)	$\mathbf{t_3}$ (mm)
Uniform	200	6.1	18.8	20.0	-	-	1.7	-	-
Stepped	272	8.7	20.0	17.9	20.0	-	1.0	5.0	-
Linear	256	8.3	20.0	15.7	20.0	-	1.0	5.0	-
Parabolic	247	7.5	18.9	14.3	20.0	-	1.0	5.0	-
Hybrid Stepped	272	8.7	20.0	17.9	17.9	20.0	1.0	5.0	5.0
Hybrid Linear	272	8.7	20.0	17.9	17.9	20.0	1.0	5.0	-
Hybrid Parabolic	272	8.7	20.0	17.9	17.9	20.0	1.0	5.0	-

The stepped design can be envisioned into two designs, symmetrical and asymmetrical. The asymmetrical design can be envisioned into a cup design (shown in figure 4.7 and 4.8), where the motor is partly covered on the side, making the best use of the small volume allocated for the MBW system. Alas, previous research [27] points out that the simplest design would greatly reduce self-induced disturbances due to the small manufacturing tolerances required for a high velocity flywheel. The sacrifice of simplicity through utilising this proposed cup design does deliver an increase of approximately 20% in mass specific angular momentum, allowing for a lighter flywheel to reach the required angular momentum of 6.05 $mNms$.

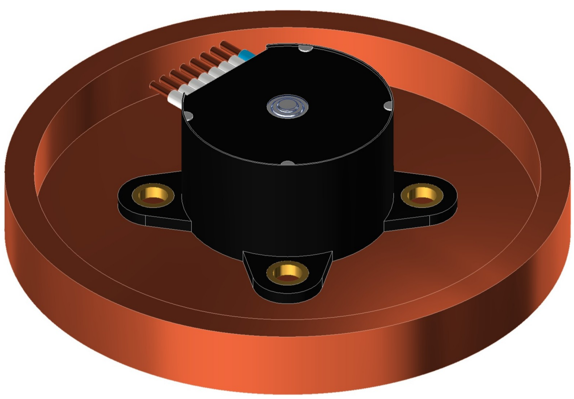

Figure 4.7: ISO view of the flywheel 'cup' design.

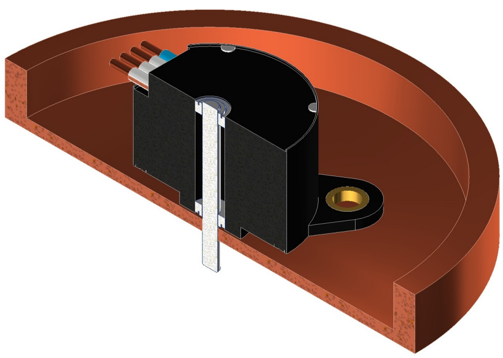

Figure 4.8: Cross section ISO view of the flywheel 'cup' design.

Finally, the manner of attaching the flywheel to the motor is dependent on the amount of contact surface between the flywheel and the motor axle, a property that decreases for the inner disc of the stepped design in comparison to the uniform thickness design. If the thickness of the flywheel around the axis of the stepped design is not sufficient to create a sufficient bond between the motor axle and the flywheel, the uniform thickness design is once again favoured, with a larger flange to connect to the motor axle. Another solution to this would be to introduce an attachment flange, as was done for the Delfi-n3Xt reaction wheel [27]. An analysis into the motor attachment will be further elaborated in subsection 4.2.4.

4.2.3. Flywheel Stress Analysis

To ensure survivability of the flywheel during operation, a stress analysis must be done. The stress requirements are set through calculations done mostly by Finite Element Analysis (FEM) [44], as they are governed by a non-homogeneous second order differential equation as stated in equation 4.22.

$$r^2\frac{d^2\Phi}{dr^2} + r\frac{d\Phi}{dr} - \Phi + (3+\nu)\cdot\rho\cdot\omega^2\cdot t\cdot r^3 - \frac{r}{t}\frac{dt}{dr}\cdot(r\frac{d\Phi}{dr} - \nu\cdot\Phi) = 0 \tag{4.22}$$

$$\sigma_r = \frac{\Phi(r)}{t\cdot r} \tag{4.23}$$

$$\sigma_\theta = \frac{1}{t}\frac{d\Phi(r)}{dr}\cdot\rho\cdot\omega^2\cdot r^2 \tag{4.24}$$

With Φ as an unknown function which is related to the radial and tangential stresses, ρ and ν as the density and Poisson's ratio of material of the flywheel and r and t as radius and thickness of the flywheel. The thickness is a function of the radius, which causes that the differential equation to be analytically unsolvable when the thickness is not uniform across the disc. When the thickness is uniform across the disc and the diameter of the hole in the centre of the disc for the axle of the motor is equal to R_1, this can solved and results in stress equations 4.25 and 4.26.

$$\sigma_r = \frac{3+\nu}{8}\cdot\rho\cdot\omega^2\cdot\left(R_2^2 + R_1^2 - \frac{R_1^2\cdot R_2^2}{r^2} - r^2\right) \tag{4.25}$$

$$\sigma_\theta = \frac{3+\nu}{8}\cdot\rho\cdot\omega^2\cdot r^2\cdot\left(R_2^2 + R_1^2 + \frac{R_1^2\cdot R_2^2}{r^2} - \frac{1+3\nu}{3+\nu}\right) \tag{4.26}$$

These equations are maximum at separate instances:

$$\begin{cases} r_{r,max} = \sqrt{R_1\cdot R_2} \\ r_{\theta,max} = R_1 \end{cases}$$

This eventually results in the following maximum stress:

$$\sigma_{r,max} = \frac{3+\nu}{8}\cdot\rho\cdot\omega^2\cdot(R_2 - R_1)^2 = 2.19\ MPa \tag{4.27}$$

$$\sigma_{\theta,max} = \frac{3+\nu}{8}\cdot\rho\cdot\omega^2\cdot R_1^2\cdot\left(2\cdot R_2^2 + R_1^2 - \frac{1+3\nu}{3+\nu}\right) = -1.37\ kPa \tag{4.28}$$

$$\tag{4.29}$$

For a uniform disc with the maximum diameter (0.020 m) as stated in section 2.1, together with the material characteristics stated in subsection 4.2.1 and a speed of 15400 rpm, a speed attainable by the selected motor, the analytically solved stresses are quite low, so a stress simulation shall be utilised to confirm these numbers. Utilising a simplified 2D simulation within Solidworks yields a Von Mises stress of 5.92 MPa, which is thus in the same magnitude as the analytically solved stress, and therefore low enough to be neglected, as they do not approach yield stresses of the alloys stated in table 4.6.

However, similar to the last sections calculations, only the uniform disc design can be analytically solved. The other designs can only be time efficiently solved through stress simulating software. As the stepped design is the most mass efficient design, the stresses will be simulated by the already mentioned 2D simplified Solidworks stress simulation. Analysing a symmetrical and asymmetrical stepped design results in a maximum Von Mises stress of 14.2 and 13.6 MPa respectively, both negligible when compared to the yield stresses of the alloys stated in table 4.6, which are above 300 MPa for three of the materials. The deformed results from the stress simulation are shown in figures 4.9 and 4.10 to show the location of the highest stress, at the centre of the disc. Additionally, an interesting phenomenon is the stress concentration and deflection in the flanges of the asymmetrical stepped design, which do not resemble the stress concentrations of the symmetrical design. This is due to the greater displaced mass of the flanges, as the centre of mass of the only the flanges are not aligned with the centre of mass of the middle part and the flanges bend upward and out as seen in figure 4.10.

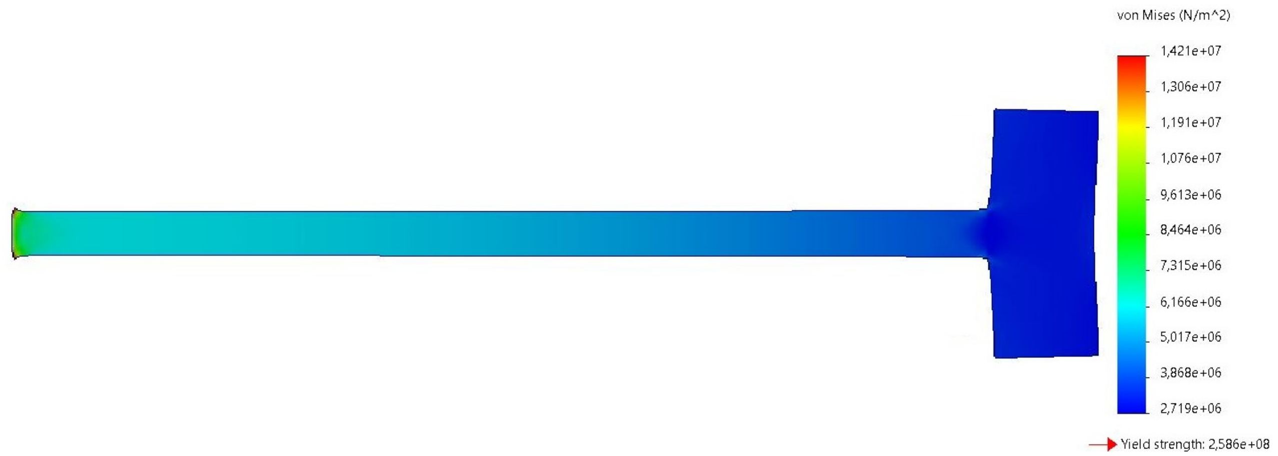

Figure 4.9: The deformed stress simulation result for a symmetrical stepped design at a deformation scale of 6000.

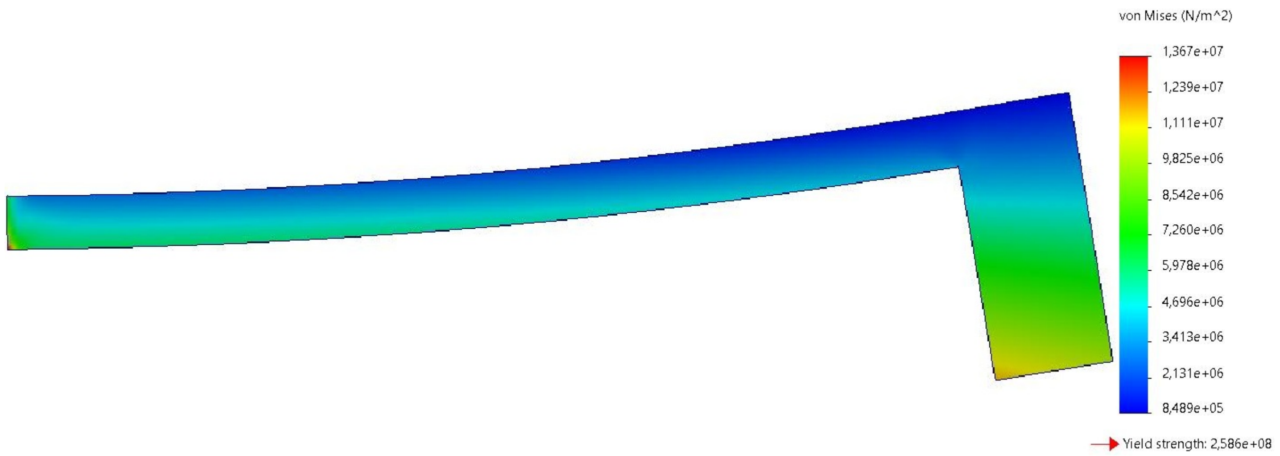

Figure 4.10: The deformed stress simulation result for an asymmetrical stepped design at a deformation scale of 6000.

Due to the magnitude of difference between the yield stress and found stress through the Solidworks simulation, further stress analyses will be neglected. This does not impact the necessity of the displacement analysis for the possible flywheel reinforcement. From the materials presented in table 4.6, the Bronze C67500 alloy shall be used, as the yield stress is no longer a crucial selection criteria and this alloy has the highest possible material density, assumed to be 8900 kg/m^3.

4.2.4. Flywheel Motor Attachment

The attachment point between the motor and the flywheel is critical to the durability of the MBW. The connection between these fundamental parts require a strong bond to ensure survival during operation. Three operations for adhering the two critical components come to mind; chemical bond adhesion, cold press fitting or thermal expansion slotting. The chemical bond adhesion would utilise a vacuum proof glue that can survive the low pressure and harsh UV environment. Cold press fitting would simply press fit the flywheel onto the motor axle, depending on the simple clamping force of the material of the flywheel. This could be achieved by drilling the centre hole slightly smaller than the axle diameter. The thermal expansion slotting would utilise the thermal expansion coefficient of the flywheel material to expand due to exposure to a certain temperature when being slotted onto the motor axle, to eventually shrink down and clamp onto the motor axle when cooled. To prevent any stresses due to temperature related material work, the latter method will be discarded and a vacuum epoxy shall be utilised to adhere the two parts together in combination with press fitting onto each other. Epoxy is used for its vacuum operability and heritage[18].

The previous Delfi ACS projects [27] [54] have also utilised glue to adhere the two components together, and used a thickness of 2 mm to do so. Hoevenaars [27] states that a reaction wheel with a thickness of 1.7 mm would also adhere well to the axle of the motor. This minimum thickness will have to be taken into account when selecting the shape of the flywheel, as the stepped design as described in subsection 4.2.2 would then require an attachment flange while the uniform design would not.

4.2.5. Flywheel Synthesis

The flywheel can be made out of two shapes; the uniform thickness design and the stepped thickness design. An additional calculation must be done from the mass budget perspective, to decide which design can be utilised. If the mass budget allows it, for the sake of simplicity, the simplest design is favoured. What this means is that a calculation is required to investigate whether the required angular momentum is attainable with the uniform thickness flywheel design. Since the axle radius (r_0) of the motor is known, the following calculation can be done to determine the required mass (m_f) of the flywheel as a function of the angular momentum (h_{req}). The density of the flywheel (ρ_f) and the speed of the motor (ω_m) are retrieved from the previous calculations. The outer radius (r_1) and thickness (t_1) of the flywheel are utilised as stated in figure 4.6.

$$h_{req} = \frac{1}{2} \cdot \rho_f \cdot \omega_m \cdot t_1 \cdot \left(r_1^4 - r_0^4\right) \tag{4.30}$$

$$m_f = \rho_f \cdot \omega_m \cdot t_1 \cdot \left(r_1^2 - r_0^2\right) \tag{4.31}$$

$$h_{req} = \frac{1}{2} \cdot \omega_m \cdot m_f \cdot \left(r_1^2 + r_0^2\right) \tag{4.32}$$

$$m_f = \frac{2 \cdot h_{req}}{\omega_m \cdot \left(r_1^2 + r_0^2\right)} \tag{4.33}$$

The outer radius (r_1) of the flywheel is dependent on the placement of the system within the PQ and the utilisation of a complete surrounding reinforcement. Having replicated a technical drawing of the PQ9 PCB backboard, the maximum radius of the flywheel between the stand-offs can be drawn. The largest radius of 20.96 mm found in figure 4.11 can be derived to a conservative value of 20.5 mm, to take the thickness of the flywheel reinforcement and the deflection of the flywheel into account. That conservative radius leads to a flywheel mass of 17.8 g and a thickness of 1.5 mm from equation 4.33.

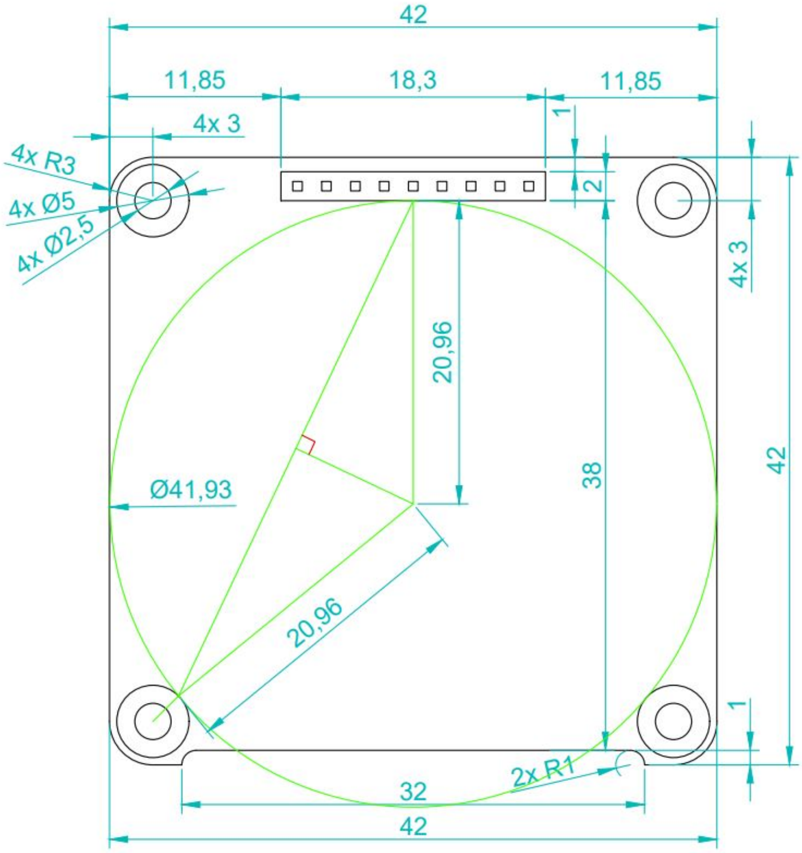

Figure 4.11: The PQ9 backboard with simple geometry to find the largest diameter possible and the centre of that largest diameter.

A thickness equal or larger than the aforementioned 1.7 mm flange thickness must be utilised in the final design for proper attachment to the motor in case of an uniform flywheel. The found 1.5 mm thickness shall therefore be increased to the stated 1.7 mm, which will increase the mass to 20.2 g and the angular momentum at 15400 rpm to 7.02 $mNms$, when utilising the 20.5 mm radius. Approaching the required angular momentum of 6.05 $mNms$ finds that for an outer radius of 20.0 mm and thickness of 1.7 mm, the angular momentum requirement is can be met met, resulting in an uniform flywheel with a mass of 18.8 g. This mass is low enough to fit the initial mass estimation, therefore the uniform flywheel design is chosen.

In summary, an uniform flywheel design is chosen, made of the copper C67500 alloy, with an outer radius of 20.0 mm, an uniform thickness of 1.7 mm. This design will feature a 1.5 mm diameter attachment hole in the centre of the flywheel for the motor axle to fit through, which will be press fit through the flywheel and adhered with vacuum rated epoxy. For a mass of 18.8 g, the flywheel will achieve the required angular momentum of 6.05 $mNms$ at 15400 rpm.

4.3. Housing Design

The housing has to be designed to support the motor and flywheel during their operational lifetime, while providing accessibility for disassembly or repairs during testing. The requirements per aspect of the housing shall be gathered and traded off between each other on criteria set between them. The combination of the won aspects will then be used to synthesise a MBW housing. Due to requirement MBW02, the mounting of the motor can way no more than 5.3 g

Back-of-the-envelope calculations show that the induced launch stresses through accelerations and the weight of the motor, flywheel and assumed are negligible, so the motor mount shall only have the purpose to clamp to motor such that it does not come loose during operation or testing.

4.3.1. Housing Motor Mount

The motor mount is dependent on the motor selection as performed in section 4.1, PQ9 backboard placement and the PQ bus fittings. Due to the height of the motor, the placement shall be on the directly on the underside of a PQ9 board, as visualised in figure A.3. This allows for the total height underneath the board to be 12.0 mm, required for the motor body height.

Clamping the motor can come in a few different options; clamping around the motor body, clamping the motor flanges, or glue. Since glueing the motor would result in no longer being able to disassemble the MBW system when needed, this will be disregarded for now. It can always be used as a secondary joining method. Clamping to the motor body itself or to the flanges can be easily traded off through the selection of material, as this sets the manufacturing method and the precision and resolution thereof. For example, if a metal is selected, the part must be machined and cannot utilise very intricate details to clamp the small motor flanges.

For the sake of volume efficiency, mass saving and strength in the part, clamping to the motor flanges is favourable. Clamping to the motor flanges also allows for the motor to be clamped in multiple directions using a very small part.

4.3.2. Housing Flywheel Reinforcement

The housing may requires to integrate a flywheel reinforcement for the induced forces on the motor axle by the high weight of the flywheel and high acceleration during launch. Since the orientation of the PQ bus and PQ deployment system within the payload is unknown, all load cases must be worked out. The two load cases the motor can experience, is axially and radially, dependent on the direction of the bus during launch. Both are dependent on the maximum launch acceleration and mass of the flywheel, resulting in the force as displayed in equation 4.34, with F_f, m_f and a as the force of the flywheel, mass of the flywheel and acceleration during launch respectively. The acceleration is equal to the value found for requirement MBW07, 8.5 g.

$$F_f = m_f \cdot a = 0.0186 \cdot 8.5 \cdot 9.81 = 1.55\ N \tag{4.34}$$

The calculated force does not exceed the maximum allowable force on the motor axle. However, to ensure other systems do not suffer when the motor axle unsuspectingly fails, a reinforcement or caging system must nonetheless be in place. This caging system is simply such that the flywheel can not shoot out when it unsuspectingly fails.

To create a feasible reinforcement system, the offset from the flywheel must be set according to the radial play of the axle. The radial play of the axle is equal or smaller than 0.015 mm, so this value shall be used as the offset for the flywheel reinforcement around the flywheel, as the maximum force value of 2 N radially does not create a feasible offset as this force would only deflect a rod with the dimensions of the axle only nanometres.

4.3.3. Housing Material Selection

Before any specific shapes are set into stone, materials must be traded off through the density, strength, manufacturability and mission performance. The density is required to be as low as possible, but most not impair the strength of part, which must be able survive the stresses during launch and operation. The manufacturability comes down to the first research question as it is required for this design to be made out of COTS or self-manufactured parts. Additive manufacturing could be used to manufacture more intricate details than machining, and machining can be done in house at the TU Delft. The mission performance is derived from the resilience against vacuum conditions, UV radiation and temperature flux.

Previous designs have utilised Teflon for its flywheel reinforcement, as this would burn away upon touching a spinning flywheel, allowing for support that would not block operations [27]. As Teflon also has great performance in vacuum conditions, great UV resilience and strength to survive the launch and operational stresses, it is one of the strong material candidates.

Other materials with space heritage such as titanium, aluminium or bronze are also considered, but weigh more, have an increase in strength that does not make a difference as the strength requirement was already met through Teflon and does not incorporate the flywheel reinforcement and can not be additively manufactured in house. Therefore, a clear winner is Teflon. For prototyping, PLA will be used, as it is similar in strength and vacuum conditions, and inexpensive.

4.3.4. Housing Synthesis

Having settled on the specifications regarding the MBW housing, the housing will clamp the motor on its flanges, using Teflon manufactured additively and incorporates a flywheel reinforcement.

To also incorporate sturdiness during testing, the PQ9 backboard stand-offs will be integrated into the design and shall support the housing frame. The clamping of the motor shall fully encapsulate the flanges, restricting movement of the motor in every direction and rotation.

4.4. Manufacturing

Manufacturing methods have to be applied and sanity checked for each manufactured component. These components are the flywheel, the flywheel reinforcements and the motor mount.

The flywheel will be made from copper, an alloy that, like its other metallic brethren, can be reshaped using casting, spinning, manual machining, automatic machining or electrical discharge machining (EDM) [51]. Since casting and spinning have a higher machining allowance than the other machining methods, therefore these two will discarded. EDM will also be discarded, to fit the financial budget. The Delft University of Technology has manual and automatic machining facilities, both lathing and milling. The devices they utilise are Fehlman and Hermle 5-axis CNC milling machines, capable of accuracy's of 0.001 mm per axis [16]. For the prototyping stage of the design, the manual lathing will be utilised, as it not as costly and complex as the CNC lathing, while the final design of the flywheel will have to be made utilising CNC lathing, due to the high accuracy required, to minimise self-induced vibrations.

The motor mount and flywheel reinforcement will be made from Teflon or PTFE, the exact material utilised in the previous Delfi ACS projects. PTFE has great heritage with moulding [51], and the shall thus be utilised for the final design. The feasibility of moulding this part for the prototype shall be looked into, as additive manufacturing solutions can also create stiff parts with the quite high precision ($\pm 0.1 mm$).

4.5. Design Outcome

The final design of the MBW ACS is presented here, after all design criteria and design have been gone through.

The motor selection and trade-off yielded the Faulhaber 1509T006B-X4192 motor as the best motor for this system. This motor can be fitted with a vacuum lubricant, is fitted with Hall sensors and is estimated to operate at 15400 rpm at max power.

The motor delivers enough rotational velocity, such that the flywheel design can be as simple as possible. The flywheel will have a radius of 20 mm and a uniform thickness of 1.7 mm, made from the Bronze C67500 alloy. This results in a mass of 18.8 g and together with the stated rotor inertia, results in a rotating inertia of 38.29 gcm^2 and an angular momentum of 6.175 $mNms$ at 15400 rpm.

The mounting of the motor and flywheel to the PQ9 backboard and the reinforcement of the flywheel is done in one part, utilising a very lightweight solution made from PTFE.

Utilising standard fasteners and the stand-offs standard to the PQ stacking, the following design is made.

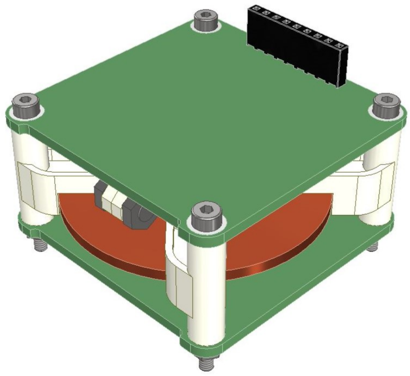

Figure 4.12: The final design contained between two PQ9 backboards.

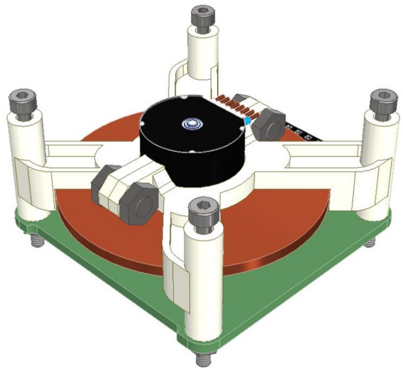

Figure 4.13: The final design without the top PQ9 backboard.

The final design shall incorporate the stand-offs between the PQ9 boards, such that the part can utilise the strength of the rod put through all the boards. As this is an independent assembly, bolts are used to stack parts appropriately. The motor mount clamp is fastened using M2 size threaded rod and nuts. The clamp is designed in such a manner that these nuts can be turned to increase the clamping force on the motor, through the slightest flexibility of the mount. Between the left and right side of the mounting clamp, a small margin is made to make this flexing possible when installed. This small margin is dependent on the manufacturing accuracy, but has to be more than 0.1 mm. Though only theoretical, but the CAD of the motor mount has been tested for eigenfrequency such that it does not come below values of the launch vibrations.

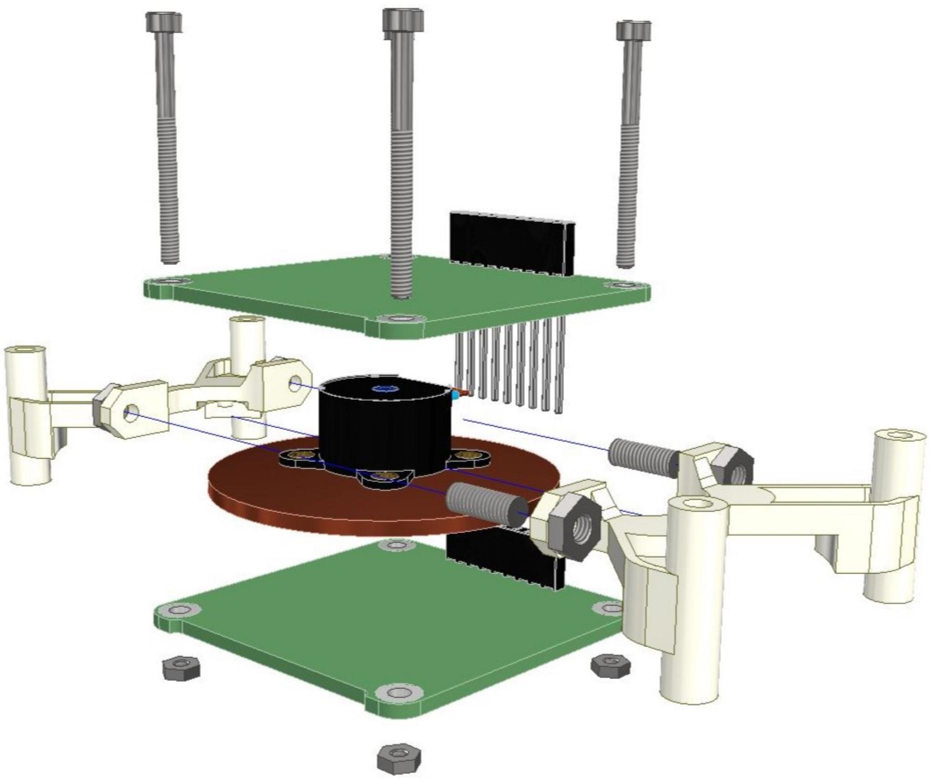

Figure 4.14: The final design exploded view, showing the individual parts.

5. Prototyping

From the design presented in the previous chapter, a realistic and test-worthy prototype must be created. This allows for the nominal operation test and vibration test to be done. The decisions regarding the differences and similarities between design and prototype will be discussed per aspect of the design.

5.1. Prototype COTS Components

An inquiry has been made into the price and customisation of the driver offered by Faulhaber, alongside the 1509B motor, the SC1801. Three types of drivers are available from the SC1801 family, the SC1801P, SC1801F and SC1801S. The SC1801P and SC1801S drivers are specifically compatible to the 1509B motor, for the digital Hall sensors and four poles the motor utilises. The SC1801P driver was chosen, due to its low weight of 4 g, in comparison to the 10 or 12 g of the SC1801F or SC1801S respectively. The difference between the standard and vacuum rated lubricant was negligible in price, so two Faulhaber 1509T006B X4192 vacuum rated motors were ordered, together with a singular SC1801P 6339 and a driver programming package, consisting of a USB programming adapter and a connection adapter for the SC1801 speed controller family. Below, in section 5.4, the cost of these components are stated.

For the sake of clarity, as the USB programmer adapter requires the conversion adapter to connect to the SC1801P, the combination of these adapters will be called the USB programming adapter throughout this thesis. This USB programming adapter can be utilised through the Faulhaber supplied programming software 'Motion Manager'. Through Motion Manager can a load case be specified, for which gain properties of the proportional integral (PI) velocity controller within the speed controller can be altered. The speed controller has a standard programming for an arbitrary load case for which it deliver the most efficient speed possible for any input voltage and control voltage.

The speed controller in question is directly connected to the motor, and functions as the main controller of the entire system. Below, in figure 5.1, a block diagram containing all parts of the SC1801P driver, showing the inner workings and manner in which the speed of the motor can be controlled.

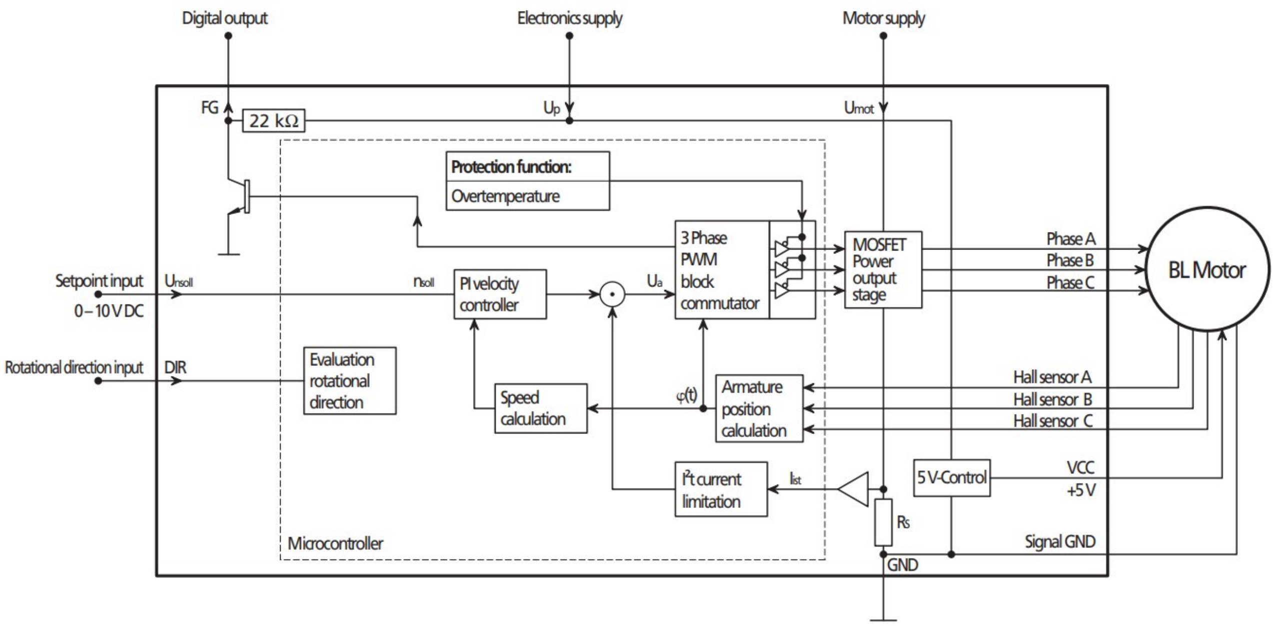

Figure 5.1: The Faulhaber SC1801P schematic block diagram.

Following the above mentioned block diagram and Faulhaber's clear instruction, the driver can be driven by setting the motor (U_{mot}) and electronics (U_{elec}) supply to a constant input voltage and controlling the speed by varying the voltage delivered to the set point input (U_{nsoll}) between 0 and 10 V. The U_{mot} input powers the metal-oxide-semiconductor field-effect transistors (MOSFETs) in the microcontroller of the speed controller, and the U_p powers the Hall sensors signals through the 5 V-Control block. The 0 to 10 V range for U_{nsoll} is programmed as standard into the speed controller.

The programming of the speed controller though Motion Manager should be able to alter the PI velocity controllers' input and output responses through its proportional controller gain G_c and integral time constant τ_I. The speed calculation block in figure 5.1 sends a signal (SC) to the PI velocity controller, which is compared to the set point signal (SP) from U_{nsoll}, calculating a response signal ($u(t)$) as done in equation 5.1 and sending this to the pulse width modulation (PWM) block commutator block, which powers the MOSFETS and thus the motor.

$$u(t) = u_{bias} + G_c \cdot (SP - SC) + \frac{G_c}{\tau_I} \int_0^t (SP - SC)\, dt \tag{5.1}$$

In equation 5.1, the term u_{bias} is added, which is a value that gives a bumpless transfer when the controller is turned on an the difference between the set point and speed calculation signal is zero. Changing the proportional control gain G_c can be utilised in this load case, as maximum torque requirement MBW13 could be achieved by simply lowering G_c such that the PI controller and thus the speed controller are simply not able to exert any higher torque than the maximum 0.0962 μNm. The integral time constant τ_I can become insignificant at a very low G_c, as it dictates the response to the fluctuation of the motor when the difference between the set point and speed calculation signal approaches zero. At very low G_c, the fluctuation around the nominally required velocity would be so small that τ_I would have an insignificant effect. Nonetheless, the time integral part is integrated within speed controller and shall therefore be used.

Finally, the Motion Manager software is able to read out the digital output of the speed controller, enabling the readout of the digital Hall sensors within the motor and the depiction of their accuracy. Most digital Hall sensors incorporate a Schmitt-trigger, resulting in a block wave over the Hall sensors' signal lines between motor and driver, which could prove handy when reading out the Hall sensor signal over an oscilloscope and using the transitions between positive and negative as interrupts. The Schmitt-trigger should eliminate the effect of any floating of the signal on the interrupt counting and thus increases the accuracy of the Hall sensors.

5.2. Prototype Manufacturing

Through the experienced help of the technicians of the manufacturing facilities at the Mechanical Engineering faculty, the flywheel and motor mount can be made in house. The flywheel is made through lathing a bought bronze rod of the chosen alloy, the motor mount is additively manufactured using hobby grade 3D printers.

5.2.1. Flywheel Manufacturing

The lathe operated in the faculty workshop utilises a semi-digital positioning system, in which the position is controlled by a hand crank, and the position is displayed in all three axes on a digital display, with a resolution of 0.01 mm. Unfortunately, no spec sheets are available of the used lathes, but a bit of play was noticeable when operating the lathe's hand cranks. This play then paves the way to the manufacturing margin and precision, which would equal to 0.01 mm.

The initial rod diameter and length were approximately 41 mm and 40 mm respectively, from which multiple prototype flywheels can be made. The rod was firstly reduced to the desired diameter of 40.00 mm over the entire length. Secondly, a hole for the axle is drilled for just over the design thickness of the flywheel, 1.7 mm. Finally, a grooving tool can be utilised to cut the flywheel of the original rod without inducing too much deviations during milling. Before the hole is drilled in the specimen, the rod is weighed and measured exactly once the exact diameter and length of 40.00 mm is achieved, to see if the rod specimen resembles the alloy density as chosen in subsection 4.2.1, 8830 kg/m^3. At the exact size of 40.00 mm by 40.00 mm, the specimen would weigh 224 g, which means that the density of this specimen is slightly larger; at 8913 kg/m^3; than the assumed density but still within the known density range for alloy C67500 as stated in table 4.6.

Through these three steps taken to manufacture the bronze flywheel, any offset in the cutting or drilling operation can create an offset between the position of the mounting hole and the centre of mass (COM) of the flywheel. These are meant to be perfectly in line, to prevent any oscillations and possible destructive vibrations. Only two steps can have an offset due to the machine offset, as the spindle with the drill bit is centred onto the main spindle of the lathe.

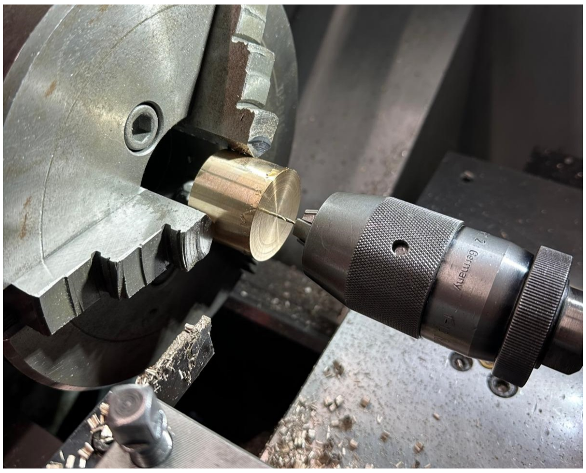

Figure 5.2: Drilling a 1.5 mm diameter hole in the centre of the rod.

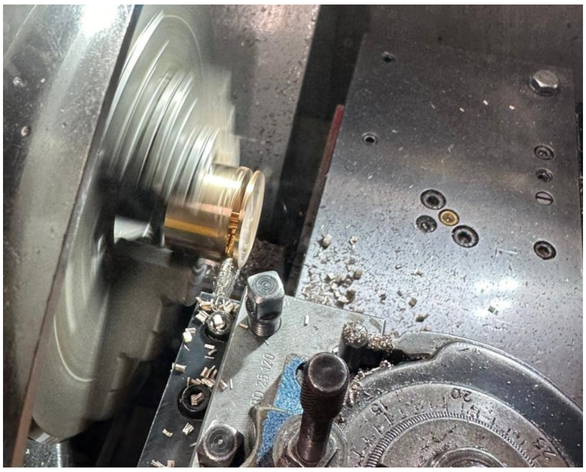

Figure 5.3: Using a grooving tool to cut a flywheel of 1.7 mm off the rod.

The three uniform thickness flywheel specimen have shown to be nearly identical to design, with some flaws or blemishes due to clamping or unseen bending during machining or handling. In figure 5.5, such a blemish is visible. The bending of the specimen can come from using the grooving tool throughout the entire diameter of the rod. Once the grooving tool would approach the centre, the part of the specimen that was being cut off began wobbling slightly. This is due to the small amount of material left to resist against the centripedal forces of the spinning lathe. This wobble can have caused an inaccuracy when cutting the final part of the flywheel. Finally, the grooving tool would cut the flywheel off which had to be caught, as it were still spinning rapidly.

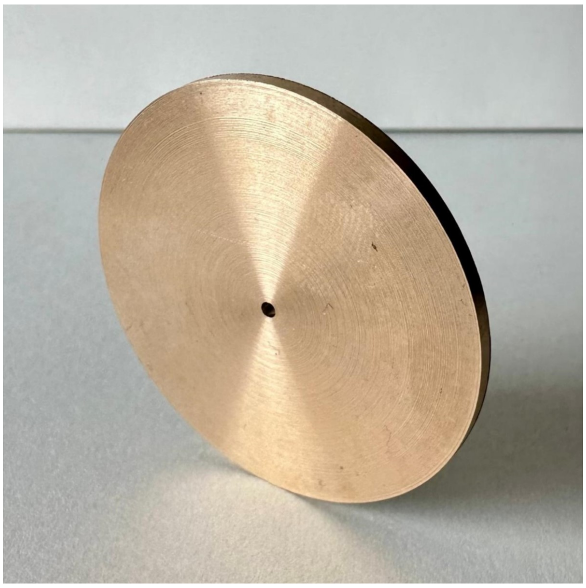

Figure 5.4: One of the flywheel three specimen.

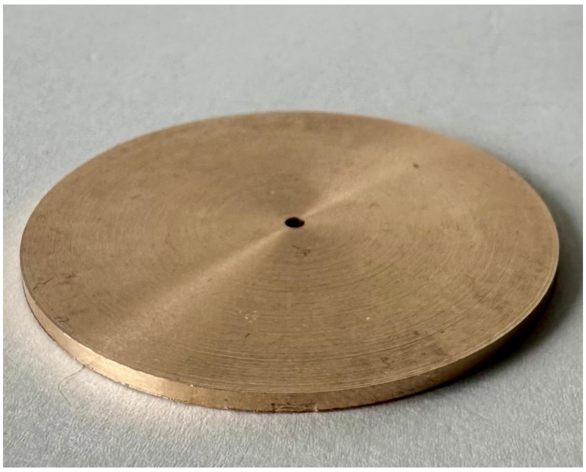

Figure 5.5: One of the flywheel three specimen, with a blemish visible.

5.2.2. Motor Mount Manufacturing

The financial benefit of prototyping using additive manufactured parts is superior to the quality aspect of those prototype parts, meaning that any parts that have an insignificant impact on performance, such as the mounting parts, are additively manufactured. Specifically, the prototype mounting parts will be manufactured using a Fused Deposition Modelling (FDM) 3D printer. Such a printer is very common and can produce parts the fastest and cheapest, made from plastics such as Polylactic Acid (PLA) or Acrylonitrile Butadiene Styrene (ABS). The faculty workshop utilises hobby grade 3D printers, Prusa Mk3 and Ultimaker S2 models, which are stated to have an accuracy of 0.2 mm equal to the extrusion thickness. This accuracy is within margin, as the parts can be post processed through filing and sanding to fit the parts.

Apart from FDM printers, the faculty also offers higher accuracy additive manufacturing services through the usage of Stereolithography (SLA) 3D printers, specifically the Elegoo Mars 3, sporting an XY accuracy of 35 μm. This can be used for the final version of the motor mount, should any changes have to be made to the motor mount.

Figure 5.6: The prototype body printed using a FDM printer, treated using hand tools to ensure acceptable margins.

Figure 5.7: The prototype body enclosing a dummy print of the Faulhaber motor and the flywheel for scale.

5.3. Prototype Assembly

Having manufactured and received all parts, assembling the protoype is done in the following steps. Firstly, the flywheel is attached to the motor. The motor is then clamped into the two part motor mount, which will be mounted between two PQ9 boards. For now, the electronics for the Faulhaber motor are mounted externally, for ease of accessibility.

Fitting the flywheel to the motor is a delicate matter, for which a specific solution had to be developed, as the load limit of the motor is easily exceeded by human operation. As explained in subsection 4.2.4, the fitting of the flywheel was done by press fitting and epoxy glue. A tool had to be developed in which the motor and flywheel could be concentrically slotted, with a M5 bolt used to slowly drive the motor into the flywheel, after a vacuum proof epoxy resin is applied into the flywheel mounting hole. This tool, as shown in figures 5.8 and 5.9, is additively manufacturing for the high accuracy achieved with this manufacturing process.

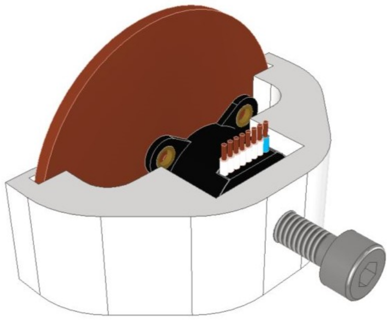

Figure 5.8: The assembly of the press fitting tool with the motor and flywheel.

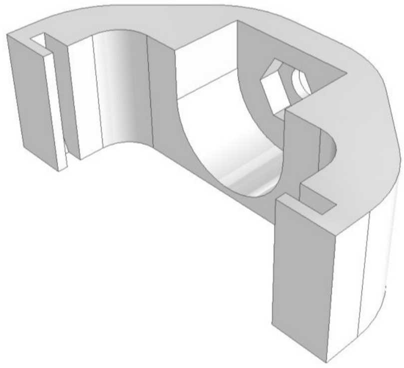

Figure 5.9: The press fitting tool, including curved slots for the motor and flywheel, perfectly aligning the centres of each part.

5.4. Prototype Cost

As requirements MBW05 states, the entire system shall cost no more than 500 Euros, which includes the parts, materials and testing equipment. As the prototyping is done, a current cost overview can be made to envision the remaining budget available for possible extra test facilities. All prices stated include VAT and delivery costs if present. Finally, the additively manufactured parts and supplied nuts and bolts, supplied by the ME faculty are included, as these are normally not gratis, so that if this research is ever reproduced, these costs will not be overlooked.

Table 5.1: All costs for creating a PQ MBW prototype.

Supplier	Article number	Description	Price (Euro)	n	Total (Euro)
Bison	8710439014142	Universal Epoxy Glue	11,99	1	11,99
Faulhaber	1509.80018	Motor 1509T006B X4192	90,60	2	181,20
Faulhaber	6500.01751	PCB SC1801P 6339	94,10	1	94,10
Faulhaber	6501.00096	Programming Adaptor	83,50	1	83,50
Faulhaber	6501.00112	Adaptor USBPA-BX4	56,80	1	56,80
KING Microschroeven	A195-020-001	Threaded Rod M2 25 cm	5,55	1	5,55
Metaalwinkel	brs04101210	Bronze Rod ∅41,L40	44,12	1	44,12
TU Delft ME	B016	3D printed motor mount	0,00	4	0,00
TU Delft ME	B301	3D printed press fitting tool	0,00	1	0,00
TU Delft ME	D001	3D printed motor dummy	0,00	2	0,00
TU Delft ME	HN-M2	M2 hex nut	0,00	16	0,00
TU Delft SpE	PQ9	PQ9 backboard	0,00	2	0,00
				Total	477,26

5.5. Prototype Outcome

Having manufactured and bought all the parts, the prototype is built and has the following specifications. The MBW is firstly only partly assembled such that only the motor can be tested. Fitting the flywheel to complete the MBW is permanent due to the combination of the epoxy glue and press fitting utilised, so the testing phase of only the motor has to be truly done before going forward.

The epoxy glue is applied lightly, the motor is then carefully press fit in through turning the M5 bolt at the end of the self made press fitting tool, until the axle protrudes 2 mm from the flywheel. Despite the correct depth, as designed for, the mount parts and flywheel touched. Slight filing and sanding was used to increase the margin between the two parts.

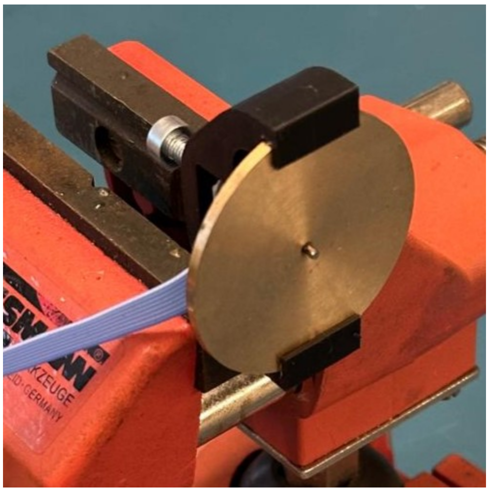

Figure 5.10: Press fitting the flywheel to the desired depth.

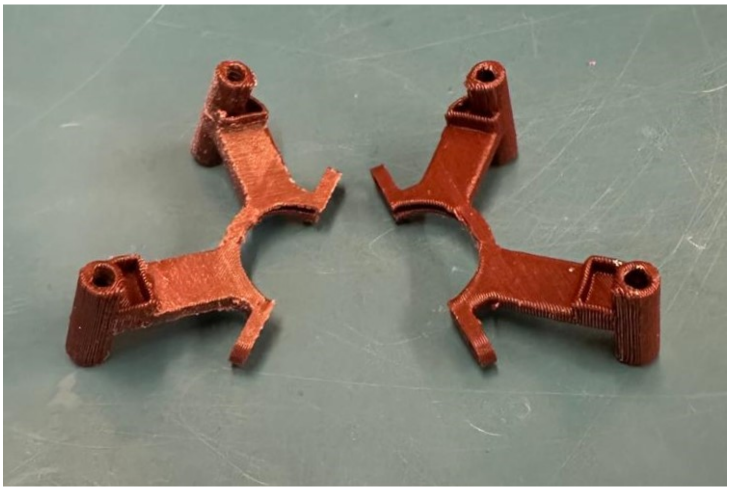

Figure 5.11: The minimal but visible required filing and sanding of the mounting parts.

All parts and the assembly have been weighed to an accuracy of 0.001 g using a Highland HCB123, to check the mass requirement and to calculate the angular momentum created during testing. The flywheel has been measured using digital calipers, with an accuracy of 2 μm and resolution of 1 μm, to check the manufacturing precision. The mass measurement and dimensions are shown in tables 5.2 and 5.3 respectively, in which the theoretical values are calculated through assumed constants from chapter 4, calculated through CAD software, or retrieved from data sheets.

Table 5.2: Mass measurements of all items used in the assembly and the assembly itself.

Item	Description	Theoretical Mass (g)	Mass (g)
A007	Assembly of the MBW system	56.19	55.267
HN-M2	M2 hex nut	0.13	0.11
TR-M2x8	M2 threaded rod 8	0.20	0.14
B016	3D printed motor mount	4.55	2.90
M012	Faulhaber 1509T006B-X4192	6.9	7.15
MBW013-1	Uniform flywheel Specimen 1	18.8	18.4
MBW013-2	Uniform flywheel Specimen 2	18.8	20.9
MBW013-3	Uniform flywheel Specimen 3	18.8	19.1

Table 5.3: Design and measured flywheel dimensions, of all manufactured specimen.

	Theoretical			Measured		
Specimen	Mass (g)	d_1 (mm)	t_1 (mm)	Mass (g)	d_1 (mm)	t_1
1	18.8	20.0	1.7	18.4	20.0	1.7-1.6
2	18.8	20.0	1.7	20.9	20.0	1.9
3	18.8	20.0	1.7	19.1	20.0	1.8-1.7

The flywheel specimen show that the best specimen in terms of deviation from the mass and thickness from the proposed design would be specimen 1. However, specimen 1 is not chosen of the final prototype, as protoype 1 and 3 both share a problem that would introduce disturbances through imbalances. The flywheel is not uniform in its thickness, which is why the thickness for these specimen is set at a range instead of a constant, such as with specimen 2. Despite the larger mass, specimen 2 will be utilised, to ensure the feasibility of this design. The task of the prototype is not to have the best possible performance, but to prove that the concept works.

From the mass measured of the flywheel, the inertia would be 42.61 gcm^2, including the inertia of the motor rotor. This would result in an angular momentum of 6.872 $mNms$ at 15400 rpm, or the required 6.05 $mNms$ at 13567 rpm. Both these speeds would satisfy requirement MBW12, as both achieve the minimum amount of angular momentum of 6.05 $mNms$. Since the design is based on a flywheel designed to achieve the required angular momentum at 15400 rpm, the required motor speed will also be 15400 rpm, to test whether this motor speed is feasible. For all tests in which a heavier flywheel would alter results, the heavier flywheel will be mentioned and the effect it caused.

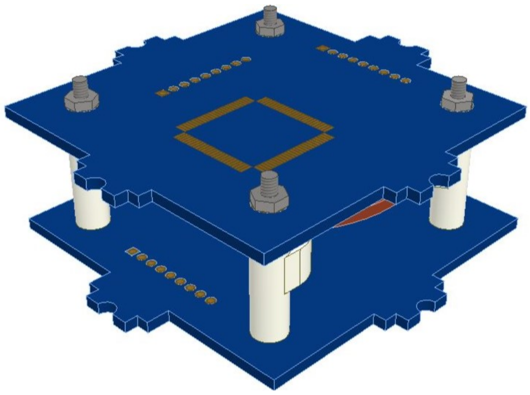

Figure 5.12: The assembly of MBW prototype.

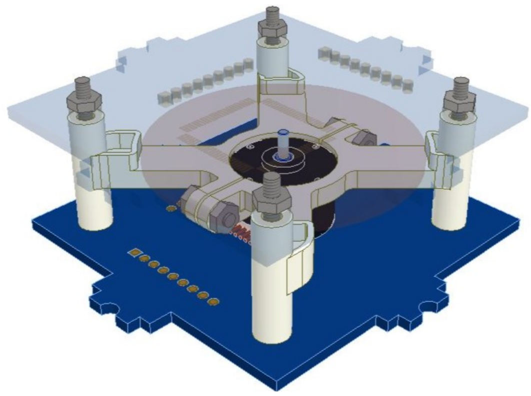

Figure 5.13: The assembly of MBW prototype, showing the internal clamping parts.

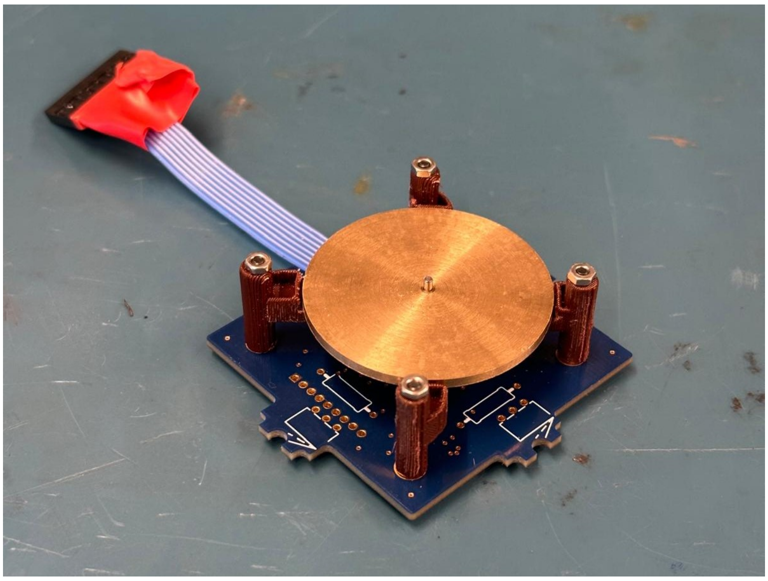

Figure 5.14: The assembly of the MBW, without the top PQ end cap.

6. Test Plan

Through the performance, vibration, vacuum and thermal tests the system will undergo, a viable design can be confirmed. The time budget spent on the testing phase of this thesis has depicted which tests can be done. For each proposed test, an assumed time consumption will be evaluated, upon which a decision will be made to do or postpone the test. The performance and vibration tests are preferred in comparison to the vacuum and thermal-vacuum tests, as the performance of the motor, the induced micro-vibrations and launch vibrations are expected to provide more insight into the performance and durability of the MBW system. All parts of the design were chosen or designed for survivability in extreme temperature of high vacuum conditions.

A testing plan will structure the objectives of the tests, in which manner the tests will be done, how the objectives are achieved and how the objectives are linked to the research objective or the design requirements, as stated in tables 1.3 or tables 2.3 and 2.4. All objectives shall be clarified in the sections dedicated to the corresponding tests.

Table 6.1: All test objectives for the PQ MBW prototype.

Test	Objective	Description	Goal
Motor functionality test	TO001	Determine motor speed capability.	MBW12
	TO002	Determine motor power draw.	MBW04
	TO003	Determine motor friction characteristics C_0 and C_v.	-
	TO004	Determine motor characteristics k_ω and k_T.	-
	TO005	Determine motor consistency between the two motors.	-
	TO006	Determine the stability of the angular velocity.	MBW14
	TO007	Determine the accuracy of the angular velocity.	-
	TO008	Determine the accuracy of the internal Hall sensors.	-
Operational testing mode 1	TO101	Determine MBW torque characteristics over the complete range of velocity.	MBW13
	TO102	Determine MBW power draw for the complete range of velocity.	MBW04
Operational testing mode 2	TO201	Determine MBW speed capability.	MBW12
	TO202	Determine MBW power draw at nominal velocity.	MBW04
	TO203	Determine stability of the MBW angular velocity.	MBW14
Launch vibration testing	TO301	Determine MBW launch vibration survivability.	MBW07
	TO302	Evaluate points of the assembly with varying resilience against launch vibrations.	-
Self-induced vibration testing	TO401	Evaluate the vibrations of only the motor.	-
	TO402	Evaluate the vibrations of the flywheel.	-
	TO403	Determine MBW micro vibration survivability.	MBW07
	TO404	Evaluate points of the assembly with varying resilience against micro vibrations.	-
Vacuum testing	TO501	Determine MBW speed capability in vacuum conditions.	MBW10
	TO502	Determine MBW torque characteristics over the complete range of velocity in vacuum conditions.	MBW10, MBW13
	TO503	Determine MBW power draw for the complete range of velocity in vacuum conditions.	MBW04, MBW10
	TO504	Determine stability of the MBW angular velocity in vacuum conditions.	MBW10, MBW14
	T0505	Determine motor friction characteristics C_0 and C_v for vacuum conditions.	MBW10
Thermal-Vacuum testing	TO601	Determine MBW speed capability in vacuum conditions for temperatures between -20 and +50°C.	MBW10, MBW11
	TO602	Determine MBW torque characteristics over the complete range of velocity in vacuum conditions for temperatures between -20 and +50°C.	MBW10, MBW11, MBW13
	TO603	Determine MBW power draw for the complete range of velocity in vacuum conditions for temperatures between -20 and +50°C.	MBW04, MBW10, MBW11
	TO604	Determine stability of the MBW angular velocity in vacuum conditions for temperatures between -20 and +50°C.	MBW10, MBW11, MBW14
	T0605	Determine motor friction characteristics C_0 and C_v for vacuum conditions for temperatures between -20 and +50°C.	MBW10, MBW11

6.1. Functionality Testing

To properly operate the MBW system, the different purchased components must be thoroughly investigated in their performance and the most efficient manner of delivering said performance. Functionality testing is in order and can be split up into three components: motor, speed controller and MBW functionality testing. The motor and speed controller functionality testing can be done to fully understand the inner workings of the motor and speed controller combination, as figure 5.1 can give a 'black box' feeling, thus does not give full insight to the workings and most efficient manner of operating the speed controller. The MBW functionality testing is done to be able to compare the no-load situation to the loaded situation and figure out the torque required to spin the MBW up to the required angular velocity, in the most power efficient manner.

As these are the first tests to be done, investigation into which electrical supplies are required will be done. Setting requirements and specifications of these supplies will be done in subsection 6.1.4.

6.1.1. Motor Functionality Testing

The motor functionality testing involves spinning the motor at various speeds while the flywheel is not yet attached. This mode is utilised such that the motor itself can be investigated for its performance and operation. The composition and the workings of the speed controller and USB programmer delivered with the two ordered motors can be tested and shall be reported upon in the next chapter, through running changing the settings of the speed controller and running the motor at a multitude of speeds and voltage input settings, such that the most power efficient running setting is found.

The test objectives TO001 and TO002 can be tested for simultaneously by spinning up the motor to the nominal angular velocity and monitoring the power usage through voltage and current readings of the motor and motor speed controller. This test will thus create a reference for all other tests as the no load characteristics of the motor can be derived. One test would involve the motor spinning up to 15400 rpm with 180 mW of power available to the motor system.

Per test, more than 3 power readings of speed controller and the motor will be done to improve the random uncertainty and assess the reproducibility of the results, from which averaged values will be used for TO003 and TO004, to calculate the motor and motor friction characteristics. Equations 4.3 to 4.12 used in section 4.1 shall be able to solve for the motor and motor friction characteristics k_ω, k_T, C_0 and C_v.

TO005 can be achieved through running both motors through each operational mode, and comparing the two results, in power draw and speed delivery. The two identical Faulhaber motors must be tested for their indistinguishability, with both motors to be used simultaneously in testing if the motors were to be identical within the stability criteria. If both are able to conform to TO001 and TO002, both will be used, but if the power draw per speed delivery of one of the motors is optimal, this motor shall be used for the bulk of the tests.

The stability of the motor and the no load angular velocity is detrimental to having a stable MBW. TO006 is directly connected to MBW14, which means the deviation of the angular momentum and angular velocity may not deviate more than 0.18%. This can be determined by running the motor for a certain length of time and calculating the consistency in velocity within the motor. TO007 can be achieved by repeating this test and checking consistency between the tests.

6.1.2. Speed Controller Functionality Testing

Referring back to figure 5.1 and regarding the speed controller as a black box and investigate what the relation is between the input and output of the speed controller is required to know what the most power efficient operating manner is of the speed controller. Over all three inputs, the input voltage and current shall be measured, through which a power calculation can be done, which will indicate the most efficient combination of voltage input values.

Three voltages are required to fully map all inputs, thus three power supply units (PSU's) must be utilised. The U_{mot} input voltage powers the MOSFETs in the microcontroller in the speed controller and shall be tested for voltages around the required angular velocity he motor has to obtain and the nominal voltage the motor requires (6 V). As the speed controller accepts a voltage input range of 4 to

18 V through its U_p input, and the electronics uses a 5 V voltage to power the Hall sensors signal, this range shall be tested around 5 V input. And as U_{nsoll} accepts 0 to 10 V over its input, this range shall be used. To make sure the testing time does not explode due to the small voltage steps taken during testing and the assumption that the U_{nsoll} port is the most sensitive to voltage changes in terms of motor speed output, the voltage steps are set at 2, 2 and 1 V for U_{mot}, U_p and U_{nsoll} respectively initially. If during testing the speed controller shows different sensitivity behaviour of voltage input to motor output, these step sizes shall be changed.

From this, a comparative power to velocity curve per voltage input scenario can be built, to visualise the most power efficient manner of spinning the motor up to the required angular velocity of 15400 rpm, meeting requirement TO010.

6.1.3. MBW Functionality Testing

The ranges performed in the motor functionality testing shall be repeated once the flywheel has been fitted to the motor. The comparison to the motor functionality testing shall be made in terms of the required torque to turn the possibly misaligned or asymmetrical flywheel, as the motor and motor friction characteristics will be assumed not to change, as both the motor and MBW functionality testing shall be done in similar environments.

6.1.4. Electrical Supplies

To measure the angular momentum and angular velocity of the motor, three measurement methods will be used. These three measurement methods will validate the measurements as the measurements will come from different sources. Through measuring the velocity from multiple sources, TO008 can be achieved. Three requirements for measuring the angular velocity are that the measurement device is able to continuously measure the rotations done by the motor and that it can do so for a range of 0 to at least 15400 rpm, and that it can measure the rotational velocity to an accuracy of 0.1%. These values are chosen to be able to confirm system requirements MBW06 and MBW14.

The velocity of the motor read through the FG port of the speed controller as shown in figure 5.1, which can be validated through multiple measurement methods, of which two will be used. Attaching an electrical frequency measuring device such as an oscilloscope or a digital multi-meter (DMM), the frequency of the Hall sensor signal can be read between one of the Hall sensor lines of the motor and the motor ground. Another method would be to create a small sized optical tachometer, marking the motor axle or flywheel with black sections, and using an optical sensor to measure the differences in reflectivity on the motor axle or flywheel to measure the angular velocity of the system.

The electrical supplies available through the workshop of the Space Engineering (SpE) department are power supply units (PSU's), digital multimeters (DMM's), oscilloscopes and wires aplenty. A selection for a PSU, DMM and oscilloscope shall be made corresponding to the MBW accuracy requirement MBW13. A good rule of thumb is to have 5 to 10 times more measurement accuracy than the motor accuracy.

Through the product data sheet of the Faulhaber motor, the response of the motor to a voltage or current change can be found, which would influence the choice of the electrical supply through the accuracy and stability requirement set for the motor. With the motor speed responding to the voltage of the power supply with 2.682 rpm per mV, the PSU would have to have an accuracy of at least 2.07 mV, when following the rule of thumb.

$$\Delta U = \frac{1}{5}\Delta\omega_{MBW} \cdot k_\omega = \frac{1}{5} \cdot 15400 \cdot 0.18\% \cdot 2.682 = 2.07mV \tag{6.1}$$

The PSU chosen is the Agilent E3631A, as it boasts the highest accuracy and stability of all available PSU's and meets the requirement of the stability. The specifications of the PSU are shown in table 6.2.

Table 6.2: Agilent E3631A PSU accuracy and stability specifications[2], all in % of output + offset.

Programming Accuracy		Stability	
Voltage	Current	Voltage	Current
0.05% + 10 mV	0.2% + 10 mA	0.02% + 1 mV	0.1% + 1 mA

Following the same measurement accuracy requirements as stated above, the Keysight 34401A DMM is chosen for its high accuracy in low current situations, and its high accuracy in frequency readings. The specifications of the DMM are shown in table 6.3.

Table 6.3: Keysight 34401A DMM accuracy specifications[28], all in % of reading + % of range.

DC Voltage		DC Current	
Range = 1.000000 V	Range = 10.00000 V	Range = 100.0000 mA	Range = 1.000000 A
0.0040 + 0.0007	0.0035 + 0.0005	0.050 + 0.005	0.100 + 0.010

The nature of measurements through oscilloscopes is based on triggers, not the continuous time as required. However, for an instance test, an oscilloscope could be utilised to validate results from the USB adapter or the optical tachometer. Most oscilloscopes surpass the accuracy requirements for this project, thus the one readily available shall be used.

The oscilloscope used is the Tektronix 2 Series Multi Signal Oscilloscope[53], which boasts the favoured ability of exporting data digitally, such that it can be post-processed quite swiftly. The timebase accuracy of this device is $+/-$ 25 ppm over any interval larger than 1 ms.

6.1.5. Tachometer

An optical tachometer is based on an optical sensor capable of discerning between reflective and non-reflective surfaces, so a small stripe by a permanent black marker on the axle of the motor or the system flywheel shall suffice such that the velocity of the motor with and without the flywheel can to be measured. This optical sensor must also be able to continuously send signals, and favourable digitalise these into data, to automate the measuring process. Therefore, a sensor compatible with computers shall be utilised.

A proposed tachometer setup utilises a ROHM RPR-220 infrared emitter sensor combination, as this sensor is widely available and a sufficient price to performance ratio. Specifically, the Grove Infrared Reflective Sensor is chosen, which incorporates the RPR-220, together with a LMV358 rail-to-rail operational amplifier and a potentiometer, to amplify the output of the phototransistor and tune the sensitivity of detection respectively. This sensor meets the speed requirement, as it boasts a response time of 10 μs, which allows the sensor to record a binary switching signal with a frequency of 50 kHz or rps in this case. As the speeds required for the MBW are two orders of magnitude lower than the max speed, more black stripes will be put on the motor axle and flywheel, for higher measuring resolution.

As the oscilloscope is not used as a continuous velocity measurement device, only the USB programming adapter and optical tachometer shall be utilised concurrently to measure the velocity of the motor, as can be seen in figure 6.1.

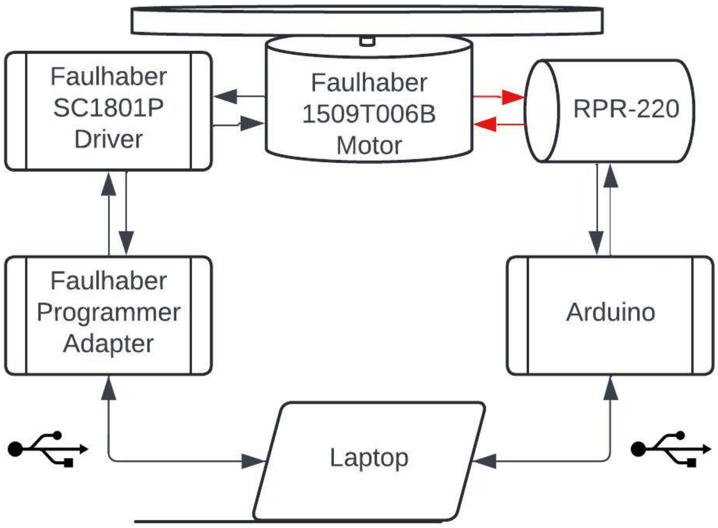

Figure 6.1: Tachometer setup utilising with magnetic and optical velocity sensors.

The script running on the Arduino board is fairly simple. The sensor is connected to the input voltage and ground as power supply and a connection through a data line from the sensor to a singular pin of the Arduino board is made. This singular pin can read out the binary switching signal the RPR-220 sensor sends in accordance to the reflectivity of the surface below the sensor, 0 for a reflective surface or 1 for a non-reflective surface. The measuring technique can be seen in figures 6.2 and 6.3.

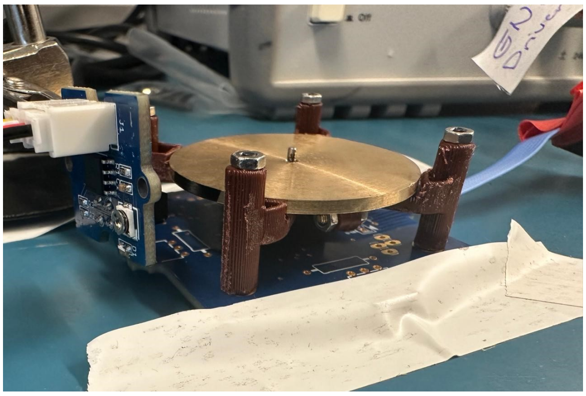

Figure 6.2: Measuring the non-reflective part of the flywheel, resulting in a binary high signal.

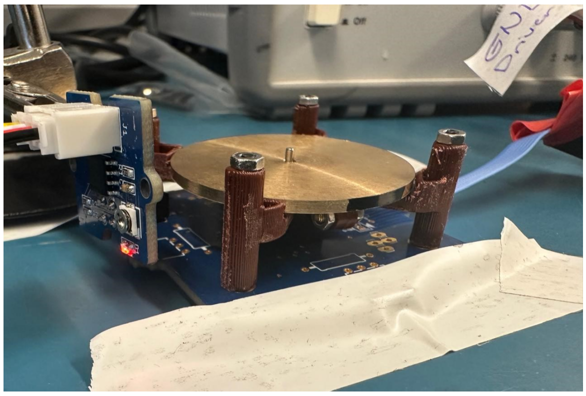

Figure 6.3: Measuring the non-reflective part of the flywheel, resulting in a binary low signal.

The changing of this binary signal from only low to high is interpreted as an interrupt, such that there is one interrupt per black marking. Two ways of calculating the velocity come from the counting of interrupts; counting the interrupts over a set amount of time and divide over that set amount of time to calculate an average speed over that set amount of time. To account for lower speeds, especially during operational testing mode 1, the measuring period is varied between 1 and 10 seconds. The measurement accuracy requirement of 0.18% dictates that at nominal speed, the resolution would have to be 10 times smaller to accurately measure the offset. Therefore the resolution has to 0.0462 rps, which can be achieved with measuring period of 2 seconds, as two markings are present on the motor axle and flywheel.

Using the Tektronix oscilloscope, the electrical signal over one of the Hall sensor lines could be extracted and be averaged in the same manner the optical tachometer would do with the counted interrupts. Spinning up the motor to its nominal velocity at 15400 rpm, and let it settle for at least 30 minutes, to minimise and mitigate any start up or warm up behaviour, can firstly specify the accuracy of the tachometer and the accuracy of the angular momentum.

6.2. Operational Testing

The operational testing of the MBW system will consist of modes in which the system will operate during a mission. Mode 1 will be the acceleration of the flywheel to mode 2, at constant operational velocity. As stated in table 6.1, each mode has its own objectives. All shall be made clear in the subsequent subsections for each mode.

6.2.1. Mode 1

Mode 1 involves the acceleration of the flywheel to the nominal velocity of 15400 rpm to deliver the required angular momentum. This mode 1 is especially important for the spin up procedure during a mission. The torque the motor delivers can not be higher than the torque a present magnetorquer can supply, otherwise the attitude control will be rendered lost. If this succeeds, TO101 is achieved.

The Faulhaber 1509T006B motor can deliver a torque range of nil up to a stall torque of 0.953 mNm. The acceleration of the flywheel is thus dependent on the supplied torque range by the Faulhaber motor and the maximum torque the MBW is allowed to exert through requirement MBW13. The maximum torque allowed can be used to investigate what the power consumption of the motor theoretically will be using the assumed values calculation in equation 4.17. With a power boundary set at 180 mW, the maximum torque from the power regime can be calculated, allowing it to change over time. The entire speed domain must be beneath the power boundary of 180 mW to achieve TO102. Furthermore, from these two torque boundaries, an angular acceleration range over time can be extracted which can be used to calculate the spin up time. Due to the inertia of the flywheel, the maximum angular acceleration is equal to 0.025 rad/s^2.

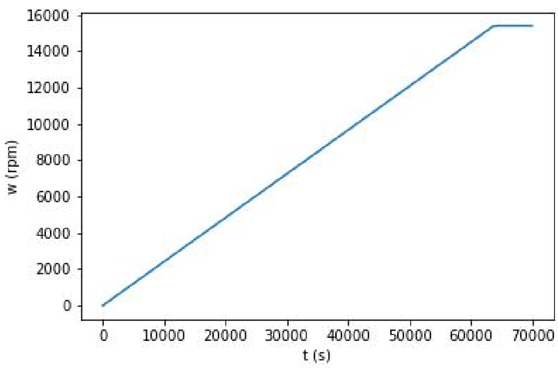

Figure 6.4: The simulated velocity curve for mode 1.

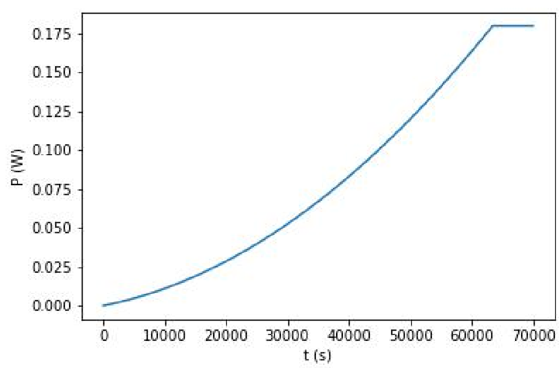

Figure 6.5: The simulated power curve for mode 1.

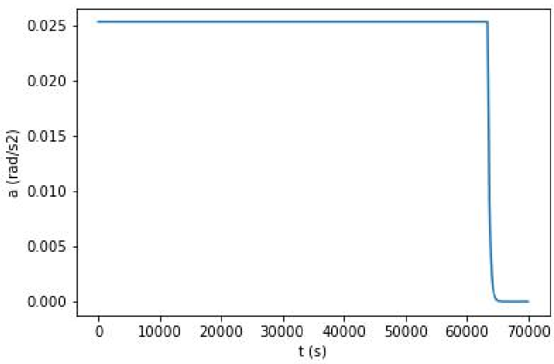

Figure 6.6: The simulated acceleration curve for mode 1.

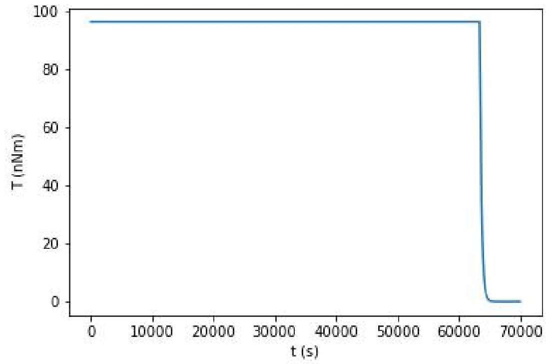

Figure 6.7: The simulated torque curve for mode 1.

As can be seen from the graph in figure 6.5, power slowly increases over time, to its limit of 180 mW, while the torque is constant until this power limit is reached. Due to the low torque, the motor can increase its velocity at a constant rate until near the end. The simulated time to spin up is equal to 65350 seconds, or around 18.15 hours. This spin up period is quite large, so shall not be tested completely due to time constraints, but rather split up into important intervals. Three intervals shall tested, in which crucial aspects shall be tested.

Interval 1 will be the start of the curve, when the velocity is zero to 1000 rpm, to investigate the performance of the motor at low velocity and investigate any minimum torque the motor has to supply to run. Interval 2 shall be in the middle of the curve, between 7000 and 8000 rpm, to investigate the performance of the motor at standard speeds for the motor. Interval 3 will be nearing the end of the curve, between 14400 and 15400 rpm, in which the torque shall vary as the power constraint is approached. This will investigate the torque agility of the motor and the power consumption towards the end of the spin up period. All three intervals will be tested at least 3 times, to minimise possible human or instrument errors. Finally, for all tests, a magnetic and optical velocity reading will be done to further increase the dataset size used to determine the accuracy of the magnetic Hall sensors and the angular velocity.

Two ways of capping the torque exerted from the motor could be envisioned: to program a torque cap into the speed controller via the USB programmer adapter, or increase the setpoint voltage with small enough increments such that the response of the motor would not exert a too high torque. The main advantage of using the former method is that it is very simple to do through the supplied programming software Motion Manager. The main disadvantage of the latter option is that it is wholly dependent on the specifications of the used power supply unit (PSU). The resolution of the chosen PSU in subsection 6.1.4 has a resolution for DC voltage of 1 mV, which would increase the velocity by 2.682 rpm, as depicted by the motor speed constant k_ω as stated on the Faulhaber 1509T006B product sheet. However, without any way of knowing beforehand what the response time of the motor to this velocity increase will be to depict the torque figure, the former torque cap option is chosen.

6.2.2. Mode 2

The second mode involves the constant nominal angular velocity of the flywheel of 15400 rpm to deliver the required angular momentum. Approaching the true mission scenario can be done by running the motor for longer periods of time and documenting the possible changes in velocity, torque or power. This is crucial for the mission, as changes in velocity can alter the angular momentum, unforeseen torque changes can distort the attitude control of the PQ and increase in power usage can result in a deficit of power for the other subsystems on board.

The three set test objectives for this test concern the reached angular velocity, the power draw for the required velocity and the stability of the system at the required velocity. TO201 and TO202 are as straightforward as stated in table 6.1. TO203 will be done similarly to TO006, in which the speed difference between measuring points will be calculated.

Similar to the other tests presented, mode 2 will be done multiple times. Each test will have a duration of larger than 600 seconds or 10 minutes, with a reassembly of the system in between to eliminate any assembly errors. During these test periods, the power usage will be logged utilising the readout of the USB programmer adapter and the multi-meter on hand. Finally, to complete the data set, velocity will be measured through the USB programming adapter and optical tachometer as displayed in figure 6.1.

6.3. Launch Vibration Testing

To be able to operate in space, any system would have to be able to survive the launch. Since the MBW design made in this thesis is highly miniaturised, only the sine vibrations induced onto the system by the launcher are tested. The force on the axle at a certain frequency is dependent on the mass of the flywheel and the acceleration for each frequency, which depicts a vibration envelope. Since the flywheel used in this prototype is 3 g heavier than the design mass, the system could fail when shaken. Nevertheless, the MBW must survive the launcher vibration envelope, as depicted by TO301. To be able to test a vibration envelope, such an envelope and a shaker able to simulate must be chosen. The vibration testing of the MBW system shall be done in house, utilising an existing vibration bench. Ideally, the shaker central in the vibrating bench has the following specifications:

- A frequency range equal or exceeding the tested frequency range/vibration envelope;
- A force rating equal or exceeding the tested accelerations per frequency;
- An adequate size such that the MBW system can be mounted directly.

The first two specifications are purely related to the selected vibration envelope, as stated in table 6.4. The latter specification is related to the manner of mounting a system to a shaker. When a mounting plate or mounting table is introduced alongside the tested system, the mass of this mounting part has to be taken into account, possibly requiring a larger shaker. The shaker specifications must be calculated from the launcher vibration envelope which can be established through the selection of the launcher. From the requirements, this is supposed to the SpaceX Falcon 9 vibration envelope.

With this vibration envelope, calculations can be done to find the shaker specifications. The mass mounting on to the shaker shall be assumed to be 60 g, due to the addition of a MBW to shaker mount. From this assumption, equations 6.2 to 6.4 can be used to find the shaker force (F_{sh}), velocity (V_{sh}) and displacement (X_{sh}) specification. Along with the vibration envelope on display in table 6.4, the shaker force, velocity and displacement specification are maximally 0.53 N, 0.16 m/s and 5.0 mm respectively.

$$F_{sh} = m \cdot a \tag{6.2}$$

$$V_{sh} = \frac{a}{2 \cdot \pi \cdot f} \tag{6.3}$$

$$X_{sh} = \frac{a}{(2 \cdot \pi \cdot f)^2} \tag{6.4}$$

The shakers available within the Aerospace Structures and Materials department are the K2007E01 Smart Shaker and the 2025E Modal Exciter, made by The Modal Shop, as provided by Dr. J. Sodja. Both shakers are capable of imitating the vibration envelope of the launcher with a large margin due to the low mass of the prototype system. Due to the inclusion of a power amplifier and the minimal size of the K2007E01 Smart Shaker, it shall be utilised for the vibration testing.

Table 6.4: The Falcon 9 vibration envelope and required shaker settings.

Frequency (Hz)	5	20	35	75	85	100
Acceleration (g)	0.5	0.8	0.8	0.8	0.9	0.9
Force (N)	0.29	0.47	0.47	0.47	0.53	0.53
Velocity (m/s)	0.16	0.062	0.036	0.017	0.017	0.014
Displacement (mm)	5.0	0.50	0.16	0.035	0.031	0.022
Amplitude (V)	0.264	0.065	0.025	0.012	0.013	0.011

Before the MBW can be fit onto the shaker and be shaken, the shaker would need to be calibrated. The calibration shall be done using the laser vibrometer and the generator function built into the power amplifier of the laser vibrometer. Following the generator interface presented in the PSV-500 software, a sinusoidal signal would be generated, with the gain settings on the smart shakers set to the preferred level. Through testing the smart shaker, the settings were set in accordance to the vibration envelope, as set in table 6.4. These values are a starting point and will be calibrated again with the mass attached, as the shaker amplitude is load dependent. These new voltage values will be put in section 7.1.9.

Even though the system only has to survive this vibration envelope only once, the direction of the vibrations is unknown. The vertically symmetrical nature of the MBW system dictates that the shaker test must be performed twice; once axially and once laterally. As the lateral loads as presented in Falcon 9 User Manual [46] are lower than the axial loads, only the axial load scenario are performed, for both mounting scenarios. Each vibration load case is performed for 4 minutes, as this is set to be the average time between launch and payload jettison [46]. In total, with the assumption of 30 minutes for the initial shaker setup and one minute in between to change the shaker settings, the test will take approximately 75 minutes.

This shaker also has an integrated M5 threaded mounting insert, supporting payloads up to 0.9 kg (2 lb). For this interface, lightweight solutions have been made to clamp onto the MBW prototype, as seen in figures 6.8 through 6.13.

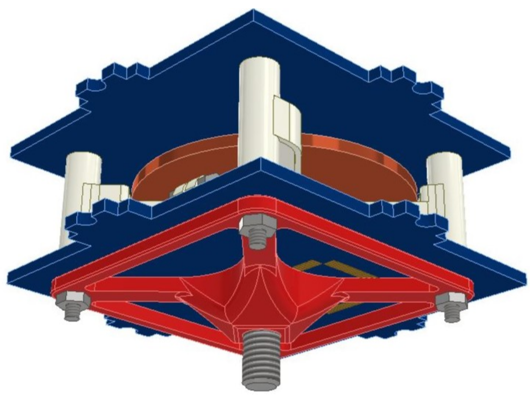

Figure 6.8: The assembly of MBW prototype and the axial shaker mount.

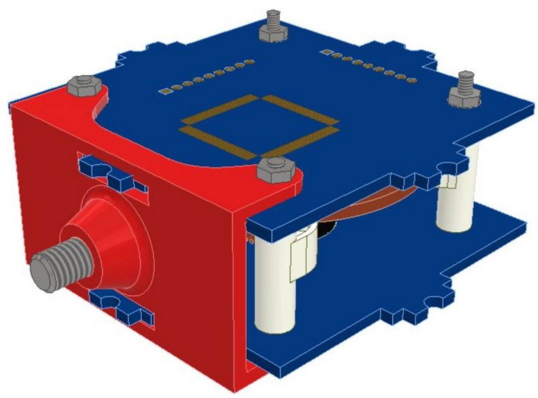

Figure 6.9: The assembly of MBW prototype and the lateral shaker mount.

The additional mass the axial and lateral shaker mount introduce are 2.03 and 3.26 g respectively. Together with the mass of the M5 10 mm bolt, the total axial and lateral vibrating mass are 59.9 and 61.2 g. These weights are within the shakers budget, therefore it shall be used.

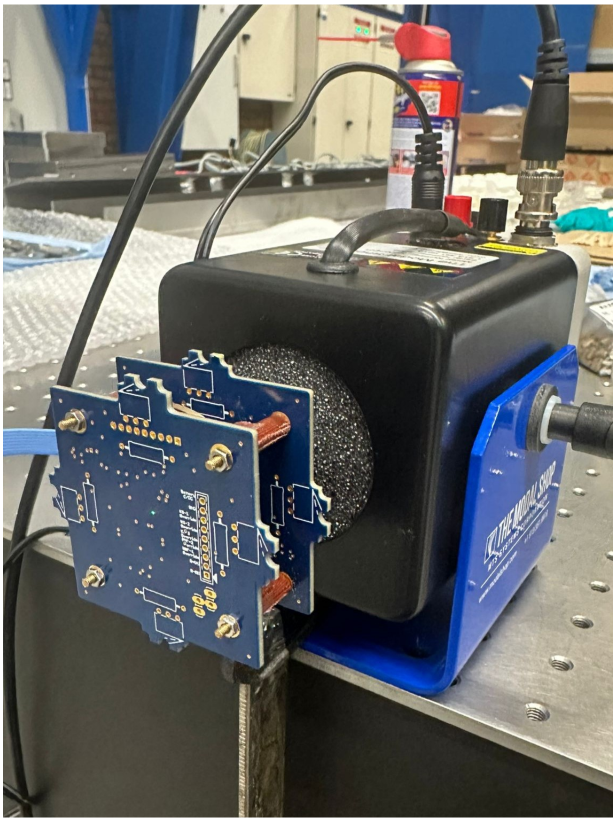

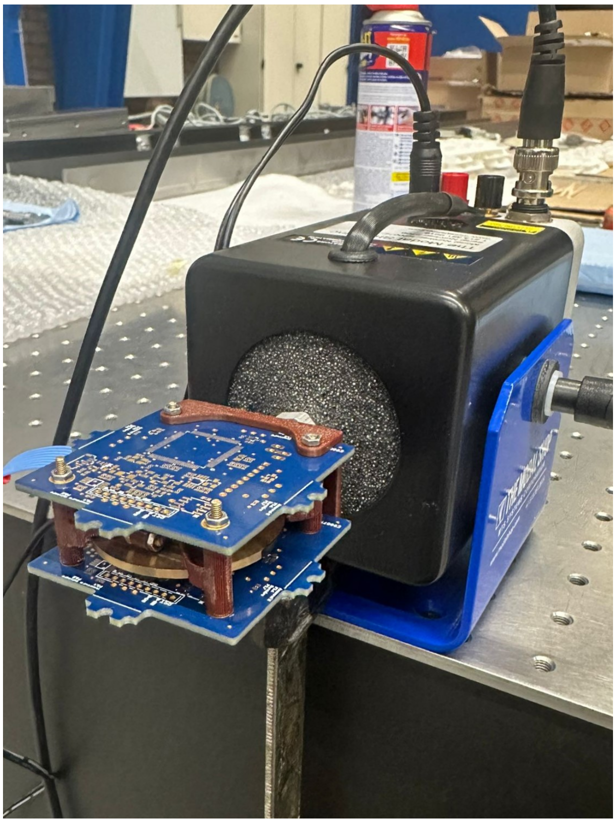

Figure 6.10: The MBW mounted axially to the shaker.

Figure 6.11: The MBW mounted laterally to the shaker.

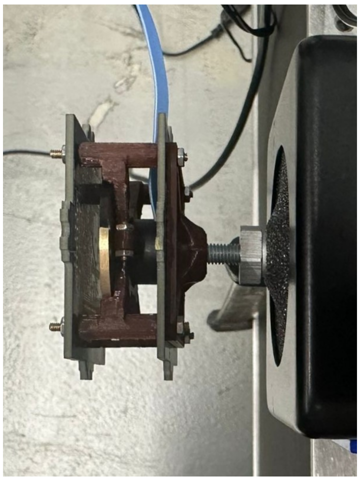

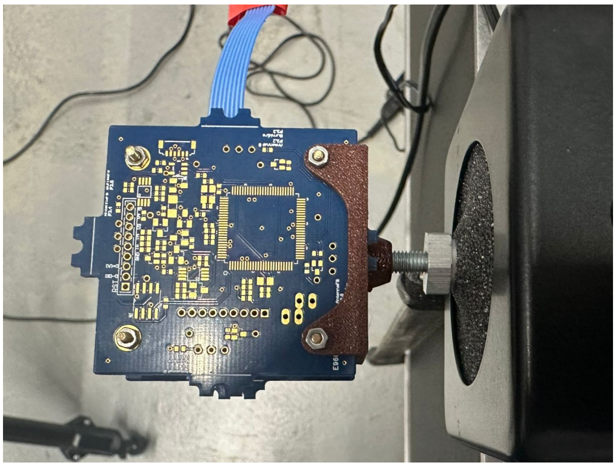

Figure 6.12: The MBW mounted axially to the shaker, as seen from the top.

Figure 6.13: The MBW mounted laterally to the shaker, as seen from the top.

Once the shaker has shaken the MBW according to the vibration envelope twice, performance testing and part inspection will be performed to find in the difference in performance and evaluate damages or resilience in parts due to the shaker tests, achieving TO302.

6.4. Micro Vibration Testing

Vibration testing for the MBW system is crucial at this scale, large stresses primarily come from vibrations rather than large accelerations. Furthermore, the high angular velocity and large size of the flywheel could create rather large destructive vibrations. Internal vibration sources can come from the misalignment of the flywheel in relation to the motor, the misalignment of the centre hole of the flywheel and the COM of the flywheel, an inconsistency in the material density of the bronze alloy, an imperfection in the motor rotor or any other imperfection in the manufacturing of the flywheel prototype. Before the motor or MBW has spun up, a measurement will be done for only the background, to possible filter this out when the noise is deemed too high in comparison to the vibration signal. Furthermore, the heavier flywheel selected in section 5.5 can more easily create large disturbances through its increased mass, even though it was chosen for its more uniform thickness.

Testing the severity of the internal vibration can simply be done by operating the MBW system. To investigate the source of each disturbance, the motor and flywheel are tested separately. Before press fitting the motor, it shall be spun on its own to investigate whether the motor contains manufacturing imperfections in the rotor. Even though these are expected to be very small to negligible, another source of disturbance once the flywheel has been press fit can come into play, through the mentioned radial play of 0.015 mm as stated in the Faulhaber product catalogue. The laser vibrometer module shall be used to measure these vibration, with three separate measuring intervals for three different speeds measured and averaged to minimise the impact of background noise.

Most crucially and most prominent will be the vibrations of the flywheel due to the flywheel. The manufacturing was done by hand and therefore shall have included some (though small) manufacturing errors, leading to a misalignment between the COM and the rotational axis of the flywheel. Once the flywheel has been press fit, the motor will be spun up to nominal operational velocity, and investigated through the usage of the vibration bench how severe the vibrations are. A laser vibrometer shall be used to measure these vibration, with three separate measuring intervals for three different speeds measured and averaged to minimise the impact of background noise.

6.4.1. Laser Vibrometer

The MBW system induces vibrations onto itself and the satellite through imperfections within the flywheel or misalignment between components. Using a vibration isolated test bench can record and extract these self induced vibrations, required for the evaluation of the MBW system.

A previous design by Vergoossen [54] has been recovered as it was still present within the Aerospace faculty, therefore it shall be adapted for the MBW system. The design utilises a seismic mass suspended by soft suspension on which the tested system is mounted, as inspired from a design of Zhou et al [57]. This soft suspension design is, through its coupled measurement, truly representative of the operational vibrations encountered. This is due to coupled vibrations the MBW causes, as the initial MBW vibrations would be passed back and forth between the rest of the PQ structure, eventually vibrating the MBW itself.

Vergoossen advices the usage of higher accuracy acceleration measurement equipment for better stabilised wheels. Since stability of the flywheel has a high priority in this project, the accelerometer used is a laser vibrometer, namely the Polytec PSV-500 Scanning Vibrometer, capable of measuring as frequent as 2 MHz, as provided by the ASM faculty department. This laser shall be set onto the four positions as stated in figure 6.17 when the MBW is at its operational velocity.

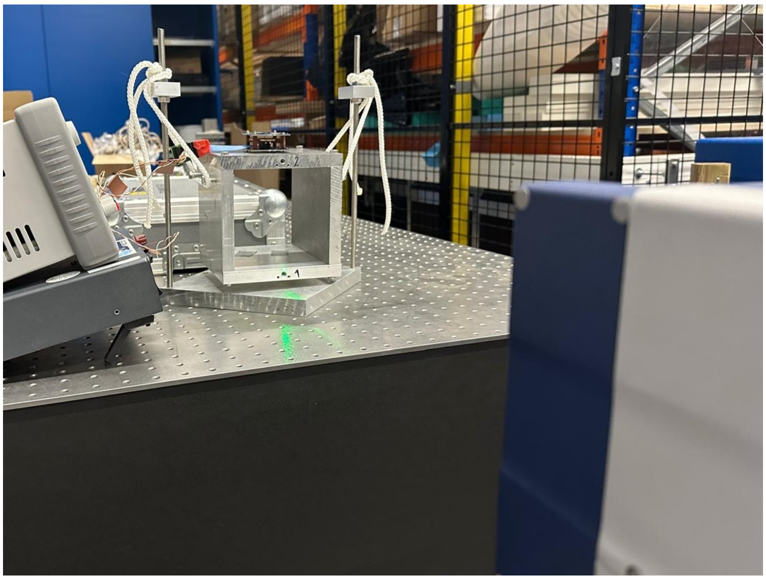

Figure 6.14: The laser vibrometer testing station.

Figure 6.15: The PSV-500 Laser Vibrometer scanning head.

The seismic mass design would set the rotating axis of the flywheel perfectly in line with the centre of mass of the seismic mass, when mounted on top. Using CAD software and a highly sensitive scale, the imperfections and asymmetrical nature of the existing seismic mass can be modelled. From this, the original COM lies 0.039 mm from the geometrical centre of the seismic mass. Adding the MBW system onto the seismic mass causes the COM to lie 0.042 mm from the geometrical centre. As this COM offset and the change in offset is insignificant, the COM will be assumed to be in the geometrical centre.

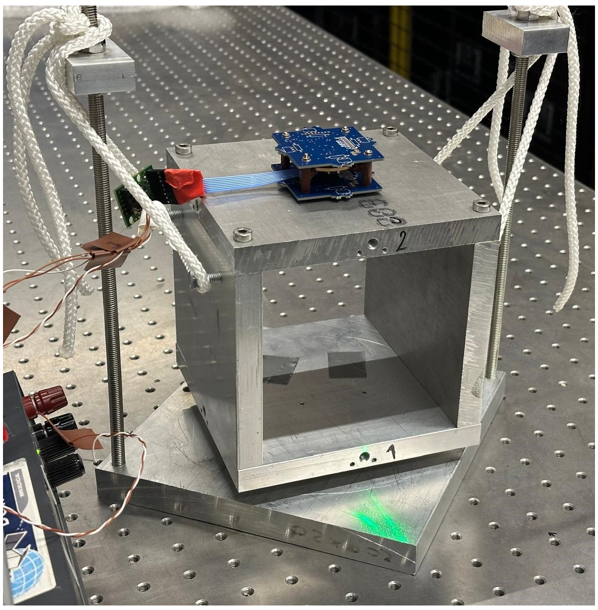

Figure 6.16: The seismic mass with the MBW on top.

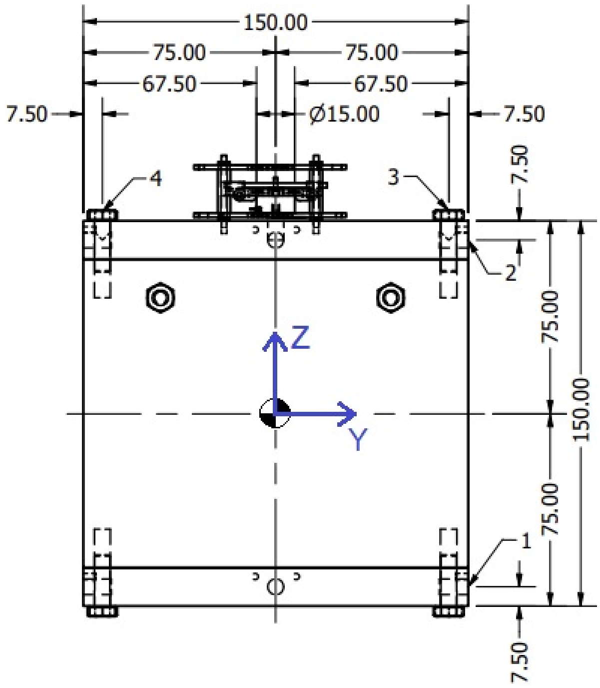

Figure 6.17: Schematic and coordinate system of the seismic mass and location of the accelerometers, centre of mass and MBW.

Four locations for accelerometers are set as to calculate the forces and moments induced by the RWS or MBW on all three axes, as can be seen in figure 6.17. Vergoossen and Zhou both used two accelerometers on the seismic mass, to measure the force and moment from the micro-vibrations of their RWS, as calculated per equation 6.5. The assumption can be made that the force and moment in y and x direction are equal, due to the symmetry of the seismic mass and MBW system. Finally, forces and moments in the z direction can be calculated using equation 6.7.

$$\begin{bmatrix} F_y \\ M_x \end{bmatrix} = \begin{bmatrix} \frac{m_{sm} \cdot d_2}{d_1 + d_2} & \frac{m_{sm} \cdot d_1}{d_1 + d_2} \\ \frac{I_{xx} - m_{sm} \cdot d_2^2}{d_1 + d_2} & \frac{-I_{xx} - m_{sm} \cdot d_1 \cdot d_2}{d_1 + d_2} \end{bmatrix} \begin{bmatrix} a_1 \\ a_2 \end{bmatrix} \tag{6.5}$$

$$\begin{bmatrix} F_y \\ M_x \end{bmatrix} = \begin{bmatrix} F_x \\ M_y \end{bmatrix} \tag{6.6}$$

$$\begin{bmatrix} F_z \\ M_{2,x} \end{bmatrix} = \begin{bmatrix} \frac{m_{sm}}{2} & \frac{m_{sm}}{2} \\ \frac{I_{xx}}{2 \cdot d_3} & \frac{I_{xx}}{2 \cdot d_3} \end{bmatrix} \begin{bmatrix} a_3 \\ a_4 \end{bmatrix} \tag{6.7}$$

The seismic mass final design specifications are put in table 6.5, which is retrieved from Vergoossens' thesis and confirmed using CAD and swing tests as done in Vergoossens' thesis. [54].

Table 6.5: Specifications of the seismic mass.

Specification	Symbol	Value	Unit
Moment of inertia in x axis	$I_{xx_{sm}}$	0.016	kgm^2
Moment of inertia in Y axis	$I_{yy_{sm}}$	0.016	kgm^2
Moment of inertia in Z axis	$I_{zz_{sm}}$	0.021	kgm^2
Natural frequency in x axis	f_{x_sm}	10.03	Hz
Natural frequency in Y axis	f_{x_sm}	11.58	Hz
First structural vibration mode	f_{z_sm}	1502.8	Hz
Mass of seismic mass	m_{sm}	3.329	kg

6.5. Vacuum Testing

The performance of vacuum lubricants is comparatively less efficient than atmospheric counterparts, according to literature and Faulhaber engineers. Therefore, the performance difference between regular testing and mission operation is hypothesised to be drastically different.

As the MBW will be tested in a new test area compared to all the other atmospheric tests, a new datum test for mode 1 and 2 will be done to be able to fully compare the performance. Once this is done, the motor is spun up to its maximum speed over an input voltage that can achieve the required speed, and the vacuum chamber lowers the pressure by steps of 100 $mbar$, to find the characteristics of the motor in vacuum. Once vacuum (near 0 mbar) has been achieved, the motor shall be spun down to zero, to begin mode 1 testing and eventually transition into mode 2 testing. Then after the mode testing is done, the pressure is slowly increased back to atmospheric pressure, and the MBW is tested in atmospheric pressure once again, to see the effects of the vacuum environment on the MBW. This manner of testing will be done thrice.

6.5.1. Vacuum chamber

The workshop and clean room at the Aerospace faculty of the Delft University of Technology houses a vacuum chamber; the Heraeus VacuTherm 6130M. This vacuum chamber can reach pressures as low as 10^{-2} $mbar$ and sustain temperature up to 200 $°C$.

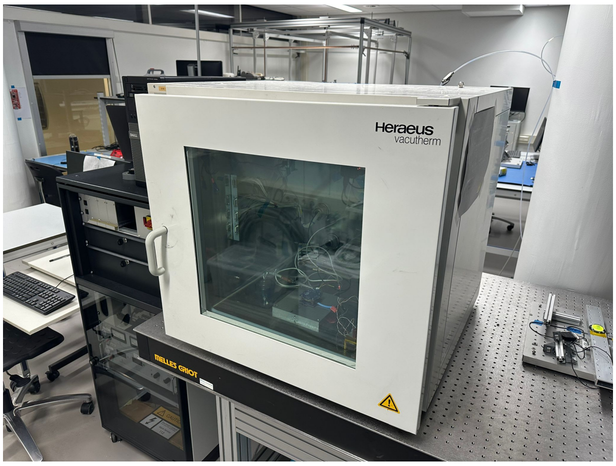

Figure 6.18: The Hermaeus Vacutherm 6130M vacuum oven used for vacuum testing.

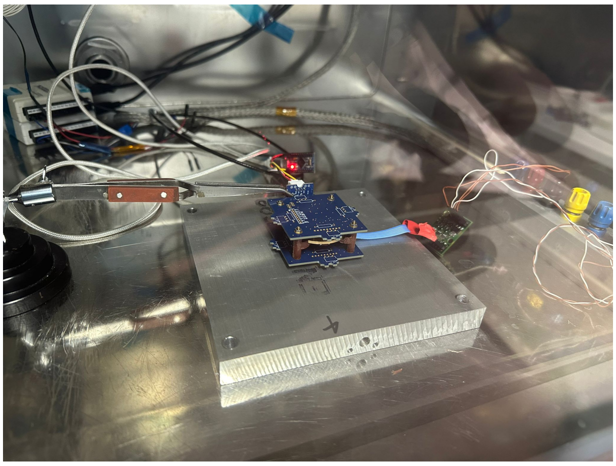

Figure 6.19: The test setup used within the chamber.

The vacuum chamber will house the MBW prototype and the tachometer to measure the velocity of the motor, and the input voltage will be measured through the power supplies. For the vacuum chamber, extra long cables for connecting the motor and tachometer to power supplies or a laptop have to be developed. Luckily, the cables used for the testing in atmospheric conditions were already long enough, and extension cables were plentiful available within the cleanroom. Furthermore, a USB hub was present within the vacuum chamber to connect the Arduino tachometer to.

The vacuum chamber is equipped with two barometers, with the readout of the digital barometer or vacuum gauge by Vacuubrand in figure 6.20 and the analogue barometer embedded into the vacuum chamber in figure 6.21. The vacuum gauge is chosen to configure the vacuum chamber, as this barometer achieves the highest accuracy. It can achieve an accuracy of 1 $mbar$, and ranges down to 0.1 $mbar$.

Figure 6.20: The digital barometer attached to the vacuum chamber, measuring 1.5 $mbar$.

Figure 6.21: The analogue barometer embedded into the vacuum chamber, measuring 1.5 $mbar$.

6.6. Thermal-Vacuum Testing

In addition to the varying performance of the vacuum lubricant, it is stated explicitly in the Faulhaber product catalogue that all data presented is tested data for 22 °C. Together with the testing of requirement MBW10 and MBW11, the MBW assembly must be tested for its operability in temperatures between -20 and +50°C. Unfortunately, the vacuum chamber introduced in subsection 6.5.1 does not have the capability to cool down, only heat up. To be able to reach the required -20°C, another testing station must be found capable of vacuum at that temperature.

If the motor characteristics change drastically throughout this temperature range, the power draw or rotational velocity could change over one orbit as well. As the MBW will spin up and nominally operate during changing environments, operational mode 1 and 2 will be tested for the aforementioned temperature range, with intervals of 10 °C. To prove the reproducibility of the results, tests shall be performed thrice.

6.7. Testing Methodology Outcome

From the research objectives came test objectives for which tests were devised. All tests and important criteria are summarised here in table 6.6. The amount the tests performed (n_t), the assumed amount of time per test in minutes (t_t) and the test facilities or instruments required are also stated for a complete overview.

The chronological order of the tests is not shown in this table, as the motor functionality and internal motor vibration testing are first. The fitting of the flywheel is permanent, so all test containing only the motor must be done first. Then, to compare the performance during all other tests, the shaker tests shall be done last.

Table 6.6: All tests for the prototype of the PQ MBW.

Test	Description	n_t	t_t	Instruments	Objective
Motor functionality	Spin up only the motor to 15400 rpm, measure voltage and current values, derive motor characteristics.	10	5	MBW without flywheel, Tachometer, DMM & 2 PSU's.	TO001 - TO008
Mode 1.1	Spin up the assembly to 1000 rpm, measure voltage and current values, derive motor characteristics.	3	40	MBW with flywheel, Tachometer, DMM & 2 PSU's.	TO101 - TO102
Mode 1.2	Spin up the assembly from 7000 to 8000 rpm, measure voltage and current values, derive motor characteristics.	3	40	MBW with flywheel, Tachometer, DMM & 2 PSU's.	TO101 - TO102
Mode 1.3	Spin up the assembly from 14400 to 15400 rpm, measure voltage and current values, derive motor characteristics.	3	40	MBW with flywheel, Tachometer, DMM & 2 PSU's.	TO101 - TO102
Mode 2	Spin up the assembly to 15400 rpm, measure voltage and current values , derive motor characteristics.	5+	10	MBW with flywheel, Tachometer, DMM & 2 PSU's.	TO201 - TO203
Axial launch vibrations	Test the assembly against the vibration envelope of the Falcon 9.	1	75	K2007E01 Smart Shaker, MBW with axial mount.	TO301, TO302
Lateral launch vibrations	Test the assembly against the vibration envelope of the Falcon 9.	1	75	K2007E01 Smart Shaker, MBW with lateral mount.	TO301, TO302
Internal vibrations motor	Spin up only the motor to 15400 rpm, measure vibrations from only the motor.	3	10	Seismic mass, laser vibrometer, 2 PSU's and the MBW without flywheel.	TO401
Internal vibrations assembly	Spin up the assembly to 15400 rpm, measure vibrations from the assembly.	3	10	Seismic mass, laser vibrometer, 2 PSU's and the MBW with flywheel.	TO402 - TO404
Vacuum testing	Repeat Mode 1 and 2 in the vacuum chamber.	3	120	Vacuum chamber, MBW with flywheel, Tachometer, DMM & 2 PSU's.	TO501 - TO505
Thermal-vacuum testing	Repeat Mode 1 and 2 in the vacuum chamber at varying temperatures in the given range.	3	200	Vacuum chamber, MBW with flywheel, Tachometer, DMM & 2 PSU's.	TO601 - TO605

7. Test and Research Outcome

This thesis has set research objectives, system and design requirements and test objectives. Below, an overview of the produced results of the tests from the previous chapter is made, after which checks have been done and displayed for the test objectives, design requirements and research objectives. From this, the research can be concluded and reflected upon in the next two chapters.

The tachometer accuracy, motor functionality, vibration and operational mode testing had the highest priority, but due to produced results in the motor functionality testing, time in the vibration and mode 1 testing was sacrificed to be able to perform vacuum tests. Namely, the motor drew more power than originally expected, and to test whether this was an effect of the atmospheric conditions on the vacuum lubricant, operational testing in vacuum conditions had to be done. With the time budget fully spent on the allocated tests, the thermal-vacuum testing could not be performed, which is why no testing station was provided in the last chapter. In comparison to the allocated tests, the thermal-vacuum testing was assumed to not yield as fruitful results.

7.1. Test Results

The testing of the prototype and its parts resulted in the following sets of data. The sets of data will be used to answer their respective test objectives, which in turn will check compliance to research objectives and design requirements. Unfortunately, the USB programmer adapter purchased from Faulhaber did not operate properly, and was declared dead after a meeting with Faulhaber. The velocity measurement through the USB programmer adapter was thus unavailable, which left the optical tachometer to measure the angular velocity of the MBW, which is testing in subsection 7.1.1. Additionally, the speed controller could not be reprogrammed to specialise the it for this specific load case, thus further work can be done once this part is reacquired. Re-ordering or returning this part was postponed to the next thesis due to the long lead times of these parts.

7.1.1. Tachometer Accuracy Results

The accuracy of the tachometer is detrimental to the test results. The optical tachometer has achieved the required accuracy of 0.1%, which can be seen in the graph and box plot in figures 7.1 and 7.2, which shows the difference between the two velocity signals. Additionally, measuring the Hall sensor signal through the oscilloscope showed a block wave, confirming that the Hall sensors do incorporate Schmitt triggers.

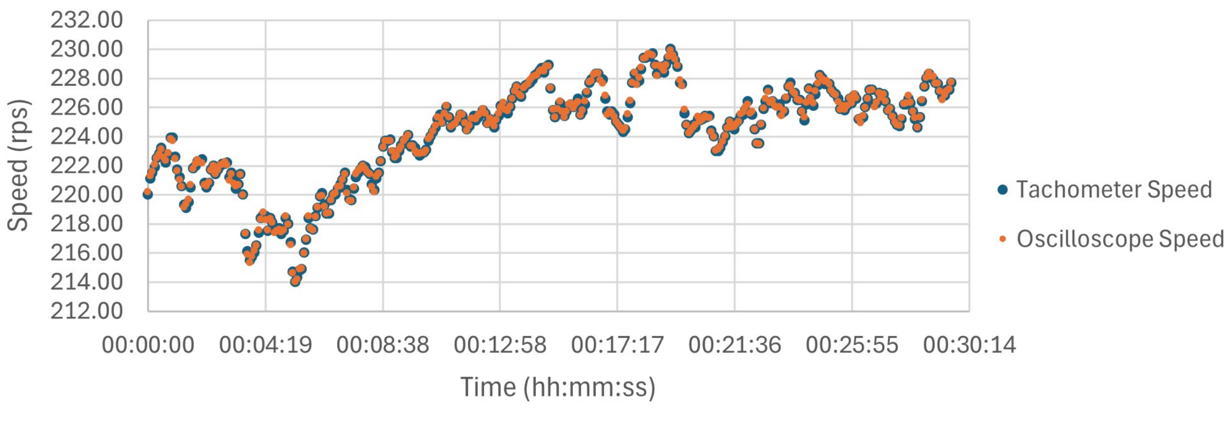

Figure 7.1: The velocity measured through the tachometer and the oscilloscope.

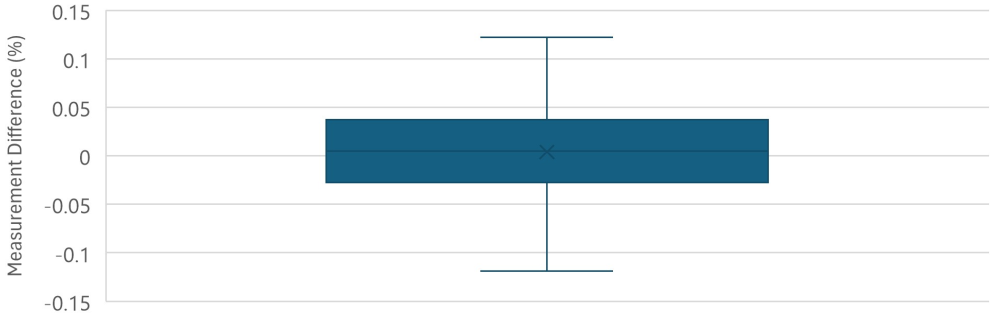

Figure 7.2: The difference in measured velocity from the tachometer and the oscilloscope ($\mu = 0.0042; \sigma = 0.049$).

Another observation that can be made is the fluctuating speed the MBW is maintaining, which could be problematic for the stability requirement.

Hypothesis for this behaviour can be the incorrect set inner working of the speed controller, possible motor manufacturing offsets or inconsistencies through temperature effects, or some other unseen effect. The inaccessibility of the gain functions of the PI controller within the Faulhaber SC1801P disables the customisation of it and the adaptation to the load case presented through the flywheel attached to the motor. It is theorised that through incorrect or suboptimal gain settings, which were factory set, the speed could fluctuate throughout testing. Manufacturing offset could induces a larger play within the axial, which could vary the required torque at the nominal velocity. A higher temperature could be caused by the friction of the vacuum lubricant and the inability to cool the motor. This higher temperature could then increase offsets between certain parts within the motor and decrease its efficiency, for which more power would be required to spin the motor at the required nominal angular velocity.

7.1.2. Motor Functionality Test Results

The motor functionality testing has yielded results and insights of the motors' performance and all the components' workings. The two motors acquired from Faulhaber have been tested for their performance. It has been found that one motor uses much more power as can be seen in figure 7.3 and is therefore also declared unfit. Together with the USB adapter, this motor shall be send back to Faulhaber for replacement. All further tests are thus done with motor number 1.

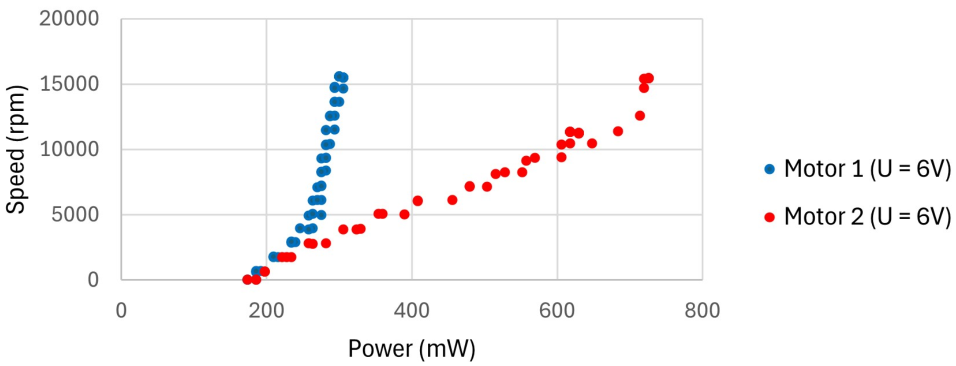

Figure 7.3: Motor 1 and 2 running on input voltage 6 V, up to the required speed.

Since the speed controller could not be programmed, the set point programming could not be altered, to ensure high accuracy of the motor. Furthermore, the 'start-up' behaviour as shown in figure 7.5 made sure that no constant speed would be attained. The accuracy testing of the angular velocity of the motor is therefore dropped until the speed control can be programmed for a low torque specification, to ensure a maximum speed.

Despite the inability to customise the speed controller via the USB programming adapter, the speed controller itself could be controlled through two separate but identical PSU's and yielded results as shown below in the graph in figure 7.4. As explained in section 5.1, the electronics and motor supply could be set constant, and the setpoint voltage could vary to change the velocity output to the motor. Therefore, the graph in figure 7.4 shows the speed output difference between three set voltages through one singular PSU for input power; 4, 6 and 8 V; with the setpoint voltage varied between 0 and 10 V through a second PSU.

Once wired, the speed controller would already draw power from this first PSU despite not turning the motor, this is probably due to the Hall sensors and position calculation going on within the speed controller. Upon increasing the voltage of the second PSU wired to the setpoint input, the speed controller would draw more current from the first PSU, which is displayed in the graph in figure 7.4.

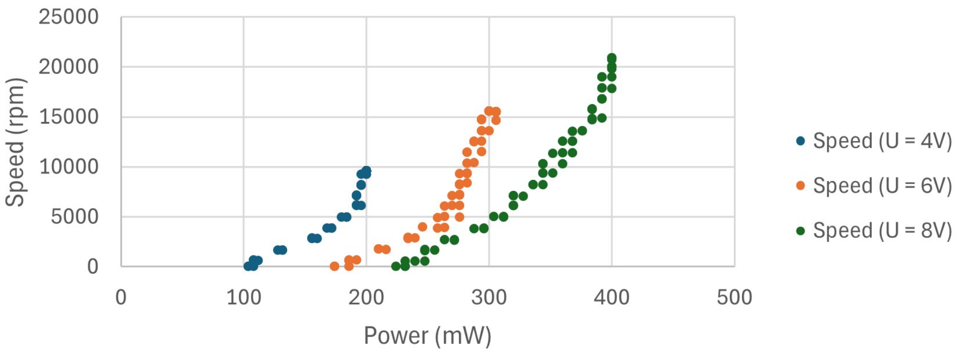

Figure 7.4: First series of measurements for input voltage between 4 to 8 V, and setpoint voltages from 0 to 10 V.

The initial motor functionality and power usage found that the power usage was higher than expected and could not fit both the power and speed requirement. Each input voltage has a maximum speed that it could reach. For 4 V, the maximum speed in this test is 10000 rpm. For 6 and 8 V, the maximum speed in this test is 15500 and 20800 rpm respectively.

The required speed of 15400 rpm would be attained most consistently for an input voltage of 6.0 V, at a current of 50 mA, resulting in a power draw of 300 mW, 66.67% over target. That the current draw is higher than the theorised power draw set in and calculated from chapters 2 and 4 respectively, is theorised to come from the low efficiency of the non-customised speed controller and the sub-optimal performance of vacuum lubricant in atmospheric conditions. Furthermore, it is visible that the power draw increases for the same speed at high input voltages. For an input voltage of 4 V, 10000 rpm is reached for 200 mW. For 6 and 8 V, 10000 rpm is reached for 270 and 325 mW respectively. Therefore it is concluded that the most power efficient manner of achieving the required nominal angular velocity in atmospheric conditions is at an input voltage of 6 V and a setpoint voltage of 10 V, resulting in a power draw of 300 mW.

Looking to the motor functionality when operating the motor continuously at the nominal required speed, the stability of the motor itself can be recorded and judged. Running the motor for at least 10 minutes attains the required angular velocity, but not the required stability; as can be seen in the graphs of figures 7.5 and 7.6. The graph in figure 7.6 is made from the data on display in figure 7.5, when calculating the difference in velocity between the two adjacent measurement points. The achieved stability can be calculated by adding the mean and three times the standard deviation, resulting in 0.2647%.

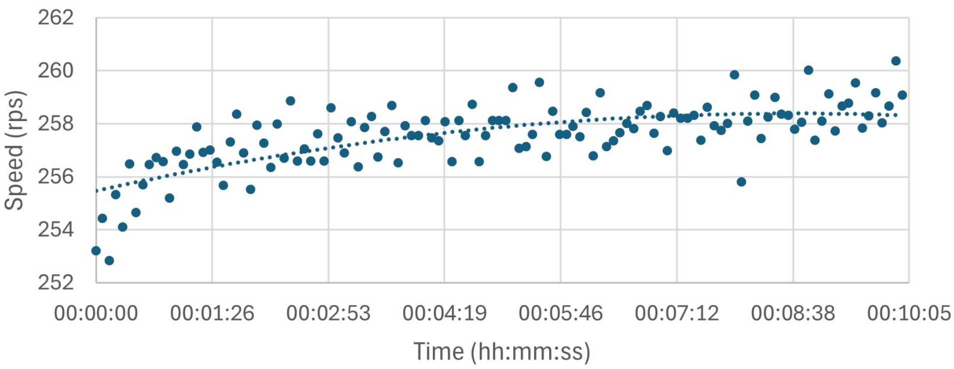

Figure 7.5: Running the motor for an extended period of time at an input voltage of 6 V.

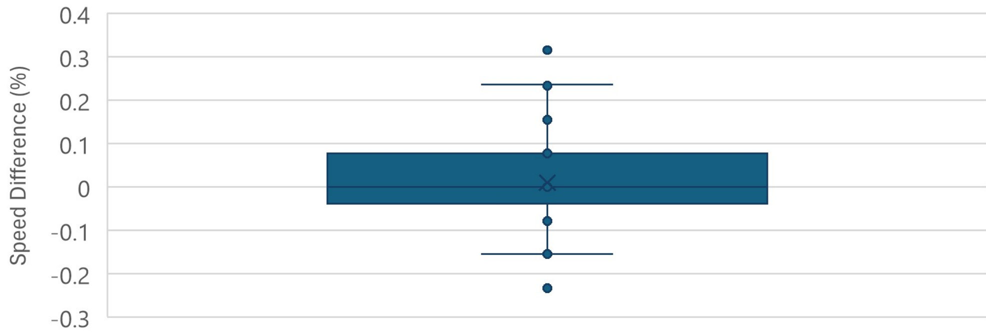

Figure 7.6: The difference between two measuring interval of the motor speed at an input voltage of 6 V, ($\mu = 0.0097; \sigma = 0.085$).

7.1.3. Speed Controller Functionality Test Results

Providing three PSU's meeting the requirements set in subsection 6.1.4 proved difficult, which meant that this test had to be postponed until after the shaker tests. Therefore, the velocity is lower than the MBW functionality testing. Furthermore, this meant that for all tests, only two PSU's could be utilised, of which one was connected to U_{mot} and U_p and the other connected to U_{nsoll}. Nevertheless, the functionality of the speed controller could be tested and yielded results conform to the assumption made in subsection 6.1.2, as the U_{nsoll} input has the highest sensitivity of motor output due to voltage input change. Therefore, the tests are carried out as set up in that subsection.

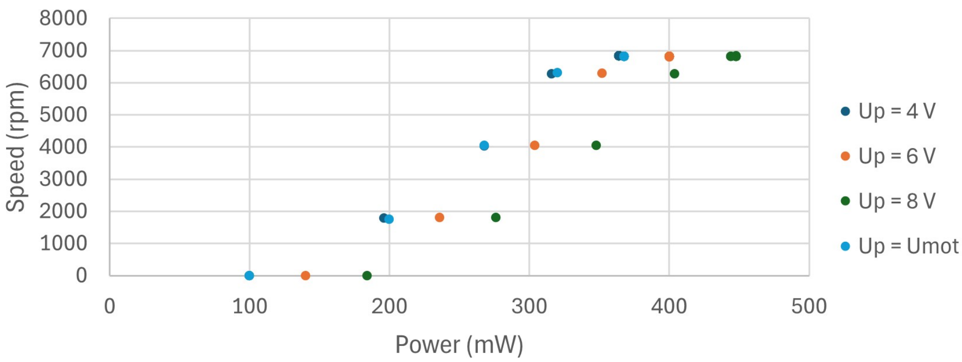

Figure 7.7: Velocity curve as a function of power for $U_mot = 4V$.

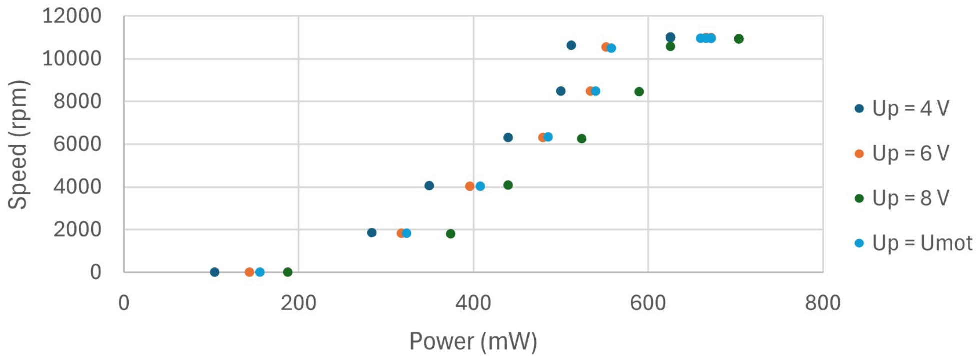

Figure 7.8: Velocity curve as a function of power for $U_mot = 6V$.

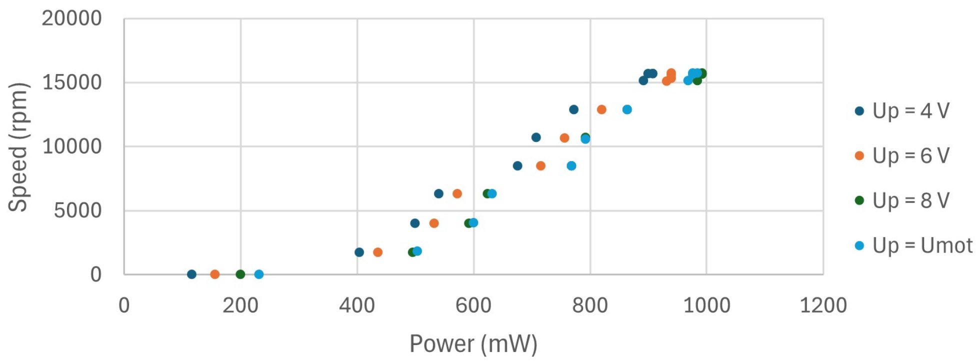

Figure 7.9: Velocity curve as a function of power for $U_mot = 8V$.

An observation of the consistency in current through the electronics power supply can be made as the current would stay the same, regardless of speed at a certain voltage over the electronics power supply. For all tested voltages; 4, 6 and 8 V, would the current stay at 22 mA, showing a clear decrease in power when supplying the speed controller with a lower voltage. The voltage supplied to the speed controller is changed and tested multiple times, showing no change in consistency in velocity and thus no change in accuracy of the Hall sensors. This would mean that at the required speed at U_{mot} =8V and U_p =4V, over 88 mW can be saved, when compared to when these voltage would be equal. The 22 mW per 1 V decrease for power usage of the electronics shows that, in combination with the power usage data of the motor functionality testing, the motor would be able to run the axle at 15400 rpm for 256 mW instead of 300 mW. This decrease is possible if the voltage over the electronics supply is changed from 6 to 4 V when three separate PSU's are used, for which the motor power draw would stay the same at 168 mW but the speed controller power draw would decrease from 132 to 88 mW. Now that the distinction can be made between what the motor and electronics power draw, the motor characteristics can be calculated for the different motor supply voltages by deducting the electronics power draw from the total power draw.

From the data collected of motor 1 and the the speed controller and using equation 4.3, to calculate the motor characteristics C_0, C_v, k_ω and k_T, arose two challenges. The calculated motor characteristics differ immensely for when the set point voltage is differed. Something that can be noticed is that when the motor is spinning at full speed (when the set point is at 10 V) for a given motor supply voltage, the values become more similar between the motor supply voltage and k_ω becomes more similar to the stated theoretical, with only a difference of -4.75%. This difference is assumed to come from the extra torque presented through the increased friction of a vacuum lubricant operating in atmospheric conditions. This will have to be confirmed by finding the experimental values of C_0 and C_v. The calculation of the values C_0, C_v and k_T has to be done by approaching the stated theoretical value of k_T by assuming values for C_0 and C_v. External torques through air friction or axle imbalance are neglected. The experimental values for atmospheric conditions at room temperature are thus shown in table 7.1.

Table 7.1: The motor functionality testing results.

	C_0 (mNm)	C_v (mNm/rpm)	k_ω (rpm/V)	k_T (Nm/A)
Theoretical value	0.019	$3.42 \cdot 10^{-6}$	2682	$3.56 \cdot 10^{-3}$
Experimental value	0.038	$6.84 \cdot 10^{-6}$	2555	$3.56 \cdot 10^{-3}$
Difference (%)	108.66	108.66	−4.651	0

These values represent a deficiency of the motor performance in atmospheric conditions and gave the final push on the decision to sacrifice time spent on the regular operational modes and vibrational testing to be able to perform a vacuum performance test through the proposed vacuum testing.

7.1.4. MBW Functionality Test Results

Before the operational modes can be set up and be tested, the new motor functionality had to be set, to check whether the required nominal angular velocity was still acquired at the same input voltage. This test came from the assumption that the flywheel induces torques through imbalances and impurities due to inaccuracies in the flywheel prototype specimen attached to the motor. Similar to the motor functionality testing of the previous subsection, a range of input voltages are tried to find at which the required speed is attained, with the setpoint voltage ranging from 0 to 10 V.

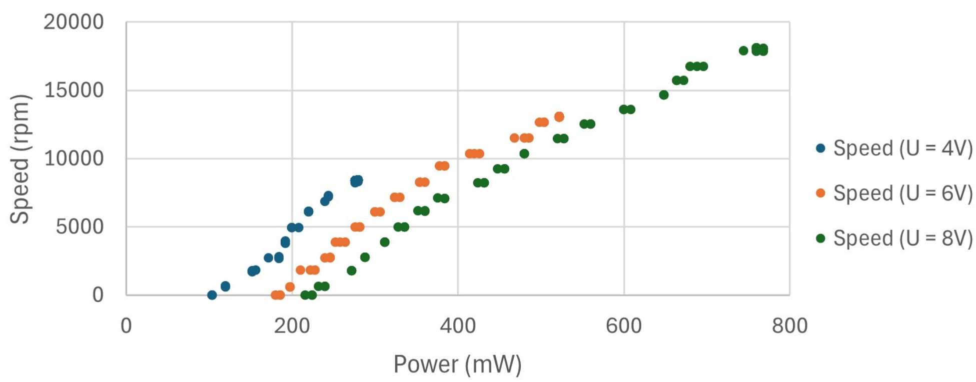

Figure 7.10: MBW speed measurements for input voltage between 4 to 8 V, and setpoint voltages from 0 to 10 V.

As assumed, the motor requires more power to turn the flywheel to its required velocity than with only the axle. This is due to the torque required through the inaccuracies in the flywheel. When combining the graphs in figures 7.4 and 7.10, a clear comparison can be made between the two scenarios, in figure 7.11.

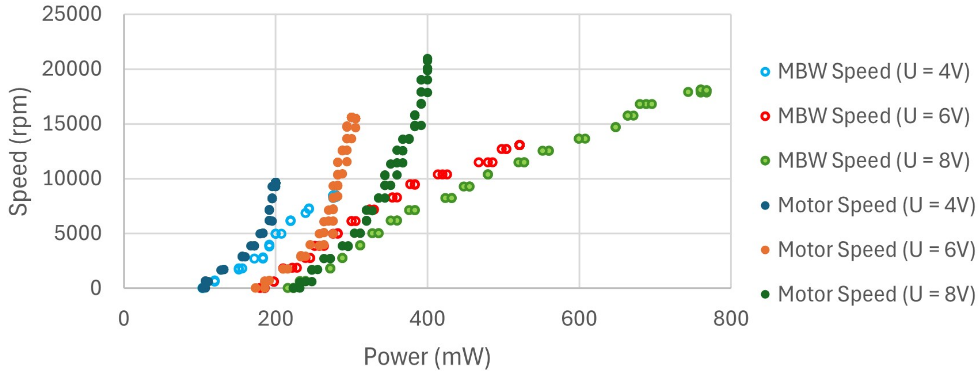

Figure 7.11: Motor and MBW speed measurements for input voltage between 4 to 8 V, and setpoint voltages from 0 to 10 V.

Further analysis was done between 6.0 and 8.0 V, to find out which input voltage would most efficiently spin the motor at its required velocity. This was found to be at 7.0 V, as is displayed in figure 7.12. The speed of 15400 rpm was most consistently and power efficiently achieved at a current draw of 86 mA, resulting in a power draw of 602 mW, 234% over target. The operational testing is therefore performed at 7.0 V.

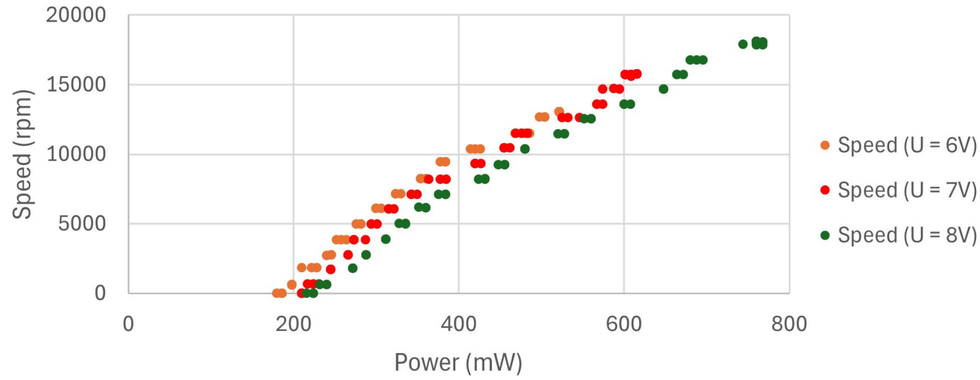

Figure 7.12: MBW speed measurements for input voltages 6, 7 and 8 V, and setpoint voltages from 0 to 10 V.

With the reduction in power draw to the lowering of the electronics supply voltage from the used 7 to 4 V, as done in subsection 7.1.3, the power draw can be reduced to 536 mW, as per the 22 mW per 1 V decrease save. This would result in the motor using 448 mW and the driver using 88 mW.

7.1.5. Operational Mode 1 Test Results

Due to the inability to program the motor through the USB programming adapter, and the sacrifice in testing required to make place for the vacuum testing, mode 1 testing has been reduced to very preliminary testing to show the motors responsiveness to small changes in voltage over the setpoint voltage. Quick tests could be done by varying the voltage by 0.1 V to a certain voltage at which the boundary in each interval was reached.

The three intervals as stated in table 6.1 are tested three times, resulting in nine measuring sessions. All values corresponding to each interval are included in each graph. The first interval is shown in the graph in figure 7.13 and shows a non-linear start to the spin up scenario. The power usage in this interval has increased with 200 mW in comparison to the theoretical values calculated in subsection 6.2.1.

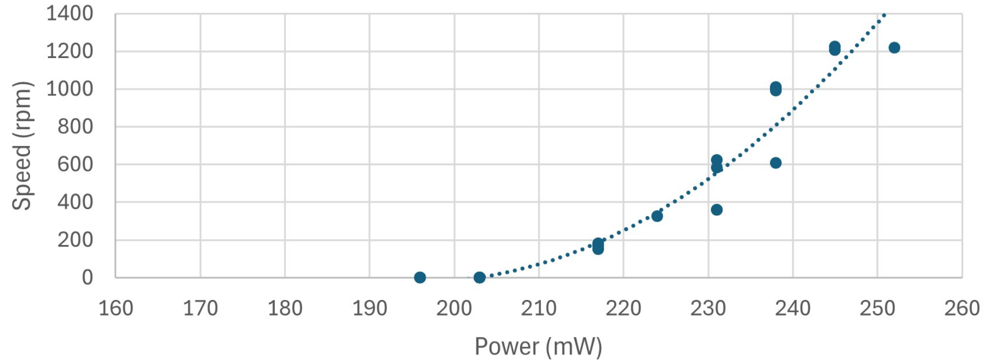

Figure 7.13: For an input voltage of 7 V, the speed interval of 0 - 1000 rpm is represented as a relation to power.

The middle part of the spin up phase is displayed in the graph in figure 7.14 and shows a linear progression of the speed in comparison to the power. The power usage of this interval has increased fourfold in comparison to the theoretical values calculated in subsection 6.2.1.

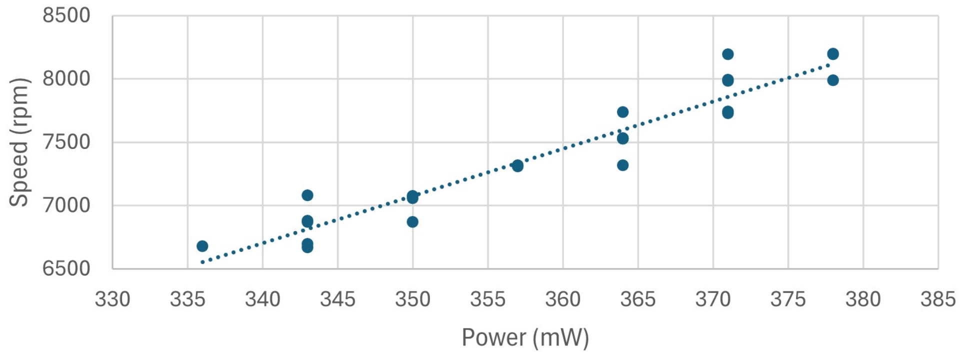

Figure 7.14: For an input voltage of 7 V, the speed interval of 7000 - 8000 rpm is represented as a relation to power.

The last part of the spin up phase is displayed in the graph in figure 7.15 and shows a linear progression of the speed in comparison to the power. The power usage of this interval has increased threefold in comparison to the theoretical values calculated in subsection 6.2.1.

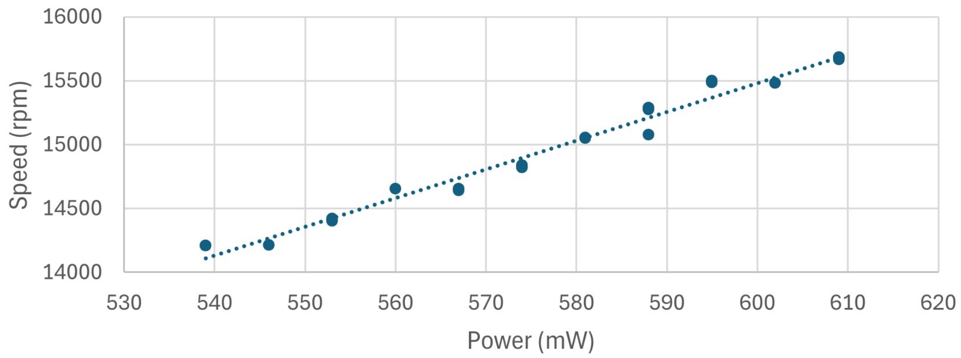

Figure 7.15: For an input voltage of 7 V, the speed interval of 14400 - 15400 rpm is represented as a relation to power.

A trend line is added to the graphs in figures 7.13 through 7.15, to envision the motor behaviour in each interval. The former interval displays a non-linear increase in speed over power, and the two latter intervals showing a linear increase in speed over power. Similar to the results found in subsection 7.1.2, the power has increased far beyond the original set power budget.

7.1.6. Operational Mode 2 Test Results

Mode 2 consisted of multiple long tests concerning the entire MBW system at the required speed. Intervals of 10 minutes were measured 10 times to increase the reproducibility of the test, out of which 3 intervals will be shown. All 10 scenarios showed the ability of the motor to attain and maintain operational velocity as required per the angular momentum requirement MBW12. In line with the graph from figure 7.15, the minimal power required for the required speed would be 602 mW, 234% over target. The three intervals shown in this subsection are hand picked in order to show the behaviour of the motor regarding to its speed and stability.

The three scenarios on display are mode 2.1, 2.2 and 2.3, which correspond to how much time has passed between the time that the PSU has been set to maximum as to attain the maximum velocity for a power supply voltage of $7\ V$. mode 2.1 shows the behaviour of the MBW when the PSU has just been set to its maximum, mode 2.2 and 2.3 show the behaviour of the MBW when the PSU has been set to its maximum for 30 and 60 minutes respectively.

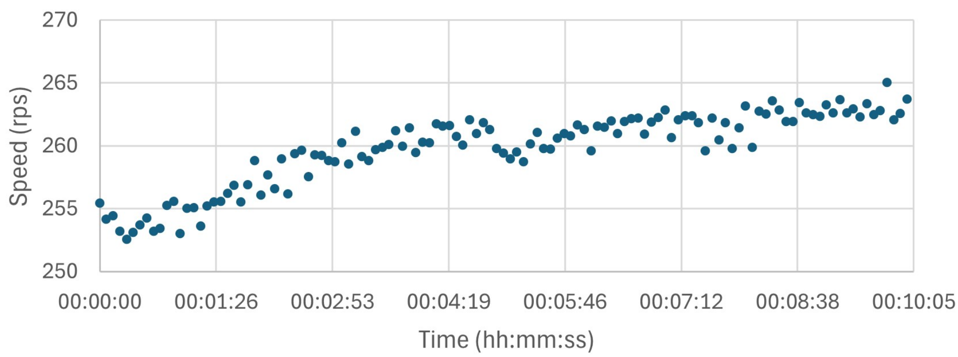

Figure 7.16: Mode 2.1; showing motor behaviour when the motor has just started spinning.

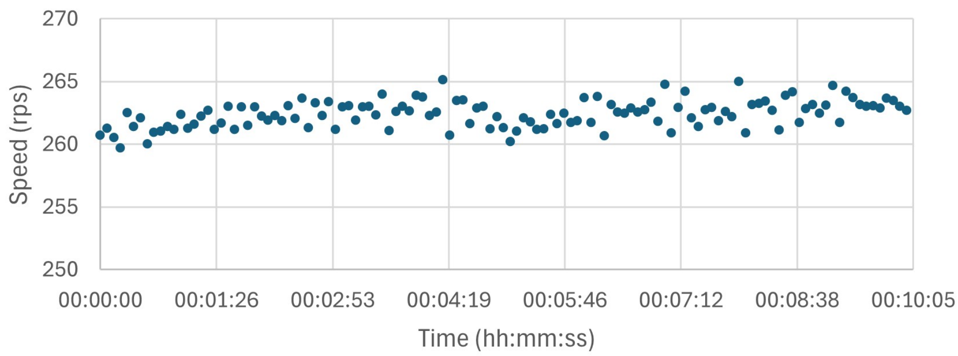

Figure 7.17: Mode 2.2; showing motor behaviour when the motor has been spinning for 30 minutes.

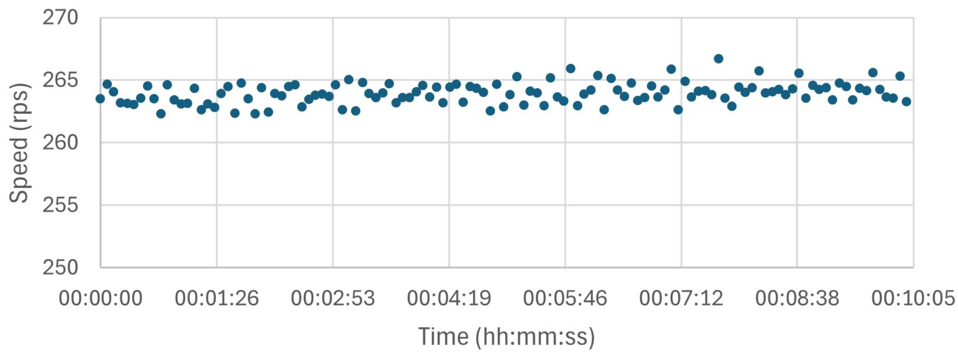

Figure 7.18: Mode 2.2; showing motor behaviour when the motor has been spinning for 60 minutes.

To visualise the stability of the velocity of the motor, a box plot can be made of the data presented in the previous graphs. The box plot in figure 7.19 shows that the deviation of the motor speed decreases over time.

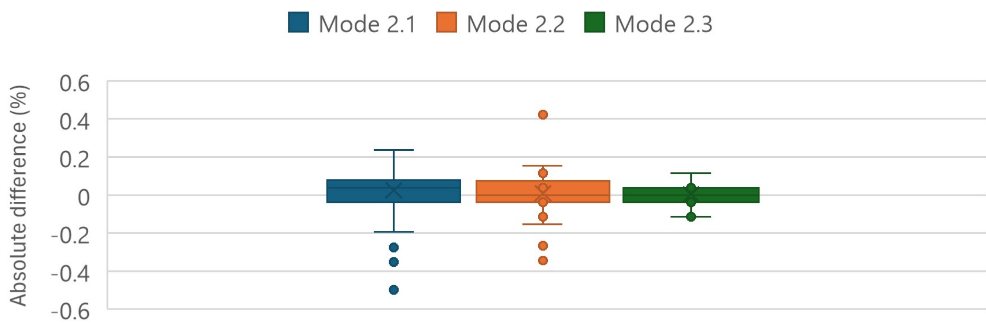

Figure 7.19: Box plot containing the speed difference between measured speed values, ($\mu_{2.1} = 0.024; \sigma_{2.1} = 0.11$, $\mu_{2.2} = 0.0086; \sigma_{2.2} = 0.062$, $\mu_{2.3} = 0.0024; \sigma_{2.3} = 0.042$).

The differences in speed and stability per scenario show that the speed attained is higher and more stable for mode 2.3. The data on show in figure 7.19 shows that the stability of the angular velocity of the motor is within required limits as of requirement MBW14. The latter measuring period shows that the deflection of the velocity would be maximally 0.1284%.

7.1.7. Self-induced Vibration Test Results

The vibrational testing of only the motor and the entirity of the MBW has yielded the following results, as presented in the graphs in figures 7.20 through 7.23. The measured frequency spectrum has been set under advice of the instructor Burhan Saify. These spectra would be able to pick up most interesting vibrating phenomena, such as the vibrations from turning the flywheel at speed, whether the MBW would resonate the seismic mass at its first structural mode, or that one of the manufactured parts would start vibrating.

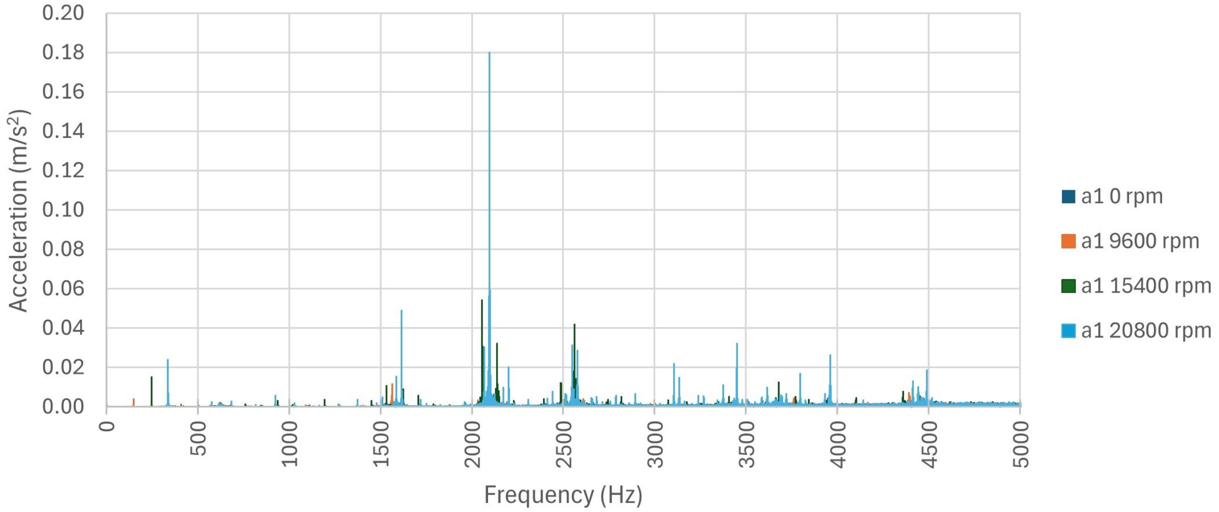

Figure 7.20: The acceleration in point 1 as depicted on figure 6.17 (+Y), induced by only the motor.

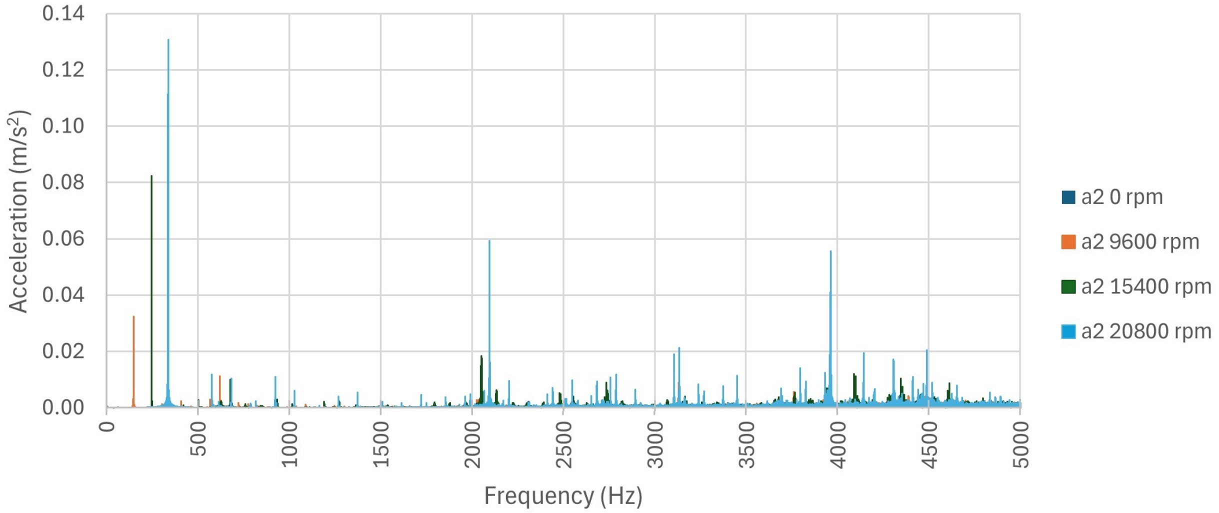

Figure 7.21: The acceleration in point 2 as depicted on figure 6.17 (+Y), induced by only the motor.

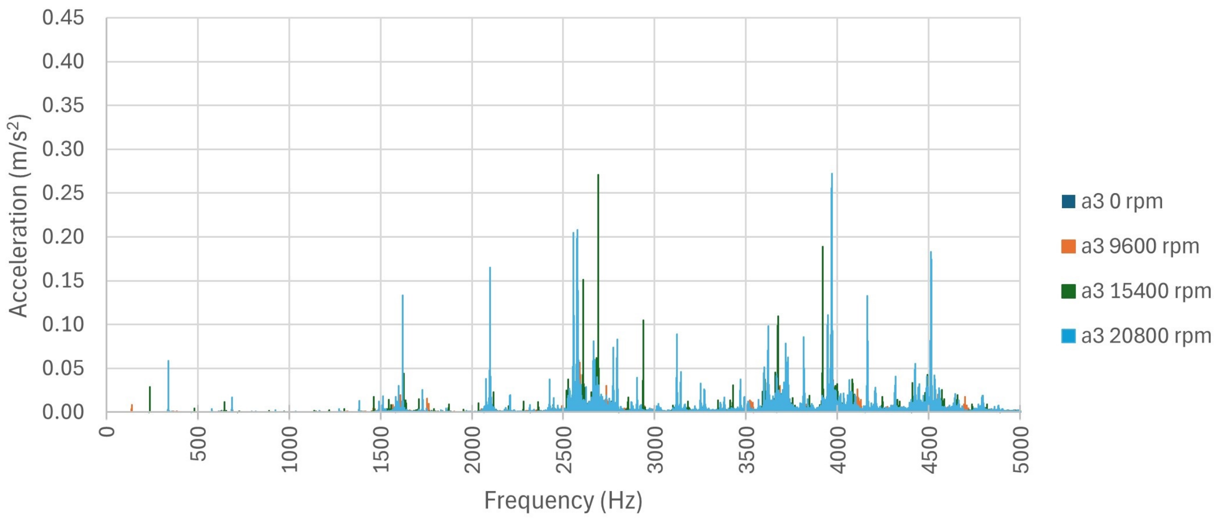

Figure 7.22: The acceleration in point 3 as depicted on figure 6.17 (+Z), induced by only the motor.

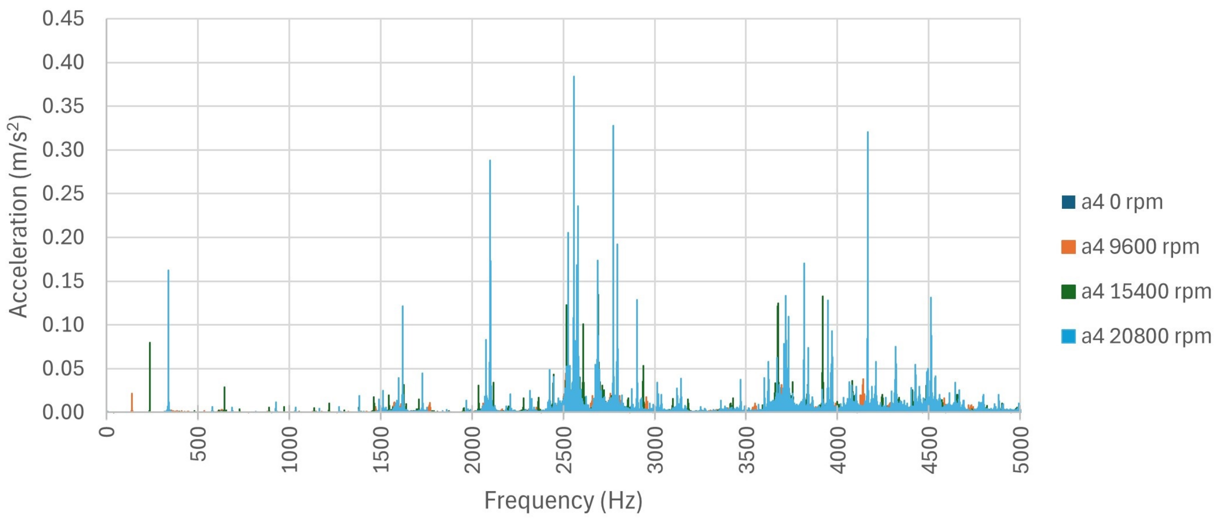

Figure 7.23: The acceleration in point 4 as depicted on figure 6.17 (+Z), induced by only the motor.

In all four points, the magnitude of the recorded noise it not visible so will not be filtered out. In all points in the spectra provided, peaks at 160.00, 256.67 and 346.67 Hz can be seen, which correspond to the velocity of the MBW, 9600, 15400 and 20800 rpm or 160.00, 256.67 and 346.67 rps. It is also clearly visible that the magnitude of the micro vibrations induced by only the motor at the frequency in correspondence to the rotational velocity are quite low in comparison to the other vibration modes in points 1, 3 and 4. In all points, a spike around 2100 Hz is visible, this is the first structural mode as stated in table 6.5.

Using equations 6.5 through 6.7, and the root mean squared (RMS) values of the frequency spectra as presented in figures 7.20 through 7.23, the forces and moments induced by only the motor can be calculated in put in table 7.2.

Table 7.2: The RMS values of acceleration at the four locations, with the forces calculated using equations 6.5 through 6.7, for only the motor.

Speed (rpm)	a_{1RMS} (mm/s^2)	a_{2RMS} (mm/s^2)	a_{3RMS} (mm/s^2)	a_{4RMS} (mm/s^2)	F_y (mN)	F_z (mN)	M_x (mNm)
0	0.483	0.469	0.507	0.529	1.586	0.863	-0.11
10000	0.677	0.716	3.498	3.257	2.319	5.622	-0.16
15500	1.357	1.334	6.224	6.403	4.479	10.51	-0.30
20800	3.285	2.431	12.47	12.52	9.513	20.79	-0.63

For the complete MBW system, the following graphs in figures 7.24 through 7.27 have been produced.

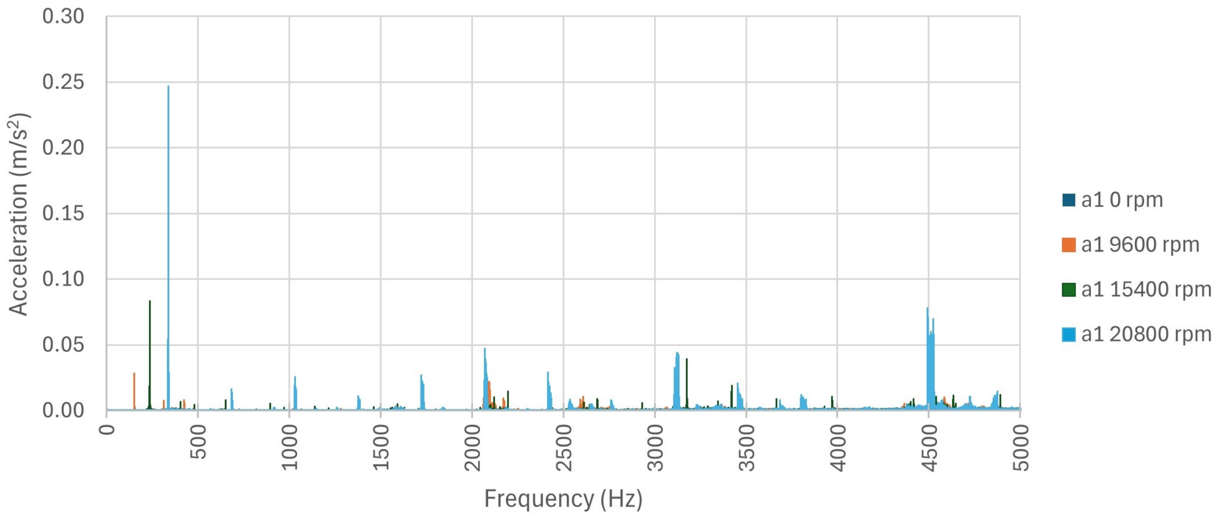

Figure 7.24: The acceleration in point 1 as depicted on figure 6.17 (+Y), induced by the complete MBW system.

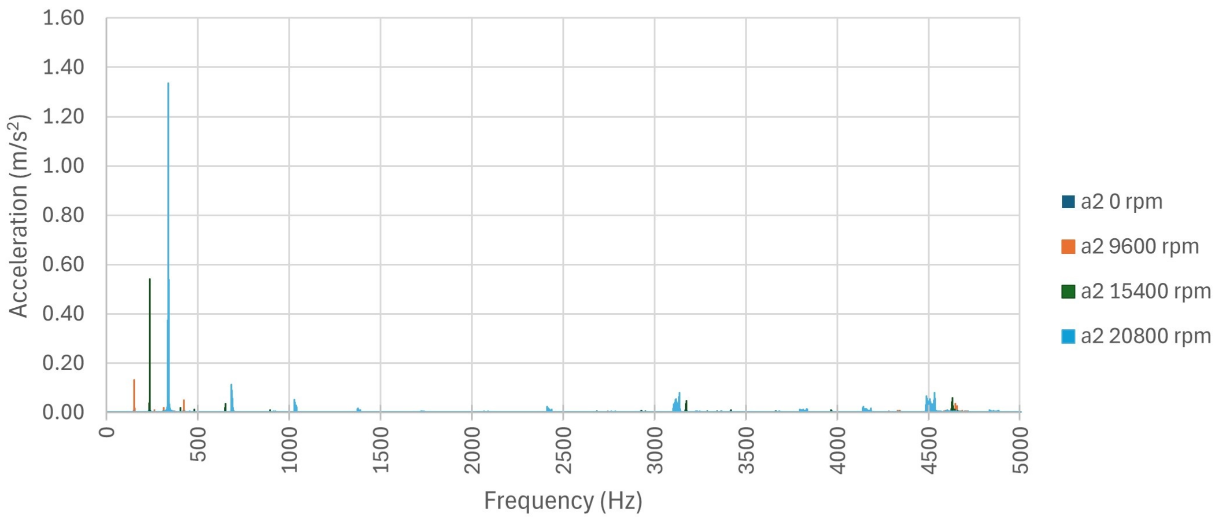

Figure 7.25: The acceleration in point 2 as depicted on figure 6.17 (+Y), induced by the complete MBW system.

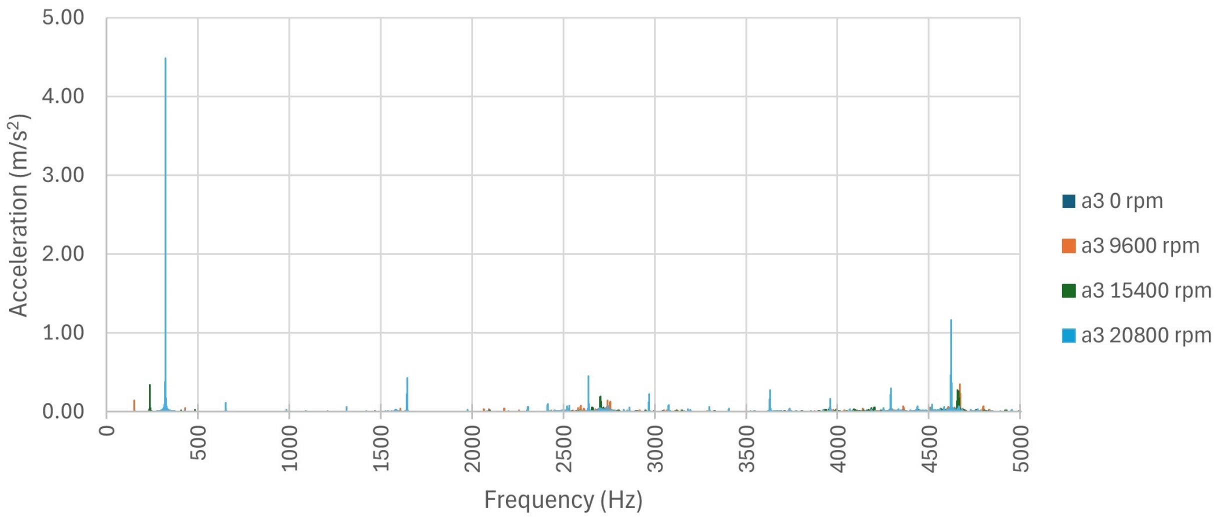

Figure 7.26: The acceleration in point 3 as depicted on figure 6.17 (+Z), induced by the complete MBW system.

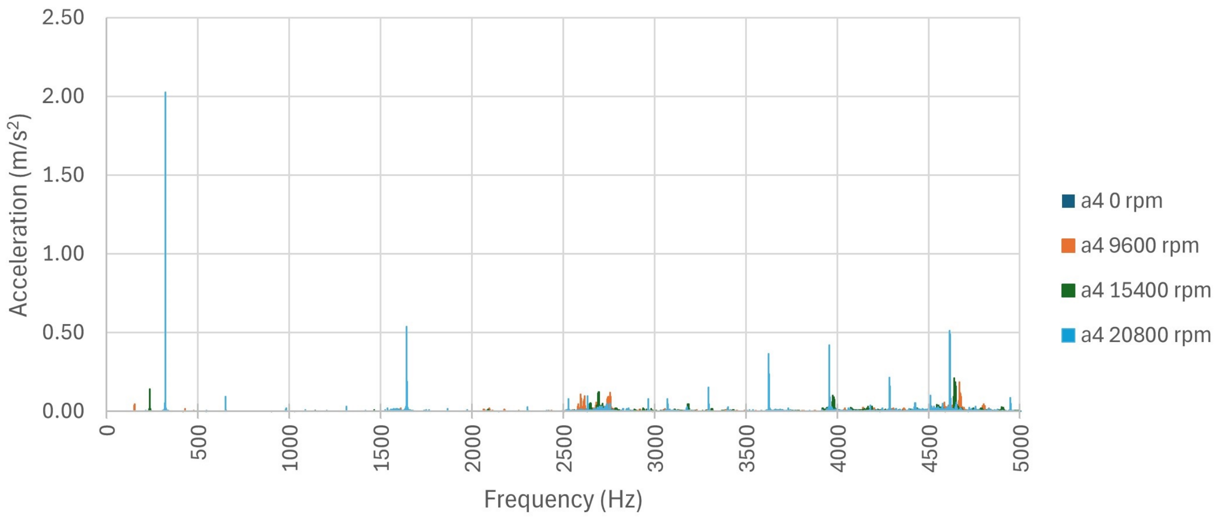

Figure 7.27: The acceleration in point 4 as depicted on figure 6.17 (+Z), induced by the complete MBW system.

Once again, the magnitude of the recorded noise it not visible in all four points, so will not be filtered out. It is however clearly visible that the magnitude of the micro vibrations induced by the complete system at the frequency in correspondence to the rotational velocity (160.00, 256.67 and 346.67 Hz) are much higher in comparison to the other vibration modes in all points. Even the first structural mode of the seismic mass at 1509 Hz is not clearly visible in all points. Furthermore, no other resonances are visible that are on similar acceleration levels as the MBW angular velocity induced vibration.

Using equations 6.5 through 6.7, and the root mean squared (RMS) values of the frequency spectra as presented in figures 7.24 through 7.27, the forces and moments induced by only the motor can be calculated in put in table 7.3.

Table 7.3: The RMS values of acceleration at the four locations, with the forces calculated using equations 6.5 through 6.7, for the complete MBW system.

Speed (rpm)	a_{1RMS} (mm/s^2)	a_{2RMS} (mm/s^2)	a_{3RMS} (mm/s^2)	a_{4RMS} (mm/s^2)	F_y (mN)	F_z (mN)	M_x (mNm)
0	0.507	0.464	0.703	0.469	1.616	0.875	-0.11
10000	1.252	2.143	10.43	8.252	5.652	15.55	-0.40
15500	1.425	5.367	13.49	10.09	11.31	19.62	-0.83
20800	6.163	22.68	48.61	24.16	48.02	60.56	-3.52

To show what part of the total disturbance from table 7.3 originate from the flywheel alone, the frequency spectra results can be subtracted from one another. The part of the disturbance forces as generated by only the flywheel have been calculated and shown in table 7.4, and the percentage these disturbances take up of the total disturbance are shown in table 7.5.

Table 7.4: The RMS values of acceleration at the four locations, with the forces for only the flywheel.

Speed (rpm)	a_{1RMS} (mm/s^2)	a_{2RMS} (mm/s^2)	a_{3RMS} (mm/s^2)	a_{4RMS} (mm/s^2)	F_y (mN)	F_z (mN)	M_x (mNm)
0	0.024	-0.005	0.196	-0.006	0.030	0.113	-0.015
10000	0.575	1.427	6.936	4.995	3.333	9.929	-0.24
15500	0.068	4.033	7.266	3.682	6.827	9.112	-0.53
20800	2.878	20.25	36.15	11.64	38.51	39.77	-2.89

Table 7.5: The percentage of acceleration at the four locations, with the forces for only the flywheel, compared to the total disturbances.

Speed (rpm)	a_{1RMS} (%)	a_{2RMS} (%)	a_{3RMS} (%)	a_{4RMS} (%)	F_y (%)	F_z (%)	M_x (%)
0	4.685	-1.268	27.83	-12.81	1.842	11.57	1.396
10000	45.96	66.57	66.47	60.53	58.97	63.85	60.34
15500	4.790	75.14	53.86	36.51	60.38	46.44	63.59
20800	46.70	89.29	74.36	48.18	80.19	65.67	82.16

Once testing was done, the MBW was disassembled to investigate any possible damages to the parts. None were found. These result shall be used in further analysis to confirm requirements SYS04 and SYS05 in subsection 7.2.3.

7.1.8. Vacuum Test Results

The tests in the vacuum chamber as described in section 6.5 have yielded the following results and observations. After the first motor functionality test was performed in the vacuum chamber at atmospheric pressure, the transition to vacuum yielded the first interesting observation. The speed of the motor increased and power usage of the system decreased when lowering the pressure, down to approximately 25 $mbar$. This behaviour is consistent across the three tests done.

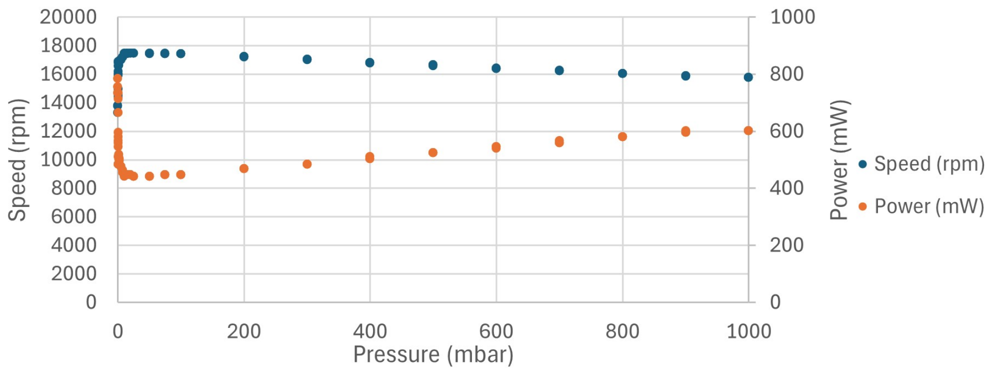

Figure 7.28: The performance of the MBW in pressures range from 0.2 to 1000 $mbar$, in the vacuum chamber.

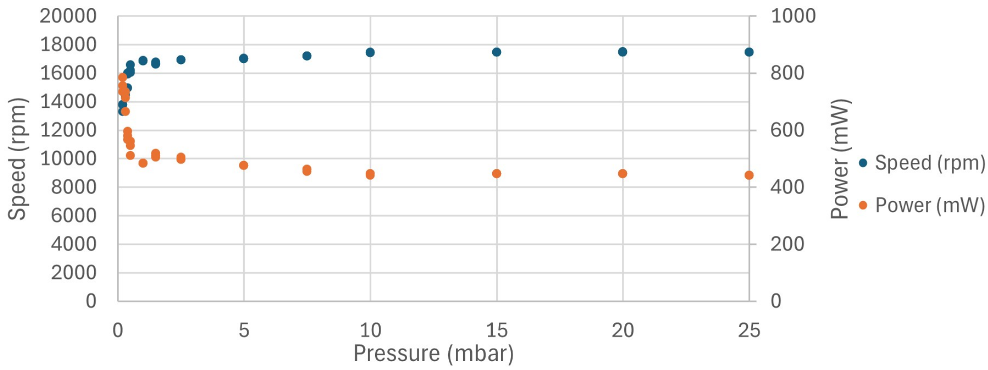

Figure 7.29: The performance of the MBW in pressures range from 0.2 to 25 $mbar$, in the vacuum chamber.

Three phenomena come to mind that can cause this behaviour: high temperature in the motor, high temperature in the speed controller or high torque due to increased friction.

High temperature in the motor causes parts to change shape, lengthen or shorten, which can cause extra distance between stator and rotor, having to use extra current to create the magnetic force needed to overcome the frictional torque. With little air available to transfer heat out of the motor through convection and with the plastic motor mount acting as insulation to further hinder this convection, the temperature of the motor can more easily rise than in atmospheric conditions.

A temperature rise in the speed controller could be picked up by two over-temperature protocols within the speed controller. Referring back to figure 5.1, the speed controller incorporates an over temperature protocol within the PWM signal generator and an I^2t protocol over the feedback line, measuring the current coming through and limiting that current when it becomes too high. This behaviour could be explained by a changing limiter on the total amount of current passing through the speed controller.

A high current draw can be related to a high torque, which is concurrent with high friction. As air friction is at negligible levels at this point, the increased friction can be assumed to come from an internal source, such as the vacuum rated lubricant or possible gunk, debris or damages within the motor. The gunk or debris could have come from the atmospheric operation or press fitting the flywheel through the epoxy used, leaking into the motor bearings. The debris does however not support the theory, as the results are consistent over multiple tests for similar pressures.

Unfortunately, these three theories can not be tested, as no temperature data is available for the motor or speed controller and no specification of the vacuum lubricant was provided from Faulhaber.

Using the data gathered from the vacuum tests and the motor characteristics in subsection 7.1.2, new friction values can be calculated for the vacuum situation. Assuming external torque levels induced by imbalances in the flywheel to be equal to the atmospheric case, the friction characteristics within the vacuum environment can be calculated.

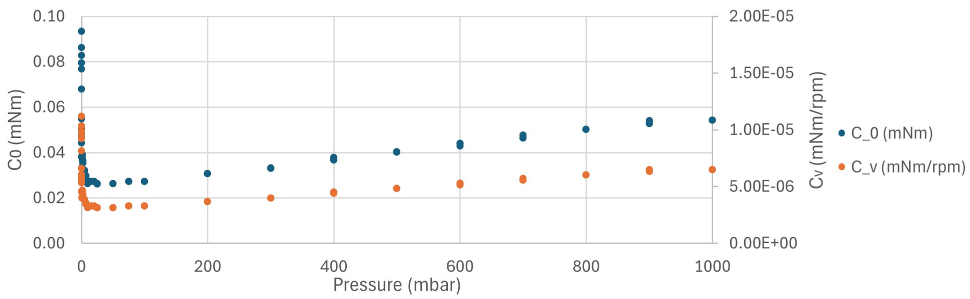

Figure 7.30: Motor friction characteristics C_0 and C_v varying over pressure.

Furthermore, it was noticed during testing that for pressures below 10 $mbar$, the speed and power draw of the motor became very inconsistent and swayed constantly, not attaining a constant speed for more than a few seconds. This behaviour became more extreme as 0 $mbar$ was approached. Such a high and highly changing torque was not assumed safe for the motor as it could induce extra torque on the vacuum exposed 3D printed mounts and possible overheat the motor. Therefore, to obtain safe, accurate and optimal readings, further vacuum testing is done at 25 $mbar$, where the speed is constant and at its maximum for the minimum amount of power. This is based on the assumption that in the future, the exact cause for the behaviour below 25 $mbar$ can be found and mitigate. If this can be mitigated, the results as 25 $mbar$ are assumed to approximate the results below 0.1 $mbar$. The power ratio between 1000 and 25 $mbar$ shall therefore be used as first assumption of the power decrease when the motor would be in high vacuum.

Calculating the power ratio between atmospheric and vacuum conditions is dependent on the difference between the power usage and speed delivered for any set supply voltage. To straightforwardly calculate the power ratio, the speed difference must be approached to zero. Therefore, while in vacuum conditions (25 $mbar$ in the vacuum chamber), the supply voltage was lowered to a voltage where the nominal velocity would be equal to the velocity at atmospheric conditions for a supply voltage of 7 V. At 6.6 V, the speed was equalled, for a current draw of 64 mA.

$$\frac{P_{vac}}{P_{atm}} = \frac{6.6 \cdot (64 - 22)}{7.0 \cdot (86 - 22)} = 0.62 \tag{7.1}$$

As the supply voltage has changed, so has the power draw for the speed controller, which will be excluded from this power ratio. Applying this power ratio to the power draw theorised in the speed controller functionality testing when the speed controller draw is already most efficient, results in a power draw of 192 mW. This can be calculated through the speed controller power draw staying constant at 88 mW, while the motor power draw at 168 mW reduces to 104 mW due to the power ratio. This would mean that if the flywheel would be perfectly balanced and does not require extra torque to be spun, the power draw of the motor would only be 192 mW, 6.7% over target.

Moving on to the mode 1 replication for before, during and after the vacuum tests, the performance of the motor for these three scenarios is displayed in the graph in figure 7.31. All tests are done with $U_p = U_{mmot} = 7\ V$ and U_{nsoll} ranging from 0 to 10 V. It is clearly visible that the motor performs better at slower speeds in vacuum than in atmospheric pressures. At higher speeds, the difference is marginal. The required speed of 15400 rpm is attained in vacuum at approximately 610 mW, slightly lower than the found 630 to 650 mW required to spin up the motor to its required operational velocity within the vacuum chamber at atmospheric pressure.

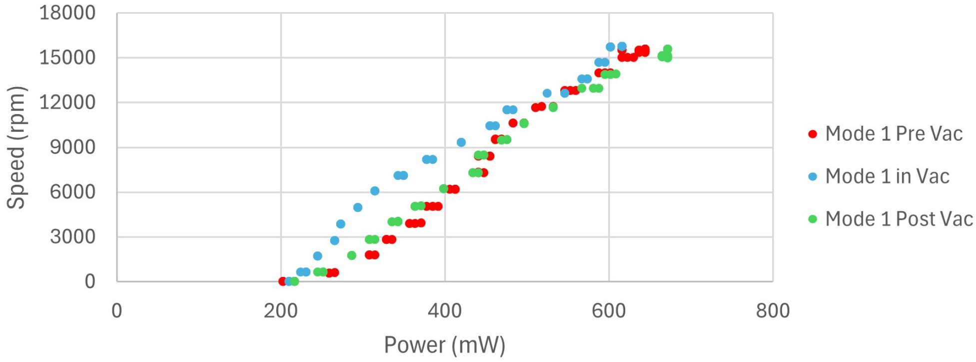

Figure 7.31: The performance of the MBW in mode 1 before, during and after the vacuum testing, in the vacuum chamber.

Conclusively, the replication of mode 2 was done for the input voltage for which the required velocity is attainable in atmospheric conditions; 7 V. Due to the earlier observation of the irregularity in the speed and power draw of the motor, the power draw was also graphed, to visualise the behaviour of the motor. The power draw in the graphs below has a resolution of 7 mW, due to the power supply voltage of 7 V and the resolution of the DMM of 1 mA. The velocity, power draw and power to velocity comparison graphs per scenario are supplied in figures 7.32 through 7.46 showing the performance before, during and after the vacuum tests. Before the MBW undergoes the vacuum environment, a datum scenario is set up,

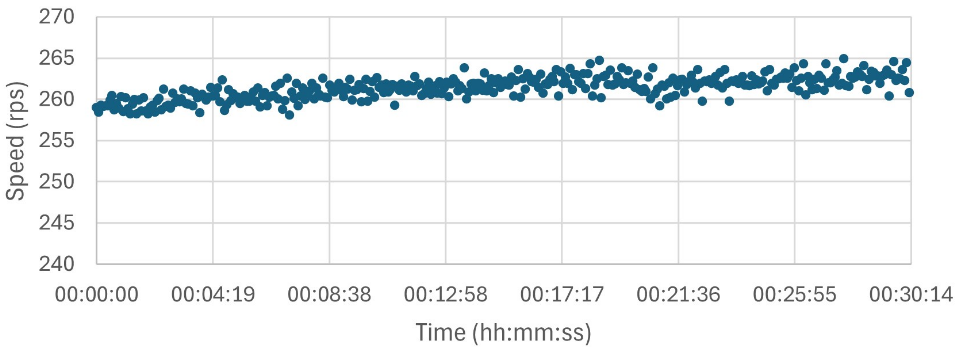

Figure 7.32: The performance of the MBW in mode 2 before the vacuum testing, in the vacuum chamber.

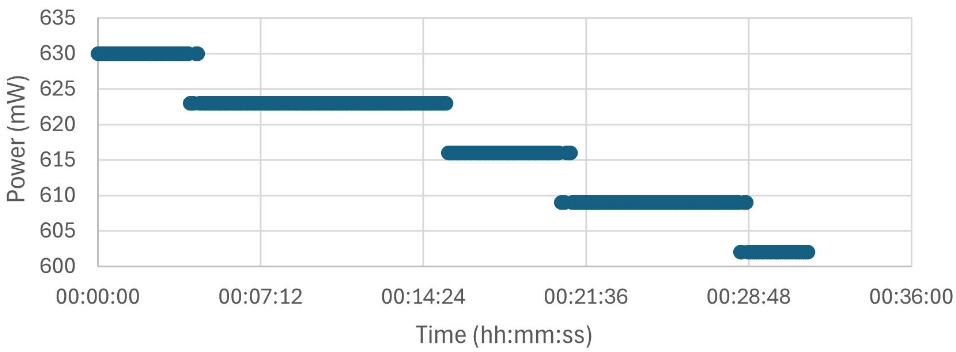

Figure 7.33: The power draw of the MBW in mode 2 before the vacuum testing, in the vacuum chamber.

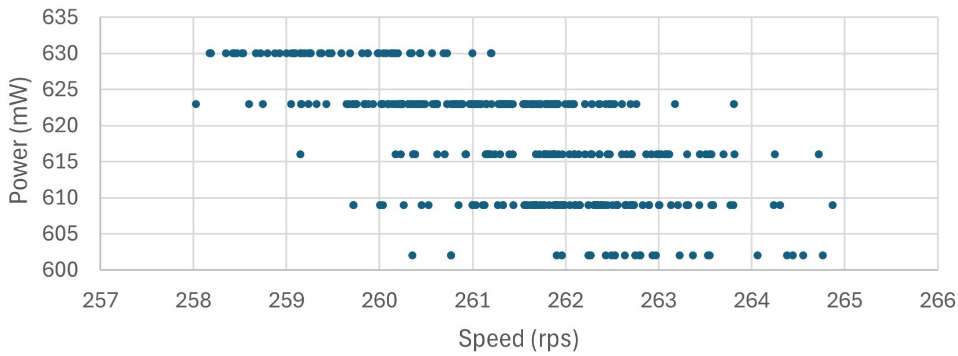

Figure 7.34: The relation between motor speed and power draw of the MBW in mode 2 before the vacuum testing, in the vacuum chamber.

In comparison to the before done mode 2 testing, the power draw has increased slightly, which will be taken into account, when determining the final power draw of the motor. Without further ado, the transition and mode 1 testing can be done to end up at the first run at mode 2 testing within the vacuum chamber at the aforementioned 25 $mbar$. The results of the first mode 2 run in the vacuum chamber are shown in graphs in figures 7.35 through 7.37.

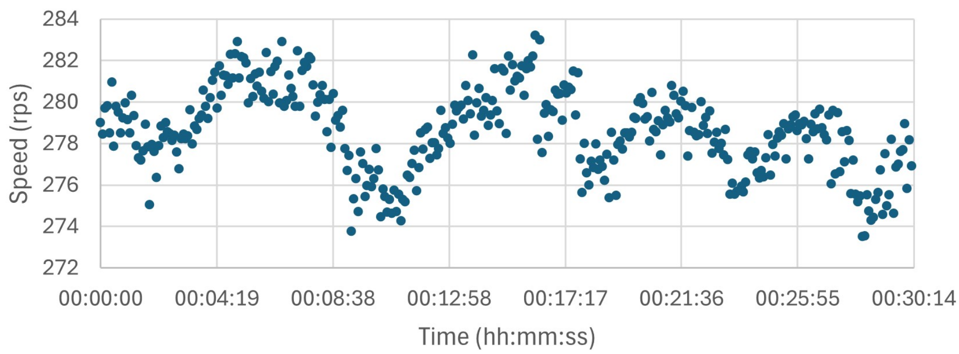

Figure 7.35: The performance during the first run of the MBW in mode 2 in vacuum at 25 $mbar$, in the vacuum chamber.

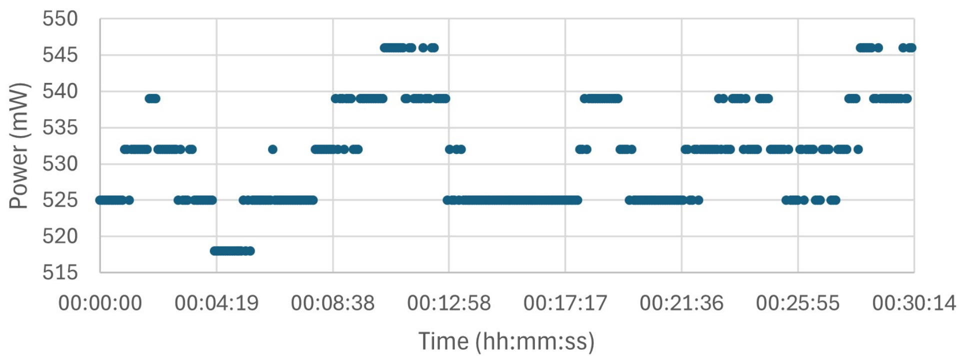

Figure 7.36: The power draw during the first run of the MBW in mode 2 in vacuum at 25 $mbar$, in the vacuum chamber.

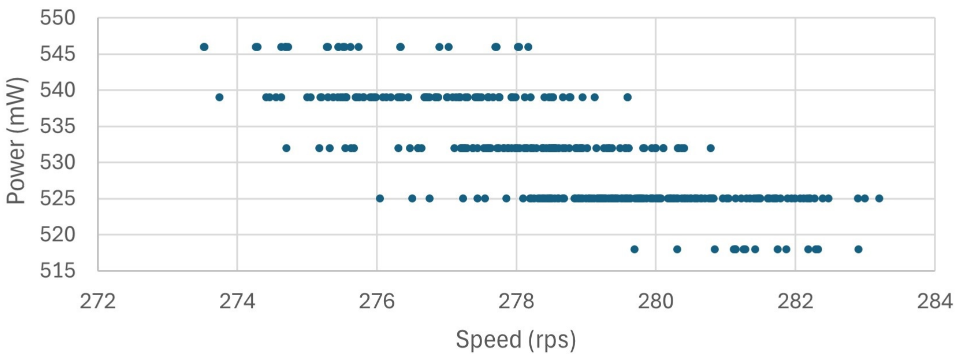

Figure 7.37: The relation between motor speed and power draw during the first run of the MBW in mode 2 in vacuum at 25 $mbar$, in the vacuum chamber.

Noticeably, the power required and velocity delivered decreased and increased respectively for the same input voltage and setpoint voltage. Due to the inconsistency in motor speed occurring during the first test within the vacuum chamber at 25 $mbar$, visible in the graphs in figures 7.35 and 7.36 more testing time was allocated to the mode 2 testing in vacuum.

With the time tested tripled, further degradation in the motor performance was visible. The speed levels after changing the MBW system between vacuum and atmospheric are lower in comparison, which can be seen in velocity graphs in figure 7.35, 7.38 and 7.41. The power draw in the following two scenarios has also increased, as can be seen in graphs in figure 7.36, 7.39 and 7.42.

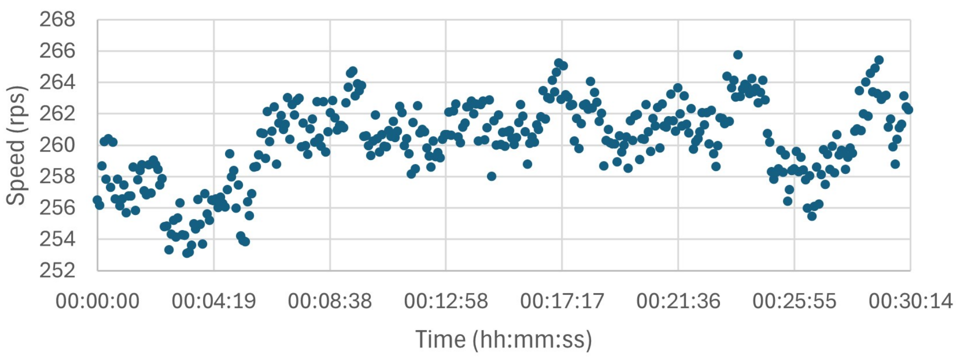

Figure 7.38: The performance during the second run of the MBW in mode 2 in vacuum at 25 $mbar$, in the vacuum chamber.

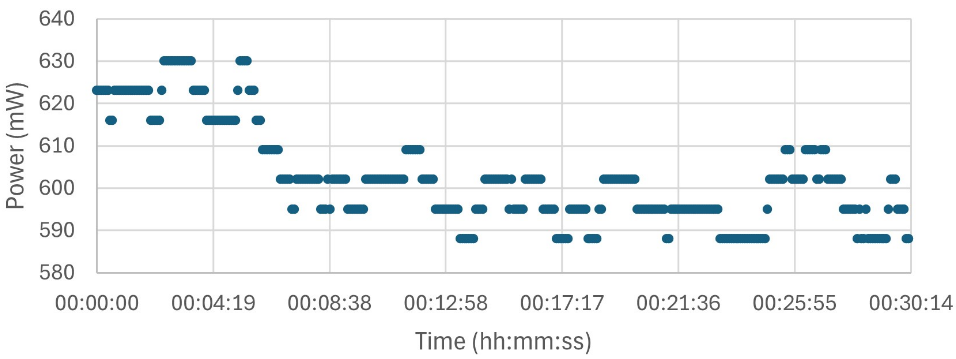

Figure 7.39: The power draw during the second run of the MBW in mode 2 in vacuum at 25 $mbar$, in the vacuum chamber.

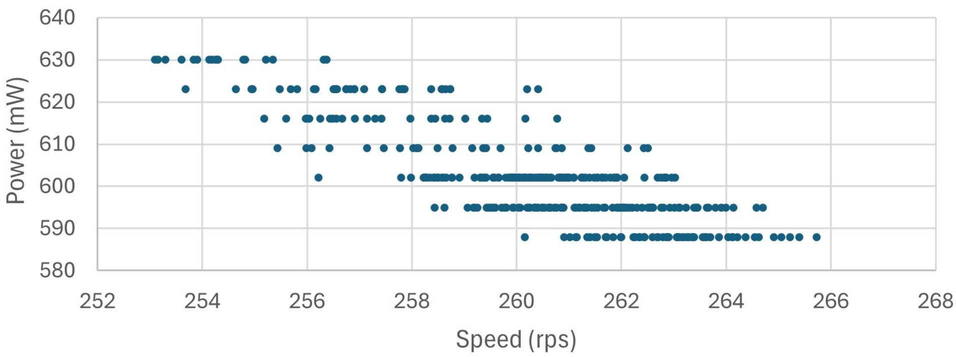

Figure 7.40: The relation between motor speed and power draw during the second run of the MBW in mode 2 in vacuum at 25 $mbar$, in the vacuum chamber.

The final vacuum scenario shows an even more fluctuating speed and power curve in comparison to the first two, which gives way to the question whether this motor does have the right vacuum lubricant. During the vacuum testing, no outgassing phenomena were observed, and inspection between vacuum sets revealed no shortcomings in the motor, motor mount or epoxy adhesive used to mount the flywheel.

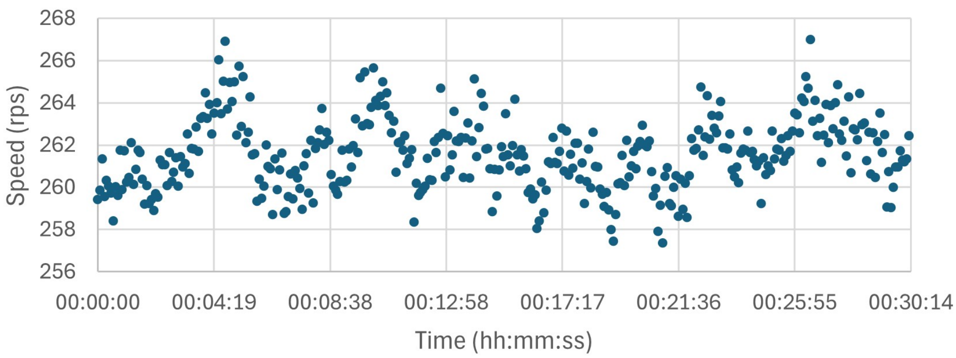

Figure 7.41: The performance during the third run of the MBW in mode 2 in vacuum at 25 $mbar$, in the vacuum chamber.

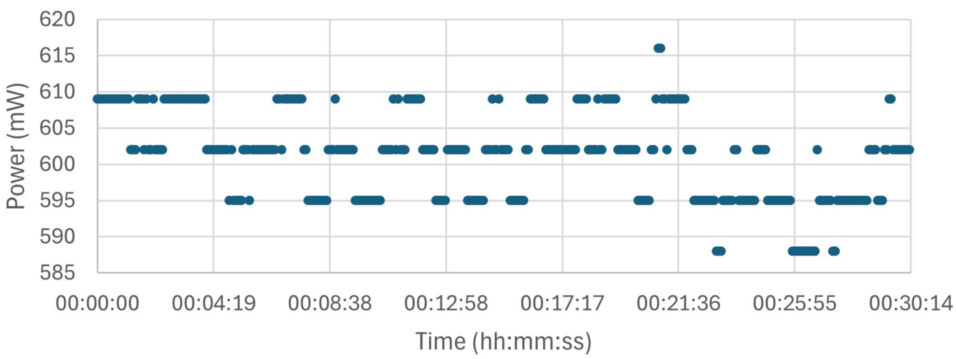

Figure 7.42: The power draw during the third run of the MBW in mode 2 in vacuum at 25 $mbar$, in the vacuum chamber.

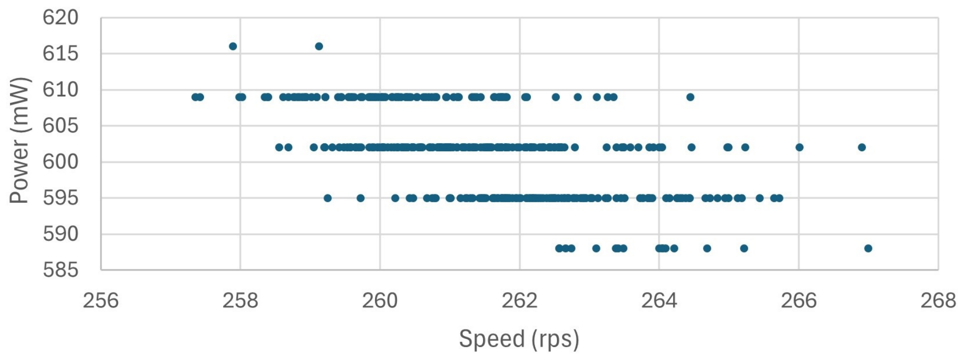

Figure 7.43: The relation between motor speed and power draw during the third run of the MBW in mode 2 in vacuum at 25 $mbar$, in the vacuum chamber.

Finally, the result of the last mode 2 testing to complete the vacuum chamber testing is stated below in graphs in figures 7.44 through 7.46. In comparison to the performance to before the vacuum testing, the motor has supplied less speed for more power.

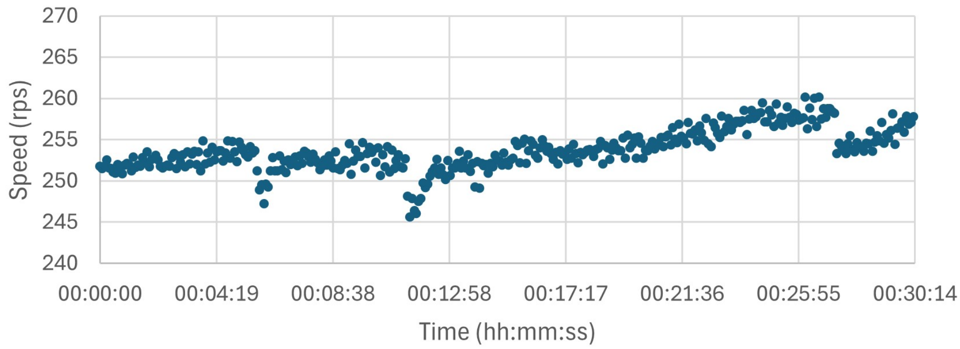

Figure 7.44: The performance of the MBW in mode 2 after the vacuum testing, in the vacuum chamber.

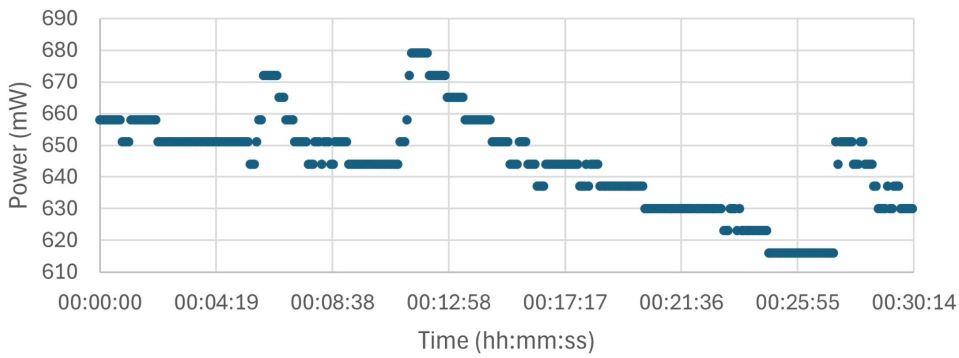

Figure 7.45: The power draw of the MBW in mode 2 after the vacuum testing, in the vacuum chamber.

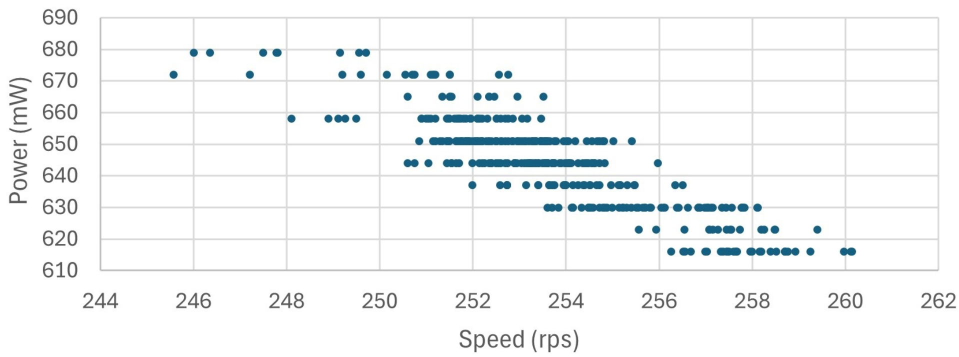

Figure 7.46: The relation between motor speed and power draw of the MBW in mode 2 after the vacuum testing, in the vacuum chamber.

To sum up and compare all scenarios, the velocity offsets of and difference between the MBW system before, during and after the vacuum tests are presented in the graphs in figures 7.47 and 7.48.

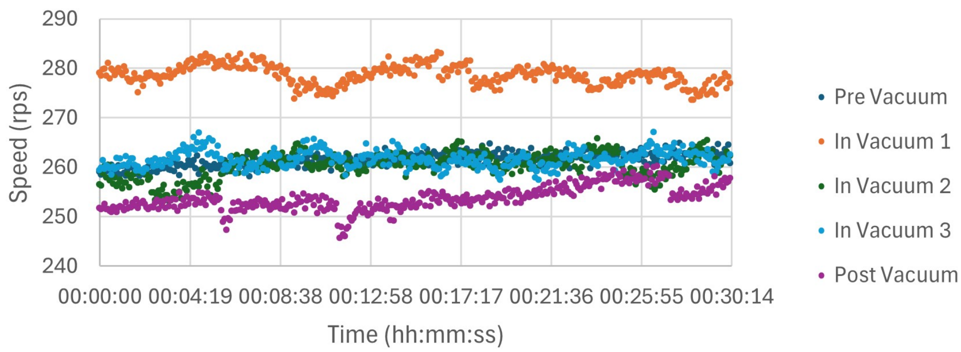

Figure 7.47: The velocity offset of the MBW before, during and after the vacuum testing.

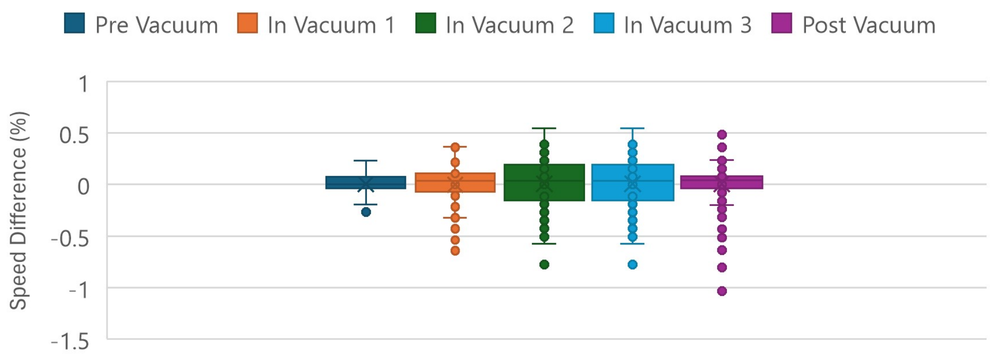

Figure 7.48: The velocity offset of the MBW before, during and after the vacuum testing, ($\mu_{prevac} = 0.039; \sigma_{prevac} = 0.082$, $\mu_{vac.1} = -0.0023; \sigma_{vac.1} = 0.15$, $\mu_{vac.2} = 0.0069; \sigma_{vac.2} = 0.23$, $\mu_{vac.3} = 0.0035; \sigma_{vac.3} = 0.19$, $\mu_{postvac} = 0.064; \sigma_{postvac} = 0.16$).

The offsets on display in the graph in figure 7.48 show that the stability requirement MBW14 can not be achieved in vacuum, as the first vacuum test run shows the smallest offset; -0.4523%. Additionally, after the vacuum tests, the motor showed signs of damage or some other alteration, as the stability went down significantly in comparison to the pre vacuum test, and the attained speed at a

7.1.9. Launch Vibration Test Results

Having done all tests, the shaker test could be done to find out the performance of the MBW after launch. The shaker setup was calibrated for both load cases, for which the corrected amplitudes are put in table 7.6.

Table 7.6: Axial and lateral vibration envelope as induced by the Falcon 9 rocket launch.

Frequency (Hz)	5	20	35	75	85	100
Acceleration (g)	0.5	0.8	0.8	0.8	0.9	0.9
Force (N)	0.29	0.47	0.47	0.47	0.53	0.53
Velocity (m/s)	0.16	0.062	0.036	0.017	0.017	0.014
Displacement (mm)	5.0	0.50	0.16	0.035	0.031	0.022
Old Amplitude (V)	0.264	0.065	0.025	0.012	0.013	0.011
Axial Amplitude (V)	0.284	0.068	0.031	0.017	0.021	0.021
Lateral Amplitude (V)	0.290	0.068	0.031	0.017	0.021	0.020

Observations regarding the performance of the motor before and after the shaker test are limited to the average decrease in speed and average increase in power for the same input voltage. Graphs corresponding to the two operational modes, before and after the shaker tests, are shown in figures 7.49 and 7.50.

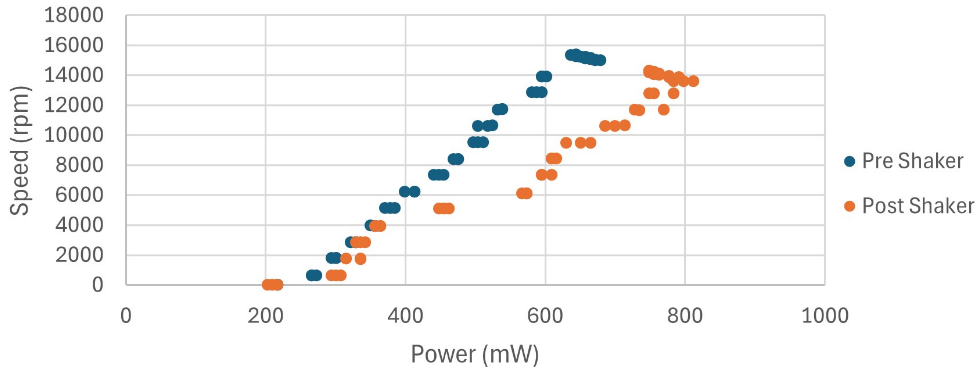

Figure 7.49: The performance of the MBW before and after the shaker test in mode 1.

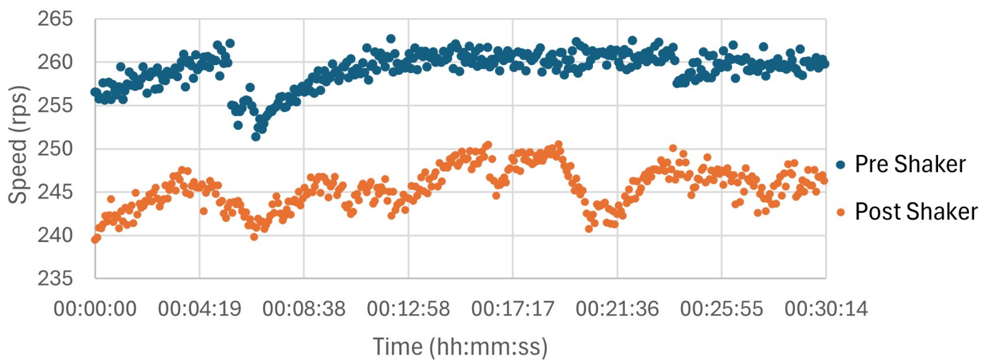

Figure 7.50: The performance of the MBW before and after the shaker test in mode 2.

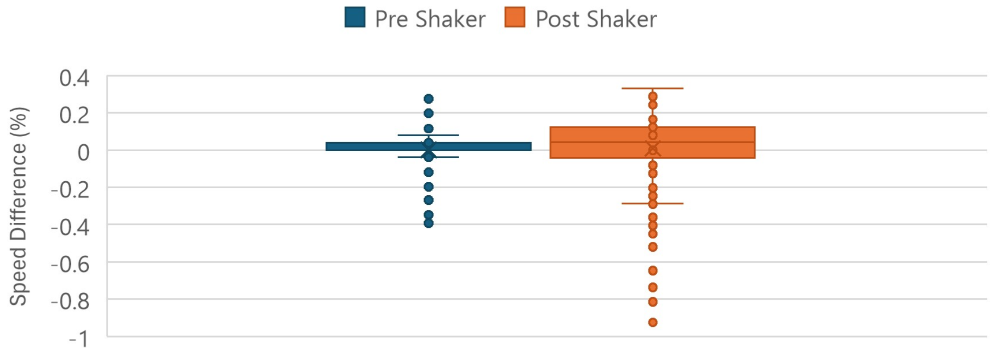

Figure 7.51: The stability of the MBW before and after the shaker test in mode 2 ($\mu_{preshaker} = 0.0041; \sigma_{preshaker} = 0.080, \mu_{postshaker} = 0.0091; \sigma_{postshaker} = 0.19$).

The velocity power curve has worsened dramatically in comparison to the performance of the motor pre shaker. Also, it can be heard and seen that the motor has sustained damage. The motor is slightly louder when spinning at its nominal operational velocity, probably due to the higher torque. The flywheel can be seen to wobble more than before the shaker test, and is tilted slightly in comparison to the level the flywheel was set to through the press fitting module in figure 5.8. Furthermore, the stability has decreased to 0.5791%.

7.2. Research Results

The key to a successful research is a check for all questions and objectives stated from the literature study to the test phase. Before the research question is answered, an overview and check of the set up requirements, for the tests, system and design shall be made in subsections 7.2.1, 7.2.2 and 7.2.3 respectively. Additionally, any analysis required regarding to an interpretation of results as presented in the previous section and the prototype results from chapter 5, or any comparison done to other attitude actuators using these retrieved values will be done here. Once the analyses are done, the thesis can be concluded in chapter 8.

7.2.1. Test Objectives Check

The test objectives have been answered through the results as posted in section 7.1. A simple binary check for achieving the test objective is summarised in table 7.7 below and a simple result for each test if the answer can be quantified. All results regarding the test objectives are retrieved from their respective results subsection between subsections 7.1.1 and 7.1.9. Any analysis requirement using these result shall be done in the following subsections, as well as checking all requirements.

Table 7.7: All test objectives for the PQ MBW prototype.

Test	Obj.	Description	Y/N	Result
Motor functionality test	TO001	Determine motor speed capability.	Yes	> 20000 rpm
	TO002	Determine motor power draw.	Yes	300 mW at 15400 rpm
	TO003	Determine motor friction characteristics C_0 and C_v.	Yes	0.038 mNm, 6.84·10^{-6} mNm/rpm
	TO004	Determine motor characteristics k_ω and k_T.	Yes	2555 rpm/V, 3.56·10^{-3} Nm/A
	TO005	Determine motor consistency between the two motors.	Yes	Not consistent
	TO006	Determine the stability of the angular velocity.	Yes	0.2647%
	TO007	Determine the accuracy of the angular velocity.	No	-
	TO008	Determine the accuracy of the internal Hall sensors.	No	-
Operational testing mode 1	TO101	Determine MBW torque characteristics over the complete range of velocity.	No	-
	TO102	Determine MBW power draw for the complete range of velocity.	Yes	Over target
Operational testing mode 2	TO201	Determine MBW speed capability.	Yes	> 20000 rpm
	TO202	Determine MBW power draw at nominal velocity.	Yes	602 mW at 15400 rpm
	TO203	Determine stability of the MBW angular velocity.	Yes	0.1284 %
Launch vibration testing	TO301	Determine MBW launch vibration survivability.	Yes	Not survived
	TO302	Evaluate points of the assembly with varying resilience against launch vibrations.	Yes	-
Self-induced vibration testing	TO401	Evaluate the vibrations of only the motor.	Yes	-
	TO402	Evaluate the vibrations of the flywheel.	Yes	-
	TO403	Determine MBW micro vibration survivability.	Yes	Survived
	TO404	Evaluate points of the assembly with varying resilience against micro vibrations.	Yes	-
Vacuum testing	TO501	Determine MBW speed capability in vacuum conditions.	Yes	> 20000 rpm
	TO502	Determine MBW torque characteristics over the complete range of velocity in vacuum conditions.	No	-
	TO503	Determine MBW power draw for the complete range of velocity in vacuum conditions.	Yes	Over target
	TO504	Determine stability of the MBW angular velocity in vacuum conditions.	Yes	0.4519%
	T0505	Determine motor friction characteristics C_0 and C_v for vacuum conditions.	Yes	0.023 mNm, 4.26·10^{-6} mNm/rpm
Thermal-Vacuum testing	TO601	Determine MBW speed capability in vacuum conditions for temperatures between -20 and +50°C.	No	-
	TO602	Determine MBW torque characteristics over the complete range of velocity in vacuum conditions for temperatures between -20 and +50°C.	No	-
	TO603	Determine MBW power draw for the complete range of velocity in vacuum conditions for temperatures between -20 and +50°C.	No	-
	TO604	Determine stability of the MBW angular velocity in vacuum conditions for temperatures between -20 and +50°C.	No	-
	T0605	Determine motor friction characteristics C_0 and C_v for vacuum conditions for temperatures between -20 and +50°C.	No	-

7.2.2. System Requirement Check

The system and MBW requirements check is to show in which areas the MBW design is to be iterated or tested, such that these missing requirements are achieved. The discussion and analysis done in this subsection shall be summarised in table 8.2 in chapter 8.

SYS01 and SYS03 are achieved through the motor functionality and operational mode testing, showing the ability to store angular momentum around its rotational axis and the ability to sustain this angular momentum over an extended period of time without any signs of short term deterioration.

SYS02 requires additional tests, such as the launch acceleration test, UV exposure testing and thermal-vacuum testing to fully confirm the systems' survivability. SYS06, SYS07 and SYS08 are achieved through the design steps taken, from which the design requirement at momentum bias wheel level have been made and will be checked in table 8.3. SYS04 and SYS05 require an analysis of a combination of results of the operational modes, the micro-vibration testing and stability testing.

The operational modes fully confirm that, for the disturbances torques estimated in section 2.2 and simulated in chapter 3, the MBW is able to keep the PocketQube satellite within the 1 deg of pointing accuracy, as the MBW is able to deliver the required angular momentum of 6.054 $mNms$, as required per calculations in chapter 2. However, for the micro-vibration induced forces on the satellite and the stability of the MBW inducing torques on the spacecraft require extra analysis through mechanical calculations to find out whether the spacecraft does stay within this required pointing accuracy.

The micro-vibrations are based on forces induced on a certain frequency that originate from the rotation of the flywheel and resonating parts or section of parts. The accelerations of the seismic mass induced by the forces and torques due to rotation of the MBW system can be utilised to calculate the maximum deviation due to these micro-vibrations. As the nature of these disturbance is purely cyclic, the cycle time must be determined, to be able to calculate the maximum deviation during this cycle time. The maximum angular velocity achieved during flight will be the required 15400 rpm or 256.67 rps angular velocity as set to attain the required angular momentum. This translates into a frequency of 256.67 Hz and a period of 3.8901 ms.

This means that the maximum acceleration as shown in figures 7.24 through 7.27 belonging to this frequency shall be utilised in this estimation, to show that this deflection is insignificant in comparison to the deviation due to accumulation of external environmental disturbance torques. Using dynamic functions to model the displacements due to the maximum force F_y torque M_x, calculated through equation 6.5 and the maximum accelerations for a_1 and a_2 from figure 7.24 and 7.25 (0.0803 and 0.540 m/s^2), results in equation 7.4 showing insignificant deflections in comparison to the set requirement of 1 to 5 deg.

$$\alpha = \frac{M_{x,max}}{I_{PQ}} \cdot sin\left(\frac{2\pi}{T}t\right) \qquad a = \frac{F_{y,max}}{m_{PQ}} \cdot sin\left(\frac{2\pi}{T}t\right) \tag{7.2}$$

$$\theta = \frac{M_{x,max}}{I_{PQ}} \cdot -\left(\frac{T}{2\pi}\right)^2 \cdot sin\left(\frac{2\pi}{T}t\right) \qquad x = \frac{F_{y,max}}{m_{PQ}} \cdot -\left(\frac{T}{2\pi}\right)^2 \cdot sin\left(\frac{2\pi}{T}t\right) \tag{7.3}$$

$$\theta_{max} = \frac{M_{x,max}}{I_{PQ}} \cdot -\left(\frac{T}{2\pi}\right)^2 = 0.00108\ deg \qquad x_{max} = \frac{F_{y,max}}{m_{PQ}} \cdot -\left(\frac{T}{2\pi}\right)^2 = 0.530\ \mu m \tag{7.4}$$

Finally, the effect of the tested stability must be interpreted as angular deviation in the rotational axis of the MBW. As the rotational velocity increases or decreases over a period of time, the difference in angular momentum difference is acted onto the spacecraft body, transferring the angular momentum to the spacecraft and must thus also be within the pointing accuracy requirement. Through the conservation of angular momentum, the relation between the angular momentum of the flywheel at nominal speed and the spacecraft at rest can be determined. The spacecraft is assumed to be at rest at the end of mode 1 and the begin of mode 2. With equations 2.21 through 2.26, which was used to set the stability requirement of 0.180%, the pointing accuracy achieved through this prototype can be completed. Since a stability of 0.1284% was achieved over a measuring period of 5 seconds with the current prototype, the maximum deflection would be 3.98 deg. When using these formulae for the achieved stability for the vacuum and post shaker tests of -0.4523 and 0.5719%, the deviation would result in -14.0 and 17.7 deg.

$$\mathbf{h} = h_{MBW} + h_{PQ} = I_{MBW} \cdot \omega_{MBW} + I_{PQ} \cdot \omega_{PQ} = h_{req} \tag{7.5}$$

$$\frac{\Delta \mathbf{h}}{\Delta t} = \mathbf{T} = T_{MBQ} + T_{PQ} = 0 \tag{7.6}$$

$$\Delta h_{MBW} = T_{MBW} \cdot \Delta t \tag{7.7}$$

$$\theta_a = \frac{1}{2}\alpha \cdot (\Delta t)^2 \tag{7.8}$$

$$\frac{\Delta h_{MBW}}{\Delta t} = T_{MBW} = T_{PQ} = I_{PQ} \cdot \alpha = \frac{1}{12} m_{PQ} \cdot \left(x^2 + y^2\right) \cdot \frac{2 \cdot \theta_a}{(\Delta t)^2} \tag{7.9}$$

$$\theta_a = \frac{6 \cdot \Delta h_{MBW} \cdot \Delta t}{m_{PQ} \cdot (x^2 + y^2)} = 3.98\ deg \tag{7.10}$$

7.2.3. Design Requirements Check

To summarise chapter 5 and section 7.1, each MBW requirement is run through and judged whether it was achieved through this thesis. Each requirement can be found in tables 2.3 and 2.4, with the summary of the check in tables 8.2 and 8.3.

MBW01 is not fully achieved, as the total required volume for the design presented in figure 4.12 through 4.14 would include the empty space between the motor mount and the edge of the PQ9 board and one of the PQ9 boards to mount the speed controller to, resulting in a total volume of 32.8 cm^3. However, this empty space between motor mount and PQ9 board can possible used for a auxiliary or secondary attitude actuator, such as small magnetorquer rods. If this assumption is taken into consideration, the precise volume the MBW takes up can be calculated through CAD software, resulting in a volume of 12.5 cm^3. The built prototype has a similar issue, where the total (including the empty space) and reduced (only the parts) volumes are 46.5 and 15.5 cm^3. In short, if no extra subsystems are able to take up the empty space near the motor mount, this requirement is not achieved. In future, it could be achieved through a design iteration, in which perhaps a smaller, more efficient motor is used together with a smaller flywheel.

MBW02 and MBW03 are similar to MBW01, which depends on which parts are counted towards the final mass and height. The final mass of the prototype is 55.3 g, exceeding the allocated mass budget. However, this includes both PQ endcaps, rather than the one PQ9 board required for the speed controller. And due to the the stacking nature of the PQ satellite bus, the other PQ9 board used for clamping the MBW in place is used for another subsystem. However, due to heavier flywheel used in testing, and the absence of the mass measurements for the actual design, this prototype and thus design have declared MBW02 to be not achieved. MBW03 can also not be set to achieved, as the distance between the bottom side of the PQ9 board and the extent of the motor axle exceeds the 12.0 mm limit and is 15.5 mm.

In each test done, the power draw was above the required 180 mW, and rose even further for the required velocity post vacuum and shaker tests. The lowest power usage at the required angular momentum of 6.05 $mNms$ would be 256 mW, when the speed controller was used in its most power efficient state and the motor had no load, which would compare to a perfectly balanced flywheel. This power draw was achieved for a scenario in motor functionality testing. The power draw achieved for a self-manufactured flywheel attached to the motor would result in 602 mW To find the power draw of the motor in vacuum conditions, a power draw ratio for the MBW is utilised to theorise a power draw in case of a perfectly balanced flywheel requiring no extra torque to be spun. This theorised power draw is equal to 192 mW, 6.7% over target. MBW04 is therefore not achieved.

Through table 5.1, MBW05 can be declared as achieved. The entire thesis has been done within this 500 Euro budget, as the optical tachometer also was purchased from this budget, resulting in a total thesis cost of 490.83 Euros.

MBW06 can be set as achieved as three Hall sensors are incorporated into the Faulhaber 1509T006B motor and are actively used in the position and velocity control of the motor through the Faulhaber SC1801P speed controller, visualised in figure 5.1.

Even though vibration and shaker testing was done for this thesis, no modal analysis was done to precisely determine the eigenfrequency of the prototype assembly. Nevertheless, the design values for the motor mount and the survivability of the assembly through the vibration and shaker test show that the eigenfrequency is high enough to have survived the launch vibration envelope, which would achieve MBW07 for these parts. This was also confirmed through the post shaker test investigation during disassembly of the MBW system, where no damages or deformations were found. The motor however showed a decrease in performance and stability of that performance, showing that the COTS component central in this design did not fully survive and thus not achieve MBW07. This decrease in performance and stability might also have an impact on the durability and lifespan of the motor; possibly shortening its lifetime dramatically due to the damage taken from the launch vibration.

MBW08 and MBW09 are unfortunately not tested during this thesis, as the acceleration forces were deemed insignificant in comparison to the sine vibrations caused during launch. However, the flywheel design and Faulhaber 1509T006B motor specifications state that survivability against these acceleration forces should be possible. MBW10 is achieved through the proof that the motor can run at the required velocity in vacuum. But as no thermal-vacuum testing was done, MBW11 is not achieved.

MBW12 is achieved as the rotating mass; the flywheel and the motor rotor; had the mass moment of inertia of 42.61 gcm^2, which would deliver an angular momentum of 6.87 $mNms$ at 15400 rpm for 602 mW, or the required 6.05 $mNms$ at 13567 rpm for 567 mW, found through the MBW functionality testing in subsection 7.1.4.

Unable to customise the speed controller of the motor due to the dead USB programming adapter, the torque limit requirement MBW13 could not be tested. The stability of the angular momentum was shown to be 0.1284% during atmospheric testing, but this was the only instance in which the stability requirement MBW14 was met. The best stability achieved in vacuum conditions only reached -0.4523%, overshooting target stability by 151%.

7.2.4. Competitiveness Check

To answer the second research question and check the competitiveness of the MBW to solely the reaction wheel or the reaction wheel systems (RWS) competitors, such as Vergoossen's Delfi-PQ RWS [54] and Hoevenaar's Delfi-n3Xt RWS [27], a comparison must be made. Vergoossen's and Hoevenaars work has been used thoroughly throughout this research to create competitive and comparable design and test requirements, and will thus also be used to answer the second research question of this thesis. As the sole reaction wheel is similar in built to a MBW, it will be included simply for comparison and inclusivity with all extra parts required for mounting and driving the motor. The 3 wheeled RWS is also included, as this, as well as the MBW, delivers 3-axis control. Approximations through technical drawings and figures from respective sources are made for the mass of the PQ RWS and the size of the n3Xt RW, as these were not given.

Table 7.8: Comparing performance criteria between the MBW and different RWS.

Criteria		Prototype MBW	Theorised MBW	PQ RW	PQ RWS	n3Xt RW	n3Xt RWS
h	**(mNms)**	6.87	6.05	0.113	0.339	1.35	4.10
m	**(g)**	55.3	53.1	14.9	45	27.3	82
V	**(cm^3)**	46.5	15.5	4.80	21.1	8	43.2
P	**(mW)**	567	192	28.2	84.7	237	710

From the summarised specifications in table 7.8, observations and relations can be made to investigate the competitiveness of the MBW design. The MBW designed is heavier, uses more power and more space to be able to service a pointing accuracy to the spacecraft that is lower than the pointing accuracy delivered by the RWS. The increase in power draw from a PQ RWS to the PQ MBW is steep, and shows that a central part of the design has a high amount of influence on the feasibility and competitiveness of an attitude actuator; the motor. The motor selected for this research was the Faulhaber 1509T006B, and the Maxon EC10 flat for the PQ RWS prototype, and the Faulhaber 1202H004BH for the Delfi-n3xt RWS. Unfortunately, the two latter options are no longer available, which are more power efficient and smaller in size. This means that the smaller motors might have been able to spin the flywheel at the required angular velocity for a lower power draw or even a higher speed for a lower power draw to be able to decrease the mass of the flywheel. But since the decrease in performance of these two smaller motors is unknown after a similar shaker test is performed for a similar large flywheel, it cannot be known whether these motors would survive the harsh launch environments with the larger flywheel. This can however be circumvented by designing a hold-down and release mechanism. This might fall beyond the scope of a PQ satellite in terms of complexity, but allows for heavier attitude actuators such as MBW to survive the launch environment.

8. Conclusion

The scope of this thesis has been to introduce a the momentum bias wheel at PocketQube scale. This feasibility study of a momentum bias wheel at PocketQube scale and whether it can perform competitively in terms of provided specific pointing accuracy has been central in this thesis, finding answers to these two research questions:

"Is a momentum bias wheel design feasible using self-manufactured and COTS components for a PocketQube satellite?"

and

"How does the momentum bias wheel design compare to a reaction wheel design in pointing accuracy, size, mass and power?"

The two research questions shall be answered in their respective sections 8.1 and 8.2. As a means to summarise and conclude the thesis, the research objectives set up from the two research questions shall be checked for in section 8.3.

8.1. Momentum Bias Wheel Feasibility

The feasibility of the momentum bias wheel (MBW) using self-manufactured and COTS components for the PocketQube (PQ) satellite scale can be answered when looking at the results of the design and testing done in this thesis. Through the design phase, all parts have been manufactured in house, but ultimately, a design that is too large and too heavy has been created, measuring in at 55.3 g and 46.5 cm^3. The parts that could not have been made in house due to restrictions in time and financial budget, such as the motor and motor driver, are commercials off the shelf (COTS) items provided by Faulhaber. The COTS items from Faulhaber required no alteration or modification to run at the required performance, but did not run as power efficient as required and specified.

Through performance testing of the designed MBW as shown within section 7.1, the power usage of the system was found to be higher than envisioned. Through the design phase the requirement was set at 180 mW, but the lowest power usage at the required angular momentum of 6.05 $mNms$ would be 256 mW (subsection 7.1.3), as the speed controller was used in its most efficient state and the motor had no load and no flywheel attached to it. To find the power draw of the motor in vacuum conditions, a power draw ratio for the MBW is utilised to theorise a power draw in case of a perfectly balanced flywheel requiring no extra torque to be spun. This theorised power draw is equal to 192 mW, closer to the target of 180 mW. When a flywheel was attached, the lowest power draw in atmospheric conditions was 602 mW and 610 mW in vacuum conditions, showing a decrease in performance in the vacuum chamber.

The rotational stability of the motor is within the required 0.180%, as a stability of 0.1284% has been achieved for atmospheric conditions. Proven through the analysis for the resistance against external and internal disturbances in subsection 7.2.2, the deviation of the spacecraft due to the stability of the MBW is the largest at 3.89 deg at maximum, which is within the required pointing accuracy of 1 to 5 deg. Another internal source that has influenced the rotational stability of the spacecraft are the micro-vibration induced torques due to defects in the flywheel, which were analysed to rotationally deviate the spacecraft by only 0.00108 deg and are therefore neglected. However, this has only been achieved for atmospheric test conditions, and was not achieved in or after the vacuum and shaker tests, where the best stability achieved were -0.4523 and 0.5719% respectively and would result in an angular deviation of -14.0 and 17.7 deg.

Conclusively, the momentum bias wheel achieved its operational angular momentum and stability, but failed to do so for a competent mass, volume and power budget and in the required environments. Therefore, a COTS momentum bias wheel for a PocketQube is not feasible, as meeting the technical budget requirements of a PocketQube mission is not feasible given the currently available COTS motors. The design principle of a wheeled attitude actuators depends heavily on the available motors and the performance these deliver. For a momentum bias wheel, where the motor central does not survive the launch environment without proper flywheel reinforcement calls for a custom solution for the motor or flywheel reinforcement, which falls beyond the scope of a PocketQube satellite.

8.2. Momentum Bias Wheel Competitiveness

The competitiveness of the momentum bias wheel to a reaction wheel system or magnetorquer of a similar quality in terms of pointing accuracy, size, mass and power can be judged when comparing the designed and tested MBW to the designed and tested reaction wheel systems by other theses. The momentum bias wheel should have an advantage in satellite stability and power draw, as the momentum bias wheel is a preventive attitude actuator and does not depend on a response time of the driver circuit and only utilises one motor instead of three as with a complete reaction wheel system. When directly comparing for the prototypes performance per unit of mass and power in subsection 7.2.4, the MBW prototype falls short in comparison to the reaction wheel systems.

As shown in table 7.8; in terms of size, mass and power, the momentum bias wheel presented in this research would of course not be competitive. The main competitor, the Delfi-PQ reaction wheel system would be approximately 20% lighter, take up half of the volume and draw six times less power when compared to the built momentum bias wheel. Pondering whether the motors used in the previous designs for the reaction wheels would fit into this design would increase the competitiveness of the momentum bias wheel design as the power draw and size of the system would decrease, but only increases the number of questions regarding the performance, survivability and durability post shaker tests. As seen in subsection 7.1.9, the larger and sturdier Faulhaber 1509T006B motor central in this design did not survive the launch vibration, which means that a small motor rated for a smaller load may even decrease further in performance in comparison to the larger motor when clamped to a similar sized flywheel.

When offered the option between a complete reaction wheel system capable of 3 axis control and a momentum bias wheel design capable of 3 axis sway limitation, with the momentum bias wheel using more mass, size and power for smaller pointing accuracy, the choice for a reaction wheel system in comparison to a momentum bias wheel comes down to the available motors. As of now, the choice comes down to neither wheel attitude actuators, making magnetorquers the superior attitude controlling option. In line with the answer to the previous research question, to make the momentum bias wheel feasible and competitive, custom solutions for the motor would be required, falling beyond the scope of a PocketQube satellite.

8.3. Research Compliance

From the two research questions, four research objectives were set out, which were explained and split up into several sub-objectives in table 1.3, of which explanation on achieving these objectives will be stated here and summarised in table 8.1. These research objectives have been central in setting up requirements for design, prototyping and testing such that the research questions can be answered.

1. To model the theoretical environment and required performance of the new attitude control system;
2. To design a momentum bias wheel actuator using the required performance parameters modelled in the theoretical environment;
3. To create a working prototype of the momentum bias wheel;
4. To test the working prototype in all its encountered environments.

Out of these four research objectives, with the twelve sub-research objectives RO01 through RO33, only two were not completed. RO22 was not completed fully as the torque limit could not be implemented into the speed controller, which lead to the scrapping of Mode 1: spin up tests, which would demonstrate the low acceleration capability of the motor as required to not fully disturb the spacecraft during spinning up of the momentum bias wheel. RO33 was not achieved, as no thermal-vacuum testing was done due to time constraints.

Any information regarding the tests done to achieve these research objectives are stated within the chapters, formulae or tables as stated in table 8.1.

Table 8.1: Sub-objectives per research objective.

Research Objective	ID	Sub-objective	Achieved	Reported in
Model the theoretical environment and required performance.	RO01	Model the environmental disturbance torques.	Yes	Chapter 2
	RO02	Derive the performance requirements from the disturbance torques.	Yes	Chapter 2, equation 2.19
	RO03	Derive required model parameters from performance requirements.	Yes	Chapter 3, appendix B
Design a momentum bias wheel using modelled performance.	RO11	Set up requirements regarding the design of the momentum bias wheel.	Yes	Chapter 2, tables 2.3, 2.4
	RO12	Explore all concurrent options regarding materials, orientations, components and manufacturing methods.	Yes	Chapter 4, appendices C, D
	RO13	Do a complete design trade-off regarding designs from combinations made from materials, orientations, components and manufacturing methods.	Yes	Chapter 4, subsection 4.1.6
	RO14	Synthesise the design from the chosen combination.	Yes	Chapter 4, section 4.5
Create a working prototype.	RO21	Manufacture the momentum bias wheel prototype based on the previously selected design.	Yes	Chapter 5
	RO22	Perform a nominal running mode test, displaying performance in all operating modes.	Not fully	Section 6.1, 6.2, subsection 7.1.2 - 7.1.6
Test the prototype in all environments.	RO31	Perform a vibration test, displaying resilience against launch and operation induced vibration forces.	Yes	Section 6.4, 6.3, subsection 7.1.7, 7.1.9
	RO32	Perform a vacuum test, displaying the performance and resilience in vacuum conditions.	Yes	Section 6.5, subsection 7.1.8
	RO33	Perform a thermal-vacuum test, displaying the performance and resilience in a simulated orbit environment.	No	Section 6.6

8.4. Design Compliance

Summarising the achievement of the system and design requirements are put below in tables 8.2 and 8.3.

Table 8.2: Top level requirements summarised and checked.

ID	Requirement Description	Compliance	Verified by
SYS01	The MBW will be able to store angular momentum around its rotational axis.	Yes	Operational Test: Mode 1 and 2
SYS02	The MBW will survive the mission environments between its insertion orbit and decay orbit.	No	Not tested
SYS03	The MBW will be able to maintain its operational angular momentum over its mission lifetime.	Yes	Operational Test: Mode 2
SYS04	The MBW will be able to limit the effect of the disturbance torques over one orbit to be within the pointing accuracy of 1-5 deg.	Yes	Analysis in subsection 7.2.2
SYS05	The MBW will enable nadir-pointing for the PQ.	Yes	Analysis in subsection 7.2.2
SYS06	The MBW will adhere to the standards and requirements set in the PocketQube Standard 1.0.	Yes	Design, appendix A
SYS07	The MBW will be mounted on the PQ9 PCB backboard.	Yes	Design, appendix A
SYS08	The MBW will not obstruct the connector pins of the PQ9 PCB backboard.	Yes	Design, subsection 4.2.5

Table 8.3: Momentum bias wheel requirements summarised and checked.

ID	Requirement Description	Compliance	Prototype	Verified by
MBW01	The maximum volume of the MBW within the PQ bus is 21.1 cm^3.	No	32.8 cm^3	Design
MBW02	The maximum mass of the MBW will be 41.1 g.	No	55.3 g	Design & prototype
MBW03	The maximum height of the MBW will be 12.0 mm.	No	15.5 mm	Design & prototype
MBW04	The maximum power of the MBW is no more than 180 mW average per orbit.	No	602 mW	Operational Test: Mode 2
MBW05	The maximum cost of the MBW is no more than 500 Euros.	Yes	490.83 Euros	Design
MBW06	The MBW motor shall have sensors to be able to correct angular velocity errors.	Yes	3 Hall sensors	Design
MBW07	The MBW shall have an eigenfrequency high enough to resist the vibration loads during launch.	No	-	No modal testing done
MBW08	The MBW will be able to withstand 8.5 g of acceleration loads.	No	-	Not tested
MBW09	The MBW will not yield the PQ9 PCB backboard due to the 8.5 g of acceleration loads.	No	-	Not tested
MBW10	The MBW will be able to operate in vacuum.	Yes	0.1 $mbar$	Vacuum Test
MBW11	The MBW will be able to operate in temperatures between -20 and +50 $°C$	No	-	Not tested
MBW12	The minimum amount of angular momentum created by the MBW will be 6.05 $mNms$.	Yes	6.872 $mNms$ at 15400 rpm	Operational Test: Mode 2
MBW13	The maximum torque the MBW will exert will be 0.0962 μNm.	No	-	Not tested
MBW14	The maximum deviation from the required angular momentum of the MBW will be 0.180%.	Yes	0.1284%	Operational Test: Mode 2

9. Reflection

The act of engineering is an iterative process, learning from each previous iteration to improve the process of design and design itself to create the best product possible within constraints set. Through answering the research questions in chapter 8, it was found that the momentum bias wheel (MBW) concept was not feasible and competitive with COTS components. Therefore, a reflection on this iteration and advices for future iterations are discussed below such that the MBW concept could achieve feasibility and competitiveness as an attitude actuator.

An improvement on the manufacturing of the flywheel can possibly be made by altering manufacturing methods. The manual lathing performed to manufacture the uniform flywheel specimen delivered sufficient accurate specimen for the MBW. However, as the high power draw as measured in the complete MBW performance tests originates from the flywheel and the torque required to spin the imbalanced specimen, improvements can be made. The switch to computerised machining through CNC lathing machines can be feasible if the devices are available in the next iteration. If a steep increase in manufacturing cost was assumed for CNC machining, but if the Faculty Workshop would include CNC machines in the tools available to the students, manufacturing the flywheel with automated manufacturing machinery would be superior in accuracy.

The USB programming adapter supplied by Faulhaber was declared dead and hindered the ability to program the Faulhaber speed controller specifically for this load case, which did not allow for mode 1 testing to be done. In future research, mode 1 operational tesitng and extensive speed controller option testing can be done when a new programming device is acquired.

Testing the MBW in mode 2 for longer amounts of time could show an even further increase in stability, as shown in subsection 7.1.6, in which the deviation in motor angular velocity decreased from 0.354% to 0.128% when it had ran for a longer period of time. Proposing testing times of multiple hours or even days is crucial to approaching and simulating mission performance.

The resolution of the speed measurements can be altered to further visualise the instability within the motor. As a measuring period of 5 seconds was satisfactory for this thesis, the next part of this research might require the same resolution for the speed measurement at a smaller time interval. This can be achieved through adding more black markings onto the flywheel, or introducing a new velocity measuring device. An oscilloscope, as used in testing the accuracy of the optical tachometer, might be the device fit for this requirement.

Extensive research must be done into the variation of performance related to the changing environment the spacecraft would find itself in during operation. The thermal vacuum tests in this research were discarded as they were not deemed as crucial as the other allocated tests, but still can provide useful insights into the characteristics of the vacuum lubricant used in the Faulhaber motor.

To make this system space-worthy, research and engineering must be done into the crucial parts of this driver, such as the PI velocity controller, PWM commutator, Mosfets and perhaps more, and see whether parts can be embedded into the PQ-9 interface, and are consistent in their performance when exposed to the harsh space environment. With a voltage regulator sat between the EPS and driver, and deliver the required power over the voltage supplies as required per the driver specifications, which can be seen in figure 5.1. These parts must also be faultless and be able to run for the mission lifetime.

A recommendation regarding the commercial motor selection can be made, expecting manufacturers to further improve current designs and offer better solutions in the future. The flat motor used in previous wheeled attitude actuators, such as the Faulhaber 1202H004BH and the Maxon EC10 Flat are no longer available, and have been replaced by the Faulhaber 1509T006B and Maxon EC42 Flat. The former motor options ran more power efficiently at the required angular velocity than its replacements, but were not specified to handle larger loads in the form of larger flywheels on their smaller axels. To circumvent this, the flywheel must be properly reinforced, through a new motor mount or a hold-down and release mechanism. The new motor mount could be in scope of a PQ project, but the hold-down and release mechanism would introduce a level of complexity to the design that is not standard for a PocketQube mission. Conclusively, new and better COTS motors might pave the way to better wheeled attitude actuators.

A. PocketQube Standards

This appendix provides the technical drawings, standards and interfaces for the PocketQube bus for one to three units, retrieved from Bouwmeester's and Radu's work [7][8][40][41].

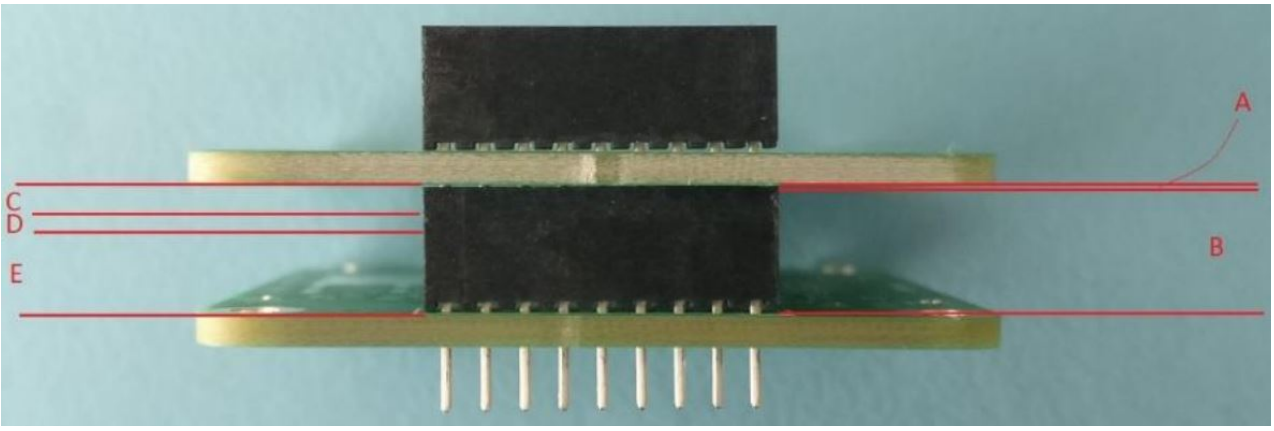

Figure A.1: Two PQ9 boards stacked directly, with out-of-plane dimensions [7].

Table A.1: Dimensions A through E from figure A.1 [7].

Symbol	**Description**	**Value** (mm)
A	Maximum soldering pad height.	0.65
B	Connector height.	6.35
C	Maximum height of components placed underneath the upper board.	2.00
D	Margin between components of two adjacent boards.	1.00
E	Maximum component height on bottom board.	4.00

Table A.2: Configuration possibilities with small and large connectors.

Option	**C**	**E**
1	4.00	2.00
2	4.00	10.0 / 11.0 / 12.0
3	4.00	9.00
4	11.0	2.00

The orange rectangular outlines visualises the available subsystem placement for each option.

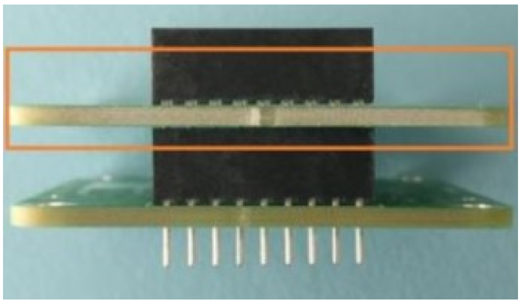

Figure A.2: PQ9 Stacking Option 1: a single small connector on top [7].

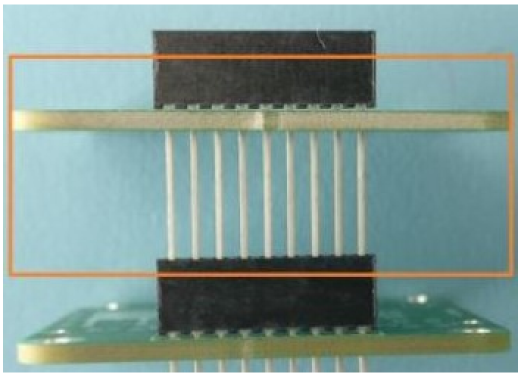

Figure A.3: PQ9 Stacking Option 2: a single large connector on top [7].

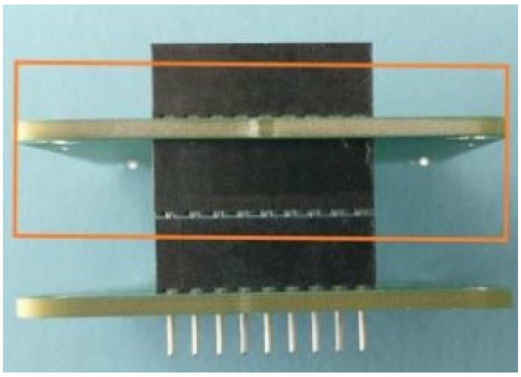

Figure A.4: PQ9 Stacking Option 3: a small connector on top and a small connector glued to bottom [7].

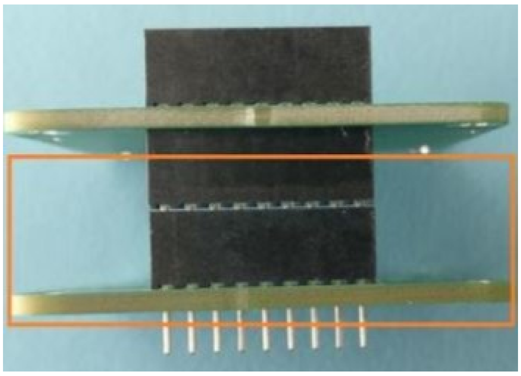

Figure A.5: PQ9 Stacking Option 4: two small connectors stacked on top [7].

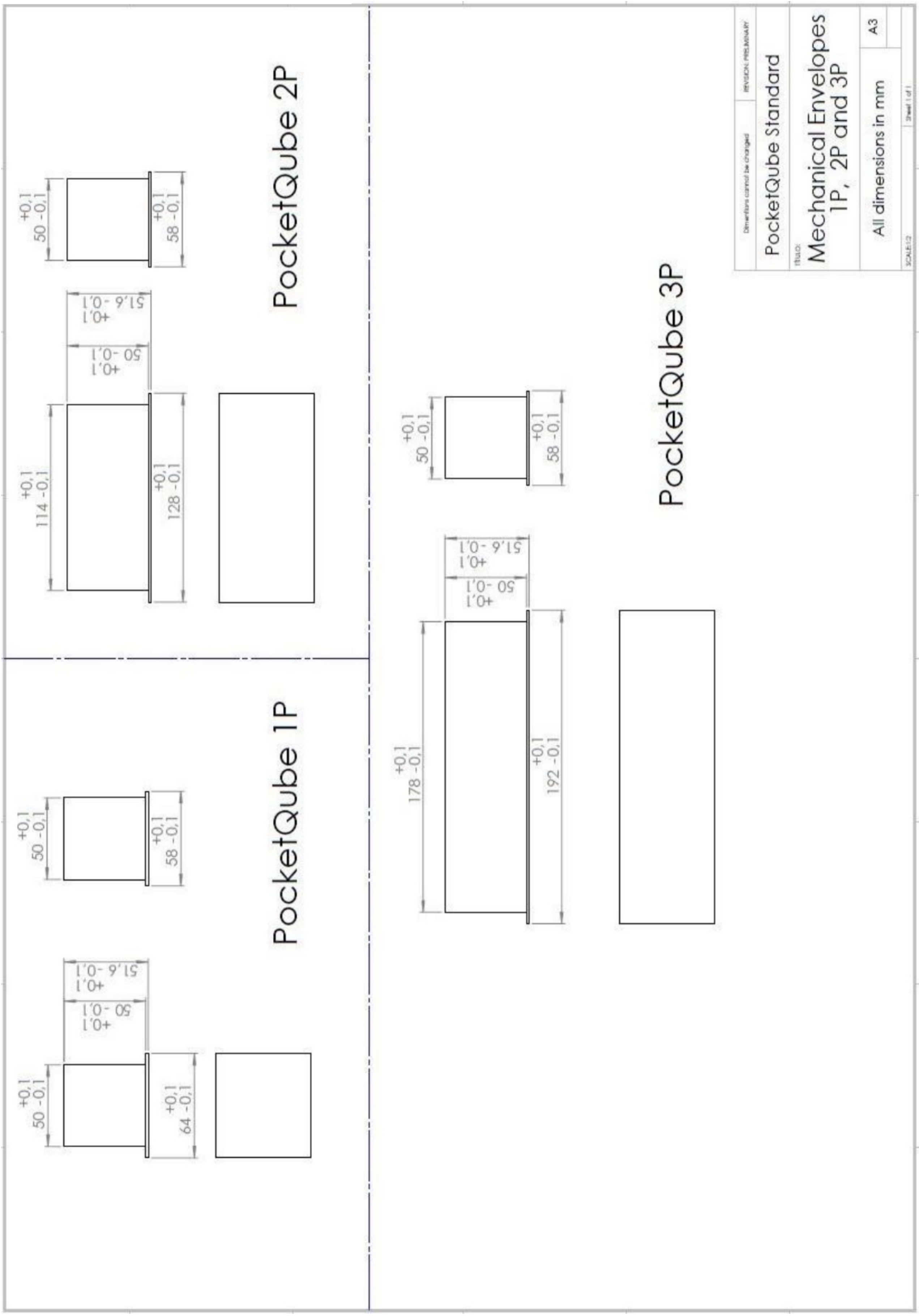
PocketQube 2P
PocketQube 1P
PocketQube 3P
50 +0,1 -0,1
58 +0,1 -0,1
51,6 +0,1 -0,1
114 +0,1 -0,1
128 +0,1 -0,1
64 +0,1 -0,1
178 +0,1 -0,1
192 +0,1 -0,1
PocketQube Standard
Mechanical Envelopes
1P, 2P and 3P
All dimensions in mm
A3

B. Equations of Motion Code

The code for simulating the Equations of Motion (EoM) in chapter 3 is shown. Firstly, the code with the selector built in.

```
# -*- coding: utf-8 -*-
"""
Equations of motion for MBW PQ

author: Jari Pols
thesis: MBW for PQ
"""
import numpy as np
import matplotlib.pyplot as plt
from scipy.integrate import odeint

#Physical properties 3p PQ
m_PQ = 0.75                                                       #mass PQ, kg
L_PQ = 0.05                                             #length of PQ unit, m
n_PQ = 3                                               #amount of PQ units, -
I1 = m_PQ/12 * ((n_PQ * L_PQ)**2 + L_PQ**2)      #moment of inertia axis 1, kgm2
I2 = m_PQ/6 * (L_PQ**2)                          #moment of inertia axis 2, kgm2

#Orbit properties
R_E = 6371E3                                                 #radius Earth, m
GP_E = 3.986004418E14                       #gravitational parameter Earth, m^3/s^2
h_i = 300E3                                                #orbit altitude, m
rho_max = 4.39E-11                     #maximum density at lowest altitude, kg/m3
n_b = np.sqrt(GP_E/(R_E+h_i)**3)                              #mean motion, rad/s
P_orbit = 2 * np.pi * np.sqrt((R_E + h_i)**3 / GP_E)       #orbital period, s

#Mission properties
theta_ss = 1 * np.pi/180                       #required pointing accuracy, rad
T_d = 83.3E-9                                  #maximum disturbance torque, Nm
h_MBW = 0.00605                                     #required MBW momentum, Nms
t_0 = 0.0                                                       #start time, s
n_orbit = 1                                    #amount of simulated orbits, -
t_end = n_orbit * 2 * np.pi * np.sqrt((R_E+h_i)**3/GP_E)          #end time, s
dt = 1.0                                                          #timestep, s
t = np.linspace(t_0,t_end,int((t_end-t_0)/dt))                  #time array, s

#Controller properties
dr = np.sqrt(2)                                              #damping ratio, -
# kp = T_d/theta_ss                               #proportional controller, -
kp = 0                                            #proportional controller, -
kd = 2 * dr * np.sqrt(kp * I1)                      #derivative controller, -

# ODE solver parameters
abserr = 1.0e-8                                      #solver error control, -
relerr = 1.0e-6                                      #solver error control, -
w0 = [0,0,0,0,0,0]                                #solver initial values, rad

# %% EoM functions

def EoMMBWX(w,t):
    x1,y1,x2,y2,x3,y3 = w
    return [y1, 1/Ixxb * (T_dx + (1 + Izzb - Iyyb) * n_b * y3 - kd * y1 - (4 * n_b**2 * (Iyyb - Izzb) + kp) * x1),
            y2, 1/Iyyb * (T_dy + 3 * n_b**2 * (Izzb - Ixxb) * x2 - h_MBW * y3 - n_b * h_MBW * x1),
            y3, 1/Izzb * (T_dz + (Iyyb - Ixxb - 1) * n_b * y1 + (Ixxb - Iyyb) * n_b**2 * x3 + h_MBW * y2 - n_b * h_MBW)]

def EoMMBWY(w,t):
    x1,y1,x2,y2,x3,y3 = w
```

```
    return [y1, 1/Ixxb * (T_dx + (h_MBW + n_b * (Izzb + Ixxb - Iyyb))*y3 + (n_b * h_MBW
        - n_b**2 * (Iyyb - Izzb))*x1),
            y2, 1/Iyyb * (T_dy - kd * y2 - (3 * n_b**2 * (Ixxb - Izzb) + kp) * x2),
            y3, 1/Izzb * (T_dz - (n_b * (Izzb + Ixxb - Iyyb) + h_MBW)*y1 + (n_b * h_MBW
                - n_b**2 * (Iyyb - Ixxb))*x3)]

def EoMMBWZ(w,t):
    x1,y1,x2,y2,x3,y3 = w
    return [y1, 1/Ixxb * (T_dx + (1 + Izzb - Iyyb) * n_b * y3 - 4 * n_b**2 * (Iyyb -
        Izzb) * x1 - h_MBW * y2 + n_b * h_MBW),
            y2, 1/Iyyb * (T_dy + 3 * n_b**2 * (Izzb - Ixxb) * x2 + h_MBW * y1 - n_b *
                h_MBW * x3),
            y3, 1/Izzb * (T_dz + (Iyyb - Ixxb - 1) * n_b * y1 - kd * y3 + ((Ixxb - Iyyb)
                 * n_b**2 - kp) * x3)]

# %% Solver
a = True

while a:
    T_dx, T_dy, T_dz = 0, 0, 0
    Ixxb, Iyyb, Izzb = I1, I1, I1
    userMBWinput = input("On which axis does the MBW operate? (X/Y/Z)")
    print("The MBW operates on the ",userMBWinput,"axis")

    userT_dinput = input("On which axis does the disturbance torque occur? (X/Y/Z)")
    print("The disturbance torque occurs on the ",userT_dinput,"axis")

    userIaxisinput = input("On which axis does the long side of the PQ start on? (X/Y/Z)
        ")
    print("The long side of the PQ lies on the ",userIaxisinput,"axis")

    if userT_dinput == 'X':
        T_dx= T_d
    elif userT_dinput == 'Y':
        T_dy= T_d
    elif userT_dinput == 'Z':
        T_dz= T_d

    if userIaxisinput == 'X':
        Ixxb = I2
    elif userIaxisinput == 'Y':
        Iyyb = I2
    elif userIaxisinput == 'Z':
        Izzb = I2

    if userMBWinput == 'X':
        theta1, thetadot1, theta2, thetadot2, theta3, thetadot3 = odeint(EoMMBWX,
            [0,0,0,0,0,0], t, atol=abserr, rtol=relerr).T
    elif userMBWinput == 'Y':
        theta1, thetadot1, theta2, thetadot2, theta3, thetadot3 = odeint(EoMMBWZ,
            [0,0,0,0,0,0], t, atol=abserr, rtol=relerr).T
    elif userIaxisinput == 'Z':
        theta1, thetadot1, theta2, thetadot2, theta3, thetadot3 = odeint(EoMMBWY,
            [0,0,0,0,0,0], t, atol=abserr, rtol=relerr).T

    plt.figure()
    plt.plot(t, theta1*180/np.pi, linewidth = 1)
    plt.title("X orientation with body in ",userIaxisinput,", MBW in ",userMBWinput,"
        and T_D in ",userT_dinput)
    plt.xlabel("Time (s)")
    plt.ylabel("Orientation (deg)")
    plt.grid(True)

    plt.figure()
    plt.plot(t, theta2*180/np.pi, linewidth = 1)
```

```
    plt.title("Y orientation with body in ",userIaxisinput,", MBW in ",userMBWinput," and T_D in ",userT_dinput)
    plt.xlabel("Time (s)")
    plt.ylabel("Orientation (deg)")
    plt.grid(True)

    plt.figure()
    plt.plot(t, theta3*180/np.pi, linewidth = 1)
    plt.title("Z orientation with body in ",userIaxisinput,", MBW in ",userMBWinput," and T_D in ",userT_dinput)
    plt.xlabel("Time (s)")
    plt.ylabel("Orientation (deg)")
    plt.grid(True)

    plt.close('all')
    print("Run again? (y/n)")
    userrenewalinput = input()
    if userrenewalinput == 'n':
        a = False
```

Now the X, Y and Z axis full analysis in order.

```python
# -*- coding: utf-8 -*-
"""
Equations of motion for MBW PQ

author: Jari Pols
thesis: MBW for PQ
"""
import numpy as np
import matplotlib.pyplot as plt
from scipy.integrate import odeint

#Physical properties 3p PQ
m_b = 0.75                          #mass PQ, kg
I1 = m_b/12 * (0.178**2 + 0.05**2)  #moment of inertia axis 1, kgm2
I2 = m_b/6 * (0.05**2)              #moment of inertia axis 2, kgm2
A_a1 = 0.05**2                      #smallest frontal area, m2
A_a2 = 0.196*0.058                  #largest frontal area, m2
dCp = 0.01                          #assumption for distance centre of mass and pressure

#Orbit properties
R_E = 6371E3                        #radius Earth, m
GP_E = 3.986004418E14               #gravitational parameter Earth, m^3/s^2
h_i = 300E3                         #orbit altitude, m
rho_max = 4.39E-11                  #maximum density at lowest altitude, kg/m3
n_b = np.sqrt(GP_E/(R_E+h_i)**3)    #mean motion, rad/s
P_orbit = 2 * np.pi * np.sqrt((R_E + h_i)**3 / GP_E) #orbital period, s

#Mission properties
theta_ss = 1 * np.pi/180.
T_d = 83.3E-9
h_MBW = 0.00605
t_0 = 0.0
n_orbit = 1
t_end = n_orbit * 2 * np.pi * np.sqrt((R_E+h_i)**3/GP_E)
dt = 1.
t = np.linspace(t_0,t_end,int((t_end-t_0)/dt))
tdays = 1/(24*3600) * t

#Controller properties
dr = np.sqrt(2)
omega_n = 0.04
# kp = T_d/theta_ss
kp = 0

# ODE solver parameters
abserr = 1.0e-8
relerr = 1.0e-6

# %% EoM functions

def EoM(w,t):
    x1,y1,x2,y2,x3,y3 = w
    return [y1,
            1/Ixxb * (T_dx + (1 + Izzb - Iyyb) * n_b * y3 - kd * y1 - (4 * n_b**2 * (
                Iyyb - Izzb) + kp) * x1),
            y2,
            1/Iyyb * (T_dy + 3 * n_b**2 * (Izzb - Ixxb) * x2 - h_MBW * y3 - n_b * h_MBW
                * x1),
            y3,
            1/Izzb * (T_dz + (Iyyb - Ixxb - 1) * n_b * y1 + (Ixxb - Iyyb) * n_b**2 * x3
                + h_MBW * y2 - n_b * h_MBW)]


```

```
# %% EoM for body in X, MBW in X and T_D in X
T_dx = T_d
T_dy = 0
T_dz = 0

Ixxb = I2                            #moment of inertia xx, kgm2
Iyyb = I1                            #moment of inertia yy, kgm2
Izzb = I1                            #moment of inertia zz,kgm2

kd = 2 * dr * np.sqrt(kp * Ixxb)

theta1, thetadot1, theta2, thetadot2, theta3, thetadot3 = odeint(EoM, [0,0,0,0,0,0], t, atol=abserr, rtol=relerr).T

plt.figure()
plt.plot(t, theta1*180/np.pi, linewidth = 1)
plt.title("X orientation with body in X, MBW in X and T_D in X")
plt.xlabel("Time (s)")
plt.ylabel("Orientation (deg)")
plt.savefig('EoM/EoM(body=X,MBW=X,T_D=X)(X).jpg')
plt.grid(True)


plt.figure()
plt.plot(t, theta2*180/np.pi, linewidth = 1)
plt.title("Y orientation with body in X, MBW in X and T_D in X")
plt.xlabel("Time (s)")
plt.ylabel("Orientation (deg)")
plt.savefig('EoM/EoM(body=X,MBW=X,T_D=X)(Y).jpg')
plt.grid(True)

plt.figure()
plt.plot(t, theta3*180/np.pi, linewidth = 1)
plt.title("Z orientation with body in X, MBW in X and T_D in X")
plt.xlabel("Time (s)")
plt.ylabel("Orientation (deg)")
plt.savefig('EoM/EoM(body=X,MBW=X,T_D=X)(Z).jpg')
plt.grid(True)

plt.close('all')

# %% EoM for body in X, MBW in X and T_D in Y
T_dx = 0
T_dy = T_d
T_dz = 0

Ixxb = I2                            #moment of inertia xx, kgm2
Iyyb = I1                            #moment of inertia yy, kgm2
Izzb = I1                            #moment of inertia zz,kgm2

kd = 2 * dr * np.sqrt(kp * Ixxb)

theta1, thetadot1, theta2, thetadot2, theta3, thetadot3 = odeint(EoM, [0,0,0,0,0,0], t, atol=abserr, rtol=relerr).T

plt.figure()
plt.plot(t, theta1*180/np.pi, linewidth = 1)
plt.title("X orientation with body in X, MBW in X and T_D in Y")
plt.xlabel("Time (s)")
plt.ylabel("Orientation (deg)")
plt.savefig('EoM/EoM(body=X,MBW=X,T_D=Y)(X).jpg')
plt.grid(True)


plt.figure()
```

```
plt.plot(t, theta2*180/np.pi, linewidth = 1)
plt.title("Y orientation with body in X, MBW in X and T_D in Y")
plt.xlabel("Time (s)")
plt.ylabel("Orientation (deg)")
plt.savefig('EoM/EoM(body=X,MBW=X,T_D=Y)(Y).jpg')
plt.grid(True)

plt.figure()
plt.plot(t, theta3*180/np.pi, linewidth = 1)
plt.title("Z orientation with body in X, MBW in X and T_D in Y")
plt.xlabel("Time (s)")
plt.ylabel("Orientation (deg)")
plt.savefig('EoM/EoM(body=X,MBW=X,T_D=Y)(Z).jpg')
plt.grid(True)

plt.close('all')

# %% EoM for body in X, MBW in X and T_D in Z
T_dx = 0
T_dy = 0
T_dz = T_d

Ixxb = I2                              #moment of inertia xx, kgm2
Iyyb = I1                              #moment of inertia yy, kgm2
Izzb = I1                              #moment of inertia zz,kgm2

kd = 2 * dr * np.sqrt(kp * Ixxb)

theta1, thetadot1, theta2, thetadot2, theta3, thetadot3 = odeint(EoM, [0,0,0,0,0,0], t, atol=abserr, rtol=relerr).T

plt.figure()
plt.plot(t, theta1*180/np.pi, linewidth = 1)
plt.title("X orientation with body in X, MBW in X and T_D in Z")
plt.xlabel("Time (s)")
plt.ylabel("Orientation (deg)")
plt.savefig('EoM/EoM(body=X,MBW=X,T_D=Z)(X).jpg')
plt.grid(True)


plt.figure()
plt.plot(t, theta2*180/np.pi, linewidth = 1)
plt.title("Y orientation with body in X, MBW in X and T_D in Z")
plt.xlabel("Time (s)")
plt.ylabel("Orientation (deg)")
plt.savefig('EoM/EoM(body=X,MBW=X,T_D=Z)(Y).jpg')
plt.grid(True)

plt.figure()
plt.plot(t, theta3*180/np.pi, linewidth = 1)
plt.title("Z orientation with body in X, MBW in X and T_D in Z")
plt.xlabel("Time (s)")
plt.ylabel("Orientation (deg)")
plt.savefig('EoM/EoM(body=X,MBW=X,T_D=Z)(Z).jpg')
plt.grid(True)

plt.close('all')

# %% EoM for body in Y, MBW in X and T_D in X
T_dx = T_d
T_dy = 0
T_dz = 0

Ixxb = I1                              #moment of inertia xx, kgm2
Iyyb = I2                              #moment of inertia yy, kgm2
```

```
Izzb = I1                            #moment of inertia zz,kgm2

kd = 2 * dr * np.sqrt(kp * Ixxb)

theta1, thetadot1, theta2, thetadot2, theta3, thetadot3 = odeint(EoM, [0,0,0,0,0,0], t,
    atol=abserr, rtol=relerr).T

plt.figure()
plt.plot(t, theta1*180/np.pi, linewidth = 1)
plt.title("X␣orientation␣with␣body␣in␣Y,␣MBW␣in␣X␣and␣T_D␣in␣X")
plt.xlabel("Time␣(s)")
plt.ylabel("Orientation␣(deg)")
plt.savefig('EoM/EoM(body=Y,MBW=X,T_D=X)(X).jpg')
plt.grid(True)


plt.figure()
plt.plot(t, theta2*180/np.pi, linewidth = 1)
plt.title("Y␣orientation␣with␣body␣in␣Y,␣MBW␣in␣X␣and␣T_D␣in␣X")
plt.xlabel("Time␣(s)")
plt.ylabel("Orientation␣(deg)")
plt.savefig('EoM/EoM(body=Y,MBW=X,T_D=X)(Y).jpg')
plt.grid(True)

plt.figure()
plt.plot(t, theta3*180/np.pi, linewidth = 1)
plt.title("Z␣orientation␣with␣body␣in␣Y,␣MBW␣in␣X␣and␣T_D␣in␣X")
plt.xlabel("Time␣(s)")
plt.ylabel("Orientation␣(deg)")
plt.savefig('EoM/EoM(body=Y,MBW=X,T_D=X)(Z).jpg')
plt.grid(True)

plt.close('all')

# %% EoM for body in Y, MBW in X and T_D in Y
T_dx = 0
T_dy = T_d
T_dz = 0

Ixxb = I1                            #moment of inertia xx, kgm2
Iyyb = I2                            #moment of inertia yy, kgm2
Izzb = I1                            #moment of inertia zz,kgm2

kd = 2 * dr * np.sqrt(kp * Ixxb)

theta1, thetadot1, theta2, thetadot2, theta3, thetadot3 = odeint(EoM, [0,0,0,0,0,0], t,
    atol=abserr, rtol=relerr).T

plt.figure()
plt.plot(t, theta1*180/np.pi, linewidth = 1)
plt.title("X␣orientation␣with␣body␣in␣Y,␣MBW␣in␣X␣and␣T_D␣in␣Y")
plt.xlabel("Time␣(s)")
plt.ylabel("Orientation␣(deg)")
plt.savefig('EoM/EoM(body=Y,MBW=X,T_D=Y)(X).jpg')
plt.grid(True)


plt.figure()
plt.plot(t, theta2*180/np.pi, linewidth = 1)
plt.title("Y␣orientation␣with␣body␣in␣Y,␣MBW␣in␣X␣and␣T_D␣in␣Y")
plt.xlabel("Time␣(s)")
plt.ylabel("Orientation␣(deg)")
plt.savefig('EoM/EoM(body=Y,MBW=X,T_D=Y)(Y).jpg')
plt.grid(True)

```

```
plt.figure()
plt.plot(t, theta3*180/np.pi, linewidth = 1)
plt.title("Z orientation with body in Y, MBW in X and T_D in Y")
plt.xlabel("Time (s)")
plt.ylabel("Orientation (deg)")
plt.savefig('EoM/EoM(body=Y,MBW=X,T_D=Y)(Z).jpg')
plt.grid(True)

plt.close('all')

# %% EoM for body in Y, MBW in X and T_D in Z
T_dx = 0
T_dy = 0
T_dz = T_d

Ixxb = I1                           #moment of inertia xx, kgm2
Iyyb = I2                           #moment of inertia yy, kgm2
Izzb = I1                           #moment of inertia zz,kgm2

kd = 2 * dr * np.sqrt(kp * Ixxb)

theta1, thetadot1, theta2, thetadot2, theta3, thetadot3 = odeint(EoM, [0,0,0,0,0,0], t,
    atol=abserr, rtol=relerr).T

plt.figure()
plt.plot(t, theta1*180/np.pi, linewidth = 1)
plt.title("X orientation with body in Y, MBW in X and T_D in Z")
plt.xlabel("Time (s)")
plt.ylabel("Orientation (deg)")
plt.savefig('EoM/EoM(body=Y,MBW=X,T_D=Z)(X).jpg')
plt.grid(True)


plt.figure()
plt.plot(t, theta2*180/np.pi, linewidth = 1)
plt.title("Y orientation with body in Y, MBW in X and T_D in Z")
plt.xlabel("Time (s)")
plt.ylabel("Orientation (deg)")
plt.savefig('EoM/EoM(body=Y,MBW=X,T_D=Z)(Y).jpg')
plt.grid(True)

plt.figure()
plt.plot(t, theta3*180/np.pi, linewidth = 1)
plt.title("Z orientation with body in Y, MBW in X and T_D in Z")
plt.xlabel("Time (s)")
plt.ylabel("Orientation (deg)")
plt.savefig('EoM/EoM(body=Y,MBW=X,T_D=Z)(Z).jpg')
plt.grid(True)

plt.close('all')

# %% EoM for body in Z, MBW in X and T_D in X
T_dx = T_d
T_dy = 0
T_dz = 0

Ixxb = I1                           #moment of inertia xx, kgm2
Iyyb = I1                           #moment of inertia yy, kgm2
Izzb = I2                           #moment of inertia zz,kgm2

kd = 2 * dr * np.sqrt(kp * Ixxb)

theta1, thetadot1, theta2, thetadot2, theta3, thetadot3 = odeint(EoM, [0,0,0,0,0,0], t,
    atol=abserr, rtol=relerr).T

```

```
plt.figure()
plt.plot(t, theta1*180/np.pi, linewidth = 1)
plt.title("X orientation with body in Z, MBW in X and T_D in X")
plt.xlabel("Time (s)")
plt.ylabel("Orientation (deg)")
plt.savefig('EoM/EoM(body=Z,MBW=X,T_D=X)(X).jpg')
plt.grid(True)


plt.figure()
plt.plot(t, theta2*180/np.pi, linewidth = 1)
plt.title("Y orientation with body in Z, MBW in X and T_D in X")
plt.xlabel("Time (s)")
plt.ylabel("Orientation (deg)")
plt.savefig('EoM/EoM(body=Z,MBW=X,T_D=X)(Y).jpg')
plt.grid(True)

plt.figure()
plt.plot(t, theta3*180/np.pi, linewidth = 1)
plt.title("Z orientation with body in Z, MBW in X and T_D in X")
plt.xlabel("Time (s)")
plt.ylabel("Orientation (deg)")
plt.savefig('EoM/EoM(body=Z,MBW=X,T_D=X)(Z).jpg')
plt.grid(True)

plt.close('all')

# %% EoM for body in Z, MBW in X and T_D in Y
T_dx = 0
T_dy = T_d
T_dz = 0

Ixxb = I1                           #moment of inertia xx, kgm2
Iyyb = I1                           #moment of inertia yy, kgm2
Izzb = I2                           #moment of inertia zz,kgm2

kd = 2 * dr * np.sqrt(kp * Ixxb)

theta1, thetadot1, theta2, thetadot2, theta3, thetadot3 = odeint(EoM, [0,0,0,0,0,0], t,
    atol=abserr, rtol=relerr).T

plt.figure()
plt.plot(t, theta1*180/np.pi, linewidth = 1)
plt.title("X orientation with body in Z, MBW in X and T_D in Y")
plt.xlabel("Time (s)")
plt.ylabel("Orientation (deg)")
plt.savefig('EoM/EoM(body=Z,MBW=X,T_D=Y)(X).jpg')
plt.grid(True)


plt.figure()
plt.plot(t, theta2*180/np.pi, linewidth = 1)
plt.title("Y orientation with body in Z, MBW in X and T_D in Y")
plt.xlabel("Time (s)")
plt.ylabel("Orientation (deg)")
plt.savefig('EoM/EoM(body=Z,MBW=X,T_D=Y)(Y).jpg')
plt.grid(True)

plt.figure()
plt.plot(t, theta3*180/np.pi, linewidth = 1)
plt.title("Z orientation with body in Z, MBW in X and T_D in Y")
plt.xlabel("Time (s)")
plt.ylabel("Orientation (deg)")
plt.savefig('EoM/EoM(body=Z,MBW=X,T_D=Y)(Z).jpg')
plt.grid(True)
```

```

plt.close('all')

# %% EoM for body in Z, MBW in X and T_D in Z
T_dx = 0
T_dy = 0
T_dz = T_d

Ixxb = I1                          #moment of inertia xx, kgm2
Iyyb = I1                          #moment of inertia yy, kgm2
Izzb = I2                          #moment of inertia zz,kgm2

kd = 2 * dr * np.sqrt(kp * Ixxb)

theta1, thetadot1, theta2, thetadot2, theta3, thetadot3 = odeint(EoM, [0,0,0,0,0,0], t,
    atol=abserr, rtol=relerr).T

plt.figure()
plt.plot(t, theta1*180/np.pi, linewidth = 1)
plt.title("X orientation with body in Z, MBW in X and T_D in Z")
plt.xlabel("Time (s)")
plt.ylabel("Orientation (deg)")
plt.savefig('EoM/EoM(body=Z,MBW=X,T_D=Z)(X).jpg')
plt.grid(True)


plt.figure()
plt.plot(t, theta2*180/np.pi, linewidth = 1)
plt.title("Y orientation with body in Z, MBW in X and T_D in Z")
plt.xlabel("Time (s)")
plt.ylabel("Orientation (deg)")
plt.savefig('EoM/EoM(body=Z,MBW=X,T_D=Z)(Y).jpg')
plt.grid(True)

plt.figure()
plt.plot(t, theta3*180/np.pi, linewidth = 1)
plt.title("Z orientation with body in Z, MBW in X and T_D in Z")
plt.xlabel("Time (s)")
plt.ylabel("Orientation (deg)")
plt.savefig('EoM/EoM(body=Z,MBW=X,T_D=Z)(Z).jpg')
plt.grid(True)

plt.close('all')
```

```python
# -*- coding: utf-8 -*-
"""
Equations of motion for MBW PQ

author: Jari Pols
thesis: MBW for PQ
"""

# %% Start cell
import numpy as np
import matplotlib.pyplot as plt
from scipy.integrate import odeint

#Physical properties 3p PQ
m_b = 0.75                          #mass PQ, kg
I1 = m_b/12 * (0.178**2 + 0.05**2)  #moment of inertia axis 1, kgm2
I2 = m_b/6 * (0.05**2)              #moment of inertia axis 2, kgm2
A_a1 = 0.05**2                      #smallest frontal area, m2
A_a2 = 0.196*0.058                  #largest frontal area, m2
dCp = 0.01                          #assumption for distance centre of mass and pressure

#Orbit properties
R_E = 6371E3                        #radius Earth, m
GP_E = 3.986004418E14               #gravitational parameter Earth, m^3/s^2
h_i = 300E3                         #orbit altitude, m
rho_max = 4.39E-11                  #maximum density at lowest altitude, kg/m3
n_b = np.sqrt(GP_E/(R_E+h_i)**3)    #mean motion, rad/s
P_orbit = 2 * np.pi * np.sqrt((R_E + h_i)**3 / GP_E) #orbital period, s

#Mission properties
theta_ss = 1 * np.pi/180.
T_d = 83.3E-9
h_MBW = 0.0605
t_0 = 0.0
n_orbit = 1
t_end = n_orbit * 2 * np.pi * np.sqrt((R_E+h_i)**3/GP_E)
dt = 1.
t = np.linspace(t_0,t_end,int((t_end-t_0)/dt))
tdays = 1/(24*3600) * t

#Controller properties
dr = np.sqrt(2)
omega_n = 0.04
# kp = T_d/theta_ss
kp = 0

# ODE solver parameters
abserr = 1.0e-8
relerr = 1.0e-6

# %% EoM functions

def theta_2(w,t):
    return [w[1], 1/Iyyb*(T_dy - kd * w[1] - (3 * n_b**2 * (Ixxb - Izzb) + kp) * w[0])]

def theta_13(w,t):
    x1,y1,x3,y3 = w
    return [y1,
            1/Ixxb * (T_dx + (h_MBW + n_b * (Izzb + Ixxb - Iyyb))*y3 + (n_b * h_MBW -
                n_b**2 * (Iyyb - Izzb))*x1),
            y3,
            1/Izzb * (T_dz - (n_b * (Izzb + Ixxb - Iyyb) + h_MBW)*y1 + (n_b * h_MBW -
                n_b**2 * (Iyyb - Ixxb))*x3)]

# %% EoM for body in X, MBW in Y and T_D in X
```

```
Ixxb = I2
Iyyb = I1
Izzb = I1

hxxw = 0
hyyw = h_MBW
hzzw = 0

kd = 2 * dr * np.sqrt(kp * Iyyb)

T_dx = T_d
T_dy = 0
T_dz = 0

theta2, thetadot2 = odeint(theta_2, [0,0], t, atol=abserr, rtol=relerr).T
theta1, thetadot1, theta3, thetadot3 = odeint(theta_13, [0,0,0,0], t, atol=abserr, rtol=
    relerr).T

# theta1, thetadot1, theta2, thetadot2, theta3, thetadot3 = odeint(EoM, [0,0,0,0,0,0], t
    , atol=abserr, rtol=relerr).T

plt.figure()
plt.plot(t, theta1*180/np.pi, linewidth = 1)
plt.title("X orientation with body in X, MBW in Y and T_D in X")
plt.xlabel("Time (s)")
plt.ylabel("Orientation (deg)")
plt.savefig('EoM/EoM(body=X,MBW=Y,T_D=X)(X).jpg')
plt.grid(True)


plt.figure()
plt.plot(t, theta2*180/np.pi, linewidth = 1)
plt.title("Y orientation with body in X, MBW in Y and T_D in X")
plt.xlabel("Time (s)")
plt.ylabel("Orientation (deg)")
plt.savefig('EoM/EoM(body=X,MBW=Y,T_D=X)(Y).jpg')
plt.grid(True)

plt.figure()
plt.plot(t, theta3*180/np.pi, linewidth = 1)
plt.title("Z orientation with body in X, MBW in Y and T_D in X")
plt.xlabel("Time (s)")
plt.ylabel("Orientation (deg)")
plt.savefig('EoM/EoM(body=X,MBW=Y,T_D=X)(Z).jpg')
plt.grid(True)

plt.close('all')
# %% EoM for body in X, MBW in Y and T_D in Y
T_dx = 0
T_dy = T_d
T_dz = 0

Ixxb = I2                          #moment of inertia xx, kgm2
Iyyb = I1                          #moment of inertia yy, kgm2
Izzb = I1                          #moment of inertia zz,kgm2

kd = 2 * dr * np.sqrt(kp * Iyyb)

theta2, thetadot2 = odeint(theta_2, [0,0], t, atol=abserr, rtol=relerr).T
theta1, thetadot1, theta3, thetadot3 = odeint(theta_13, [0,0,0,0], t, atol=abserr, rtol=
    relerr).T

plt.figure()
plt.plot(t, theta1*180/np.pi, linewidth = 1)
plt.title("X orientation with body in X, MBW in Y and T_D in Y")
```

```
plt.xlabel("Time (s)")
plt.ylabel("Orientation (deg)")
plt.savefig('EoM/EoM(body=X,MBW=Y,T_D=Y)(X).jpg')
plt.grid(True)

plt.figure()
plt.plot(t, theta2*180/np.pi, linewidth = 1)
plt.title("Y orientation with body in X, MBW in Y and T_D in Y")
plt.xlabel("Time (s)")
plt.ylabel("Orientation (deg)")
plt.savefig('EoM/EoM(body=X,MBW=Y,T_D=Y)(Y).jpg')
plt.grid(True)

plt.figure()
plt.plot(t, theta3*180/np.pi, linewidth = 1)
plt.title("Z orientation with body in X, MBW in Y and T_D in Y")
plt.xlabel("Time (s)")
plt.ylabel("Orientation (deg)")
plt.savefig('EoM/EoM(body=X,MBW=Y,T_D=Y)(Z).jpg')
plt.grid(True)

plt.close('all')
# %% EoM for body in X, MBW in Y and T_D in Z
T_dx = 0
T_dy = 0
T_dz = T_d

Ixxb = I2                           #moment of inertia xx, kgm2
Iyyb = I1                           #moment of inertia yy, kgm2
Izzb = I1                           #moment of inertia zz,kgm2

kd = 2 * dr * np.sqrt(kp * Iyyb)

theta2, thetadot2 = odeint(theta_2, [0,0], t, atol=abserr, rtol=relerr).T
theta1, thetadot1, theta3, thetadot3 = odeint(theta_13, [0,0,0,0], t, atol=abserr, rtol=relerr).T

plt.figure()
plt.plot(t, theta1*180/np.pi, linewidth = 1)
plt.title("X orientation with body in X, MBW in Y and T_D in Z")
plt.xlabel("Time (s)")
plt.ylabel("Orientation (deg)")
plt.savefig('EoM/EoM(body=X,MBW=Y,T_D=Z)(X).jpg')
plt.grid(True)

plt.figure()
plt.plot(t, theta2*180/np.pi, linewidth = 1)
plt.title("Y orientation with body in X, MBW in Y and T_D in Z")
plt.xlabel("Time (s)")
plt.ylabel("Orientation (deg)")
plt.savefig('EoM/EoM(body=X,MBW=Y,T_D=Z)(Y).jpg')
plt.grid(True)

plt.figure()
plt.plot(t, theta3*180/np.pi, linewidth = 1)
plt.title("Z orientation with body in X, MBW in Y and T_D in Z")
plt.xlabel("Time (s)")
plt.ylabel("Orientation (deg)")
plt.savefig('EoM/EoM(body=X,MBW=Y,T_D=Z)(Z).jpg')
plt.grid(True)

plt.close('all')
# %% EoM for body in Y, MBW in Y and T_D in X
T_dx = T_d
T_dy = 0
```

```
T_dz = 0

Ixxb = I1                           #moment of inertia xx, kgm2
Iyyb = I2                           #moment of inertia yy, kgm2
Izzb = I1                           #moment of inertia zz,kgm2

kd = 2 * dr * np.sqrt(kp * Iyyb)

theta2, thetadot2 = odeint(theta_2, [0,0], t, atol=abserr, rtol=relerr).T
theta1, thetadot1, theta3, thetadot3 = odeint(theta_13, [0,0,0,0], t, atol=abserr, rtol=
    relerr).T

plt.figure()
plt.plot(t, theta1*180/np.pi, linewidth = 1)
plt.title("X␣orientation␣with␣body␣in␣Y,␣MBW␣in␣Y␣and␣T_D␣in␣X")
plt.xlabel("Time␣(s)")
plt.ylabel("Orientation␣(deg)")
plt.savefig('EoM/EoM(body=Y,MBW=Y,T_D=X)(X).jpg')
plt.grid(True)

plt.figure()
plt.plot(t, theta2*180/np.pi, linewidth = 1)
plt.title("Y␣orientation␣with␣body␣in␣Y,␣MBW␣in␣Y␣and␣T_D␣in␣X")
plt.xlabel("Time␣(s)")
plt.ylabel("Orientation␣(deg)")
plt.savefig('EoM/EoM(body=Y,MBW=Y,T_D=X)(Y).jpg')
plt.grid(True)

plt.figure()
plt.plot(t, theta3*180/np.pi, linewidth = 1)
plt.title("Z␣orientation␣with␣body␣in␣Y,␣MBW␣in␣Y␣and␣T_D␣in␣X")
plt.xlabel("Time␣(s)")
plt.ylabel("Orientation␣(deg)")
plt.savefig('EoM/EoM(body=Y,MBW=Y,T_D=X)(Z).jpg')
plt.grid(True)

plt.close('all')
# %% EoM for body in Y, MBW in Y and T_D in Y
T_dx = 0
T_dy = T_d
T_dz = 0

Ixxb = I2                           #moment of inertia xx, kgm2
Iyyb = I1                           #moment of inertia yy, kgm2
Izzb = I1                           #moment of inertia zz,kgm2

kd = 2 * dr * np.sqrt(kp * Iyyb)

theta2, thetadot2 = odeint(theta_2, [0,0], t, atol=abserr, rtol=relerr).T
theta1, thetadot1, theta3, thetadot3 = odeint(theta_13, [0,0,0,0], t, atol=abserr, rtol=
    relerr).T

plt.figure()
plt.plot(t, theta1*180/np.pi, linewidth = 1)
plt.title("X␣orientation␣with␣body␣in␣Y,␣MBW␣in␣Y␣and␣T_D␣in␣Y")
plt.xlabel("Time␣(s)")
plt.ylabel("Orientation␣(deg)")
plt.savefig('EoM/EoM(body=Y,MBW=Y,T_D=Y)(X).jpg')
plt.grid(True)

plt.figure()
plt.plot(t, theta2*180/np.pi, linewidth = 1)
plt.title("Y␣orientation␣with␣body␣in␣Y,␣MBW␣in␣Y␣and␣T_D␣in␣Y")
plt.xlabel("Time␣(s)")
plt.ylabel("Orientation␣(deg)")
```

```
plt.savefig('EoM/EoM(body=Y,MBW=Y,T_D=Y)(Y).jpg')
plt.grid(True)

plt.figure()
plt.plot(t, theta3*180/np.pi, linewidth = 1)
plt.title("Z orientation with body in Y, MBW in Y and T_D in Y")
plt.xlabel("Time (s)")
plt.ylabel("Orientation (deg)")
plt.savefig('EoM/EoM(body=Y,MBW=Y,T_D=Y)(Z).jpg')
plt.grid(True)

plt.close('all')
# %% EoM for body in Y, MBW in Y and T_D in Z
T_dx = 0
T_dy = 0
T_dz = T_d

Ixxb = I2                               #moment of inertia xx, kgm2
Iyyb = I1                               #moment of inertia yy, kgm2
Izzb = I1                               #moment of inertia zz,kgm2

kd = 2 * dr * np.sqrt(kp * Iyyb)

theta2, thetadot2 = odeint(theta_2, [0,0], t, atol=abserr, rtol=relerr).T
theta1, thetadot1, theta3, thetadot3 = odeint(theta_13, [0,0,0,0], t, atol=abserr, rtol=
    relerr).T

plt.figure()
plt.plot(t, theta1*180/np.pi, linewidth = 1)
plt.title("X orientation with body in Y, MBW in Y and T_D in Z")
plt.xlabel("Time (s)")
plt.ylabel("Orientation (deg)")
plt.savefig('EoM/EoM(body=Y,MBW=Y,T_D=Z)(X).jpg')
plt.grid(True)

plt.figure()
plt.plot(t, theta2*180/np.pi, linewidth = 1)
plt.title("Y orientation with body in Y, MBW in Y and T_D in Z")
plt.xlabel("Time (s)")
plt.ylabel("Orientation (deg)")
plt.savefig('EoM/EoM(body=Y,MBW=Y,T_D=Z)(Y).jpg')
plt.grid(True)

plt.figure()
plt.plot(t, theta3*180/np.pi, linewidth = 1)
plt.title("Z orientation with body in Y, MBW in Y and T_D in Z")
plt.xlabel("Time (s)")
plt.ylabel("Orientation (deg)")
plt.savefig('EoM/EoM(body=Y,MBW=Y,T_D=Z)(Z).jpg')
plt.grid(True)

plt.close('all')
# %% EoM for body in Z, MBW in Y and T_D in X
T_dx = T_d
T_dy = 0
T_dz = 0

Ixxb = I1                               #moment of inertia xx, kgm2
Iyyb = I1                               #moment of inertia yy, kgm2
Izzb = I2                               #moment of inertia zz,kgm2

kd = 2 * dr * np.sqrt(kp * Iyyb)

theta2, thetadot2 = odeint(theta_2, [0,0], t, atol=abserr, rtol=relerr).T
theta1, thetadot1, theta3, thetadot3 = odeint(theta_13, [0,0,0,0], t, atol=abserr, rtol=
```

```
    relerr).T

plt.figure()
plt.plot(t, theta1*180/np.pi, linewidth = 1)
plt.title("X orientation with body in Z, MBW in Y and T_D in X")
plt.xlabel("Time (s)")
plt.ylabel("Orientation (deg)")
plt.savefig('EoM/EoM(body=Z,MBW=Y,T_D=X)(X).jpg')
plt.grid(True)

plt.figure()
plt.plot(t, theta2*180/np.pi, linewidth = 1)
plt.title("Y orientation with body in Z, MBW in Y and T_D in X")
plt.xlabel("Time (s)")
plt.ylabel("Orientation (deg)")
plt.savefig('EoM/EoM(body=Z,MBW=Y,T_D=X)(Y).jpg')
plt.grid(True)

plt.figure()
plt.plot(t, theta3*180/np.pi, linewidth = 1)
plt.title("Z orientation with body in Z, MBW in Y and T_D in X")
plt.xlabel("Time (s)")
plt.ylabel("Orientation (deg)")
plt.savefig('EoM/EoM(body=Z,MBW=Y,T_D=X)(Z).jpg')
plt.grid(True)

plt.close('all')
# %% EoM for body in Z, MBW in Y and T_D in Y
T_dx = 0
T_dy = T_d
T_dz = 0

Ixxb = I1                           #moment of inertia xx, kgm2
Iyyb = I1                           #moment of inertia yy, kgm2
Izzb = I2                           #moment of inertia zz,kgm2

kd = 2 * dr * np.sqrt(kp * Iyyb)

theta2, thetadot2 = odeint(theta_2, [0,0], t, atol=abserr, rtol=relerr).T
theta1, thetadot1, theta3, thetadot3 = odeint(theta_13, [0,0,0,0], t, atol=abserr, rtol=
    relerr).T

plt.figure()
plt.plot(t, theta1*180/np.pi, linewidth = 1)
plt.title("X orientation with body in Z, MBW in Y and T_D in Y")
plt.xlabel("Time (s)")
plt.ylabel("Orientation (deg)")
plt.savefig('EoM/EoM(body=Z,MBW=Y,T_D=Y)(X).jpg')
plt.grid(True)

plt.figure()
plt.plot(t, theta2*180/np.pi, linewidth = 1)
plt.title("Y orientation with body in Z, MBW in Y and T_D in Y")
plt.xlabel("Time (s)")
plt.ylabel("Orientation (deg)")
plt.savefig('EoM/EoM(body=Z,MBW=Y,T_D=Y)(Y).jpg')
plt.grid(True)

plt.figure()
plt.plot(t, theta3*180/np.pi, linewidth = 1)
plt.title("Z orientation with body in Z, MBW in Y and T_D in Y")
plt.xlabel("Time (s)")
plt.ylabel("Orientation (deg)")
plt.savefig('EoM/EoM(body=Z,MBW=Y,T_D=Y)(Z).jpg')
plt.grid(True)
```

```
plt.close('all')
# %% EoM for body in Z, MBW in Y and T_D in Z
T_dx = 0
T_dy = 0
T_dz = T_d

Ixxb = I1                           #moment of inertia xx, kgm2
Iyyb = I1                           #moment of inertia yy, kgm2
Izzb = I2                           #moment of inertia zz,kgm2

kd = 2 * dr * np.sqrt(kp * Iyyb)

theta2, thetadot2 = odeint(theta_2, [0,0], t, atol=abserr, rtol=relerr).T
theta1, thetadot1, theta3, thetadot3 = odeint(theta_13, [0,0,0,0], t, atol=abserr, rtol=
    relerr).T

plt.figure()
plt.plot(t, theta1*180/np.pi, linewidth = 1)
plt.title("X␣orientation␣with␣body␣in␣Z,␣MBW␣in␣Y␣and␣T_D␣in␣Z")
plt.xlabel("Time␣(s)")
plt.ylabel("Orientation␣(deg)")
plt.savefig('EoM/EoM(body=Z,MBW=Y,T_D=Z)(X).jpg')
plt.grid(True)

plt.figure()
plt.plot(t, theta2*180/np.pi, linewidth = 1)
plt.title("Y␣orientation␣with␣body␣in␣Z,␣MBW␣in␣Y␣and␣T_D␣in␣Z")
plt.xlabel("Time␣(s)")
plt.ylabel("Orientation␣(deg)")
plt.savefig('EoM/EoM(body=Z,MBW=Y,T_D=Z)(Y).jpg')
plt.grid(True)

plt.figure()
plt.plot(t, theta3*180/np.pi, linewidth = 1)
plt.title("Z␣orientation␣with␣body␣in␣Z,␣MBW␣in␣Y␣and␣T_D␣in␣Z")
plt.xlabel("Time␣(s)")
plt.ylabel("Orientation␣(deg)")
plt.savefig('EoM/EoM(body=Z,MBW=Y,T_D=Z)(Z).jpg')
plt.grid(True)

plt.close('all')
```

```
# -*- coding: utf-8 -*-
"""
Equations of motion for MBW PQ

author: Jari Pols
thesis: MBW for PQ
"""
import numpy as np
import matplotlib.pyplot as plt
from scipy.integrate import odeint

#Physical properties 3p PQ
m_b = 0.75                          #mass PQ, kg
I1 = m_b/12 * (0.178**2 + 0.05**2)  #moment of inertia axis 1, kgm2
I2 = m_b/6 * (0.05**2)              #moment of inertia axis 2, kgm2
A_a1 = 0.05**2                      #smallest frontal area, m2
A_a2 = 0.196*0.058                  #largest frontal area, m2
dCp = 0.01                          #assumption for distance centre of mass and pressure

#Orbit properties
R_E = 6371E3                        #radius Earth, m
GP_E = 3.986004418E14               #gravitational parameter Earth, m^3/s^2
h_i = 300E3                         #orbit altitude, m
rho_max = 4.39E-11                  #maximum density at lowest altitude, kg/m3
n_b = np.sqrt(GP_E/(R_E+h_i)**3)    #mean motion, rad/s
P_orbit = 2 * np.pi * np.sqrt((R_E + h_i)**3 / GP_E) #orbital period, s

#Mission properties
theta_ss = 1 * np.pi/180.
T_d = 83.3E-9
h_MBW = 0.00605
t_0 = 0.0
n_orbit = 1
t_end = n_orbit * 2 * np.pi * np.sqrt((R_E+h_i)**3/GP_E)
dt = 1.
t = np.linspace(t_0,t_end,int((t_end-t_0)/dt))
tdays = 1/(24*3600) * t

#Controller properties
dr = np.sqrt(2)
omega_n = 0.04
# kp = T_d/theta_ss
kp = 0

# ODE solver parameters
abserr = 1.0e-8
relerr = 1.0e-6

# %% EoM functions

def EoM(w,t):
    x1,y1,x2,y2,x3,y3 = w
    return [y1,
            1/Ixxb * (T_dx + (1 + Izzb - Iyyb) * n_b * y3 - 4 * n_b**2 * (Iyyb - Izzb) *
                 x1 - h_MBW * y2 + n_b * h_MBW),
            y2,
            1/Iyyb * (T_dy + 3 * n_b**2 * (Izzb - Ixxb) * x2 + h_MBW * y1 - n_b * h_MBW
                * x3),
            y3,
            1/Izzb * (T_dz + (Iyyb - Ixxb - 1) * n_b * y1 - kd * y3 + ((Ixxb - Iyyb) *
                n_b**2 - kp) * x3)]


# %% EoM for body in X, MBW in Z and T_D in X
T_dx = T_d
```

```
T_dy = 0
T_dz = 0

Ixxb = I2                           #moment of inertia xx, kgm2
Iyyb = I1                           #moment of inertia yy, kgm2
Izzb = I1                           #moment of inertia zz,kgm2

kd = 2 * dr * np.sqrt(kp * Izzb)

theta1, thetadot1, theta2, thetadot2, theta3, thetadot3 = odeint(EoM, [0,0,0,0,0,0], t,
    atol=abserr, rtol=relerr).T

plt.figure()
plt.plot(t, theta1*180/np.pi, linewidth = 1)
plt.title("X␣orientation␣with␣body␣in␣X,␣MBW␣in␣Z␣and␣T_D␣in␣X")
plt.xlabel("Time␣(s)")
plt.ylabel("Orientation␣(deg)")
plt.savefig('EoM/EoM(body=X,MBW=Z,T_D=X)(X).jpg')
plt.grid(True)


plt.figure()
plt.plot(t, theta2*180/np.pi, linewidth = 1)
plt.title("Y␣orientation␣with␣body␣in␣X,␣MBW␣in␣Z␣and␣T_D␣in␣X")
plt.xlabel("Time␣(s)")
plt.ylabel("Orientation␣(deg)")
plt.savefig('EoM/EoM(body=X,MBW=Z,T_D=X)(Y).jpg')
plt.grid(True)

plt.figure()
plt.plot(t, theta3*180/np.pi, linewidth = 1)
plt.title("Z␣orientation␣with␣body␣in␣X,␣MBW␣in␣Z␣and␣T_D␣in␣X")
plt.xlabel("Time␣(s)")
plt.ylabel("Orientation␣(deg)")
plt.savefig('EoM/EoM(body=X,MBW=Z,T_D=X)(Z).jpg')
plt.grid(True)

plt.close('all')

# %% EoM for body in X, MBW in Z and T_D in Y
T_dx = 0
T_dy = T_d
T_dz = 0

Ixxb = I2                           #moment of inertia xx, kgm2
Iyyb = I1                           #moment of inertia yy, kgm2
Izzb = I1                           #moment of inertia zz,kgm2

kd = 2 * dr * np.sqrt(kp * Izzb)

theta1, thetadot1, theta2, thetadot2, theta3, thetadot3 = odeint(EoM, [0,0,0,0,0,0], t,
    atol=abserr, rtol=relerr).T

plt.figure()
plt.plot(t, theta1*180/np.pi, linewidth = 1)
plt.title("X␣orientation␣with␣body␣in␣X,␣MBW␣in␣Z␣and␣T_D␣in␣Y")
plt.xlabel("Time␣(s)")
plt.ylabel("Orientation␣(deg)")
plt.savefig('EoM/EoM(body=X,MBW=Z,T_D=Y)(X).jpg')
plt.grid(True)


plt.figure()
plt.plot(t, theta2*180/np.pi, linewidth = 1)
plt.title("Y␣orientation␣with␣body␣in␣X,␣MBW␣in␣Z␣and␣T_D␣in␣Y")
```

```
plt.xlabel("Time␣(s)")
plt.ylabel("Orientation␣(deg)")
plt.savefig('EoM/EoM(body=X,MBW=Z,T_D=Y)(Y).jpg')
plt.grid(True)

plt.figure()
plt.plot(t, theta3*180/np.pi, linewidth = 1)
plt.title("Z␣orientation␣with␣body␣in␣X,␣MBW␣in␣Z␣and␣T_D␣in␣Y")
plt.xlabel("Time␣(s)")
plt.ylabel("Orientation␣(deg)")
plt.savefig('EoM/EoM(body=X,MBW=Z,T_D=Y)(Z).jpg')
plt.grid(True)

plt.close('all')

# %% EoM for body in X, MBW in Z and T_D in Z
T_dx = 0
T_dy = 0
T_dz = T_d

Ixxb = I2                              #moment of inertia xx, kgm2
Iyyb = I1                              #moment of inertia yy, kgm2
Izzb = I1                              #moment of inertia zz,kgm2

kd = 2 * dr * np.sqrt(kp * Izzb)

theta1, thetadot1, theta2, thetadot2, theta3, thetadot3 = odeint(EoM, [0,0,0,0,0,0], t,
    atol=abserr, rtol=relerr).T

plt.figure()
plt.plot(t, theta1*180/np.pi, linewidth = 1)
plt.title("X␣orientation␣with␣body␣in␣X,␣MBW␣in␣Z␣and␣T_D␣in␣Z")
plt.xlabel("Time␣(s)")
plt.ylabel("Orientation␣(deg)")
plt.savefig('EoM/EoM(body=X,MBW=Z,T_D=Z)(X).jpg')
plt.grid(True)


plt.figure()
plt.plot(t, theta2*180/np.pi, linewidth = 1)
plt.title("Y␣orientation␣with␣body␣in␣X,␣MBW␣in␣Z␣and␣T_D␣in␣Z")
plt.xlabel("Time␣(s)")
plt.ylabel("Orientation␣(deg)")
plt.savefig('EoM/EoM(body=X,MBW=Z,T_D=Z)(Y).jpg')
plt.grid(True)

plt.figure()
plt.plot(t, theta3*180/np.pi, linewidth = 1)
plt.title("Z␣orientation␣with␣body␣in␣X,␣MBW␣in␣Z␣and␣T_D␣in␣Z")
plt.xlabel("Time␣(s)")
plt.ylabel("Orientation␣(deg)")
plt.savefig('EoM/EoM(body=X,MBW=Z,T_D=Z)(Z).jpg')
plt.grid(True)

plt.close('all')

# %% EoM for body in Y, MBW in Z and T_D in X
T_dx = T_d
T_dy = 0
T_dz = 0

Ixxb = I1                              #moment of inertia xx, kgm2
Iyyb = I2                              #moment of inertia yy, kgm2
Izzb = I1                              #moment of inertia zz,kgm2

```

```
kd = 2 * dr * np.sqrt(kp * Izzb)

theta1, thetadot1, theta2, thetadot2, theta3, thetadot3 = odeint(EoM, [0,0,0,0,0,0], t,
    atol=abserr, rtol=relerr).T

plt.figure()
plt.plot(t, theta1*180/np.pi, linewidth = 1)
plt.title("X orientation with body in Y, MBW in Z and T_D in X")
plt.xlabel("Time (s)")
plt.ylabel("Orientation (deg)")
plt.savefig('EoM/EoM(body=Y,MBW=Z,T_D=X)(X).jpg')
plt.grid(True)


plt.figure()
plt.plot(t, theta2*180/np.pi, linewidth = 1)
plt.title("Y orientation with body in Y, MBW in Z and T_D in X")
plt.xlabel("Time (s)")
plt.ylabel("Orientation (deg)")
plt.savefig('EoM/EoM(body=Y,MBW=Z,T_D=X)(Y).jpg')
plt.grid(True)

plt.figure()
plt.plot(t, theta3*180/np.pi, linewidth = 1)
plt.title("Z orientation with body in Y, MBW in Z and T_D in X")
plt.xlabel("Time (s)")
plt.ylabel("Orientation (deg)")
plt.savefig('EoM/EoM(body=Y,MBW=Z,T_D=X)(Z).jpg')
plt.grid(True)

plt.close('all')

# %% EoM for body in Y, MBW in Z and T_D in Y
T_dx = 0
T_dy = T_d
T_dz = 0

Ixxb = I1                          #moment of inertia xx, kgm2
Iyyb = I2                          #moment of inertia yy, kgm2
Izzb = I1                          #moment of inertia zz,kgm2

kd = 2 * dr * np.sqrt(kp * Izzb)

theta1, thetadot1, theta2, thetadot2, theta3, thetadot3 = odeint(EoM, [0,0,0,0,0,0], t,
    atol=abserr, rtol=relerr).T

plt.figure()
plt.plot(t, theta1*180/np.pi, linewidth = 1)
plt.title("X orientation with body in Y, MBW in Z and T_D in Y")
plt.xlabel("Time (s)")
plt.ylabel("Orientation (deg)")
plt.savefig('EoM/EoM(body=Y,MBW=Z,T_D=Y)(X).jpg')
plt.grid(True)


plt.figure()
plt.plot(t, theta2*180/np.pi, linewidth = 1)
plt.title("Y orientation with body in Y, MBW in Z and T_D in Y")
plt.xlabel("Time (s)")
plt.ylabel("Orientation (deg)")
plt.savefig('EoM/EoM(body=Y,MBW=Z,T_D=Y)(Y).jpg')
plt.grid(True)

plt.figure()
plt.plot(t, theta3*180/np.pi, linewidth = 1)
```

```
plt.title("Z orientation with body in Y, MBW in Z and T_D in Y")
plt.xlabel("Time (s)")
plt.ylabel("Orientation (deg)")
plt.savefig('EoM/EoM(body=Y,MBW=Z,T_D=Y)(Z).jpg')
plt.grid(True)

plt.close('all')

# %% EoM for body in Y, MBW in Z and T_D in Z
T_dx = 0
T_dy = 0
T_dz = T_d

Ixxb = I1                          #moment of inertia xx, kgm2
Iyyb = I2                          #moment of inertia yy, kgm2
Izzb = I1                          #moment of inertia zz,kgm2

kd = 2 * dr * np.sqrt(kp * Izzb)

theta1, thetadot1, theta2, thetadot2, theta3, thetadot3 = odeint(EoM, [0,0,0,0,0,0], t,
    atol=abserr, rtol=relerr).T

plt.figure()
plt.plot(t, theta1*180/np.pi, linewidth = 1)
plt.title("X orientation with body in Y, MBW in Z and T_D in Z")
plt.xlabel("Time (s)")
plt.ylabel("Orientation (deg)")
plt.savefig('EoM/EoM(body=Y,MBW=Z,T_D=Z)(X).jpg')
plt.grid(True)


plt.figure()
plt.plot(t, theta2*180/np.pi, linewidth = 1)
plt.title("Y orientation with body in Y, MBW in Z and T_D in Z")
plt.xlabel("Time (s)")
plt.ylabel("Orientation (deg)")
plt.savefig('EoM/EoM(body=Y,MBW=Z,T_D=Z)(Y).jpg')
plt.grid(True)

plt.figure()
plt.plot(t, theta3*180/np.pi, linewidth = 1)
plt.title("Z orientation with body in Y, MBW in Z and T_D in Z")
plt.xlabel("Time (s)")
plt.ylabel("Orientation (deg)")
plt.savefig('EoM/EoM(body=Y,MBW=Z,T_D=Z)(Z).jpg')
plt.grid(True)

plt.close('all')

# %% EoM for body in Z, MBW in Z and T_D in X
T_dx = T_d
T_dy = 0
T_dz = 0

Ixxb = I1                          #moment of inertia xx, kgm2
Iyyb = I1                          #moment of inertia yy, kgm2
Izzb = I2                          #moment of inertia zz,kgm2

kd = 2 * dr * np.sqrt(kp * Izzb)

theta1, thetadot1, theta2, thetadot2, theta3, thetadot3 = odeint(EoM, [0,0,0,0,0,0], t,
    atol=abserr, rtol=relerr).T

plt.figure()
plt.plot(t, theta1*180/np.pi, linewidth = 1)
```

```
plt.title("X orientation with body in Z, MBW in Z and T_D in X")
plt.xlabel("Time (s)")
plt.ylabel("Orientation (deg)")
plt.savefig('EoM/EoM(body=Z,MBW=Z,T_D=X)(X).jpg')
plt.grid(True)


plt.figure()
plt.plot(t, theta2*180/np.pi, linewidth = 1)
plt.title("Y orientation with body in Z, MBW in Z and T_D in X")
plt.xlabel("Time (s)")
plt.ylabel("Orientation (deg)")
plt.savefig('EoM/EoM(body=Z,MBW=Z,T_D=X)(Y).jpg')
plt.grid(True)

plt.figure()
plt.plot(t, theta3*180/np.pi, linewidth = 1)
plt.title("Z orientation with body in Z, MBW in Z and T_D in X")
plt.xlabel("Time (s)")
plt.ylabel("Orientation (deg)")
plt.savefig('EoM/EoM(body=Z,MBW=Z,T_D=X)(Z).jpg')
plt.grid(True)

plt.close('all')

# %% EoM for body in Z, MBW in Z and T_D in Y
T_dx = 0
T_dy = T_d
T_dz = 0

Ixxb = I1                            #moment of inertia xx, kgm2
Iyyb = I1                            #moment of inertia yy, kgm2
Izzb = I2                            #moment of inertia zz,kgm2

kd = 2 * dr * np.sqrt(kp * Izzb)

theta1, thetadot1, theta2, thetadot2, theta3, thetadot3 = odeint(EoM, [0,0,0,0,0,0], t,
    atol=abserr, rtol=relerr).T

plt.figure()
plt.plot(t, theta1*180/np.pi, linewidth = 1)
plt.title("X orientation with body in Z, MBW in Z and T_D in Y")
plt.xlabel("Time (s)")
plt.ylabel("Orientation (deg)")
plt.savefig('EoM/EoM(body=Z,MBW=Z,T_D=Y)(X).jpg')
plt.grid(True)


plt.figure()
plt.plot(t, theta2*180/np.pi, linewidth = 1)
plt.title("Y orientation with body in Z, MBW in Z and T_D in Y")
plt.xlabel("Time (s)")
plt.ylabel("Orientation (deg)")
plt.savefig('EoM/EoM(body=Z,MBW=Z,T_D=Y)(Y).jpg')
plt.grid(True)

plt.figure()
plt.plot(t, theta3*180/np.pi, linewidth = 1)
plt.title("Z orientation with body in Z, MBW in Z and T_D in Y")
plt.xlabel("Time (s)")
plt.ylabel("Orientation (deg)")
plt.savefig('EoM/EoM(body=Z,MBW=Z,T_D=Y)(Z).jpg')
plt.grid(True)

plt.close('all')
```

```

# %% EoM for body in Z, MBW in Z and T_D in Z
T_dx = 0
T_dy = 0
T_dz = T_d

Ixxb = I1                           #moment of inertia xx, kgm2
Iyyb = I1                           #moment of inertia yy, kgm2
Izzb = I2                           #moment of inertia zz,kgm2

kd = 2 * dr * np.sqrt(kp * Izzb)

theta1, thetadot1, theta2, thetadot2, theta3, thetadot3 = odeint(EoM, [0,0,0,0,0,0], t,
    atol=abserr, rtol=relerr).T

plt.figure()
plt.plot(t, theta1*180/np.pi, linewidth = 1)
plt.title("X orientation with body in Z, MBW in Z and T_D in Z")
plt.xlabel("Time (s)")
plt.ylabel("Orientation (deg)")
plt.savefig('EoM/EoM(body=Z,MBW=Z,T_D=Z)(X).jpg')
plt.grid(True)


plt.figure()
plt.plot(t, theta2*180/np.pi, linewidth = 1)
plt.title("Y orientation with body in Z, MBW in Z and T_D in Z")
plt.xlabel("Time (s)")
plt.ylabel("Orientation (deg)")
plt.savefig('EoM/EoM(body=Z,MBW=Z,T_D=Z)(Y).jpg')
plt.grid(True)

plt.figure()
plt.plot(t, theta3*180/np.pi, linewidth = 1)
plt.title("Z orientation with body in Z, MBW in Z and T_D in Z")
plt.xlabel("Time (s)")
plt.ylabel("Orientation (deg)")
plt.savefig('EoM/EoM(body=Z,MBW=Z,T_D=Z)(Z).jpg')
plt.grid(True)

plt.close('all')
```

C. Motor Selection

Manufacturer	Model	D_b (mm)	L_b (mm)	m_m (g)	Commutation	ω_0 (rpm)	U_n (V)	I_0 (mA)	T_{min} $(°C)$	T_{max} $(°C)$	Bearing material/type	p_{min} (Pa)	Sensors	Trade-off
Precision Microdrives	310-003	10	3.4	1.1	Brushed Coreless Flat	10000	1.5	40	-20	60	Sintered bronze	NG	None	
Precision Microdrives	310-103	10	2.7	1	Brushed Coreless Flat	12200	3	58	-20	70	Sintered bronze	NG	None	
Precision Microdrives	310-118	10	2.1	0.8	Brushed Coreless Flat	14000	3	60	-20	60	Sintered bronze	NG	None	
Precision Microdrives	308-100	8	3.4	0.8	Brushed Coreless Flat	12500	3	70	-20	60	Sintered bronze	NG	None	
Precision Microdrives	306-103	6	12.2	2.7	Brushed Coreless	14300	3	66	-20	60	Sintered bronze	NG	None	
Precision Microdrives	304-11J	4.5	6.2	0.9	Brushed	10400	3	78	-20	70	Sintered bronze	NG	None	
Precision Microdrives	304-100	4.4	10.2	1	Brushed Coreless	16900	3	64	-20	60	Sintered bronze	NG	None	
Precision Microdrives	304-129	4.4	6	0.6	Brushed	15300	2.7	61	-20	70	Sintered bronze	NG	None	
Precision Microdrives	103-100	3.2	8.1	0.3	Brushed Coreless	34100	3	51	-30	70	Sintered bronze	NG	None	
Precision Microdrives	104-001	4.1	7.9	0.5	Brushed Coreless	35200	3	41	-10	50	Sintered bronze	NG	None	
Precision Microdrives	104-100	4	11	0.8	Brushed Coreless	15000	1.5	85	-20	60	Sintered bronze	NG	None	
Precision Microdrives	303-102	3.2	8.1	1	Brushed Coreless	14500	3	81	-30	70	Sintered bronze	NG	None	
Orbray	BMN04-0829	4	8.5	0.7	BLDC	24200	3	53	-20	80	Sleeve bearing	NG	None	
Orbray	BMS10-1003	10	10	4.5	BLDC	30400	4	384	-20	80	Sleeve bearing	NG	Hall sensors	
Maxon Motors	DCX 6M	6	18	2.4	Brushed	17300	1.5	34	-30	85	Ball/sleave bearing	NG	Maxon encoder	
Maxon Motors	ECX Speed 4M	4	18.5	1.2	BLDC	35300	3	29	-20	80	Ball bearing	NG	Hall sensors	Yes
Maxon Motors	ECX Speed 4L	4	26.55	1.8	BLDC	40700	3	56	-20	80	Ball bearing	NG	Hall sensors	Yes
Maxon Motors	ECX Speed 6M	6	22.8	3	BLDC	44200	6	47	-20	80	Ball bearing	NG	Hall sensors	Yes
Maxon Motors	EC 10 Flat	10	5.05	0.82	BLDC	16600	4	15	-40	85	Ball bearing	NG	Hall sensors	
Maxon Motors	EC 9.2 Flat	10	14.8	3	BLDC	13900	3	52	-20	85	Ball bearing	NG	Hall sensors	Yes
Maxon Motors	EC 14 Flat	13.6	11.7	8	BLDC	20000	6	156	-40	100	Ball bearing	NG	None	
Faulhaber	0308H003B	3	8.4	0.35	BLDC	61000	3	27	-30	60	Ruby ball bearing	NG	None	
Faulhaber	0515G006B	5	14	1.6	BLDC	43000	6	56	-30	80	Sintered bronze	NG	None	
Faulhaber	0620K006B-K179	6	21.9	2.5	BLDC	48600	6	56	-20	100	Ball bearing	10^{-5}	Hall sensors	Yes
Faulhaber	0824K006B-K179	8	26	5.2	BLDC	35100	6	55	-20	100	Ball bearing	10^{-5}	Hall sensors	Yes
Faulhaber	1028S006B-K179	10	30	9.4	BLDC	32300	6	121	-20	100	Ball bearing	10^{-5}	Hall sensors	Yes
Faulhaber	1202H004BH	12	2.04	1.1	BLDC	41740	3	28	-30	85	Ball bearing	10^{-5}	Hall sensors	
Faulhaber	1506N003SR	15	6.2	4.3	Brushed	11200	3	8	-25	80	Sintered bronze	NG	None	
Faulhaber	1509T006B-X4192	15	8.8	6.9	BLDC	15000	6	19	-25	80	Ball bearing	10^{-5}	Hall sensors	Yes
Ineed Electronics	JT0408SH-1	4	8	NG	Brushed Coreless	33000	3	60	NG	NG	NG	NG	None	
Ineed Electronics	YQ0408-002	4	8	NG	Brushed Coreless	38000	3	60	NG	NG	NG	NG	None	
Ineed Electronics	YQ0610-002	6	10.3	NG	Brushed Coreless	40880	3	73	NG	NG	NG	NG	None	
Ineed Electronics	YQ0410L-001	4	10	2	Brushed Coreless	21000	1.3	50	-30	70	NG	NG	None	
Portescap	08ECP20 8B 84	8	21.95	9	BLDC	22700	6	40	-30	100	Ball bearing	NG		
Portescap	12ECP48 8B 21	12	52.5	30	BLDC	36000	9	200	-30	100	Ball bearing	NG		
Vybronics	VW0625AB001G	6	2.5	0.9	Brushed Coreless	15000	3	90	-20	60	NG	NG	None	
Vybronics	VW0825AB002G	8	2.5	0.83	Brushed Coreless	13500	3	80	-20	60	SIM	NG	None	
Vybronics	VW0620AB001U	6	2	0.37	Brushed Coreless	13000	3	80	-20	60	NG	NG	None	
Vybronics	VCDM1027B003L	10	2.7	NG	Brushed Coreless	13000	3	53	-30	70	NG	NG	None	
Vybronics	VZ30C1T8460002L	3	6.8	0.9	Brushed Coreless Flat	15000	85	2.7	-30	70	NG	NG	None	
Vybronics	VZ30L4B8790008L	3.15	6.55	1.1	Brushed Coreless Flat	14000	3	58	-30	70	NG	NG	None	
Vybronics	VZ43FC1B5640005L	4.3	5.5	1.1	Brushed Coreless Flat	9000	1.3	120	-30	70	Copper	NG	None	
Vybronics	VQ4TL2BQ360003	4	8	NG	BLDC	36000	3	55	-20	60	NG	NG	None	
Vybronics	VQ4TL2BQ380001	4	8	NG	BLDC	38000	3	60	-30	70	NG	NG	None	

D. Flywheel Design Derivations

Below the derivation the specific mass moment of inertia calculation and utilisation for all flywheel designs is shown. These calculations have been checked utilising CAD software Autodesk Inventor and Dassault Systems Solidworks.

D.1. Uniform Thickness

The simplest shape of all designs has a uniform thickness across its radius. The specific mass moment of inertia is thus calculated.

$$\dot{I} = \frac{I}{m} = \frac{\rho \cdot \pi \cdot \frac{1}{2} \cdot r_1^4 \cdot t_1}{\rho \cdot \pi \cdot r_1^2 \cdot t_1} = \frac{1}{2} r_1^2 \tag{D.1}$$

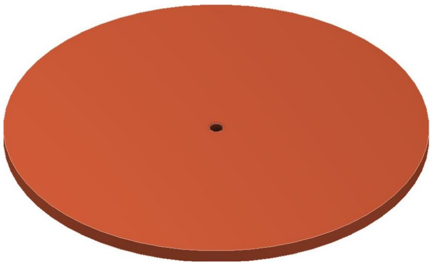

Figure D.1: ISO view of flywheel with uniform thickness.

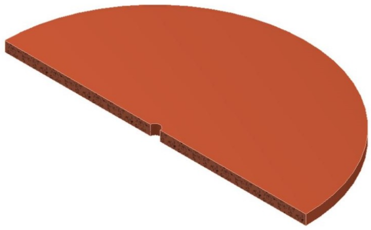

Figure D.2: Cross section ISO view of flywheel with uniform thickness.

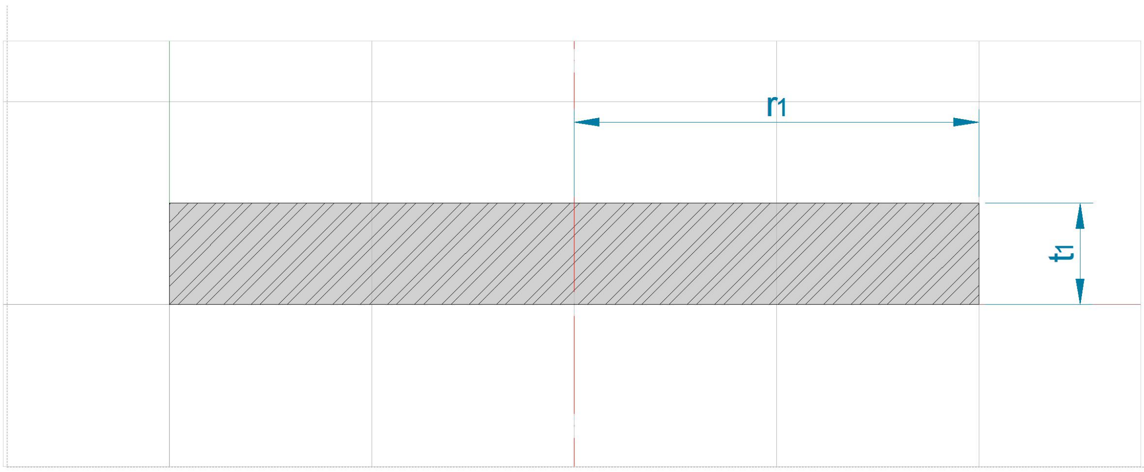

Figure D.3: Cross sectional drawing of the uniform thickness design with all variables noted.

D.2. Multiple Uniform Thickness

The multiple uniform thickness design allows for a simple increase of moment of inertia and thus angular momentum. The specific mass moment of inertia is calculated for two and three thicknesses, to check whether two steps would be more mass efficient than other designs calculated here. For the double thickness design:

$$m = \rho \cdot \pi \cdot (r_1^2 \cdot t_1 + (r_2^2 - r_1^2) \cdot t_2) \tag{D.2}$$

$$I = \rho \cdot \pi \cdot \frac{1}{2} \cdot (r_1^4 \cdot t_1 + (r_2^4 - r_1^4) \cdot t_2) \tag{D.3}$$

$$\dot{I} = \frac{1}{2} \frac{r_1^4 \cdot t_1 + (r_2^4 - r_1^4) \cdot t_2}{r_1^2 \cdot t_1 + (r_2^2 - r_1^2) \cdot t_2} \tag{D.4}$$

Figure D.4: ISO view of flywheel with stepped uniform thickness.

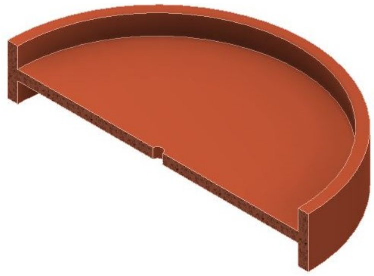

Figure D.5: Cross section ISO view of flywheel with stepped uniform thickness.

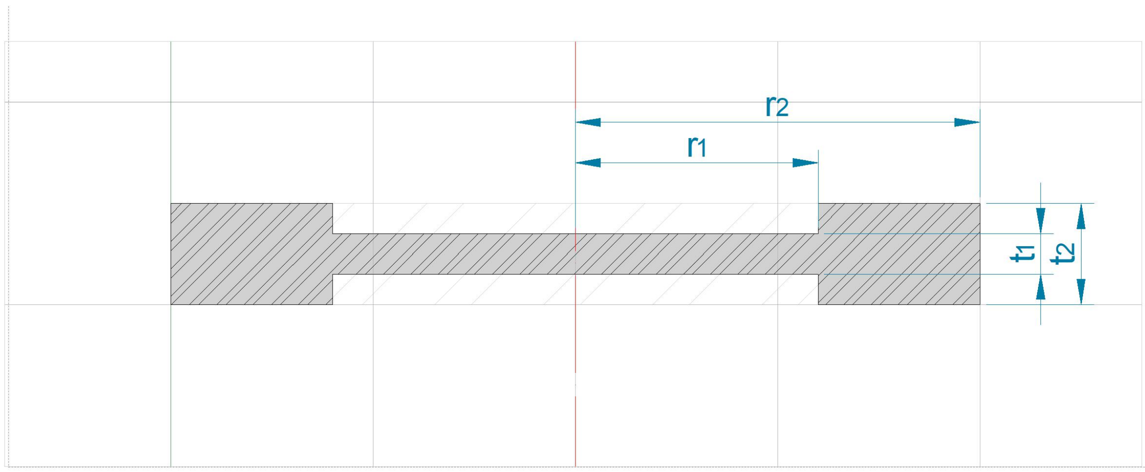

Figure D.6: Cross sectional drawing of the double thickness design with all variables noted.

And for the triple thickness design:

$$m = \rho \cdot \pi \cdot (r_1^2 \cdot t_1 + (r_2^2 - r_1^2) \cdot t_2 + (r_3^2 - r_2^2) \cdot t_3) \tag{D.5}$$

$$I = \rho \cdot \pi \cdot \frac{1}{2} \cdot (r_1^4 \cdot t_1 + (r_2^4 - r_1^4) \cdot t_2 + (r_3^4 - r_2^4) \cdot t_3) \tag{D.6}$$

$$\dot{I} = \frac{1}{2} \frac{r_1^4 \cdot t_1 + (r_2^4 - r_1^4) \cdot t_2 + (r_3^4 - r_2^4) \cdot t_3}{r_1^2 \cdot t_1 + (r_2^2 - r_1^2) \cdot t_2 + (r_3^2 - r_2^2) \cdot t_3} \tag{D.7}$$

Figure D.7: ISO view of flywheel with hybrid stepped design.

Figure D.8: Cross section ISO view of flywheel with hybrid stepped design.

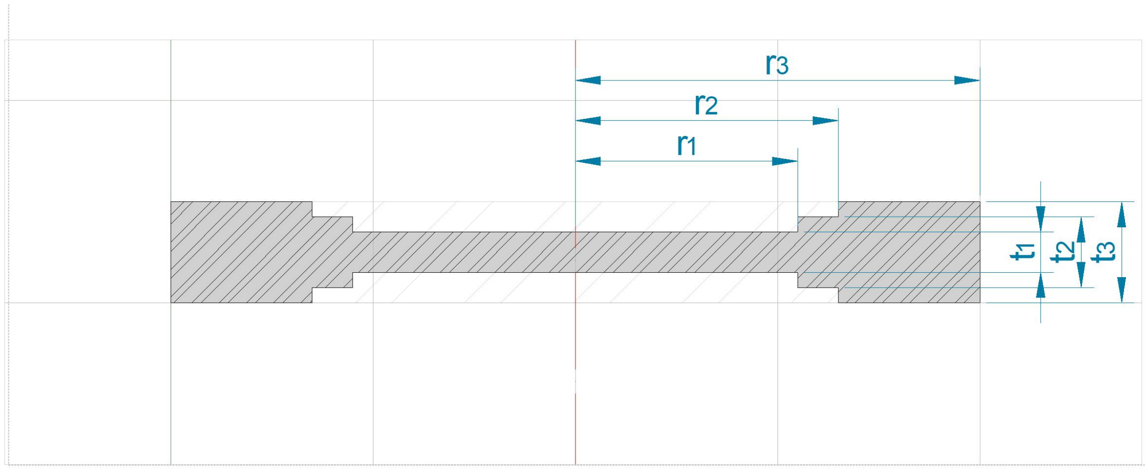

Figure D.9: Cross sectional drawing of the triple thickness design with all variables noted.

D.3. Linear Increasing Thickness

Implementing infinitely many uniform thicknesses into a design would eventually result in something similar to a linear increasing thickness over a certain range of radius. For this, the specific mass moment of inertia can be calculated through the usage of volume integrals. Just as with the multiple uniform thickness design, the calculation is split up and results in the following relation, but due to the thickness increasing, an integral containing a changing density is utilised, which will derived in this section.

$$\mathbf{m} = \rho \cdot \pi \cdot \left(r_2^2 \cdot t_1 + \left(r_2^2 \cdot (t_2 - t_1) - \int_0^{t_2 - t_1} \mathbf{r}^2 d\mathbf{t} \right) \right) = \rho \cdot \pi \cdot \left(r_2^2 \cdot t_1 \right) + \int_0^{2\pi} \int_{r_1}^{r_2} \rho(\mathbf{r}) \mathbf{r} d\mathbf{r} d\theta \tag{D.8}$$

$$\mathbf{I} = \frac{1}{2} \cdot \rho \cdot \pi \cdot r_2^4 \cdot t_1 + \int_0^{2\pi} \int_{r_1}^{r_2} \rho(\mathbf{r}) \mathbf{r}^3 d\mathbf{r} d\theta \tag{D.9}$$

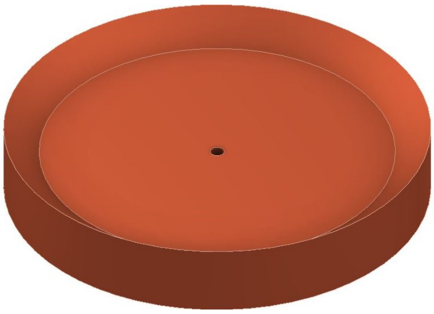

Figure D.10: ISO view of flywheel with linear increasing thickness.

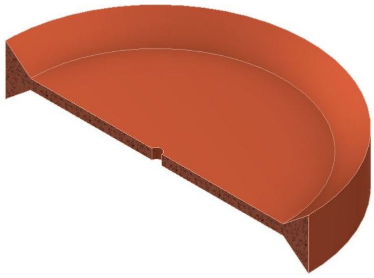

Figure D.11: Cross section ISO view of flywheel with linear increasing thickness.

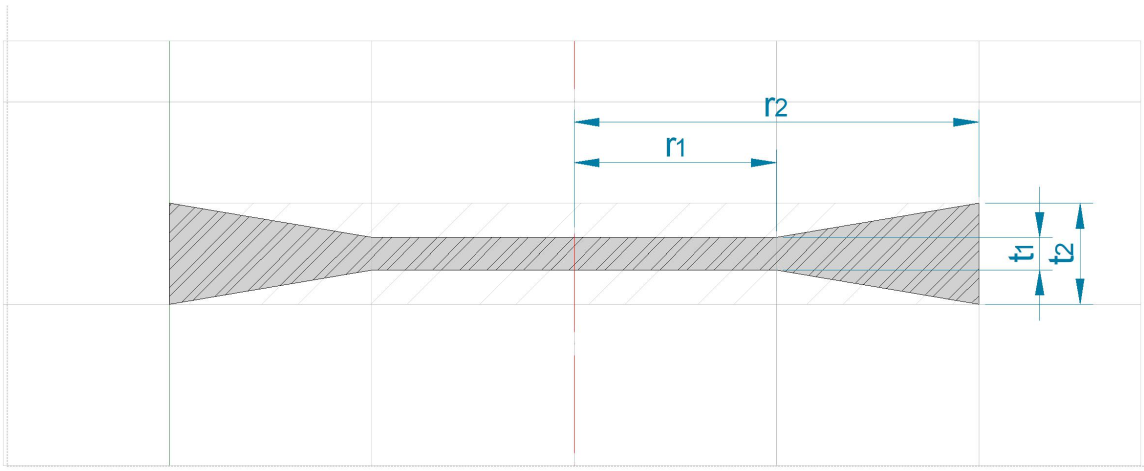

Figure D.12: Cross sectional drawing of the linearly increasing thickness design with all variables noted.

The integral within the left side of the mass equation relies on the changing thickness of the triangular part, which is a function of the radius. The cross sectional area of the disc design with a linearly increasing thickness shows the way to interpret this relation. The linearly increasing thickness will start at a certain r_1 and increase the thickness linearly from t_1 to t_2 at r_2. This would result in the following relations for the dimensions.

$$\mathbf{t} = (t_2 - t_1) \cdot \left(\frac{\mathbf{r} - r_1}{r_2 - r_1} \right) \tag{D.10}$$

$$\mathbf{r} = r_1 + (r_2 - r_1) \cdot \frac{\mathbf{t}}{t_2 - t_1} \tag{D.11}$$

Working out the integral in the left side of the mass function in equation D.8, results in the following relation.

$$\mathbf{m} = \rho \cdot \pi \cdot \left(r_2^2 \cdot t_1 + (r_2^2 \cdot (t_2 - t_1) - \int_0^{t_2 - t_1} \left(r_1 + (r_2 - r_1) \cdot \frac{\mathbf{t}}{t_2 - t_1} \right)^2 d\mathbf{t} \right) \tag{D.12}$$

$$\mathbf{m} = \rho \cdot \pi \cdot \left(r_2^2 \cdot t_1 + (r_2^2 \cdot (t_2 - t_1) - \left[r_1^2 \cdot \mathbf{t} + \frac{r_1 \cdot (r_2 - r_1)}{t_2 - t_1} \cdot \mathbf{t}^2 + \frac{1}{3} \cdot \left(\frac{r_2 - r_1}{t_2 - t_1} \right)^2 \cdot \mathbf{t}^3 \right]_0^{t_2 - t_1} \right) \tag{D.13}$$

$$\mathbf{m} = \rho \cdot \pi \cdot \left(r_2^2 \cdot t_1 + (r_2^2 \cdot (t_2 - t_1) - \left(r_1^2 \cdot (t_2 - t_1) + r_1 \cdot (r_2 - r_1) \cdot (t_2 - t_1) + \frac{1}{3} \cdot (r_2 - r_1)^2 \cdot (t_2 - t_1) \right) \right) \tag{D.14}$$

$$\mathbf{m} = \rho \cdot \pi \cdot \left(r_2^2 \cdot t_1 + (r_2^2 \cdot (t_2 - t_1) - (t_2 - t_1) \cdot \left(r_1^2 + r_1 \cdot (r_2 - r_1) + \frac{1}{3} \cdot (r_2 - r_1)^2 \right) \right) \tag{D.15}$$

$$\mathbf{m} = \rho \cdot \pi \cdot \left(r_2^2 \cdot t_1 + (t_2 - t_1) \cdot \left(\frac{2}{3} r_2^2 - \frac{1}{3} r_1 \cdot r_2 - \frac{1}{3} r_1^2 \right) \right) \tag{D.16}$$

The changing density as stated in equation D.9 will be assumed to be equal to $k \cdot r$, with k as a constant which will be derived through the mass.

$$\mathbf{I} = \frac{1}{2} \cdot \rho \cdot \pi \cdot r_2^4 \cdot t_1 + \int_0^{2\pi} \int_{r_1}^{r_2} \left(k \cdot \mathbf{r}^4 \right) d\mathbf{r} d\theta \tag{D.17}$$

$$\mathbf{I} = \frac{1}{2} \cdot \rho \cdot \pi \cdot r_2^4 \cdot t_1 + \frac{2\pi \cdot k}{5} \cdot \left[\mathbf{r}^5 \right]_{r_1}^{r_2} \tag{D.18}$$

$$\mathbf{I} = \frac{1}{2} \cdot \rho \cdot \pi \cdot r_2^4 \cdot t_1 + \frac{2\pi \cdot k}{5} \cdot \left(r_2^5 - r_1^5 \right) \tag{D.19}$$

The mass of the triangular part of the disc can be calculated utilising the same variable k, and it shall be equalled to the derivation of the mass of the triangular part as stated in equation D.16.

$$\mathbf{m}_l = \int_0^{2\pi} \int_{r_1}^{r_2} \left(k \cdot \mathbf{r}^2 \right) d\mathbf{r} d\theta \tag{D.20}$$

$$\mathbf{m}_l = 2\pi \cdot k \cdot \left[\frac{1}{3} \mathbf{r}^3 \right]_{r_1}^{r_2} \tag{D.21}$$

$$\mathbf{m}_l = \frac{2}{3} \pi \cdot k \cdot \left(r_2^3 - r_1^3 \right) = \rho \cdot \pi \cdot (t_2 - t_1) \cdot \left(\frac{2}{3} r_2^2 - \frac{1}{3} r_1 \cdot r_2 - \frac{1}{3} r_1^2 \right) \tag{D.22}$$

$$k = \frac{\rho \cdot (t_2 - t_1) \cdot \left(2r_2^2 - r_1 \cdot r_2 - r_1^2 \right)}{2 \cdot \left(r_2^3 - r_1^3 \right)} \tag{D.23}$$

Inserting equation D.23 into equation D.19 results in equation D.24.

$$\mathbf{I} = \frac{1}{2} \cdot \rho \cdot \pi \cdot r_2^4 \cdot t_1 + \frac{\pi \cdot \rho \cdot (t_2 - t_1) \cdot \left(2r_2^2 - r_1 \cdot r_2 - r_1^2 \right) \cdot \left(r_2^5 - r_1^5 \right)}{5 \cdot \left(r_2^3 - r_1^3 \right)} \tag{D.24}$$

Combining equations D.24 and D.16 results in the following specific moment of inertia.

$$\dot{I} = \frac{\frac{1}{2} \cdot r_2^4 \cdot t_1 + \frac{(t_2 - t_1) \cdot \left(2r_2^2 - r_1 \cdot r_2 - r_1^2 \right) \cdot \left(r_2^5 - r_1^5 \right)}{5 \cdot \left(r_2^3 - r_1^3 \right)}}{r_2^2 \cdot t_1 + (t_2 - t_1) \cdot \left(\frac{2}{3} r_2^2 - \frac{1}{3} r_1 \cdot r_2 - \frac{1}{3} r_1^2 \right)} \tag{D.25}$$

D.4. Parabolic Increasing Thickness

The manner of calculating the specific mass moment of inertia of the parabolic increasing thickness design must be done in sections. The mass and mass moment of inertia can be calculated in a similar manner to the last sections calculation.

$$\mathbf{m} = \rho \cdot \pi \cdot \left(r_2^2 \cdot t_1 + \left(r_2^2 \cdot (t_2 - t_1) - \int_0^{t_2 - t_1} \mathbf{r}^2 d\mathbf{t} \right) \right) = \rho \cdot \pi \cdot \left(r_2^2 \cdot t_1 \right) + \int_0^{2\pi} \int_{r_1}^{r_2} \rho(\mathbf{r}) \mathbf{r} d\mathbf{r} d\theta \tag{D.26}$$

$$\mathbf{I} = \frac{1}{2} \cdot \rho \cdot \pi \cdot r_2^4 \cdot t_1 + \int_0^{2\pi} \int_{r_1}^{r_2} \rho(\mathbf{r}) \mathbf{r}^3 d\mathbf{r} d\theta \tag{D.27}$$

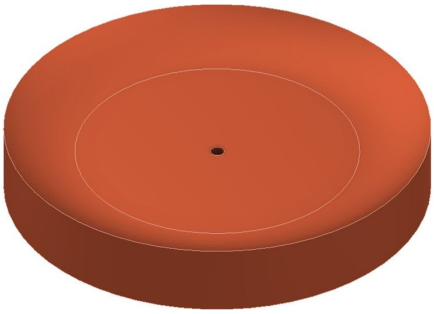

Figure D.13: ISO view of flywheel with parabolic increasing thickness.

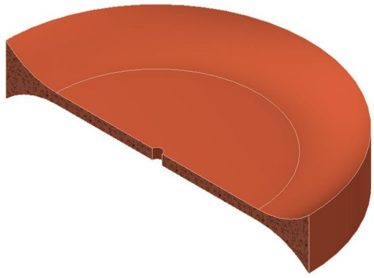

Figure D.14: Cross section ISO view of flywheel with parabolic increasing thickness.

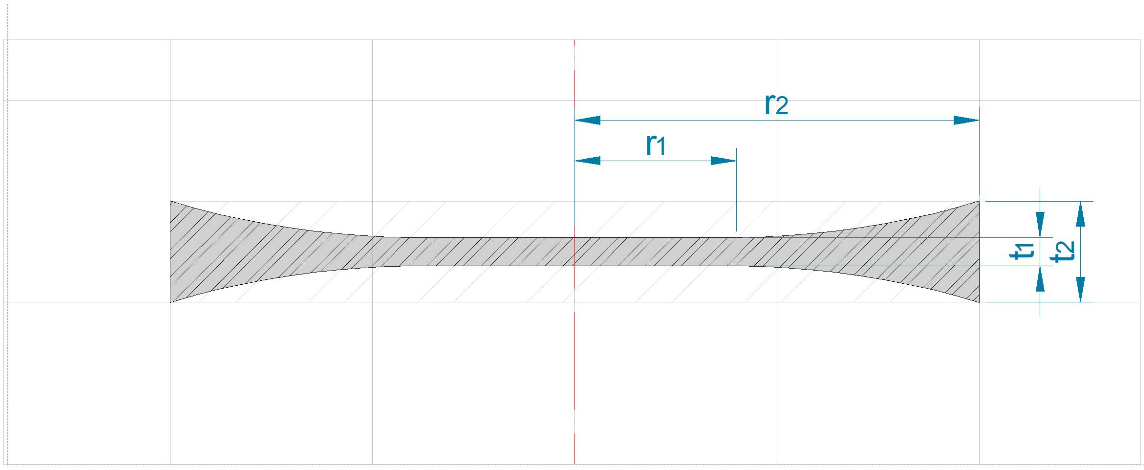

Figure D.15: Cross sectional drawing of the exponentially increasing thickness design with all variables noted.

The last two function rely on the changing thickness of the exponential part, which is a function of the radius. The cross sectional area of the disc design with a parabolic increasing thickness shows the way to interpret this relation. The parabolic increasing thickness will start at a certain r_1 and increase the thickness exponentially from t_1 to t_2 at r_2. This would result in the following relations for the dimensions.

$$\mathbf{t} = (t_2 - t_1) \cdot \left(\frac{\mathbf{r} - r_1}{r_2 - r_1} \right)^2 \tag{D.28}$$

$$\mathbf{r} = r_1 + (r_2 - r_1) \cdot \sqrt{\frac{\mathbf{t}}{t_2 - t_1}} \tag{D.29}$$

Working out the integral within the mass function in equation D.26, results in the following relation.

$$\mathbf{m} = \rho \cdot \pi \cdot \left(r_2^2 \cdot t_1 + \left(r_2^2 \cdot (t_2 - t_1) - \int_0^{t_2 - t_1} \left(r_1 + (r_2 - r_1) \cdot \sqrt{\frac{\mathbf{t}}{t_2 - t_1}} \right)^2 d\mathbf{t} \right) \right) \tag{D.30}$$

$$\mathbf{m} = \rho \cdot \pi \cdot \left(r_2^2 \cdot t_1 + \left(r_2^2 \cdot (t_2 - t_1) - \left[r_1^2 \cdot \mathbf{t} + \frac{4}{3} \frac{r_1 \cdot (r_2 - r_1)}{\sqrt{t_2 - t_1}} \cdot \mathbf{t}\sqrt{\mathbf{t}} + \frac{(r_2 - r_1)^2}{2 \cdot (t_2 - t_1)} \cdot \mathbf{t}^2 \right]_0^{t_2 - t_1} \right) \right) \tag{D.31}$$

$$\mathbf{m} = \rho \cdot \pi \cdot \left(r_2^2 \cdot t_1 + \left(r_2^2 \cdot (t_2 - t_1) - \left(r_1^2 \cdot (t_2 - t_1) + \frac{4}{3} r_1 \cdot (r_2 - r_1) \cdot (t_2 - t_1) + \frac{1}{2} (r_2 - r_1)^2 \cdot (t_2 - t_1) \right) \right) \right) \tag{D.32}$$

$$\mathbf{m} = \rho \cdot \pi \cdot \left(r_2^2 \cdot t_1 + (t_2 - t_1) \cdot \left(\frac{1}{2} r_2^2 - \frac{1}{3} r_1 \cdot r_2 - \frac{1}{6} r_1^2 \right) \right) \tag{D.33}$$

The changing density as stated in equation D.27 will be assumed to be equal to $k \cdot r^2$, with k as a constant which will be derived through the mass.

$$\mathbf{I} = \frac{1}{2} \cdot \rho \cdot \pi \cdot r_2^4 \cdot t_1 + \int_0^{2\pi} \int_{r_1}^{r_2} \left(k \cdot \mathbf{r}^5 \right) d\mathbf{r} d\theta \tag{D.34}$$

$$\mathbf{I} = \frac{1}{2} \cdot \rho \cdot \pi \cdot r_2^4 \cdot t_1 + \frac{\pi \cdot k}{3} \cdot \left[\mathbf{r}^6 \right]_{r_1}^{r_2} \tag{D.35}$$

$$\mathbf{I} = \frac{1}{2} \cdot \rho \cdot \pi \cdot r_2^4 \cdot t_1 + \frac{\pi \cdot k}{3} \cdot \left(r_2^6 - r_1^6 \right) \tag{D.36}$$

The mass of the parabolic part of the disc can be calculated utilising the same variable k, and it shall be equalled to the derivation of the mass of the parabolic part as stated in equation D.33.

$$\mathbf{m}_p = \int_0^{2\pi} \int_{r_1}^{r_2} \left(k \cdot \mathbf{r}^3 \right) d\mathbf{r} d\theta \tag{D.37}$$

$$\mathbf{m}_p = 2\pi \cdot k \cdot \left[\frac{1}{4} \mathbf{r}^4 \right]_{r_1}^{r_2} \tag{D.38}$$

$$\mathbf{m}_p = \frac{1}{2} \pi \cdot k \cdot \left(r_2^4 - r_1^4 \right) = \rho \cdot \pi \cdot (t_2 - t_1) \cdot \left(\frac{1}{2} r_2^2 - \frac{1}{3} r_1 \cdot r_2 - \frac{1}{6} r_1^2 \right) \tag{D.39}$$

$$k = \frac{\rho \cdot (t_2 - t_1) \cdot \left(3r_2^2 - 2r_1 \cdot r_2 - r_1^2 \right)}{3 \cdot \left(r_2^4 - r_1^4 \right)} \tag{D.40}$$

Inserting equation D.40 into equation D.36 results in equation D.41.

$$\mathbf{I} = \frac{1}{2} \cdot \rho \cdot \pi \cdot r_2^4 \cdot t_1 + \frac{\pi \cdot \rho \cdot (t_2 - t_1) \cdot \left(3r_2^2 - 2r_1 \cdot r_2 - r_1^2 \right) \cdot \left(r_2^6 - r_1^6 \right)}{9 \cdot \left(r_2^4 - r_1^4 \right)} \tag{D.41}$$

Combining equations D.41 and D.33 results in the following specific moment of inertia.

$$\dot{I} = \frac{\frac{1}{2} \cdot r_2^4 \cdot t_1 + \frac{(t_2 - t_1) \cdot \left(3r_2^2 - 2r_1 \cdot r_2 - r_1^2 \right) \cdot \left(r_2^6 - r_1^6 \right)}{9 \cdot \left(r_2^4 - r_1^4 \right)}}{r_2^2 \cdot t_1 + (t_2 - t_1) \cdot \left(\frac{1}{2} r_2^2 - \frac{1}{3} r_1 \cdot r_2 - \frac{1}{6} r_1^2 \right)} \tag{D.42}$$

D.5. Linear Hybrid Design

Using the previous made derivations stated in equation D.25, a new relation can be made utilising a new radius r_3, simply added into the equations of moment of inertia and mass, resulting in equation D.43.

$$\dot{I} = \frac{\frac{1}{2}\cdot(r_3^4 - r_2^4)\cdot t_2 + \frac{1}{2}\cdot r_2^4 \cdot t_1 + \frac{(t_2-t_1)\cdot\left(2r_2^2 - r_1\cdot r_2 - r_1^2\right)\cdot\left(r_2^5 - r_1^5\right)}{5\cdot\left(r_2^3 - r_1^3\right)}}{(r_3^2 - r_2^2)\cdot t_2 + r_2^2\cdot t_1 + (t_2 - t_1)\cdot\left(\frac{2}{3}r_2^2 - \frac{1}{3}r_1\cdot r_2 - \frac{1}{3}r_1^2\right)} \tag{D.43}$$

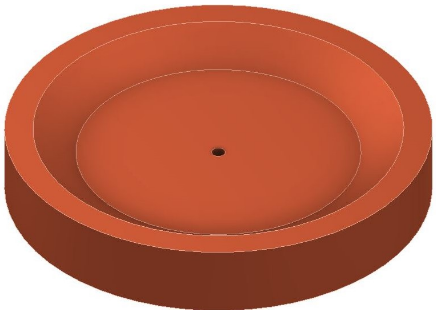

Figure D.16: ISO view of flywheel with hybrid linear design.

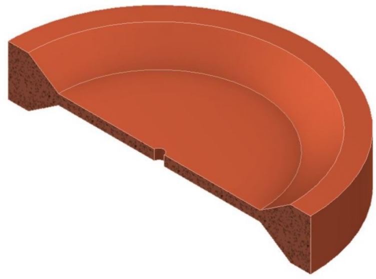

Figure D.17: Cross section ISO view of flywheel with hybrid linear design.

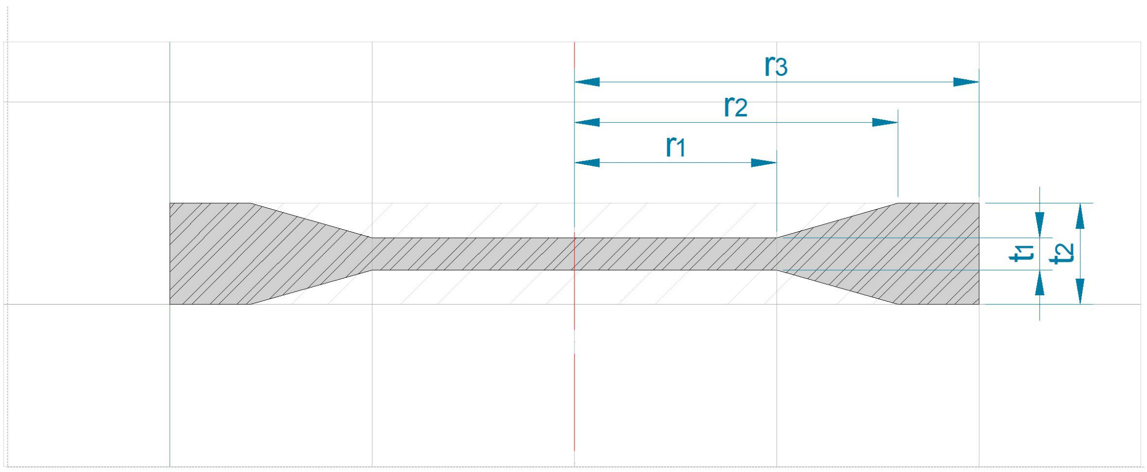

Figure D.18: Cross sectional drawing of the linearly increasing thickness hybrid design with all variables noted.

D.6. Parabolic Hybrid Design

Using the previous made derivations stated in equation D.42, a new relation can be made utilising a new radius r_3, simply added into the equations of moment of inertia and mass, resulting in equation D.44.

$$\dot{I} = \frac{\frac{1}{2}\cdot(r_3^4 - r_2^4)\cdot t_2 + \frac{1}{2}\cdot r_2^4 \cdot t_1 + \frac{(t_2-t_1)\cdot\left(3r_2^2 - 2r_1\cdot r_2 - r_1^2\right)\cdot\left(r_2^6 - r_1^6\right)}{9\cdot\left(r_2^4 - r_1^4\right)}}{(r_3^2 - r_2^2)\cdot t_2 + r_2^2\cdot t_1 + (t_2 - t_1)\cdot\left(\frac{1}{2}r_2^2 - \frac{1}{3}r_1\cdot r_2 - \frac{1}{6}r_1^2\right)} \tag{D.44}$$

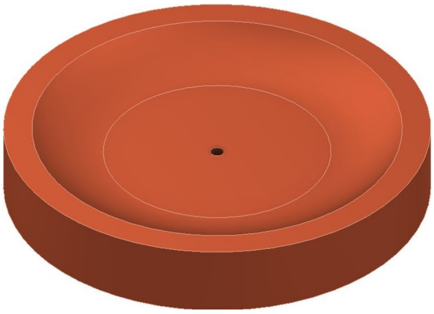

Figure D.19: ISO view of flywheel with hybrid parabolic design.

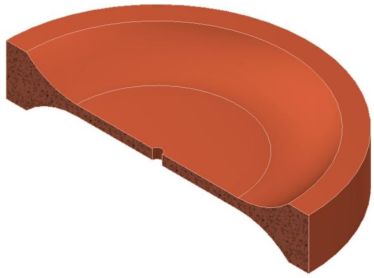

Figure D.20: Cross section ISO view of flywheel with hybrid parabolic design.

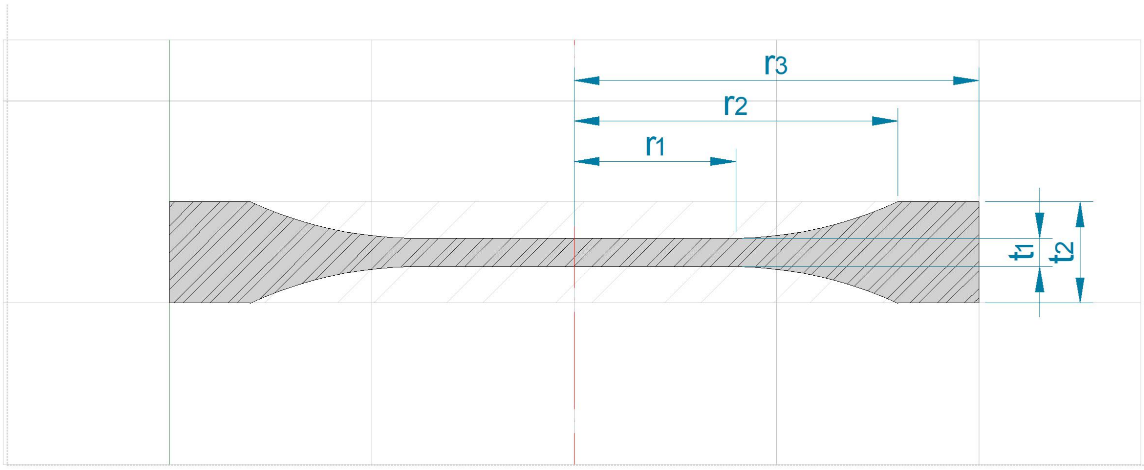

Figure D.21: Cross sectional drawing of the exponentially increasing thickness hybrid design with all variables noted.

Bibliography

[1] Adam Sidelsky (2020). Trapezoidal Motors vs. Sinusoidal Motors. https://e2e.ti.com/support/motor-drivers-group/motor-drivers/f/motor-drivers-forum/909911/faq-trapezoidal-motors-vs-sinusoidal-motors. Accessed: 07-07-2024.

[2] Agilent Technologies (2024). E3631A 80W Triple Output Power Supply. https://www.keysight.com/nl/en/assets/7018-06785/data-sheets/5968-9726.pdf. Accessed: 22-08-2024.

[3] Atzori, A. V. (2023). Satellite miniaturization study and experimental integration of reaction wheels in a pocketqube satellite. *Thesis Repository: Politecnico di Torino*.

[4] Baldacchino, D., Debattista, D., Rotin, R., Cachia, D., Azzopardi, M. A., Fabri, S. G., and Bugeja, M. K. (2017). Review and feasibility of active attitude control and detumbling for the uombsat-1 pocketqube pico-satellite. *Mediterranean Conference on Control and Automation (MED)*.

[5] Battista, D. D., Fabri, S. G., Bugeja, M. K., and Azzopardi, M. A. (2020). Pocketqube pico-satellite attitude control: Implementation and testing. *IEEE Journal on Miniaturization for Air and Space Systems*, 1:90–102.

[6] Bos, M. F. V. D. (2019). Design and testing of magnetic torquers for pico satellite attitude control electric magnetic torquers for dell pocketqube satellites. *Thesis Repository: Delft University of Technology*.

[7] Bouwmeester, J. (2018). Pq9 & cs14 electrical and mechanical subsystem interface standard for pocketqubes and cubesats.

[8] Bouwmeester, J. (2021). The architecture of cubesats and pocketqubes towards a lean and reliable implementation of subsystems and their interfaces. *[Dissertation (TU Delft), Delft University of Technology]*.

[9] Bouwmeester, J. and Guo, J. (2010). Survey of worldwide pico- and nanosatellite missions, distributions and subsystem technology. *Acta Astronautica*, 67:854–862.

[10] Bouwmeester, J., Radu, S., Uludag, M. S., Chronas, N., Speretta, S., Menicucci, A., and Gill, E. K. (2020). Utility and constraints of pocketqubes. *CEAS Space Journal*, 12:573–586.

[11] Buttery, M. (2010). An evaluation of liquid, solid, and grease lubricants for space mechanisms using a spiral orbit tribometer.

[12] Cachia, D., Camilleri, J., Azzopardi, M., Azzopardi, M. A., Angling, M., and Sammut, A. (2016). Feasibility study of a pocketqube platform to host an ionospheric impedance probe. https://www.researchgate.net/publication/307876621.

[13] Cengel, Y. A. and Cimbala, J. M. (2018). *Fluid Mechanics Fundamental and Application*. McGraw-Hill Education, 4th edition.

[14] Chulliat, A., Meyer, B., Paniccia, M., Brown, W., Alken, P., Beggan, C., Nair, M., Cox, G., Woods, A., and Macmillan, S. (2020). The us/uk world magnetic model for 2020-2025. *National Centers for Environmental Information, NOAA*.

[15] CubeSpace (2023). ADCS Actuators Gen 2. www.cubespace.co.za. Accessed: 21-3-2024.

[16] Delft University of Technology (2024). DEMO Faciliteiten. https://www.tudelft.nl/demo/faciliteiten. Accessed: 25-06-2024.

[17] Douglas, E. S., Tracy, K., and Manchester, Z. (2021). Practical limits on nanosatellite telescope pointing: The impact of disturbances and photon noise. *Frontiers in Astronomy and Space Sciences*, 8.

[18] Dursch, H. W., Keough, B. K., and Pippin, H. G. (1995). Evaluation of adhesive materials used on the long duration exposure facility.

[19] ECSS Secretariat (2020). Space engineering - Space environment (ECSS-E-ST-10-04C-Rev.1). https://ecss.nl/standard/ecss-e-st-10-04c-rev-1-space-environment-15-june-2020/. Accessed: 17-04-2024.

[20] ESA Space Debris Mitigation Working Group (2023). ESA Space Debris Mitigation Requirements (ESSB-ST-U-007 Issue 1). https://technology.esa.int/upload/media/DGHKMZ_6542582e18e33.pdf. Accessed: 17-04-2024.

[21] Faulhaber (2024). Drive Systems; Standard product portfolio. https://cdn.faulhaber.com/media/DAM/Documents/Datasheets%20Portfolio%20Collection/standard-datasheets-portfolio-en.pdf. Accessed: 22-05-2024.

[22] Fonod, R. . and Gill, E. (2018). Magnetic detumbling of fast-tumbling picosatellites. *Proceedings of 69th International Astronautical Congress: Bremen, Germany*, pages 1–5.

[23] Gaude, A. and Lappas, V. (2020). Design and structural analysis of a control moment gyroscope (cmg) actuator for cubesats. *Aerospace*, 7.

[24] Gleydura, A. and Mackunis, W. (2023). Pico-torquer: Magnetorquer-only attitude control for a 1p pocketqube using pcb-embedded coils. https://gitlab.com/deepspace-engineering.

[25] Gurrisi, C., Seidel, R., Dickerson, S., Didziulis, S., Frantz, P., and Ferguson, K. (2010). Space station control moment gyroscope lessons learned. *Proceedings of the 40th Aerospace Mechanisms Symposium, NASA Kennedy Space Center*.

[26] Hall, N. (2021). Earth atmosphere model; metric units. https://www.grc.nasa.gov/www/k-12/airplane/atmosmet.html. Accessed: 13-04-2024.

[27] Hoevenaars, A. G. L. (2012). Design, integration and verification of the delfi-n3xt reaction wheel system.

[28] Keysight (2024). Keysight 34401A 6½ Digit Multimeter. https://www.keysight.com/nl/en/assets/9018-01063/user-manuals/9018-01063.pdf. Accessed: 22-08-2024.

[29] Lappas, V., Oosthuizen, P., Madle, P., Cowie, L., Gokhan, Y., and Fertin, D. (2005). Micro cmgs for agile small satellites: Design and in-orbit tests. https://www.researchgate.net/publication/234224351.

[30] Maxon Group (2024). Production Range 2024/25. https://online.flippingbook.com/view/1042987/. Accessed: 22-05-2024.

[31] Maxon Motors (2024a). Brushed DC motors. https://www.maxongroup.com/en/drives-and-systems/brushed-dc-motors. Accessed: 04-06-2024.

[32] Maxon Motors (2024b). Brushless DC motors with ironless or iron core winding. https://www.maxongroup.com/en/drives-and-systems/brushless-dc-motors. Accessed: 04-06-2024.

[33] McDowell, J. C. (2020). The low earth orbit satellite population and impacts of the spacex starlink constellation. *The Astrophysical Journal Letters*, 892:L36.

[34] Monolithic Power Systems (2024). Brushless Vs Brushed DC Motors: When and Why to Choose One Over the Other. https://www.monolithicpower.com/brushless-vs-brushed-dc-motors. Accessed: 04-06-2024.

[35] NSK (2016). Rolling Bearings for Industrial Machinery. https://www.nsk.com/content/dam/nsk/common/catalogs/ctrgPdf/bearings/e1103b.pdf. Accessed: 29-5-2024.

[36] NSK (2024). SpaceA; Bearings, Ball Screws and NSK linear Guides, for Special Environments. https://www.nsk.com/content/dam/nsk/common/catalogs/ctrgPdf/bearings/e1258f.pdf. Accessed: 29-5-2024.

[37] Our World in Data (2019). Cost of space launches to low Earth orbit. https://ourworldindata.org/grapher/cost-space-launches-low-earth-orbit?time=2016..latest&country=Electron~Shian+Quxian. Accessed: 29-03-2024.

[38] Paluszek, M. (2023). *ADCS - Spacecraft Attitude Determination and Control*. Elsevier.

[39] Portescap (2024). Product Catalog; Miniature motion solutions for perfomance critical applications. https://www.portescap.com/-/media/project/automation-specialty/portescap/portescap/pdf/full-catalog/digital_product_catalog.pdf. Accessed: 22-05-2024.

[40] Radu, S., S., U., Speretta, S., Bouwmeester, J., Dunn, A., Walkinshaw, T., Cas, P. K. D., and Cappelletti, C. (2018a). *The PocketQube Standard*.

[41] Radu, S., Uludag, S., Speretta, S., Bouwmeester, J., Gill, E., and Foteinakis, N. (2018b). Delfi-PQ: The first pocketqube of Delft University of Technology. In *Proceedings of 69th International Astronautical Congress: Bremen, Germany*. International Astrnautical Federation, IAF.

[42] Reichel, F., Bangert, P., Busch, S., Ravandoor, K., and Schilling, K. (2013). The attitude determination and control system of the picosatellite UWE-3. *IFAC Proceedings Volumes (IFAC-PapersOnline)*, 19:271–276.

[43] Rothstein, B. (2024). How market volatility affects steel prices and order quantities. https://www.meadmetals.com/blog/how-market-volatility-affects-steel-prices-and-order-quantities. Accessed: 20-06-2024.

[44] Rózewicz, M. (2014). Shape Optimization of a Flywheel. *AUTOMATYKA/AUTOMATICS*, 18.

[45] Sellers, R. (2013). A gravity gradient, momentum-biased attitude control system for a cubesat.

[46] SpaceX (2021). Falcon User's Guide. https://www.spacex.com/media/falcon-users-guide-2021-09.pdf. Accessed: 17-04-2024.

[47] Speretta, S. ., Soriano, T., Bouwmeester, J. ., Godínez, J., Menicucci, A. ., Watts, T. ., Sundaramoorthy, P. ., Guo, J. ., and Gill, E. . (2016). Cubesats to pocketqubes opportunities and challenges cubesats to pocketqubes: Opportunities and challenges.

[48] Starin, S. R. and Eterno, J. (2011). Attitude determination and control systems.

[49] Steyn, W. H. and Kearney, M.-A. (2014). An attitude control system for za-aerosat subject to significant aerodynamic disturbances.

[50] Streetman, B., Shoer, J., and Singh, L. (2017). Limitations of scaling momentum control strategies to small spacecraft.

[51] Swift, K. G. and Booker, J. B. (2013). *Manufacturing Process Selection Handbook*, volume 1. Butterworth-Heinemann.

[52] Takatsuka, N., Yamada, K., and Jikuya, I. (2010). Original paper spacecraft attitude control using a double-gimbal control moment gyro.

[53] Tektronix (2024). 2 Series Mixed Signal Oscilloscope Datasheet. https://www.tek.com/en/datasheet/2-series-mso-mixed-signal-oscilloscope-datasheet. Accessed: 22-08-2024.

[54] Vergoossen, T. (2017). Design, integration and testing of the pocketqube reaction wheel. *Thesis Repository: Delft University of Technology*.

[55] Wertz, J. R., Everett, D. F., and Puschell, J. J. (2015). *Space Mission Engineering: The New SMAD*. Microcosm Press.

[56] Xiang, T., Meng, T., Wang, H., Han, K., and Jin, Z. H. (2012). Design and on-orbit performance of the attitude determination and control system for the zdps-1a pico-satellite. *Acta Astronautica*, 77:182–196.

[57] Zhou, W. Y., Aglietti, G. S., and Zhang, Z. (2011). Modelling and testing of a soft suspension design for a reaction/momentum wheel assembly. *Journal of Sound and Vibration*, 330:4596–4610.